Zhengshun Cheng

Integrated Dynamic Analysis of Floating Vertical Axis Wind Turbines

Thesis for the degree of Philosophiae Doctor

Trondheim, March 2016

Norwegian University of Science and Technology
Faculty of Engineering Science and Technology
Department of MarineTechnology

NTNU
Norwegian University of
Science and Technology

NTNU
Norwegian University of Science and Technology

Thesis for the degree of Philosophiae Doctor

Faculty of Engineering Science and Technology
Department of MarineTechnology

ISBN 978-82-326-1692-3 (printed version)
ISBN 978-82-326-1693-0 (electronic version)
ISSN 1503-8181

Doctoral theses at NTNU, 2016:177

Printed by Skipnes Kommunikasjon as

Abstract

In recent years offshore wind power has been playing an increasingly vital role in the wind energy market. Wind turbines are usually categorized into horizontal axis wind turbines (HAWTs) and vertical axis wind turbines (VAWTs). Currently offshore wind turbines installed are mainly bottom-fixed HAWTs. Floating HAWTs are also widely studied for deep water application, and several prototypes have been developed and tested at sea. The VAWT, which was commercialized in the USA in the 1980s, lost the competition with the HAWT because of its low efficiency and severe fatigue problems.

However, as wind farms are moving towards deeper water, the floating VAWT seems to be a very promising alternative to the floating HAWT due to its potential cost-of-energy reduction. Hence, the interest in the development of VAWTs for offshore application has been resurging.

State of the art the development of floating VAWTs is still at an early stage. Available fully coupled simulation tools for floating VAWTs are still very limited, and more sophisticated simulation tools are required, so that the dynamic response characteristics of different floating VAWT concepts can be investigated in a fully integrated manner. Therefore, this thesis addresses the development, verification and application of fully integrated methods for numerical modeling and dynamic analysis of floating VAWTs.

An aerodynamic model, based on the actuator cylinder (AC) flow model, was established for floating VAWTs. It accounts for the effect of wind shear and turbulence, dynamic inflow as well as dynamic stall using the Beddoes-Leishman model. It has been verified by comparison with the double multi-streamtube (DMS) model and validated with experimental data.

The developed AC model was coupled with the SIMO-RIFLEX code to achieve a fully coupled simulation tool, namely SIMO-RIFLEX-AC, for numerical modeling and dynamic analysis of floating VAWTs. The aerodynamics, hydrodynamics, structural dynamics and control system dynamics are considered systematically with high fidelity. This tool has been extensively verified by a series of code-to-code comparisons.

Fully coupled time domain simulations were carried out to investigate the dynamic response characteristics of different floating VAWT concepts with curved and straight blades. Considering floating VAWTs with straight and parallel blades, with identical solidity and with a blade number ranging from two to four, the effect of blade number on the dynamics was comprehensively studied. It was found that the aerodynamic loads and structural responses are strongly dependent on the number of blades, while the gener-

ator power production, platform motions and tension in mooring lines are not. In particular, by increasing the number of blades from two to three reduces the variation in the tower base bending moment more significantly than increasing it from three to four.

Dynamic responses of a spar, semi-submersible and TLP VAWT with a two-bladed Darrieus rotor were thoroughly investigated. A significant response at the 2P (twice per revolution) frequency has been demonstrated and can be mitigated by a compliant catenary mooring system.

The effect of difference-frequency force and wave-wind misalignment on the dynamics of a semi-submersible VAWT with a two-bladed Darrieus rotor was also studied. It has been shown that the mean values of global responses are not significantly affected by the wave-wind misalignment. Their standard deviations and maximum values are slightly more sensitive to the wave-wind misalignment and second-order difference-frequency force, especially at high significant wave height conditions.

In addition, a comparative study on the dynamics of a spar-type HAWT and VAWT was conducted, which indicated that due to different aerodynamic load characteristics and control strategies, the current design of the spar VAWT leads to larger mean values and standard deviations in the tower and mooring lines and requires further improvements.

As a whole, a fully coupled method for numerical modeling and analysis of floating VAWTs is developed, verified and applied to reveal the dynamic response characteristics of different floating VAWT concepts. The demonstration of the merits and disadvantages of different floating VAWT concepts can serve as a basis for their further development and will improve their competitiveness in the future wind energy market.

Preface

This thesis is submitted to the Norwegian University of Science and Technology (NTNU) for partial fulfilment of the requirements for the degree of philosophiae doctor.

This doctoral work has been carried out at the Department of Marine Technology, Centre for Ships and Ocean Structures (CeSOS), and Centre for Autonomous Marine Operations and Systems (AMOS), NTNU, Trondheim, Norway, with Professor Torgeir Moan as main supervisor and with co-supervisors Professor Zhen Gao at Department of Marine Technology, NTNU and Professor Helge Aagaard Madsen at Department of Wind Energy, Technical University of Denmark (DTU), Denmark.

The work was financially supported by the EU FP7 Marie Curie ITN project MARE WINT (Project NO. 309395) and the Research Council of Norway through the Department of Marine Technology, CeSOS and AMOS, NTNU from June 2013 to May 2016. This support is greatly appreciated.

Acknowledgement

First and foremost, I would like to express my deepest gratitude to my supervisor Professor Torgeir Moan. He gave me the chance to pursue my PhD at NTNU, provided me careful guidances and enlightening instructions to overcome scientific challenges, and encouraged me to become an independent researcher. I gained a lot from his deep knowledge, experience and enthusiasm on scientific research.

I would like to extend my gratitude to my co-supervisor Professor Zhen Gao. During the three years of PhD study, he always gave me generous support and guidance, insightful discussions and comments about my work. I would also like to deeply thank my co-supervisor Professor Helge Aagaard Madsen from DTU, Denmark. He gave me careful guidance on the development of aerodynamic code, and provided valuable discussions and comments about my research.

I would like to appreciate the time and work of my thesis committee members: Professor Carlos Simão Ferreira, Dr. Maurizio Collu and Professor Jørgen R. Krokstad.

I appreciate the Department of Wind Energy for kindly hosting me during my visit at DTU, Denmark. I would also like to thank Mr. Torben Juul Larsen and Anders Yde for kindly discussions and comments, and Mrs Naja Møller and Dr. Flemming Rasmussen for their kindly help.

I am very grateful to Dr. Kai Wang for his generous help and valuable discussions and comments. I would also like to thank Dr. Erin Bachynski for her help on the compiling of dynamic link library between the aerodynamic code and SIMO/RIFLEX. I am thankful to my colleagues and friends at NTNU, Wilson Guachamin Acero, Xiaopeng Wu, Lin Li, Zhiyu Jiang, Wei Chai, Yugao Shen, Zhaolong Yu, Ling Wan, Ming Song, Amir R. Nejad, Yuna Zhao, to name a few who are always helpful. I would also like to appreciate the kind help from the administrative staffs, including Sigrid Bakken Wold, Annika Bremvåg, Marit Nordtiller, Oddny Kristine Østhus, and Jannike Gripp.

Finally, I would like to give my special thanks to my parents in China. Without their encouragement and love, I can never reach where I am today.

Zhengshun Cheng
May 2016
Trondheim, Norway

List of Appended Papers

This thesis consists of an introductory part, six papers and some additional work.
The following six papers are given in the Appendix A.

Paper 1:
Aerodynamic modeling of floating vertical axis wind turbines using the actuator cylinder flow method.
Zhengshun Cheng, Helge Aagaard Madsen, Zhen Gao, Torgeir Moan
Revision submitted to *Energy Procedia*, 2016

Paper 2:
A fully coupled method for numerical modeling and dynamic analysis of floating vertical axis wind turbines.
Zhengshun Cheng, Helge Aagaard Madsen, Zhen Gao, Torgeir Moan
Submitted to *Renewable Energy*, 2016

Paper 3:
Effect of the number of blades on the dynamics of floating straight-bladed vertical axis wind turbines.
Zhengshun Cheng, Helge Aagaard Madsen, Zhen Gao, Torgeir Moan
Submitted to *Renewable Energy*, 2016

Paper 4:
Dynamic response analysis of three floating wind turbine concepts with a two-bladed Darrieus rotor.
Zhengshun Cheng, Kai Wang, Zhen Gao, Torgeir Moan
Published in *Journal of Ocean and Wind Energy*, 2:213-222, 2015, DOI: 10.17736/jowe.2015.jcr33

Paper 5:
Effect of difference-frequency forces on the dynamics of a semi-submersible type FVAWT in misaligned wave-wind condition.
Kai Wang, Zhengshun Cheng, Torgeir Moan, Martin Otto Laver Hansen
Published in *Proceedings of the Twenty-fifth (2015) International Ocean and Polar Engineering Conference*, Kona, Big Island, Hawaii, USA, June 21-26, 2015

Paper 6:

A comparative study on dynamic responses of spar-type floating horizontal and vertical axis wind turbines.
Zhengshun Cheng, Kai Wang, Zhen Gao, Torgeir Moan
Revision submitted to *Wind Energy*, 2016

Declaration of Authorship

All the six papers that serve as the core content of this thesis are co-authored. For *papers 1, 2, 3, 4 and 6*, I was the first author and responsible for initiating ideas, establishing the models, performing the calculations, providing and analyzing the results, and writing the papers. Professors Torgeir Moan and Zhen Gao have contributed to providing the support, helpful corrections and constructive comments to increase the scientific quality of the publications. Professor Helge Aagaard Madsen (the second coauthor in *papers 1, 2 and 3*) assisted to develop the AC model, and provided helpful corrections and valuable comments. Dr. Kai Wang (the second coauthor in *papers 4 and 6*) provided kind helps on use of the SIMO-RIFLEX-DMS code and also gave valuable comments.

Regarding the *paper 5*, I was the second author and responsible for calculating the mean drift force and second order difference frequency force, analyzing the results, plotting the figures and contributing to writing sections of methodology, load cases, and results and discussions. Dr. Kai Wang initiated the idea and wrote the other part. Professor Torgeir Moan and Associate Professor Martin Otto Laver Hansen gave valuable comments for this paper.

Additional Papers

The following publications have been produced during the doctoral work but are not included in this thesis.

Paper 7:

Dynamic modelling and analysis of three floating wind turbine concepts with vertical axis rotor.

Zhengshun Cheng, Kai Wang, Zhen Gao, Torgeir Moan

Proceedings of the Twenty-fifth (2015) *International Ocean and Polar Engineering Conference*, Kona, Big Island, Hawaii, USA, June 21-26, 2015

(Not included because of the overlap with *Paper 4*)

Paper 8:

Comparative study of spar type floating horizontal and vertical axis wind turbines subjected to constant winds.

Zhengshun Cheng, Kai Wang, Zhen Gao, Torgeir Moan

Proceedings of the EWEA Offshore 2015, Copenhagen, Denmark

(Not included because of the more comprehensive study in *Paper 6*)

Paper 9:

Dynamic response analysis of floating wind turbines with emphasis on vertical axis rotors.
Zhengshun Cheng, Torgeir Moan, Zhen Gao
Book chapter in Wieslaw Ostachowicz, Malcolm McGugan, Jens Uwe Schröder Hinrichs and Marcin Luczac (Eds): *MARE-WINT, New Materials and Reliability in Offshore Wind Turbine Technology.* Springer. 2016
(Not included since it is a summary of *Papers 1, 2, 4 and 6*)

Abbreviations

2P	Twice per revolution
AC	Actuator Cylinder
BEM	Blade Element Momentum
CACTUS	Code for Axial and Cross-flow TUrbine Simulation
CALHYPSO	CALcul HYdrodynamique Pour les Structures Offshore
CFD	Computational Fluid Dynamics
DLL	Dynamic Link Library
DMS	Double Multi-Streamtube
EDF	Electricité de France
EU	European Union
FAST	Fatigue, Aerodynamics, Structures and Turbulence
FHAWT	Floating Horizontal Axis Wind Turbine
FloVAWT	Floating Vertical Axis Wind Turbines
FP7	7th Framework Programme
FVAWT	Floating Vertical Axis Wind Turbine
GDW	Generalized Dynamic Wake
GW	Gigawatt
HAWC2	Horizontal Axis Wind turbine simulation Code 2nd generation

HAWT	Horizontal Axis Wind Turbine
IEC	International Electrotechnical Commission
JONSWAP	Joint North Sea Wave Project
LC	Load Case
MARIN	Maritime Research Institute Netherlands
MSS	Marine Systems Simulator
MW	Megawatt
NREL	National Renewable Energy Laboratory
OC3	Offshore Code Comparison Collaboration
OC4	Offshore Code Comparison Collaboration Continuation
OWENS	Offshore Wind ENergy Simulation
PI	Proportional-Integral (control)
QTF	Quadratic Transfer Function
RAO	Response Amplitude Operator
TLP	Tension Leg Platform
VAWT	Vertical Axis Wind Turbine
WAMIT	Wave Analysis Massachusetts Institute of Technology

Contents

List of Tables **xv**

List of Figures **xvii**

1 Introduction **1**
1.1 Background & Motivation 1
1.2 Floating Vertical Axis Wind Turbines 4
1.2.1 Floating VAWT concepts 6
1.2.2 Fully coupled simulation tools of floating VAWTs . . . 8
1.2.3 State of the art study on dynamic behavior of floating VAWTs 11
1.3 Aim & Scope 14
1.4 Thesis Outline 17

2 Aerodynamics of a Vertical Axis Wind Turbine **19**
2.1 Overview of Aerodynamic Models 19
2.2 Double Multi-Streamtube (DMS) Model 21
2.3 Actuator Cylinder (AC) Flow Model 23
2.3.1 Linear solution 24
2.3.2 Modified linear solution 25
2.3.3 Dynamic stall and dynamic inflow 26
2.4 Validation of the Present Models 27

3 Integrated Modeling of a Floating VAWT System **29**
3.1 General 29
3.2 Fully Coupled Methods for Floating VAWTs 29
3.2.1 Aerodynamics 32
3.2.2 Hydrodynamics 32
3.2.3 Structural dynamics 33
3.2.4 Control system 33

3.3 Code-to-code Comparisons of the Fully Coupled Tools 36

4 Landbased and Floating Wind Turbine Concepts 39
4.1 VAWT Concepts with a Two-bladed Darrieus Rotor 39
4.2 VAWT Concepts with Straight Blades 41
4.3 HAWT Concepts 43
4.4 Environmental Conditions 44

5 Dynamic Response Analysis of Floating VAWTs 47
5.1 General 47
5.2 Dynamic Analysis of Floating VAWTs with Straight Blades . 47
5.3 Dynamic Analysis of a Spar, Semi-submersible and TLP VAWT 52
5.4 Effect of Difference-frequency Force on the Dynamics of a Semi-submersible VAWT in Misaligned Wave-wind Conditions 56
5.5 Comparative Study of Spar-type HAWT and VAWT 60

6 Conclusions and Recommendations for Future Work 65
6.1 Conclusions 65
6.2 Original Contributions 68
6.3 Recommendations for Future Work 69

References 71

A Appended papers 81
A.1 Paper 1 81
A.2 Paper 2 97
A.3 Paper 3 129
A.4 Paper 4 157
A.5 Paper 5 169
A.6 Paper 6 179

B List of previous PhD theses at Dept. of Marine Tech. 209

List of Tables

1.1 Current floating VAWT concepts 7
1.2 Current coupled codes for floating VAWTs 9

4.1 Specifications of the Darrieus 5 MW wind turbine 40
4.2 Properties of the three floating wind turbine systems 40
4.3 Specifications of three straight-bladed VAWTs. 41
4.4 Properties of three floating straight-bladed VAWT systems. . 42
4.5 Specifications of HAWT and VAWT 44
4.6 Properties of the spar-type HAWT and VAWT system . . . 45
4.7 The turbulent wind and irregular wave condition 46

List of Figures

1.1 Global cumulative installed wind capacity 2000-2015 2
1.2 Substructures for offshore wind turbines. 3
1.3 Horizontal and vertical axis wind turbines. 3
1.4 Current floating VAWT concepts. 6
1.5 Scope of this thesis and interconnection between the appended papers. 15

2.1 Double Multiple-Streamtube (DMS) model for a Darriues wind turbine. 22
2.2 The Actuator Cylinder (AC) flow model representation of a VAWT. 23
2.3 Flow chart of modeling of a floating VAWT using AC method. 27
2.4 Comparison of power coefficient curve between simulation model and experimental data. 28

3.1 Overview of the fully coupled simulation tool SIMO-RIFLEX-AC and SIMO-RIFLEX-DMS. 30
3.2 The structural model and external force model of a floating VAWT. 31
3.3 The generator torque control algorithm for a floating VAWT based on a PID architecture. 34
3.4 The relationship between the reference rotor rotational speed and wind speed for the baseline and improved controller. . . . 35
3.5 Comparison of the rotational speed, thrust, side force and aerodynamic torque of the landbased VAWT using three codes with U_w=8 m/s. 37
3.6 Comparison of the rotational speed, thrust, side force and aerodynamic torque of the landbased VAWT using three codes with U_w=14 m/s. 37

3.7 Comparison of simulated blade normal force F_n and tangential force F_t at midpoint of the blade using SIMO-RIFFLEX-AC and HAWC2. 38
3.8 Mean values and standard deviations of tower base fore-aft bending moment M_{FA} and side-side bending moment M_{SS} of the semi VAWT simulated using SIMO-RIFLEX-AC and SIMO-RIFLEX-DMS. 38

4.1 Landbased and floating VAWT concepts with a two-bladed Darrieus rotor: landbased, spar, semi-submersible and TLP. 40
4.2 Sketch of landbased and floating VAWT concepts with straight and parallel blades. 42
4.3 The mean value of the generator power of the landbased and floating VAWTs with the improved controller. 43
4.4 Schematic of the spar-type HAWT and VAWT system. 44

5.1 The mean value and standard deviation of the (a) generator power production, (b) thrust, (c) side force, and (d) rotor rotational speed of three floating VAWTs. 49
5.2 The mean value and standard deviation of the pitch and yaw motions of three floating VAWTs. 49
5.3 The mean value and standard deviation of tower base fore-aft and side-side bending moments of three floating VAWTs. . . 50
5.4 Power spectra of the tower base fore-aft bending moment and side-side bending moment of three floating VAWTs. 51
5.5 The mean value and standard deviation of the tension in mooring line 2 of three floating VAWTs. 52
5.6 Mean power production for the three floating VAWT concepts with error bar indicating the standard deviation. 53
5.7 Power spectra of tower base fore-aft and side-side bending moment for the three floating VAWT concepts. 54
5.8 Mean values, standard deviations, and maximum values of the tower base fore-aft bending moment for the three floating VAWT concepts. 55
5.9 A horizontal cross section of the rotor showing the wave direction distribution in misaligned wave-wind conditions. . . . 56
5.10 Standard deviations of the platform motions as a function of the wave direction β_{wave} for all load cases. 57

5.11 Mean value, standard deviation and maximum value of the tower base fore-aft bending moment M_{FA} and side-side bending moment M_{SS} as a function of wave direction β_{wave} for all load cases. 59
5.12 Mean values and standard deviations of generator power and thrust for the spar-type HAWT and VAWT. 61
5.13 Power spectra of the tower base fore-aft bending moment and side-side bending moment for the spar HAWT and VAWT. . 62
5.14 1 Hz damage equivalent fatigue loads (DEFLs) of the tower base fore-aft bending moment (M_{FA}) and side-side bending moment (M_{SS}) for the spar HAWT and VAWT. 62
5.15 1 Hz damage equivalent fatigue loads (DEFLs) of the tension in the lower lines and delta lines for the spar HAWT and VAWT. 63

Chapter 1

Introduction

1.1 Background & Motivation

Wind has a singular history among the prime movers for human beings [1]. It has been used for grinding grain, pumping water and sailing ships for over 3000 years. At the late nineteenth century, the wind turbine was initially developed and used to generate electricity by Charles Brush in the USA and by Poul la Cour in Denmark. In 1941, the world's first megawatt (MW) wind turbine, the 1.25 MW Smith-Putnam wind turbine, was built in the USA [2] and remained as the largest wind turbine ever built until 1979.

In recent years, the scientific investigation and technical development for exploiting energy from the wind has been increasingly simulated due to the global warming, environmental pollution and energy crisis all over the world. The global wind power industry has increased at a rapid pace by deploying megawatt scale wind turbines on land (onshore) or at sea (offshore). Figure 1.1 demonstrates the global cumulative installed wind capacity during 2000-2015 [3]. The global wind power installation increased by 63.01 GW in 2015, bringing the total installed capacity up to 432.42 GW. The new installed capacity is mainly driven by the continuing boom in the USA, Germany, and especially in China which contributed to a capacity of 30.5 GW, nearly half of 63.01 GW installed in 2015. Among the global wind power installation, offshore wind power currently makes up only a small percentage, reaching a total global installed capacity of 12.11 GW by the end of 2015 [3]. However, the offshore wind capacity was increased by 3.39 GW in 2015, which composed approximately 28% of the total installed offshore wind power up to now. Offshore wind power is playing and will play an increasingly vital role in the wind energy market.

To date, most offshore wind turbines are installed on fixed-bottom sup-

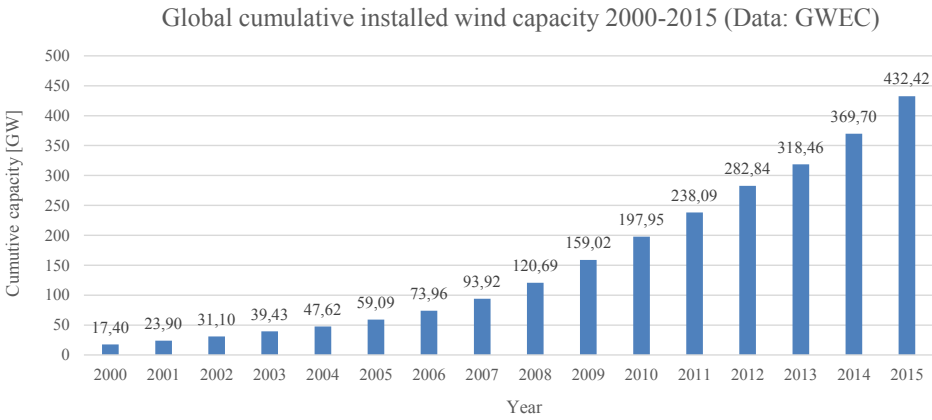

Figure 1.1: Global cumulative installed wind capacity 2000-2015 [3].

port structures, including gravity bases, monopiles used in water depth of about 30 m and jackets used in water to about 50 m [4], as shown in Figure 1.2. However, for countries like Norway, USA, China, Japan and many other countries, the vast offshore wind resource potential is located in deeper water, where the wind is generally stronger, less turbulent, and more consistent than onshore or near-shore [1]. In deeper water, floating support platform would be the more economical and thus more desirable. Based on the experience from the offshore oil and gas industry, several floating structures are feasible for offshore wind turbines and have been widely studied by many researchers, including the barge [5], spar [6, 7], semi-submersible [8, 9, 10, 11], and TLP [12, 13] combined with different mooring methods. In addition, floating prototype wind turbines have been developed and tested, such as the Hywind demo in Norway, the WindFloat demo in Portugal, the VolturnUS turbine off the coast of Maine in the USA, and the floating wind turbines off the Fukushima coast in northeast Japan and off the Goto island in southwest Japan.

Wind turbines can usually be categorized into horizontal axis wind turbines (HAWTs) and vertical axis wind turbines (VAWTs) in terms of the orientation of the rotating axis, as demonstrated in Figure 1.3. Currently, most commercial wind farms are using HAWTs, as aforementioned. However, the VAWT was also once commercialized by the FloWind Corporation in the USA in the 1980s [15]. Due to its low efficiency and fatigue problems within the bearings and blades, the VAWT gradually lost the competition with the HAWT.

Recently, as wind farms are moving towards deeper water, the traditional

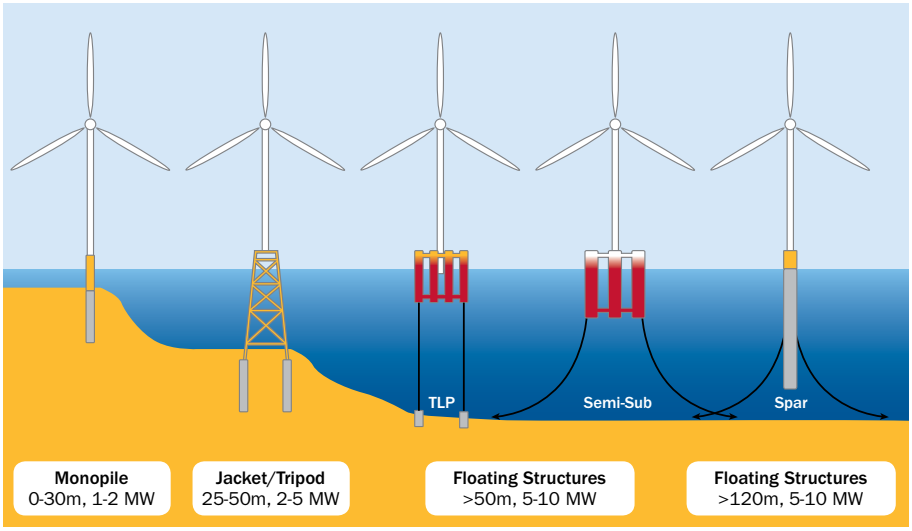

Figure 1.2: Substructures for offshore wind turbines: monopile, tripod/-Jacket, spar, semi-submersible and TLP [14].

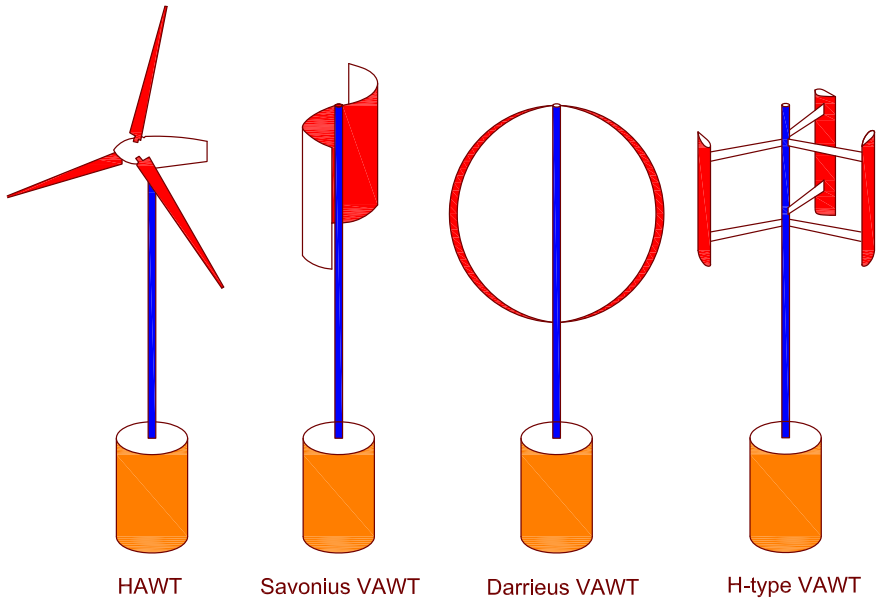

Figure 1.3: Horizontal and vertical axis wind turbines: HAWT, Savonius VAWT, Darrieus VAWT and H-type VAWT

floating HAWT concept is facing the challenge of much higher cost of energy compared to the onland or near-shore one. Due to its lower center of gravity, independence of wind direction, reduced machine complexity and excellent potential to reduce the cost of energy compared with the floating HAWT [16], the floating VAWT is a very promising alternative to harvest offshore wind energy resource. Hence, the interest in the development of VAWTs for offshore application has been resurging. Several floating VAWT concepts have been proposed, as summarized in Section 1.2.1.

State of the art the development of floating VAWT is still at an early stage. The available fully coupled simulation tool for floating VAWTs is very limited, and a more sophisticated simulation tool that integratedly considers the aerodynamics, hydrodynamics, structural dynamics and control system dynamics is required. The dynamic response characteristics of different floating VAWT concepts needs to be further investigated in a fully integrated approach.

This thesis aims to develop and verify a fully coupled method for numerical modeling and analysis of floating VAWTs and to demonstrate the dynamic response characteristics of different floating VAWT concepts. The revealed merits and disadvantages of different floating VAWT concepts will benefit their further development and improve their competitiveness in the future wind energy market.

1.2 Floating Vertical Axis Wind Turbines

Vertical axis wind turbines are a type of turbine where the blades rotate about a vertically-orientated main shaft, driving a generator to convert the mechanical power to electrical power directly or through a gearbox. They are generally categorized as drag driven type or lift driven type based on the aerodynamic characteristics, as depicted in Figure 1.3. The Savonius turbine is usually considered as a drag driven VAWT, while the Darrieus curve-bladed turbine and straight-bladed (H-type) turbine are regarded as lift-driven devices. Other VAWT configurations, such as the variable geometry oval trajectory Darrieus turbine, Darrieus-Masgrowe (two-tier) rotor, crossflex turbine, combine Savonius and Darrieus rotor, Zephyr turbine etc. are also proposed and used, as summarized by Aslam et al. [17]. Among these configurations, the lift-driven rotor with curved or straight blades has undergone considerable scientific research and technical development. They also represent the two rotor types considered in this thesis.

During the 1970s and 1980s, considerable efforts were devoted to investigate and develop Darrieus VAWTs, mainly in the USA and Canada [18].

Sandia National Laboratories proposed and tested a set of VAWTs with a size gradually increasing from 2 m to 34 m diameter and corresponding a power up to 500 kW. Based on the 34-m turbine, the FloWind Corporation in the USA developed and built two versions of commercial VAWTs with a diameter of 34 m and 38 m [19]. More than 500 turbines were installed in California's Altamont and Tehachapi passes, and the total installed capacity reached 95 MW by the end of 1985. Unfortunately, the turbines began collapsing because of fatigue failures in the joints between the sections of aluminum blades, and the the FloWind Corporation went bankrupt in 1997. After that, the VAWTs gradually lost the competition with the HAWTs in the commercial market and a variety of VAWTs are limited to small-scale individual use.

Compared with HAWTs, the most critical issues that limited the use of VAWTs in commercial wind farms were the low power efficiency and fatigue problem. However, the efficiency of a wind farm with VAWTs can be improved by optimizing the turbine distribution. Kinzel et al. [20] stated that the wake generated by a pair of counter-rotating H-type rotors can dissipate more quickly than the wake generated by HAWTs, allowing them to be installed in parks with smaller separations. Moreover, the average power generated by a pair of H-rotors at all azimuth angles is higher than that of an isolated turbine [21], implying that the conversion efficiency of VAWTs can be improved. The fatigue issue is usually caused by periodically varying aerodynamic loads, especially for VAWTs with two blades. Currently, it can be overcome by the use of modern composite materials [22]; it can also be alleviated by increasing the blade number [23], using helical blades, or employing a more advanced control strategy. Employing a catenary moored floating substructure can help to mitigate the fatigue damage at tower base suffered by the onshore VAWTs as well [24].

Therefore, VAWTs are very promising for offshore application and the key advantages can be summarized as follows [16, 25]:

- Insensitivity to wind direction
- Reduced mechanical complexity (no yaw control system, direct drive generator, etc.)
- Lower machinery position and reduced floater cost since the transmission and generation systems are located at the bottom, causing a lower center of gravity.
- Lower installation, operation and maintenance costs
- excellent potential in upscaling
- potentially high aerodynamic efficiency

1.2.1 Floating VAWT concepts

Due to the aforementioned features and advantages, the interest in the development of floating VAWTs has been stimulated and increased, and several floating VAWT concepts have recently been proposed, including the DeepWind [26, 27], Spinfloat [28], Aerogenerator X [29, 30], INFLOW [31], floating tilted axis [32] and Gwind [33] concepts, as depicted in Figure 1.4. A summary of these concepts with respect to their capacity, rotor and floater type, project or company name and region is given in Table 1.1.

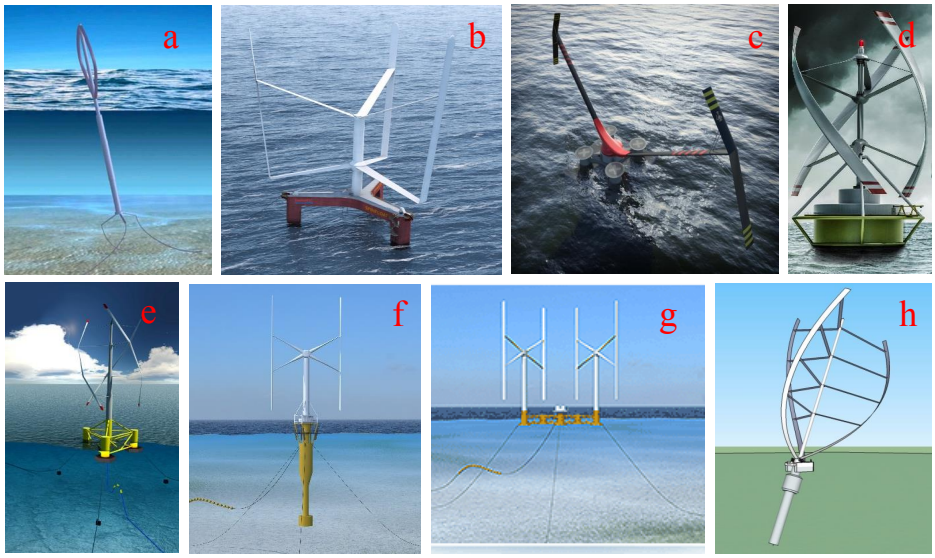

Figure 1.4: Current floating VAWT concepts: (a) DeepWind concept (b) Spinfloat (c)Aerogenerator X (d) Gwind concept (e, f, g) INFLOW concepts (h) floating tilted axis concept, see details in Table 1.1.

The DeepWind concept [26, 27] was proposed in the DeepWind project which was funded by the EU 7th Framework Programme (FP7) and aimed to develop a novel floating VAWT concept. The proposed concept is composed of a two-bladed 5 MW Darrieus rotor, a rotating spar buoy with torque arm at the bottom, and three catenary mooring lines. Model test in the MARIN (Maritime Research Institute Netherlands) and prototype demonstrator in Roskilde Fjord were carried out.

The Spinfloat [28] is an innovative floating VAWT concept developed by an French consortium EOLFI and launched in 2014. A vertical axis rotor with three straight blades is mounted on the Tri-Floater semi-submersible designed by GustoMSC [35]. Characterized by a vertical axis and pitched

Table 1.1: Current floating VAWT concepts

Concept	Source	Capacity	Rotor	Floater	Development status	Project or Company	Region
DeepWind	[26, 27]	5 MW	Darrieus curved blades	Spar	Prototype	DeepWind	EU
Spinfloat	[28]	6 MW	Straight blades	Semi-submersible	Concept	EOLFI	France
Aerogenerator X	[29, 30]	10 MW	V-shape blades	Semi-submersible	Concept	Wind Power Limited	UK
Gwind	[33]	-	Helical blades	Buoy	Prototype	Gwind	Norway
INFLOW I (VertiWind)	[34, 31]	2 MW	Helical blades	Semi-submersible	Concept	INFLOW	EU
INFLOW II	[31]	2 MW	Straight blades	Spar	Concept	INFLOW	EU
INFLOW III	[31]	2 MW	Two turbine with two straight blades each	Semi-submersible	Concept	INFLOW	EU
Floating tilted axis concept	[32]	3 MW	Curved blades	Spar	Concept	-	Korea & Japan

blades, Spinfloat exhibits an enhanced aerodynamic performance. Its prototype will be tested at sea according to the development pipeline [28].

The Aerogenerator X concept [29, 30] has a 10 MW vertical axis turbine supported by a semi-submersible. Different from other VAWT concepts, it uses a V-shape rotor which is half of the height of an equivalent horizontal axis turbine.

The Gwind concept [33] is a helical-bladed turbine designed by a Norwegian Gwind research project. Gwind is developing a gyro-stabilized floating VAWT for offshore and near shore applications. A prototype, Spinwind 1, has been built to explore the dynamic characteristics of this floating VAWT concept.

The INFLOW concepts, as illustrated in Figure 1.4 (e), (f) and (g), are three concepts developed in the INFLOW [31] project, which was also funded by the EU 7th Framework Programme (FP7) and aimed to demonstrate an innovative, competitive, robust and cost efficient solution for exploiting offshore wind resource. The INFLOW concept I, also known as the VertiWind concept [34], was a 2 MW three helical-bladed rotor mounted on a semi-submersible platform. This configuration can reduce the variation in aerodynamic loads acting on the rotor and mitigate the sway and yaw motions. The onshore prototype of the VertiWind project has been tested. This design has evolved toward an optimized system with two contra-rotating turbines with two straight blades each, as shown in Figure 1.4 (g).

The floating tilted axis turbine is a concept proposed by Akimoto et al. [32]. Preliminary estimation and comparisons were conducted and indicated that economic performance of the new concept can be higher than those of horizonal and vertical axis wind turbines.

1.2.2 Fully coupled simulation tools of floating VAWTs

A floating wind turbine system usually consists of a turbine harvesting wind energy, a floater supporting the rotor and a mooring system keeping the floater in position. Design and analysis of a floating wind turbine system require global response analysis for conceptual design and local structural analysis for detailed design. Global response analysis can evaluate its performance and also provide the basis for detailed structural design. In this thesis, global response analysis of floating wind turbine systems is emphasized.

To perform the global response analysis of a floating wind turbinesystem, a model should be developed to represent the dynamics of the rotor, floater and mooring system in a fully coupled way. In other words, a fully coupled aero-hydro-servo-elastic simulation tool is required to account for the aerodynamics, hydrodynamics, structural dynamics, control system dynamics and mooring line dynamics.

Such aero-hydro-servo-elastic simulation tools have been developed, verified and validated for floating HAWTs by several research institutes, such as the FAST (Fatigue, Aerodynamics, Structures and Turbulence) developed by NREL [36], the HAWC2 developed by DTU Wind Energy [37], the SIMO-RIFLEX-AeroDyn developed by NTNU/MARINTEK [38], the Bladed by Garrad Hassan [39] and so on. The dynamic behavior of a floating VAWT can be modeled in a similar way as that of a floating HAWT, but with different aerodynamic and control modules due to its distinct aerodynamic characteristic. Most fully coupled codes for floating HAWTs are based on the BEM (Blade Element Momentum) theory or GDW (Generalized Dynamic Wake) theory for aerodynamic loads prediction due to their accuracy and computational efficiency, while the DMS (double multi-streamtube) model or AC (actuator cylinder) flow model, as described in Sections 2.2 and 2.3, are usually employed for prediction of aerodynamic loads in the fully coupled analysis of floating VAWTs. Moreover, a generator torque controller and PI-based blade pitch controller are usually used for floating HAWTs, while floating VAWTs usually only employ a PI generator torque controller because of the fixed blade pitch angle. In addition, for both floating HAWTs and VAWTs the hydrodynamic loads are computed based on the potential flow theory and/or Morison's equation, and the structural dynamics of slender components, such as blades, tower and shaft, are usually modeled as flexible beam elements and calculated using the finite element method (FEM) or multi-body (MB) dynamics.

To date, several coupled simulation tools have been developed for floating VAWTs, such as the FloVAWT code by Cranfield University [40], the

CALHYPSO code from EDF [41], the OWENS toolkit by Sandia National Laboratories [42], the HAWC2 by DTU Wind Energy [43, 37], the SIMO-RIFLEX-DMS [44] and SIMO-RIFLEX-AC [45] code by NTNU/MARINTEK. Among these codes, the HAWC2 and SIMO-RIFLEX-AC code use the AC method to calculate the aerodynamic loads while the others mainly employ the DMS method. An overview of the capability of these codes is given in Table 1.2.

Table 1.2: Current coupled codes for floating VAWTs

	Aerodynamics (aero)	Hydrodynamics (hydro)	Structural dynamics (elastic)	Control system (servo)
FloVAWT[40]	DMS+Berg DS	Airy + PF + ME	-	-
CALHYPSO[41]	DMS+Berg DS	Airy + PF + ME	-	-
OWENS[42]	CACTUS	Airy + PF + ME	FEM	-
SIMO-RIFLEX-DMS[44]	DMS+BL DS	Airy + PF + ME	FEM	UD DLL
HAWC2[43, 37]	AC+Stig Øye DS	Airy + ME	MB	UD DLL
SIMO-RIFLEX-AC[45]	AC+BL DS	Airy + PF + ME	FEM	UD DLL

DMS: Double multi-streamtube; AC: Actuator cylinder; DS: Dynamic stall; BL: Beddoes-Leishman; Airy: Airy wave theory; PF: Potential flow; ME: Morison's equation; FEM: Finite element method; MB: Multi-body simulation; UD DLL: user defined external dynamic link library; CACTUS: Code for Axial and Cross-flow TUrbine Simulation.

To provide a simplified coupled tool for the preliminary design of floating VAWTs, Collu et al. [40] from the Cranfield University developed the FloVAWT (Floating Vertical Axis Wind Turbines) code. The aerodynamic load is computed based on the DMS model with modifications to include Gormont-Berg dynamic stall, tower shadow, tip losses, junction losses, and 3D effects. The hydrodynamic loads acting on the floater is estimated using the MSS (Marine Systems Simulator) toolbox [46], and including the 1st order wave excitation force, wave drift forces, state-space approximation of radiation force, linear damping and global quadratic drag force. Main drawbacks of this code are that the dynamic mooring model, structural dynamics and control system are missing [47].

The aero-hydro simulation code CALHYPSO (CALcul HYdrodynamique Pour les Structures Offshore) was developed for floating horizontal and vertical axis wind turbines at the EDF (Electricité de France), Chatou, France [41]. However, the structural elasticity and control system are neglected in the coupled code. The aerodynamic load is estimated using the DMS method including the Berg's dynamic stall model, while the effects of rotor deformability, dynamic inflow, streamtube expansion and local flow curvature are omitted. The hydrodynamic load is based on the 1st order potential flow theory and the viscous force is considered using Morison's equation.

The mooring system is simplified using a linearized or quasi-static mooring line model.

The OWENS (Offshore Wind ENergy Simulation) toolkit [42] was developed to evaluate innovative floating VAWT configurations by the Sandia National Laboratories in conjunction with its partner including the Texas A&M University and University of Maine. It aims at establishing a robust and flexible finite element framework and VAWT mesh generation utility, coupled with a modular interface that allows users to integrate easily with existing codes, such as aerodynamic and hydrodynamic codes. The finite element method is used with an energy preserving time integration method [48], and a loose coupling approach is introduced to the external loading modules to allow a greater degree of modularity and flexibility [42]. An analysis of a VAWT with aerodynamic and platform forcing were carried out through a one-way coupling to the CACTUS code [49] developed by the Sandia National Laboratories, and the effect of blade deformation on the aerodynamics was not considered [42]. Recently, iteration at each time step using a predictor-corrector approach was considered, such that a hydrodynamic module can be included by coupling the wave-to-wire numerical model, WaveEC2Wire, with OWENS [50].

The SIMO-RIFLEX-DMS code was developed by Wang et al. [44] to perform the fully coupled aero-hydro-servo-elastic simulations for floating VAWTs. This code is based on the SIMO [51] and RIFLEX [52] code which has been extensively used and validated for offshore structures subjected to wave loads. It integrates the models of turbulent wind inflow, aerodynamics, hydrodynamics, control dynamics, structural dynamics and mooring line dynamics in a fully coupled way in the time domain. The aerodynamic loads are calculated using the DMS method with the Beddoes-Leishman dynamic stall model; the hydrodynamic loads are computed based on a combination of potential flow theory and Morison's equation; and the structural dynamics of blades, tower, shaft and mooring lines, which are modeled as flexible finite elements, are solved using a nonlinear FEM solver. A PI generator torque controller can also be implemented to regulate the rotor rotational speed. This simulation tool provides an approach with high fidelity for numerical modeling and analysis of floating VAWTs. The detailed modeling method used in the SIMO-RIFLEX-DMS code is described in Wang [25] as well as in Section 3.2. This code is used to study the dynamic behavior of floating VAWTs in this thesis (*Papers 4, 5, 6*).

The HAWC2, a state-of-the-art aero-hydro-servo-elastic code originally used for floating HAWTs [37], has been developed to have capability of simulating a floating VAWT in the time domain [43]. Instead of the DMS

model, the actuator cylinder (AC) flow model developed by Madsen [53] is implemented to calculate the aerodynamic loads on the blade due to its advantages in the aerodynamic and aeroelastic simulations for VAWTs. The structural dynamics is modeled using the beam element and based on the multibody formulation that can handle complex structures as well as bodies with arbitrary large rotations. The hydrodynamic model is originally based on Morison's equation, but coupling with WAMIT [54] through an external dynamic link library (DLL) is currently available such that the hydrodynamic loads can be computed using the potential flow theory.

A fully coupled simulation tool, SIMO-RIFLEX-AC, was recently developed for numerical modeling and dynamic analysis of floating VAWTs by Cheng et al. [45] in this thesis work. As stated by Ferreira et al. [55], the DMS method is inaccurate compared with the AC method. The aerodynamic model was thus established based on the AC method with consideration of the effects of wind shear and turbulence, dynamic inflow as well as dynamic stall using the Beddoes-Leishman model [56] (*Paper 1*). The developed AC model was then coupled with the SIMO [51] and RIFLEX [52] code to achieve a fully coupled simulation tool, which accounts for the turbulent wind inflow, aerodynamics, hydrodynamics, structural dynamics, control system dynamics and mooring line dynamics with high fidelity. In the SIMO-RIFLEX-AC code, the hydrodynamic loads are based on a combination of potential flow theory and Morison's equation; the blades, tower, shaft and mooring lines are modeled as flexible finite elements and the structural dynamics are solved using RIFLEX, a nonlinear FEM solver. A generator torque controller is also implemented to regulate the rotor rotational speed based on a PI control algorithm. The development and verification of the SIMO-RIFLEX-AC code is described by Cheng et al. [45] (*Paper 2*) and also detailed in Chapter 3.

1.2.3 State of the art study on dynamic behavior of floating VAWTs

Considerable efforts have been made to study the dynamic behavior of different floating VAWT concepts in the normal operating and fault conditions by many researchers using the aforementioned codes. The control strategy for a floating VAWT has been studied as well.

Paulsen et al. proposed the well-known DeepWind floating VAWT concept [57] and conducted the first baseline design of a 5 MW Darrieus rotor using the code HAWC2 together with the DMS implementation for the aerodynamics [58]. Later a design optimization of the first baseline design was

performed using the updated HAWC2 code with the AC implementation to obtain an improved design with an optimized blade profile and with less weight and higher stiffness [59].

Using the baseline rotor proposed in the DeepWind project, Wang [44, 24, 60, 61], Borg [62, 63] and Cheng [64, 65] conducted a series of studies to investigate the dynamic response characteristics of several floating VAWT concepts. Wang et al. proposed a floating VAWT concept with this Darrieus rotor mounted on a semi-submersible [44] and carried out fully coupled aero-hydro-servo-elastic time-domain simulations using the SIMO-RIFLEX-DMS code with emphasis on stochastic dynamic responses [24], effects of second order difference-frequency force and wind-wave misalignment [60] (*Paper 5*), and emergency shutdown process with consideration of faults [61]. Using the semi-submersible VAWT concept proposed by Wang et al. [44], Borg and Collu [63] investigated the aerodynamic characteristics of a floating VAWT in the frequency domain. Borg and Collu [62] also carried out a preliminary comparison on the dynamics of floating VAWTs with a spar, semisubmersible, and TLP floater; however, the yaw of the spar and the surge and sway of the TLP were disabled during the simulations. Moreover, the structural elasticity and variable speed control were not considered and the mooring systems were simplified as springs. Cheng et al. [64, 65] (*Paper 4 and Additional paper 7*) performed a more comprehensive comparison on the dynamic responses of these three floating VAWT concepts using fully coupled aero-hydro-servo-elastic simulations.

Studies on floating VAWT concepts with straight blades have also been conducted. Borg et al. [66] used a wave energy converter as a motion suppression device for a floating VAWT with a straight-bladed H-type rotor mounted on a semi-submersible. Anagnostopoulou [67] performed the concept design and dynamic analyses of a floating VAWT with a straight-bladed rotor mounted on a semi-submersible for power supply to offshore Greek islands; however, the wind loads acting on the rotor is very simplified without considering a aerodynamic model for the rotor. Cheng et al. [23] (*Paper 3*) systematically investigated the effect of blade number on the dynamic behavior of floating straight-bladed VAWTs using fully coupled time domain simulations. Three VAWTs with a identical solidity and a blade number ranging from two to four were designed and then adapted to a semi-submersible platform.

The control strategy for large megawatt floating VAWTs has been studied by several researchers as well. It is to some extent different from that of floating HAWTs, since floating VAWTs usually operate with variable rotational speed at a fixed blade pitch angle, and the aerodynamic loads

acting on the rotor vary periodically when it rotates. For the DeepWind 5 MW Darrieus rotor, Merz and Svendsen [68, 69] proposed a generator torque controller to regulate the rotational speed. The controller aims at minimizing the error between the measured rotational speed and reference rotational speed by adjusting the generator torque using a PI algorithm. The typical relationship between the reference rotational speed and wind speed of a floating VAWT is illustrated by Cheng [70, 45, 71]. A similar control strategy is also applied to regulate the rotor rotational speed of floating straight-bladed VAWTs [23]. In addition, a control system for the start-up and shut-down of the DeepWind floating VAWT is presented and analyzed by Svendsen and Merz [72].

Up to now, there are very limited studies on the effect of faults on the dynamic responses of floating VAWTs. For a VAWT without blade pitching, the rotor will accelerate and even break down when a generator failure occurs. To prevent the rotor from overspeeding and subsequent disaster, additional mechanical or hydrodynamic brakes should be provided. Wang et al. [61] presented a novel hydrodynamic brake and stated that the hydrodynamic brake is expected to be efficient for the emergency shutdown of a floating VAWT. A shutdown scheme for the DeepWind floating VAWT was also proposed by Svendsen and Merz [72] using an additional brake.

Comparative studies of floating HAWTs and VAWTs are also of great interest and carried out by several researchers. Borg and Collu [73] carried out a preliminary comparison between the floating HAWT and VAWT based on prime principles with emphasis on the aerodynamic forces and their impact on the static and dynamic responses. But limited comparison regarding the dynamic behavior was conducted and no structural elasticity and controller were included for the floating VAWT. Wang et al. [74] and Cheng et al. [75, 70] (*Paper 6 and Additional paper 8*) conducted more comprehensive comparisons on the performance and dynamic responses of floating HAWTs and VAWTs using the fully coupled aero-hydro-servo-elastic simulations. Wang et al. [74] performed a comparative study of a semi-submersible VAWT with the DeepWind 5 MW Darrieus rotor [26] with the NREL 5 MW wind turbine [76]. Cheng et al. [75] (*Additional paper 8*) studied the same rotors with a spar buoy subjected to constant wind. However, the wind fields were created with respect to different reference heights for the floating HAWT and VAWT, which implies that a slightly different wind field was used, though its effect was very small. Moreover, the generator power of the floating VAWT exceeds 5 MW above the rated wind speed and could even reach up to 9 MW. Thus, an improved control strategy was proposed and a more comprehensive comparative study was conducted by Cheng et

al. [70] (*Paper 6*).

1.3 Aim & Scope

The main goal of this thesis is to develop and verify a fully coupled method for numerical modeling and dynamic analysis of floating vertical axis wind turbines (VAWTs) and to demonstrate the dynamic response characteristics of different floating VAWT concepts. To accomplish it, the following sub-objectives are defined and achieved.

- To establish an aerodynamic model for VAWTs based on the actuator cylinder (AC) flow theory and considering the effects of turbulence, dynamic inflow and dynamic stall, and to validate it by comparison with other numerical model and experimental data.
- To develop a fully coupled aero-hydro-servo-elastic simulation tool by coupling the AC model to the SIMO-RIFLEX code for numerical modeling and dynamic analysis of floating VAWTs, and to verify it by comparison with other computer codes.
- To demonstrate the effect of blade number on the dynamics of floating VAWTs with straight and parallel blades.
- To characterize the dynamic responses of a spar, semi-submersible and TLP VAWT with a two-bladed Darrieus rotor.
- To investigate the effect of difference-frequency force and wave-wind misalignment on the dynamics of a semi-submersible VAWT.
- To reveal the merits and disadvantages on the dynamic responses of a spar-type HAWT and VAWT.

This thesis is written in the form of a summary provided in Chapter 1-6 and a collection of five journal articles and one conference paper in the Appendix A. The scope of this thesis is shown in Figure 1.5 where the main topics and the interconnection between appended papers are illustrated. The six papers in the Appendix A are summarized as follows:

Paper 1 This paper deals with the development of an aerodynamic code to model floating VAWTs based on the AC method, which was initially developed by Madsen [53]. The developed AC code includes the tangential load term when calculating induced velocities, employs

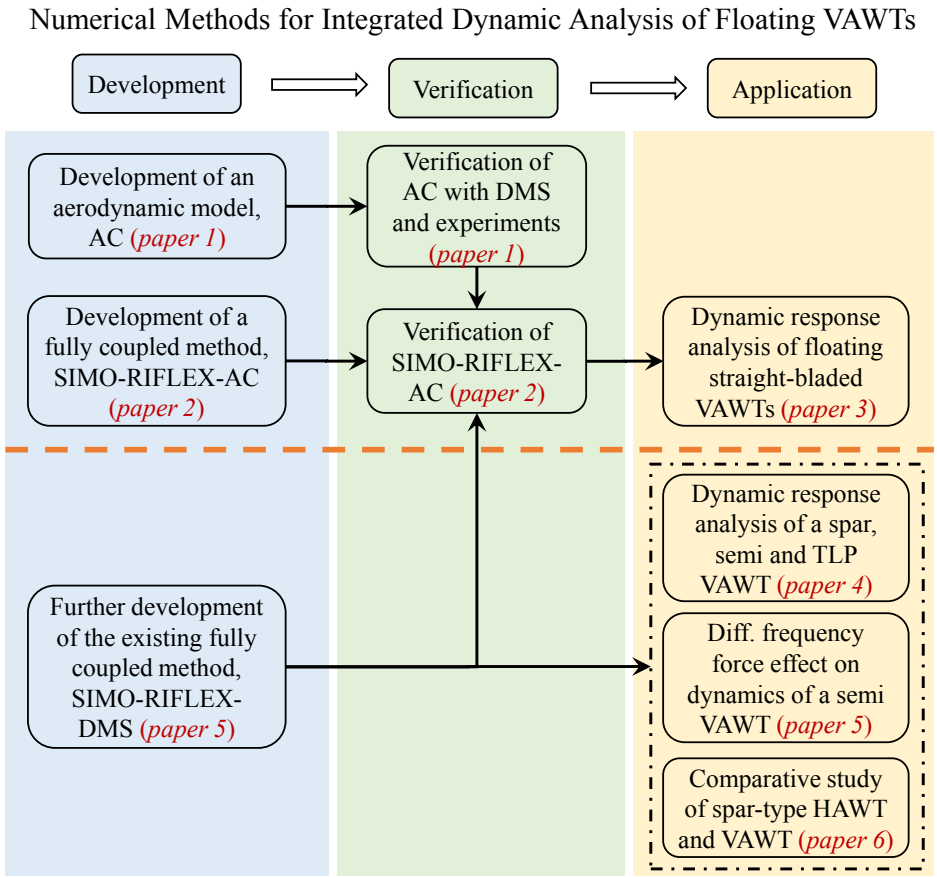

Figure 1.5: Scope of this thesis and interconnection between the appended papers.

two different approaches to calculate the normal and tangential loads acting on the rotor, and proposes an improved linear solution. The effect of dynamic stall was also considered using the Beddoes-Leishman model. The developed code was verified by a series of comparisons against other numerical models and experimental results. In addition, a comparison of the AC method and the double multi-streamtube (DMS) method was also performed.

Paper 2 This paper addresses the development and verification of a fully coupled method for numerical modeling and dynamic analysis of floating VAWTs. Based on the AC method, aerodynamic modeling of floating VAWTs was established with consideration of the effects of

wind shear and turbulence, dynamic inflow as well as dynamic stall using the Beddoes-Leishman model. The developed AC code was then integrated with the SIMO and RIFLEX code to achieve a fully coupled simulation tool, namely SIMO-RIFLEX-AC, which can account for the turbulent and dynamic inflow, aerodynamics, hydrodynamics, structural dynamics, control system dynamics and mooring line dynamics with high fidelity. A series of code-to-code comparisons with the HAWC2 [37] and SIMO-RIFLEX-DMS [44] code were conducted using a landbased and semi-submersible VAWT. The capability of these three codes in the prediction of dynamic responses of floating VAWTs was also discussed and demonstrated.

Paper 3 This paper deals with the effect of the number of blades on the dynamic behavior of floating VAWTs. Three VAWTs with straight and parallel blades, with identical solidity and with a blade number varying from two to four, were firstly designed using the AC method and then adapted to a semi-submersible. A generator torque controller was also designed and used to regulate the rotational speed based on a proportional-integral (PI) control algorithm. The eigen-frequency analysis, free decay tests and white noise wave simulations were conducted to identify the properties of the floating VAWT systems, including the eigen-frequency and eigen modes, natural periods of rigid-body motions and response amplitude operators (RAOs) for wave loads. Steady wind simulations were used to capture the effect of blade number on the structural responses of landbased and floating VAWTs. The impact of blade number for floating VAWTs was further thoroughly studied using turbulent wind and irregular wave simulations.

Paper 4 This paper deals with the dynamic responses of three floating VAWT concepts with a two-bladed 5 MW Darrieus rotor mounted on a spar, semi-submersible and TLP floater, respectively. Free decay tests, white noise and regular wave simulations were firstly carried out to identify the properties of these three concepts, including the natural periods of rigid body motions and RAOs for wave loads. A series of load cases with turbulent wind and irregular waves were carried out to investigate the dynamic responses of these three concepts by estimating the generator power production, platform motions, tower base bending moments, and mooring line loads.

Paper 5 This paper addresses the effect of second-order difference-frequency force on the dynamics of a semi-submersible VAWT in misaligned

wave-wind conditions. A 5 MW Darrieus rotor mounted on a semi-submersible with a catenary mooring system was considered. One wind direction and four wave directions were simulated considering the first-order force, first-order force and mean drift force, and first-order force and second-order difference-frequency force, respectively. A series of load cases with correlated turbulent wind and irregular waves were conducted to investigate the dynamic responses, including the platform motions, tower base bending moments and mooring line tensions. The effect of second-order difference-frequency force and wave-wind misalignment on the dynamic behavior of the semi-submersible VAWT was addressed.

Paper 6 This paper deals with a comparative study on the dynamics of a spar-type HAWT and VAWT. The 5 NREL 5MW wind turbine and a 5 MW Darrieus rotor, both mounted on the OC3 spar buoy, were considered. An improved control strategy was introduced for the spar VAWT to achieve an approximately constant mean generator power for the above rated wind speeds. a series of fully coupled time domain simulations were carried out using identical, directional aligned and correlated wind and wave conditions. The comparative study was conducted with respect to the generator power production, platform motions, tower base bending moments, and mooring line loads.

1.4 Thesis Outline

The summary section of this thesis includes six chapters. A brief description of each chapter is provided as follows:

Chapter 1: Introduction
This chapter includes the background, motivations, aim and scope and outline of the thesis.

Chapter 2: Aerodynamics of a Vertical Axis Wind Turbine
Aerodynamic models of a vertical axis wind turbine (VAWT) is reviewed in this chapter. Among them, the Double Multi-Streamtube (DMS) model and Actuator Cylinder (AC) flow model are further detailed. Validation of the DMS and AC models is also presented. This chapter covers main results from *Paper 1*.

Chapter 3: Integrated Modeling of a Floating VAWT System

This chapter deals with the development and verification of fully coupled methods, namely SIMO-RIFLEX-DMS and SIMO-RIFLEX-AC, for integrated modeling and analysis of a floating VAWT system. Models of the aerodynamics, hydrodynamics, structural dynamics and control system are all introduced. This chapter covers main results from *Paper 2*.

Chapter 4: Landbased and Floating Wind Turbine Concepts
The floating wind turbine concepts used in this thesis are briefly described in this chapter: the floating VAWTs with a two-bladed 5 MW Darrieus rotor supported by a spar, semi-submersible and TLP floater, the semi-submersible VAWTs with three 5 MW straight-bladed rotors, and the spar-type HAWT with the NREL 5 MW wind turbine.

Chapter 5: Dynamic Response Analysis of Floating VAWTs
This chapter deals with the dynamic response characteristics of different floating VAWT concepts using fully coupled time domain simulations. It covers the following aspects: the effect of blade number on the dynamic behavior of floating straight-bladed VAWTs; the dynamic response of a spar, semi-submersible and TLP VAWT with a two-bladed Darrieus rotor; the effect of second-order difference-frequency force on the dynamics of a semi-submersible VAWT in misaligned wave-wind conditions. Lastly, a comparative study of a spar-type HAWT and VAWT is also presented. This chapter covers main results from *Papers 3, 4, 5, 6*.

Chapter 6: Conclusions and Recommendations for Future Work
Conclusions, original contributions and recommendations for future study are presented in this chapter.

Chapter 2

Aerodynamics of a Vertical Axis Wind Turbine

This chapter starts with an overview of aerodynamic models for predicting aerodynamic loads on a vertical axis wind turbine (VAWT) in Section 2.1. Among them, the Double Multi-Streamtube (DMS) model used in *papers 4, 5, 6* and the Actuator Cylinder (AC) flow model used in *papers 1, 2, 3* are further detailed in Sections 2.2 and 2.3, respectively. Validation of the DMS and AC models is presented in Section 2.4.

2.1 Overview of Aerodynamic Models

Since Sandia National Laboratories started the study of VAWTs in the 1970s, a variety of aerodynamic models have been proposed to calculate aerodynamic loads on VAWTs. These include streamtube models [77, 78, 18], actuator cylinder (AC) flow model [53, 79, 43, 56, 45], vortex models [80, 81, 82, 83], panel models [80, 84, 85] and computational fluid dynamics (CFD) methods [86, 87, 88, 89]. An detailed overview of these models has been conducted by Borg at al. [90] and Wang [25]. This section only highlights the main principle of each model.

The streamtube models are based on the conservation of mass and momentum in a quasi-steady flow. They equate the forces on the rotor blades to the change in the streamwise momentum through the turbine. They can be categorized into three models: single streamtube model [77], multi-streamtube model [78] and double multi-streamtube (DMS) [18] model. The single streamtube model [77] assumes that the entire rotor represented by an actuator disk is enclosed in one streamtube; the multi-streamtube model [78] extends the single streamtube model by dividing the rotor into a series

of adjacent streamtubes and the DMS model [18] assumes that the vertical axis turbine can be represented by a pair of actuator disks in tandem at each level of the rotor.

The actuator cylinder (AC) flow model is a 2D quasi-steady model developed by Madsen [53] in his PhD study. This model extends the actuator disc concept to an actuator surface coinciding with the swept area of the 2D VAWT. In the AC model, the normal and tangential forces resulting from the blade forces are applied on the flow as volume force perpendicular and tangential to the rotor plane, respectively. The induced velocities are thus related to the volume force based on the continuity equation and Euler equation. The induced velocity includes a linear part and a nonlinear part; the linear part can be computed analytically given the normal and tangential loads. However, it's to some extent time-consuming to compute the nonlinear solution directly. A simple correction is therefore introduced for the linear solution to make it in better agreement with the fully nonlinear solution. Recently the AC model has been implemented in the HAWC2 code for fully coupled analysis of VAWTs [43] and further discussion and development of the AC model was carried out by Cheng et al. [56] (*Paper 1*).

The vortex model assumes a potential flow that calculates the velocity field of the rotor considering the influence of vorticity in the wake of the blades. In the vortex model, the blades are modeled as a number of blade elements and each element is represented as a bound vortex filament, namely lifting line. The fluid velocity at any point in the flow field is the sum of the undisturbed free stream velocity and velocity induced by all vortex filaments. The aerodynamic loads on an element is determined by the strength of the bound vortex as well as the relative flow velocity. Application of vortex models for a VAWT was conducted, including a single blade element by Larsen [91], a 2D model by Holme [92] and a 3D model by Strickland et al. [83].

The panel model is also based on the potential flow theory [93]. In the panel model, the blades are discretized into a number of panels. The source or doublet with a unknown strength is then placed on each panel. The velocity potential, which is related to the source or doublet, can thus be solved by satisfying a no penetration Dirchelet boundary condition on the body and the Kutta condition at the trailing edge. A potential flow panel model was developed by Ferreira [84] in his PhD study, which represents each blade by a 2D distribution of source and doublet panels over the blade's surface. The 2D panel model was further developed by Zanon et al. [80] to a double wake vortex panel model coupled with the integral boundary layer

equations on the airfoil surface for simulating the unsteady 2D flow past a VAWT.

Due to the improvements of high-performance computing, CFD models are becoming more extensively applied in the aerodynamic calculations of VAWTs in recent years. Kanner and Persson [87] developed and validated a high-order large eddy simulation (LES) solver for a VAWT. Liu and Xiao [86] investigated the fluid structure interaction of Darrieus type straight blade vertical axis wind turbine. Castelli et al. [89] proposed a new performance prediction model based on CFD for the Darrieus wind turbine.

Among the aforementioned models, the DMS is widely used for aerodynamic loads prediction and aeroelastic analysis of VAWTs due to its simplicity and computational efficiency. Wang et al. [94] improved the DMS model by considering the effect of tower tilt on the aerodynamics of floating VAWTs. More details about this DMS model is presented in Section 2.2.

However, by considering a 2D VAWT rotor, Ferreira et al. [55] compared different models for VAWTs, including the multi-streamtube model, DMS model, AC [53] model, U2DiVA [84] using panel model and CACTUS [49] using vortex model, and stated that the DMS model seems to be less accurate than the AC, panel and vortex models. Roscher [95] also compared these models and demonstrated the merits of AC model with respect to the complexity, accuracy, computational cost, suitability for optimization and aeroelastic analysis. Therefore, the AC model is another favorable method suitable for integrated modeling and analysis of VAWTs. In this thesis, the AC model, originally developed by Madsen [53], is further discussed and improved, as described by Cheng et al. [56] (*Paper 1*) and presented in Section 2.3.

2.2 Double Multi-Streamtube (DMS) Model

In order to account for the effect of tower tilt on the aerodynamics of a floating VAWT, the traditional DMS model [18] was reformulated by Wang et al. [94]. Assuming the tilt angle caused by the pitch and roll motions of a floating VAWT is denoted as ϕ, the freestream velocity can then be decomposed into a component parallel to the tilted tower and a component perpendicular to it. In this way, the tilted floating VAWT with a freestream velocity U is equivalent to a VAWT with a non-tilting tower and with a horizontal velocity component $U\cos\phi$ and a vertical velocity component $U\sin\phi$, as shown in Figure 2.1.

As in the traditional DMS model [18], the flow through the rotor is divided into a sufficiently large number of aerodynamically independent

streamtubes and in each streamtube a pair of actuator disks is placed in tandem, as depicted in Figure 2.1. Assuming the induction factor at the upwind and downwind disk are given as a_u and a_d, respectively, then the upwind horizontal velocity U_u, the upwind vertical velocity V_u, the equilibrium velocity U_e and the downwind horizontal velocity U_d can be written as follows

$$U_u = (\cos\phi - a_u)U \tag{2.1}$$

$$V_u = U\sin\phi \tag{2.2}$$

$$U_e = (\cos\phi - 2a_u)U \tag{2.3}$$

$$U_d = (1 - a_d)U_e = (1 - a_d)(\cos\phi - 2a_u)U \tag{2.4}$$

Based on a combination of the Glauert momentum theory and blade element theory, the induction factor a_u and a_d can be estimated using numerical methods and the aerodynamic loads can thus be determined accordingly.

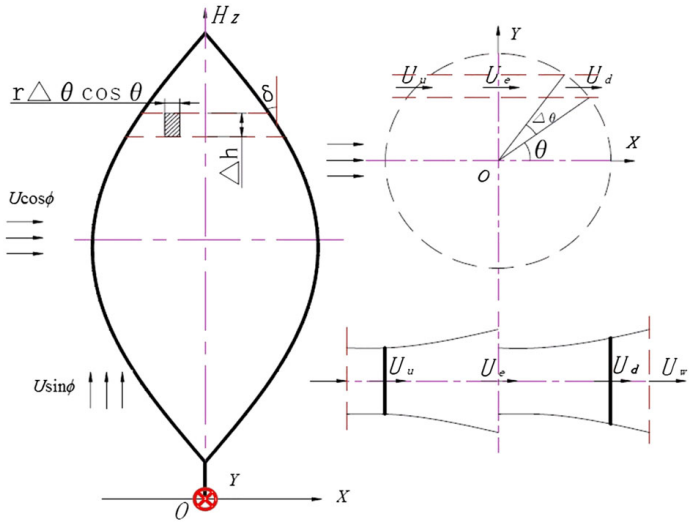

Figure 2.1: Double Multiple-Streamtube Model for a Darriues wind turbine with two actuator disk in tandem with a horizontal and vertical inflow [94].

The effect of dynamic stall was considered by Wang et al. [94]. Three dynamic stall models were implemented and compared, including the Gormont's model with the adaption of Strickland, Gormont's model with the modification of Berg and the Beddoes-Leishman dynamic stall model.

2.3 Actuator Cylinder (AC) Flow Model

Considering a 2D quasi-static flow problem as shown in Figure 2.2, the basic equations are the Euler equation and continuity equation. For simplicity the equations are non-dimensionalized with the basic dimensions R, V_∞ and ρ, which are rotor radius, free stream velocity and flow density, respectively. The velocity components can thus be written as

$$v_x = 1 + w_x \tag{2.5}$$

$$v_y = w_y \tag{2.6}$$

where w_x and w_y are local velocities representing the changes in wind speed due to the presence of the VAWT.

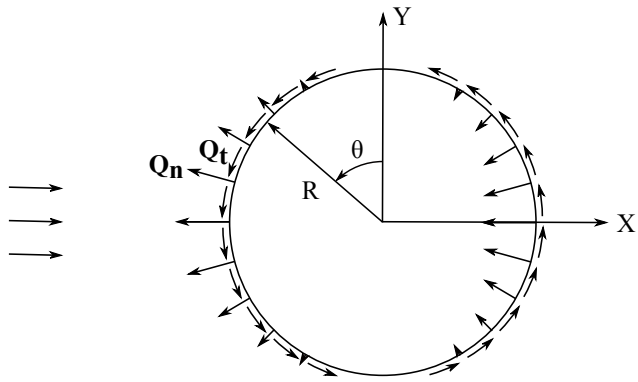

Figure 2.2: The actuator cylinder flow model representation of a VAWT with volume forces normal and tangential to the circle. Note that the force direction is from the VAWT noto the flow. [79]

Based on the continuity equation and Euler equation, the induced velocities w_x and w_y are related to volume forces as well as the normal and tangential loads Q_n and Q_t. In the AC method, the tangential and normal loads Q_n and Q_t are non-dimensionalized and computed as follows [56]

$$Q_t = -\frac{BF_{tA}}{2\pi R\rho V_{wB}^2 \sin(\beta)} \tag{2.7}$$

$$Q_n = \frac{BF_{nA}}{2\pi R\rho V_{wB}^2 \sin(\beta)} \tag{2.8}$$

where B is the number of blades, ρ the air density, R the radius of the disk considered, β the blade angle with the vertical direction, and V_{wB} the

local free wind speed. F_{tA} and F_{nA} are the tangential load and normal load acting on the local element, respectively.

Therefore, the final velocity can be divided into a linear part which is a function of the prescribed normal and tangential loads Q_n and Q_t and a nonlinear part that is a function of the induced velocities. Detailed derivations regarding this 2D quasi-static flow problem is described by Madsen et al. [79], and the linear solution of this problem is derived by Cheng et al. [56] (*Paper 1*).

2.3.1 Linear solution

The linear solution of the induced velocities can be analytically computed, which is given by Cheng et al. [56] as follows.

$$\begin{aligned} w_x = &-\frac{1}{2\pi}\int_0^{2\pi} Q_n(\theta)\frac{-(x+\sin\theta)\sin\theta+(y-\cos\theta)\cos\theta}{(x+\sin\theta)^2+(y-\cos\theta)^2}d\theta \\ &-\frac{1}{2\pi}\int_0^{2\pi} Q_t(\theta)\frac{-(x+\sin\theta)\cos\theta-(y-\cos\theta)\sin\theta}{(x+\sin\theta)^2+(y-\cos\theta)^2}d\theta \\ &-(Q_n(\arccos y))^* + (Q_n(-\arccos y))^{**} \\ &-\left(Q_t(\arccos y)\frac{y}{\sqrt{1-y^2}}\right)^* - \left(Q_t(-\arccos y)\frac{y}{\sqrt{1-y^2}}\right)^{**} \end{aligned} \tag{2.9}$$

$$\begin{aligned} w_y = &-\frac{1}{2\pi}\int_0^{2\pi} Q_n(\theta)\frac{-(x+\sin\theta)\cos\theta-(y-\cos\theta)\sin\theta}{(x+\sin\theta)^2+(y-\cos\theta)^2}d\theta \\ &-\frac{1}{2\pi}\int_0^{2\pi} Q_t(\theta)\frac{(x+\sin\theta)\sin\theta-(y-\cos\theta)\cos\theta}{(x+\sin\theta)^2+(y-\cos\theta)^2}d\theta \end{aligned} \tag{2.10}$$

where θ is the azimuth angle, the term marked with $*$ in Eq. 2.9 shall only be added inside the cylinder whereas in the wake behind the cylinder both the term marked with $*$ and $**$ shall be added. Compared with the results by Madsen et al. [79], the effect of tangential load on the computed induced velocity is considered here.

Assuming that the loading is piecewise constant, the integral part in Eqs. 2.9 and 2.10 can be rewritten as

$$\begin{aligned} w_x = &-\frac{1}{2\pi}\sum_{i=1}^{i=N} Q_{n,i}\int_{\theta_i-\frac{1}{2}\Delta\theta}^{\theta_i+\frac{1}{2}\Delta\theta}\frac{-(x+\sin\theta)\sin\theta+(y-\cos\theta)\cos\theta}{(x+\sin\theta)^2+(y-\cos\theta)^2}d\theta \\ &-\frac{1}{2\pi}\sum_{i=1}^{i=N} Q_{t,i}\int_{\theta_i-\frac{1}{2}\Delta\theta}^{\theta_i+\frac{1}{2}\Delta\theta}\frac{-(x+\sin\theta)\cos\theta-(y-\cos\theta)\sin\theta}{(x+\sin\theta)^2+(y-\cos\theta)^2}d\theta \end{aligned} \tag{2.11}$$

$$w_y = -\frac{1}{2\pi}\sum_{i=1}^{i=N} Q_{n,i}\int_{\theta_i-\frac{1}{2}\Delta\theta}^{\theta_i+\frac{1}{2}\Delta\theta}\frac{-(x+\sin\theta)\cos\theta-(y-\cos\theta)\sin\theta}{(x+\sin\theta)^2+(y-\cos\theta)^2}d\theta + \frac{1}{2\pi}\sum_{i=1}^{i=N} Q_{t,i}\int_{\theta_i-\frac{1}{2}\Delta\theta}^{\theta_i+\frac{1}{2}\Delta\theta}\frac{-(x+\sin\theta)\sin\theta+(y-\cos\theta)\cos\theta}{(x+\sin\theta)^2+(y-\cos\theta)^2}d\theta \tag{2.12}$$

where N is the total number of calculation points, $\Delta\theta = \frac{2\pi}{N}$ and $\theta_i = \frac{\pi}{N}(2i-1)$ for $i = 1, 2, ..., N$.

Since only induced velocities at the cylinder are of concern, the total velocity solution at the calculation point (x_j, y_j) (for $j = 1, 2, ..., N$) on the cylinder can then be rewritten as

$$\begin{aligned} w_{x,j} =& -\frac{1}{2\pi}\left(\sum_{i=1}^{i=N} Q_{n,i}I_{1,i,j} + \sum_{i=1}^{i=N} Q_{t,i}I_{2,i,j}\right) \\ & -\left(Q_{n,N+1-j}\right)^* - \left(Q_{t,N+1-j}\frac{y_j}{\sqrt{1-y_j^2}}\right)^* \end{aligned} \tag{2.13}$$

$$w_{y,j} = -\frac{1}{2\pi}\left(\sum_{i=1}^{i=N} Q_{n,i}I_{2,i,j} - \sum_{i=1}^{i=N} Q_{t,i}I_{1,i,j}\right) \tag{2.14}$$

where the terms marked with $*$ in Eqs. 2.13 and 2.14 are only added for $j > \frac{N}{2}$ (the leeward part of the AC with $x_j > 0$). $I_{1,i,j}$ and $I_{2,i,j}$ are influence coefficients at point j influenced by other point i and are given by

$$I_{1,i,j} = \int_{\theta_i-\frac{1}{2}\Delta\theta}^{\theta_i+\frac{1}{2}\Delta\theta}\frac{-(x_j+\sin\theta)\sin\theta+(y_j-\cos\theta)\cos\theta}{(x_j+\sin\theta)^2+(y_j-\cos\theta)^2}d\theta \tag{2.15}$$

$$I_{2,i,j} = \int_{\theta_i-\frac{1}{2}\Delta\theta}^{\theta_i+\frac{1}{2}\Delta\theta}\frac{-(x_j+\sin\theta)\cos\theta-(y_j-\cos\theta)\sin\theta}{(x_j+\sin\theta)^2+(y_j-\cos\theta)^2}d\theta \tag{2.16}$$

in which $x_j = -\sin(j\Delta\theta - \frac{1}{2}\Delta\theta)$, $y_j = \cos(j\Delta\theta - \frac{1}{2}\Delta\theta)$. It can be found that the influence coefficients $I_{1,i,j}$ and $I_{2,i,j}$ are irrespective of time and can thus be integrated once and for all.

2.3.2 Modified linear solution

It's to some extent time-consuming to compute the nonlinear solution directly. In order to make the final solution in better agreement with the fully nonlinear solution, a correction is required for the linear solution. A simple correction [79] is suggested by multiplying the velocities from the linear

solution w_x and w_y with a factor k_a that is related to the axial induction factor. However, Cheng et al. [56] stated that the correction proposed by Madsen et al. [79] can give some deviation in the power coefficient at high tip speed ratios when comparing with experimental data. Thus a new modification which corrects the k_a at a high induction factor, which corresponds to a large tip speed ratio, was proposed by Cheng et al. [56].

$$k_a = \begin{cases} \frac{1}{1-a}, & (a \leq 0.15) \\ \frac{1}{1-a}(1 - 0.35\,(1 - \exp\,(-4.5(a - 0.15)))), & (a > 0.15) \end{cases} \tag{2.17}$$

where the induction factor a is found based on a relationship between the induction a and the average thrust coefficient C_T, and the empirical parameters are determined by comparing with the experimental data, as described by Cheng et al. [56].

2.3.3 Dynamic stall and dynamic inflow

In the implementation of the AC model by Cheng et al. [56, 45], the effects of wind shear and turbulence, dynamic stall and dynamic inflow were also considered.

The induced velocities calculated using the AC method are based on a steady state equilibrium without time. However, the mass flow through the rotor is substantial. In order to account for the time delay before the induced velocities are in equilibrium with the aerodynamic loads, a dynamic flow model should be applied. Currently there is no sophisticated dynamic flow model for VAWTs. The dynamic flow model proposed by Larsen and Madsen [43] was employed here. The dynamic inflow is modeled using a low pass filtering of the calculated steady state induced velocities.

The Beddoes-Leishman dynamic stall model was used to predict the VAWT's aerodynamic loads. It is a semi-empirical model which can represent the physical phenomenon to a certain extent through a superposition of separate indicial functions. The Beddoes-Leishman model is original developed to simulate the dynamic stall effect on the helicopter [96]. The adaptation of this model has been studied for HAWTs by Gupta and Leishman [97] and VAWTs by Dyachuk et al. [98].

The dynamic stall model and dynamic inflow model used are described in detail by Cheng et al. [45]. Integration of the Beddoes-Leishman dynamic stall model the dynamic inflow model into the AC model in the time domain is illustrated in the flow chart in Figure 2.3. At each time step, the induced velocity calculated using the AC model is filtered through a dynamic inflow

model, then the relative velocity and angle of attack are calculated and become inputs into the Beddoes-Leishman dynamic stall model. By including the dynamic stall effect the normal force coefficient and chordwise force coefficient are corrected and the lift coefficient and drag coefficient are thus obtained.

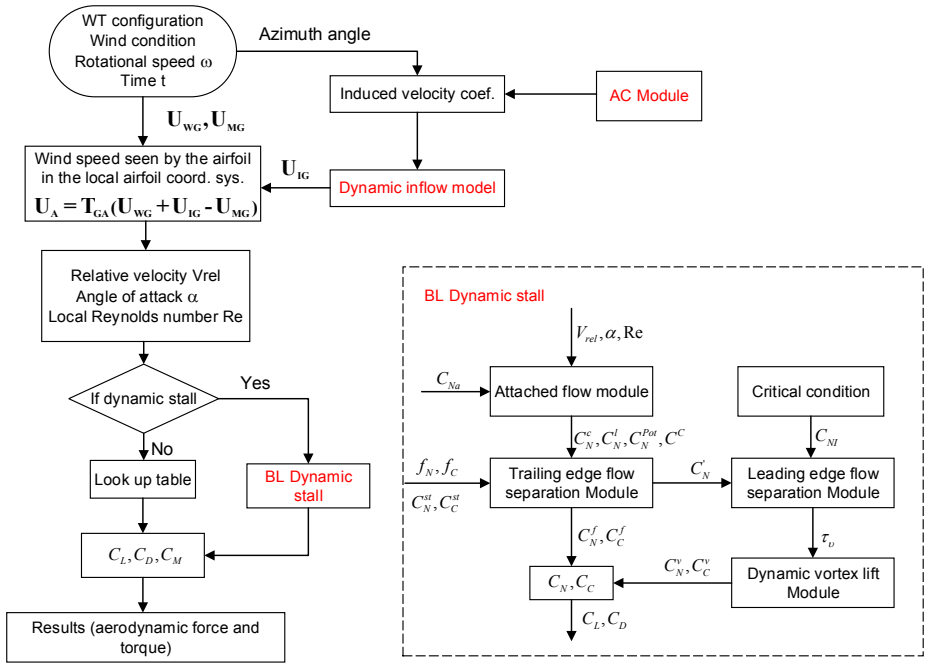

Figure 2.3: Flow chart of modeling of a floating VAWT using AC method. The models of dynamic inflow and dynamic stall are included [45].

2.4 Validation of the Present Models

Validation of the DMS and AC model has been conducted by comparison with experimental data. Wang et al. validated the DMS model using the experimental data of the Sandia Darrieus rotors [44] and using the experimental result of an H-Darrieus VAWT in skewed flow [94]. The AC model [56, 45] was verified by comparison with the DMS model and validated using the experimental data of the Sandia Darrieus rotors, as demonstrated in Figure 2.4 [71]. These validations were mainly conducted with respect to the generator power, since limited blade forces were measured or provided. Figure 2.4 shows that the developed DMS model and AC model can predict

the aerodynamic power of a VAWT accurately.

A more comprehensive comparison of the DMS model and AC model was conducted using the 2-bladed Sandia 17 m Darrieus rotor by Cheng et al. [56]. The thrust, side force and aerodynamic torque were studied as a function of the azimuth angle. The comparison showed that the AC model can predict more accurate aerodynamic loads and power than the DMS model.

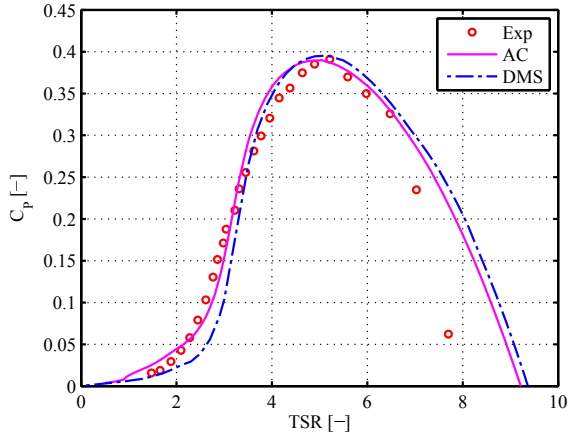

(a) The 3-bladed Sandia 5 m Darrieus rotor

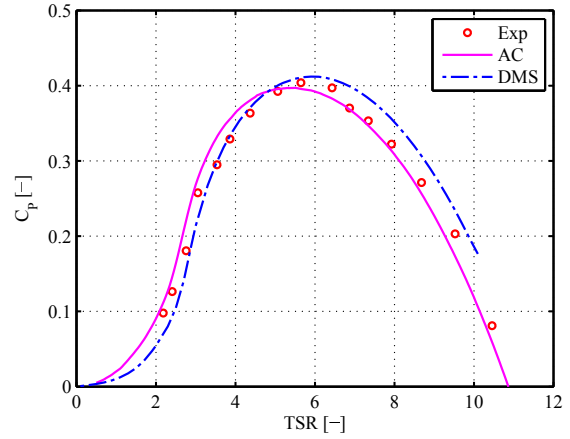

(b) The 2-bladed Sandia 17 m Darrieus rotor

Figure 2.4: Comparison of power coefficient curve between simulation model and experimental data. (a): the 3-bladed Sandia 5 m Darrieus rotor at rotational speed of 150 rpm, (b): the 2-bladed Sandia 17 m Darrieus rotor at rotational speed of 50.6 rpm. Here the TSR denotes tip speed ratio.

Chapter 3

Integrated Modeling of a Floating VAWT System

3.1 General

A floating VAWT system is usually comprised of a rotor harvesting wind energy, a floater supporting the rotor and a mooring system keeping the floater in position. To evaluate its performance in turbulent wind and irregular waves, a fully coupled aero-hydro-servo-elastic simulation tool is required to carry out the time domain simulations. This coupled code should integratedly account for the aerodynamics, hydrodynamics, structural dynamics, control system dynamics and mooring line dynamics.

To date the publicly available simulation tools that can model a floating VAWT system in a fully coupled way are limited, but are emerging, including the FloVAWT code by Cranfield University [40], the CALHYPSO code from EDF [41], the OWENS toolkit by Sandia National Laboratories [42], the HAWC2 by DTU Wind Energy [43, 37], the SIMO-RIFLEX-DMS [44] and SIMO-RIFLEX-AC [45] codes by NTNU/MARINTEK. An overview of these tools and their capacity was provided in Section 1.2.2. In this chapter, the development and verification of the SIMO-RIFLEX-DMS code [44] and, especially the SIMO-RIFLEX-AC code [45] in this thesis, is described in detailed. It is also included in *Paper 2*.

3.2 Fully Coupled Methods for Floating VAWTs

Recently, two fully coupled codes, namely SIMO-RIFLEX-DMS [44] and SIMO-RIFLEX-AC [45], were developed at NTNU to conduct fully coupled

aero-hydro-servo-elastic modeling and analysis of a floating VAWT system. These two codes were achieved by coupling the DMS model [94] and AC model [56], as described in Sections 2.2 and 2.3, with the SIMO-RIFLEX code. The codes SIMO[51] and RIFLEX[52] were developed by MARINTEK and widely used in the offshore oil and gas industry. The SIMO-RIFLEX wind turbine module has previously been verified [99, 100].

As illustrated in Figure 3.1, each of these two coupled codes integrates three computer codes. SIMO [51] computes the rigid body hydrodynamic forces and moments on the hull; RIFLEX [52] serves as a nonlinear finite element solver and provides the links to an external controller and the code AC or DMS; AC or DMS calculates the aerodynamic loads on the blades. The external controller, which is written in Java, is used to regulate the rotor rotational speed for a VAWT with a fixed blade pitch. This combination provides a comprehensive aero-hydro-servo-elastic simulation tool with well-known aerodynamics, sophisticated hydrodynamics, a stable nonlinear finite element solver, and user-defined control logic.

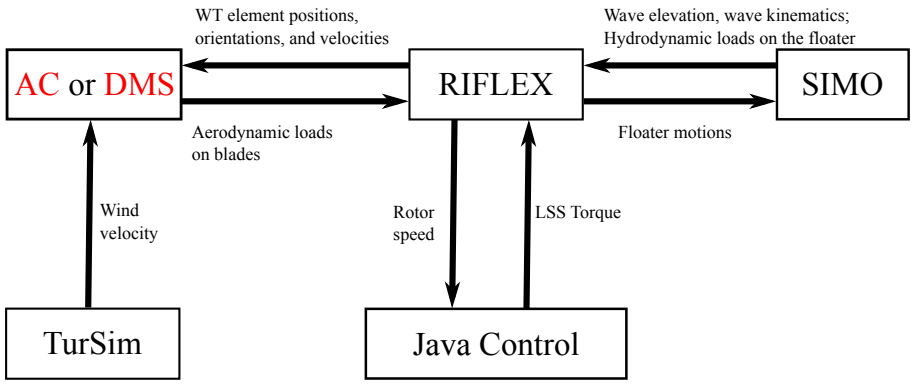

Figure 3.1: Overview of the fully coupled simulation tool SIMO-RIFLEX-AC and SIMO-RIFLEX-DMS.

Figure 3.2 shows the structural model and external load model of a floating VAWT system in the coupled code SIMO-RIFLEX-DMS and SIMO-RIFLEX-AC. The blades, shaft, tower and mooring lines are modeled using nonlinear flexible finite elements while the floating platform is considered as a rigid body. The dynamics of the floating platform is represented using the equation of motion proposed by [101]

$$(\mathbf{M}+\mathbf{A}_{\infty})\ddot{\mathbf{x}}(t)+\int_{-\infty}^{\infty}\kappa(t-\tau)\,\dot{\mathbf{x}}(t)\,d\tau+(\mathbf{K_m}(\mathbf{x},t)+\mathbf{K_h})\,\mathbf{x}(t)=\mathbf{F_{exc}}(\mathbf{x},\dot{\mathbf{x}},t) \tag{3.1}$$

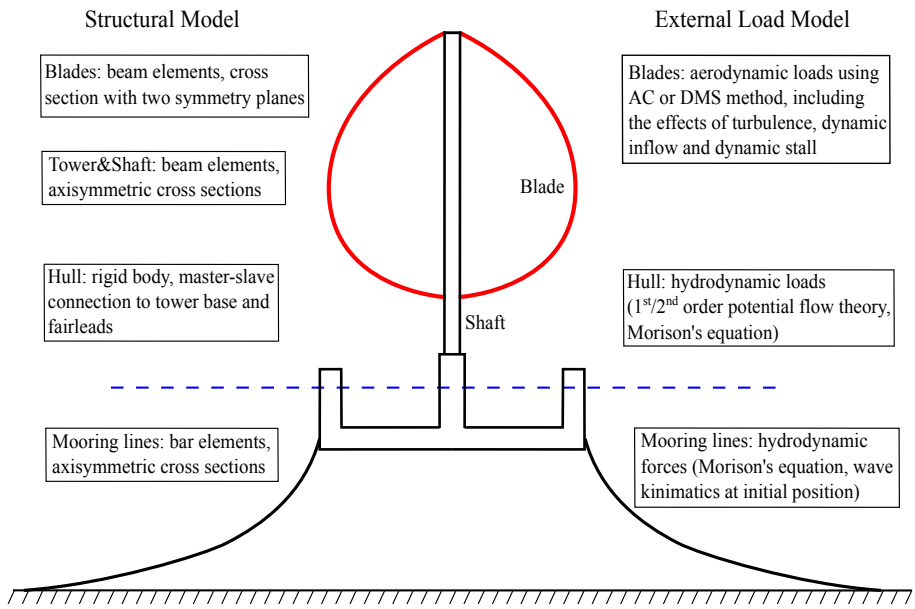

Figure 3.2: The structural model and external force model of a floating VAWT.

where $\mathbf{M}$ is the mass matrix of the floating system, $\mathbf{A}_\infty$ is the added mass matrix at infinite frequencies, $\mathbf{x}$, $\dot{\mathbf{x}}$ and $\ddot{\mathbf{x}}$ are the displacement, velocity and acceleration of the platform, respectively. $\kappa(t-\tau)$ is the retardation function which represents the fluid memory effect. $\mathbf{K_h}$ is the hydrostatic restoring matrix and $\mathbf{K_m}$ is the nonlinear restoring matrix from the mooring system. $\mathbf{F_{exc}}$ is the excitation forces which includes the Froude-Krylov force $\mathbf{F^{FK}}$, diffraction force $\mathbf{F^D}$, aerodynamic force $\mathbf{F^{Aero}}$ and viscous force $\mathbf{F^{Drag}}$.

$$\mathbf{F_{exc}}(\mathbf{x},\dot{\mathbf{x}},t) = \mathbf{F^{FK}}(t) + \mathbf{F^D}(t) + \mathbf{F^{Aero}}(\mathbf{x},\dot{\mathbf{x}},t) + \mathbf{F^{Drag}}(\dot{\mathbf{x}},t) \tag{3.2}$$

The aerodynamic force $\mathbf{F^{Aero}}$ is computed in the AC or DMS model as distributed lift and drag forces along the blade and then transfered from the rotor to the generator. The first- and second-order wave excitation forces on the floater are pre-generated in SIMO [51], while the viscous drag forces on the floater are updated. At each time step, the dynamic equilibrium equations of the rotor, platform and mooring lines are solved in RIFLEX and the rotor rotational speed is regulated through the external controller. Then the platform motions are transfered to SIMO to update the hydrodynamic loads, while the positions, velocities and accelerations of the blade elements are transfered to the AC or DMS model to update the aerodynamic loads.

3.2.1 Aerodynamics

The main difference between these two coupled codes is the aerodynamic model used to predict the aerodynamic loads on the blades of a VAWT. The aerodynamic model, i.e. the DMS model [94] and AC model [56], were comprehensively described in Sections 2.2 and 2.3.

In the SIMO-RIFLEX-DMS and SIMO-RIFLEX-AC code, the relative velocity seen at a blade section is the vector sum of the incoming wind velocity, the induced velocity and subtracting the velocities due to the rotor rotation, platform motion and blade elastic deformation. The effects of variation in the Reynolds number, wind shear and turbulence, and dynamic stall were all taken into account. The Beddoes-Leishman dynamic stall model was implemented to predict the unsteady aerodynamic loads accurately. In addition, the effect of dynamic inflow was also considered in the SIMO-RIFLEX-AC code.

3.2.2 Hydrodynamics

The hydrodynamic loads are computed using a combination of the potential flow theory and Morison's equation. In this thesis, a spar, semi-submersible and TLP floater were used to support VAWTs, as described in Chapter 4. For large volume structures like the platform hull of each floater, the added mass, radiation damping, and first order wave forces were obtained from a potential flow model and applied in the time domain using the convolution technique [102]. Moreover, second-order wave forces were also considered for the spar, semi-submersible, and TLP, respectively. For the spar hull, the mean wave drift forces were applied, and Newman's approximation was used to estimate the second-order differencefrequency wave excitation forces. Regarding the semi-submersible platform, the second-order difference-frequency wave excitation force was considered, using the full quadratic transfer function (QTF). With respect to the TLP FVAWT, second-order differencefrequency wave excitation forces using Newman's approximation and sum-frequency wave excitation forces using the full QTF were applied.

Regarding the slender structures where the diameter D is small compared to the wavelength λ (roughly, $\frac{D}{\lambda} < \frac{1}{5}$), the Morison equation is applied to calculate the inertial load and viscous drag load [102]. The transverse hydrodynamic force per unit length is given by

$$dF = \rho_w \pi \frac{D^2}{4} \dot{u_w} + \rho_w \pi C_a \frac{D^2}{4} (\dot{u_w} - \dot{u_b}) + \frac{1}{2} \rho_w C_d D (u_w - u_b) \left| u_w - u_b \right| \quad (3.3)$$

where ρ_w is the water density, u_w is the transverse wave particle velocity, u_b is the local transverse body velocity. C_a and C_d are the added mass and quadratic drag coefficients, respectively, and the values for the spar, semi-submersible and TLP considered are those used by Bachynski et al. [103]. In addition, viscous forces on large volume structures are also be incorporated through the Morison's equation by considering only the quadratic viscous drag term in Eq. 3.3.

3.2.3 Structural dynamics

In the structural model, the blades are modeled as flexible beam elements with two symmetric planes to differ the flapwise stiffness and edgewise stiffness. The tower and shaft are modeled as axisymmetric beam elements while the mooring lines are considered as nonlinear bar element. A very short tower close to the tower base is used to connect the rotating shaft and floater through a flexible joint. The electric torque from the generator is applied at this joint to regulate the rotational speed according to the prescribed control strategy. Moreover, master-slave connections are applied to integrate the motions between the tower base and fairleads.

Therefore, the dynamic equilibrium of the whole floating VAWT system can be expressed as the following equation by assuming a linear elastic material,

$$\mathbf{M_g}\ddot{\mathbf{r}} + \mathbf{B_g}\dot{\mathbf{r}} + \mathbf{K_g}\mathbf{r} = \mathbf{R^E}\left(\mathbf{r}, \dot{\mathbf{r}}, t\right) \tag{3.4}$$

where $\mathbf{M_g}$, $\mathbf{B_g}$ and $\mathbf{K_g}$ are the global mass, damping and stiffness matrices, respectively. r, $\dot{r}$ and $\ddot{r}$ are the system displacement, velocity and acceleration vectors, respectively. The structural damping here is specified using the Rayleigh damping, which is a linear combination of the mass $\mathbf{M_g}$, and stiffness $\mathbf{K_g}$ matrices as in the following equation.

$$\mathbf{B_g} = \alpha_1 \mathbf{M_g} + \alpha_2 \mathbf{K_g} \tag{3.5}$$

In which α_1 and α_2 are the mass and stiffness proportional coefficients, respectively. A coefficient of α_1=0 and α_2=0.03 was specified for the slender structures. In RIFLEX, the dynamic equilibrium equations can be solved in the time domain using the Newmark-β numerical integration ($\beta = 0.256$, $\gamma = 0.505$).

3.2.4 Control system

In the previous studies [75, 64, 65, 60, 24, 25], a PI generator torque control, developed by Svendsen et al. [68] and Merz and Svendsen[69], was used

to enable variable-speed and fixed-pitch operations. This control strategy, denoted as the baseline control strategy, is able to maximize the power capture for wind speeds below the wind speed for the rated rotational speed and maintain the rotational speed approximately constant for wind speeds above it, as illustrated in Figure 3.4.

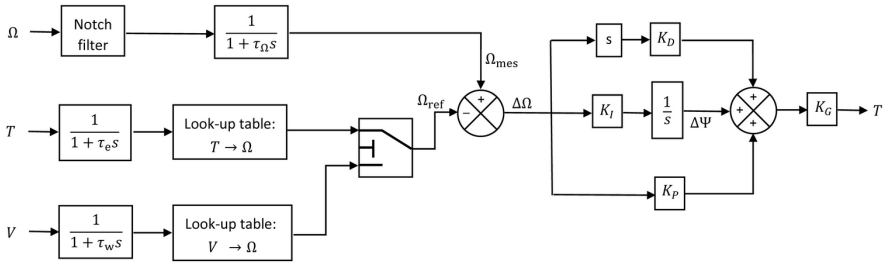

Figure 3.3: The generator torque control algorithm for a floating VAWT based on a PID architecture.

The architecture of the generator torque controller is shown in Figure 3.3. The generator rotational speed and electric torque are measured and low-pass filtered. The controller aims to minimize the error between the measured and filtered rotational speed Ω_{mes} and the reference rotational speed Ω_{ref},

$$\Delta\Omega = \Omega_{mes} - \Omega_{ref} \tag{3.6}$$

in which the reference rotational speed Ω_{ref} is defined as a function of the measured wind speed and the measured and low-pass filtered electric torque. The rotational speed error $\Delta\Omega$ is then fed through the proportional, integral and derivative paths to obtain an updated value of the required electric torque, as follows,

$$T(t) = K_G \left(K_P \Delta\Omega(t) + K_I \int_0^t \Delta\Omega(\tau) d\tau + K_D \frac{d}{dt} \Delta\Omega(t) \right) \tag{3.7}$$

in which K_G is the generator stiffness, and K_P, K_I and K_D are the proportional, integral and derivative gains, respectively.

However, the above baseline control strategy does not limit the generator power and the generator power increases as the wind speed increases, even at above the rated wind speed V_N. At very high wind speed, very large aerodynamic thrust and torque are thus expected, which can cause large structural responses. Hence, Cheng et al. [70] improved the baseline control

strategy by limiting and adjusting the rotational speed above the rated wind speed so as to hold an approximately constant generator power production. This control strategy is denoted as the improved control strategy herein.

Therefore, considering a typical floating VAWT, the relationship between the reference rotational speed and wind speed is illustrated in Figure 3.4. According to the operating conditions, it can be divided into three regions, as highlighted in Figure 3.4. In region I where wind speeds ranges from V_{in} to V_{Ω_N}, the rotor operates at the optimal tip speed ratio so as to achieve the highest power coefficient. In region II, the rotor operates at a moderate tip speed ratio and holds the rotational speed constant at the rated one. The control targets in region I and II are to maximize the power capture and to hold the rotational speed not larger than the rated one in the meantime.

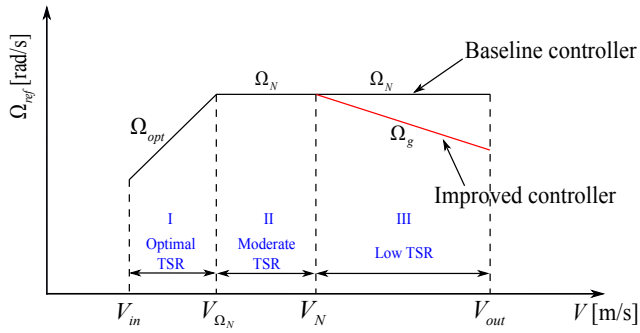

Figure 3.4: The relationship between the reference rotor rotational speed and wind speed for the baseline and improved controller. V_{in}, V_N and V_{out} are the cut-in, rated, and cut-out wind speed, respectively; V_{Ω_N} is the wind speed for rated rotational speed; Ω_N is the rated rotational speed; Ω_{opt} is the optimal rotational speed that can maximize the power capture; Ω_g is the rotational speed that can hold the mean generator power approximately constant [45].

However, the control targets in region III shift to limit the aerodynamic loads acting on the rotor by regulating the rotational speed. In this case, the rotor rotates at relatively low tip speed ratios and two control strategies, i.e. the baseline controller and improved controller, are considered here, as illustrated in Figure 3.4. This baseline controller is capable of maximizing the power capture for wind speeds below V_{Ω_N} and maintaining the rotational speed for wind speeds above V_{Ω_N}, while the improved controller aims to maximize the power capture for wind speeds below V_N and maintaining the power capture approximately constant for the above rated wind speeds.

In addition, a notch filter is implemented in the controller to isolate the

electric torque from the variation of aerodynamic loads. For turbulent wind conditions the wind speed is measured and low-pass filtered.

3.3 Code-to-code Comparisons of the Fully Coupled Tools

The SIMO-RIFLEX has been widely used and validated in the offshore oil and gas industry. The DMS and developed AC code has been validated with experimental data (see Section 2.4). The SIMO-RIFLEX-DMS code was also verified by validating each module separately by Wang et al. [44]. Due to limited experimental data of floating VAWTs, code-to-code comparisons were used to verify the SIMO-RIFLEX-AC code by Cheng et al. [45].

Considering a landbased 5 MW Darrieus rotor, these three codes, i.e. SIMO-RIFLEX-DMS, SIMO-RIFLEX-AC and HAWC2, are verified with each other by comparing the thrust, side force and aerodynamic torque in steady wind conditions, as shown in Figures 3.5 and 3.6. The load cases shown in these two figures correspond to a tip speed ratio of 4.39 and 2.51, which locate in region I and II as illustrated in Figure 3.4, respectively. Here the effect of dynamic stall is not included since these three codes use different dynamic stall model. The developed codes SIMO-RIFLEX-DMS and SIMO-RIFLEX-AC are accurate enough in predicting aerodynamic loads for landbased VAWTs.

In order to reveal the essential reasons for the different resultant aerodynamic loads, the normal and tangential load acting on the blade element are studied, as shown in Figure 3.7. Figure 3.7 shows the time history of blade normal and tangential loads at the midpoint of the blades simulated using the SIMO-RIFLEX- AC and HAWC2 code. It is seen that the negative normal loads differ notably. The possible reason for this deviation is that the SIMO-RIFLEX-AC code accounts for the tangential term when calculating the induced velocity, while HAWC2 ignores it. It has been shown by Cheng et al. [56] that including the tangential term when calculating the induced velocity can modify the behavior of normal loads in the downwind part as depicted in Figure 3.7, which corresponds to negative normal loads.

In addition, the semi-submersible VAWT described in Section 4.1 is used to verify the capability of the SIMO-RIFLEX-DMS and SIMO-RIFLEX-AC code in performing integrated modeling and dynamic analysis of floating VAWTs. Figure 3.8 demonstrates the mean value and standard deviation of the tower base fore-aft and side-side bending moment for the semi-submersible VAWT. The code SIMO-RIFLEX-AC gives a little smaller values than the code SIMO-RIFLEX-DMS in the mean value and standard

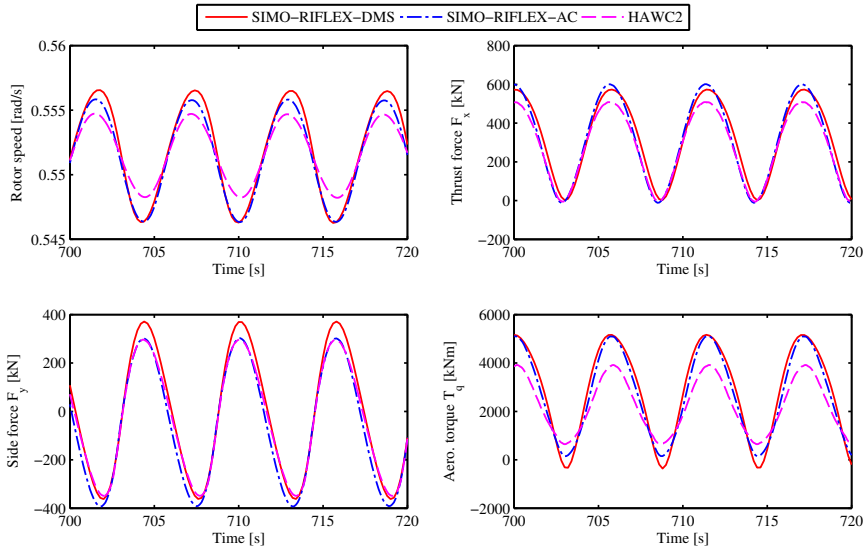

Figure 3.5: Comparison of the rotational speed, thrust, side force and aerodynamic torque of the landbased VAWT using three codes without considering the effect of dynamic stall in the steady wind case with a wind speed of 8 m/s [45].

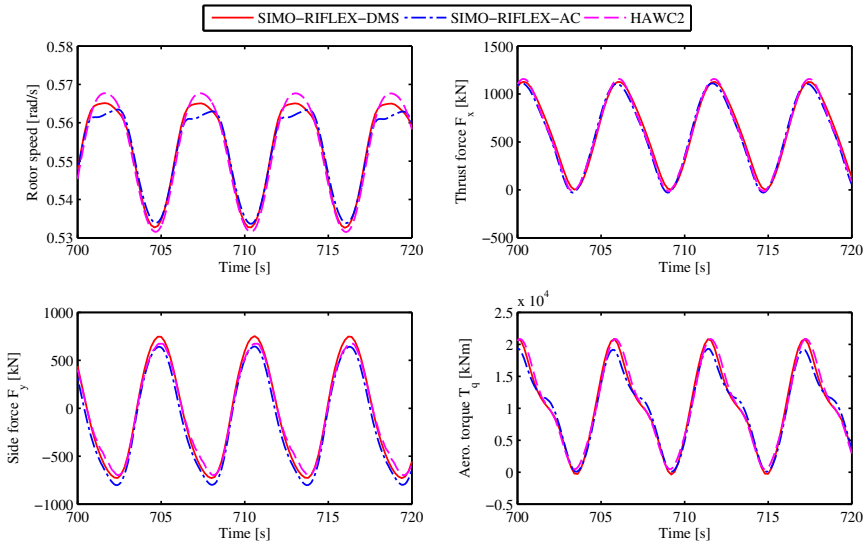

Figure 3.6: Comparison of the rotational speed, thrust, side force and aerodynamic torque of the landbased VAWT using three codes without considering the effect of dynamic stall in the steady wind case with a wind speed of 14 m/s [45].

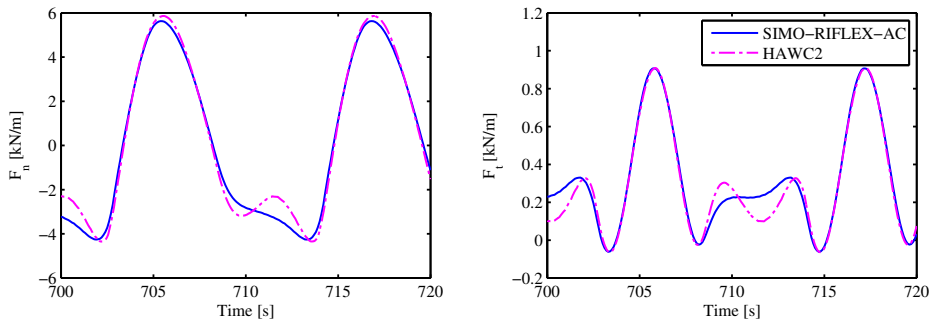

Figure 3.7: Comparison of simulated blade normal force F_n and tangential force F_t at midpoint of the blade using the SIMO-RIFFLEX-AC and HAWC2 code in the steady wind case with a wind speed of 8 m/s. The effect of dynamic stall is not considered [45].

deviation of the fore-aft bending moment. Regarding the side-side bending moment, its mean value is significantly different for these two codes and its standard deviation predicted by the SIMO-RIFLEX-AC code is smaller than that by the SIMO-RIFLEX-DMS code. The code SIMO-RIFLEX-AC can to some extent predict more accurate dynamic responses than the code SIMO-RIFLEX-DMS.

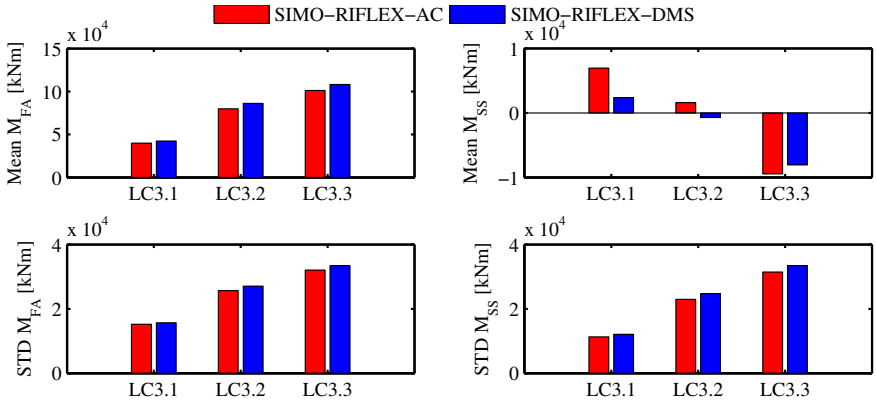

Figure 3.8: Mean values and standard deviations of tower base fore-aft bending moment M_{FA} and side-side bending moment M_{SS} of the semi VAWT simulated using SIMO-RIFLEX-AC and SIMO-RIFLEX-DMS [45]. LC3.1, 3.2 and 3.3 correspond to LC 2, 5 and 6 in Table 4.7, respectively.

Chapter 4

Landbased and Floating Wind Turbine Concepts

Various wind turbine concepts used in this thesis are described in this chapter, including the landbased and floating VAWTs with a two-bladed Darrieus rotor used in *Paper 2, 4, 5, 6*, the landbased and floating VAWTs with straight blades used in *Paper 3* and the landbased and floating HAWTs with the NREL 5 MW wind turbine [76] used in *Paper 6*. Those wind turbine concepts are introduced in Sections 4.1, 4.2 and 4.3, respectively. The environmental condition used for the turbulent wind and irregular wave simulations is also given in Section 4.4.

4.1 VAWT Concepts with a Two-bladed Darrieus Rotor

A 5MW Darrieus rotor, which is the baseline design developed in the DeepWind project [27], was used in this thesis to study the dynamic response characteristics of floating VAWTs. As illustrated in Figure 4.1, the rotor is comprised of two blades and one rotating tower that spans from the top to the bottom which is connected to the generator. Main specifications of this rotor are summarized in Table 4.1. The generator considered here was assumed to be placed at the tower base.

Three floating support structures were considered to support the Darrieus rotor: namely a spar, semi-submersible and TLP, as depicted in Figure 4.1 and listed in Table 4.2. These three substructures were originally designed to support the NREL 5 MW wind turbine [76] and were considered in the water depth where they were designed, ranging from 150 m for the

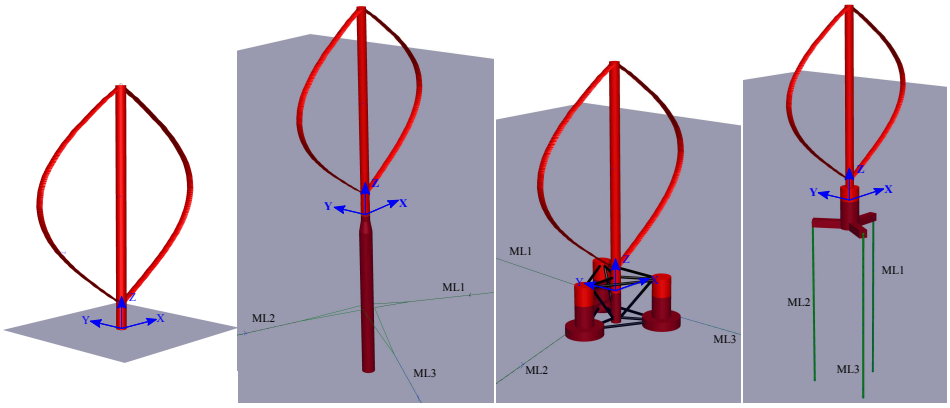

Figure 4.1: Landbased and floating VAWT concepts with a two-bladed Darrieus rotor: landbased, spar, semi-submersible and TLP.

Table 4.1: Specifications of the Darrieus 5 MW wind turbine

Rated power [MW]	5
Rotor radius [m]	63.74
Rotor height, root-to-root [m]	129.56
Chord length [m]	7.45
Cut-in, rated, cut-out wind speed [m/s]	5.0 , 14.0 , 25.0
Rated rotor rotational speed [rpm]	5.26
Total mass, including rotor, shaft and tower [kg]	754,226
Location of overall center of mass [m]	(0 , 0 , 75.6)

Table 4.2: Properties of the three floating wind turbine systems

Floater	spar	semi-submersible	TLP
Water depth [m]	320	200	150
Draft [m]	120	20	22
Diameter at mean water line [m]	6.5	12.0/6.5	14.0
Platform mass, including ballast and generator [ton]	7308.3	13353.7	2771.9
Center of mass for platform [m]	(0, 0, -89.76)	(0, 0, -13.42)	(0,0,-15.38)
Buoyancy in undisplaced position [kN]	80710	139816	56804
Center of buoyancy [m]	(0, 0, -62.07)	(0, 0, -13.15)	(0, 0, -14.20)
Surge/Sway natural period [s]	130.8	114.0	45.3
Heave natural period [s]	27.3	17.1	0.6
Roll/Pitch natural period [s]	34.5	31.0	4.5/4.9
Yaw natural period [s]	8.5	79.7	19.3

TLP, 200 m for the semi-submersible to 320 m for the spar. Reasonable modifications were made on each platform to support the 5 MW Darrieus rotor, such as adjusting the ballast of the spar and semi-submersible, and the tendon pretension of the TLP. For each platform, the draft and displacement were maintained the same as the original one. Details regarding the adjustment is described by Cheng et al. [64, 65]. Properties related to the three floating VAWT systems are given in Table 4.2 where the generator mass is incorporated in the platform hull mass. The first 10 eigenmodes of the landbased VAWT were estimated by Wang et al. [44]. The natural periods of rigid body motions for the floating systems were estimated by conducting free decay tests using numerical simulations [64, 65].

Since the difference in mass between the 5 MW Darrieus rotor and the NREL 5 MW wind turbine was small compared to the displacement of these three concepts, it was assumed that such modifications would not alter the hydrostatic performance of each platform significantly, which was verified by the simulations in Chapter 5. After these modifications, these substructures supporting the 5 MW Darrieus rotor may not be optimal from an economical point of view, but they are sufficient to demonstrate the inherent motion and structural response characteristics of each concept.

4.2 VAWT Concepts with Straight Blades

To investigate the effect of blade number on the dynamic behavior of floating VAWTs, three VAWTs with straight and parallel blades were designed by Cheng et al. [23] (*Paper 3*), as shown in Figure 4.2. These three rotors hold identical solidity while the number of blades varies from two to four. Specifications of these three rotors are given in Table 4.3. Structural property of the three VAWTs is estimated on the basis of the DeepWind 5 MW Darrieus Deepwind rotor and described by Cheng et al. [23].

Table 4.3: Specifications of three straight-bladed VAWTs.

	H2	H3	H4
Rated power [MW]	5.21	5.30	5.35
Blade number [-]	2	3	4
Rotor radius [m]	39.0	39.0	39.0
Height [m]	80.0	80.0	80.0
Chord length [m]	4.05	2.7	2.03
Tower top height [m]	79.78	79.78	79.78
Aerofoil section	NACA 0018	NACA 0018	NACA 0018
Cut-in, rated and cut-out wind speed [m/s]	5.0, 14.0, 25.0	5.0, 14.0, 25.0	5.0, 14.0, 25.0
Rated rotational speed [rad/s]	1.08	1.08	1.08

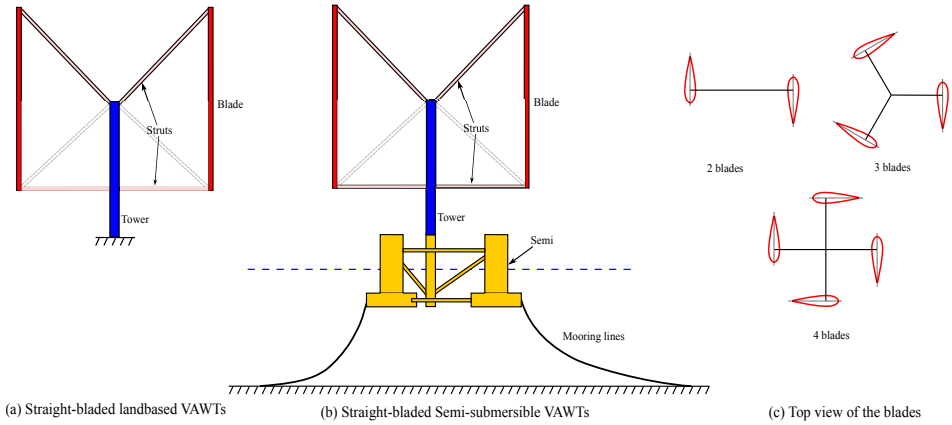

Figure 4.2: Sketch of landbased and floating VAWT concepts with straight and parallel blades.

Table 4.4: Properties of three floating straight-bladed VAWT systems.

	Semi H2	Semi H3	Semi H4
Water depth [m]	200	200	200
Draft [m]	20	20	20
Diameter at mean water line [m]	12.0/6.5	12.0/6.5	12.0/6.5
Rotor mass [ton]	350.1	315.3	287.7
Center of mass for rotor [m]	(0, 0, 51.03)	(0, 0, 48.14)	(0, 0, 45.34)
Platform mass, including ballast and generator [ton]	13761.3	13796.1	13823.7
Center of mass for platform [m]	(0, 0, -13.44)	(0, 0, -13.43)	(0, 0, -13.43)
Buoyancy in undisplaced position [kN]	139816	139816	139816
Center of buoyancy [m]	(0, 0, -13.15)	(0, 0, -13.15)	(0, 0, -13.15)
Surge/Sway natural period [s]	113.15	113.15	113.15
Heave natural period [s]	17.04	17.04	17.04
Pitch/Roll natural period [s]	21.17	20.68	20.32
Yaw natural period [s]	80.38	80.44	80.49

The OC4 semi-submersible [9] , which was originally designed to support the NREL 5 MW wind turbine [76], was used to support the three straight-bladed VAWTs. The considered water depth was assumed to be 200 m. Due to the difference in rotor mass, the ballast of the semi-submersible was adjusted to maintain the same draft and displacement when supporting three different VAWTs. Properties of the three floating VAWT systems are given in Table 4.4. The generator was assumed to be located at the tower base and its mass was incorporated in the platform mass. The natural periods of rigid-body motions were estimated by conducting numerical decay tests [23]. More details about the floating VAWT systems are described by Cheng et al. [23]. Since the difference in mass between the NREL 5 MW wind tur-

bine and three designed rotors is small compared to the displacement of the semi-submersible, it is therefore assumed that such modification will not significantly affect its hydrostatic performance. In addition, A generator torque controller was designed to regulate the rotor rotational speed using the improved control strategy described in Section 3.2.4. The mean generator power of landbased and floating VAWTs is shown in Figure 4.3.

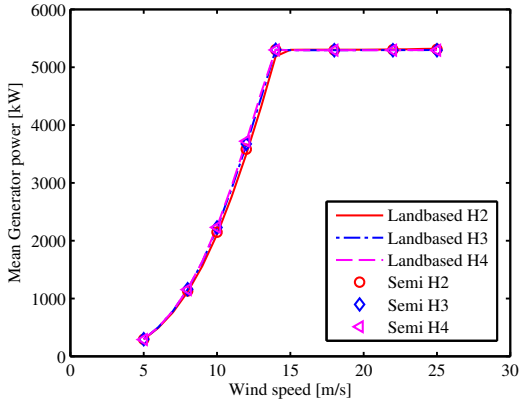

Figure 4.3: The mean value of the generator power of the landbased and floating VAWTs with the improved controller.

The rotor and substructure were designed with similar overall aerodynamic and hydrodynamic behavior. Although the structural properties of the rotors and the design of the substructure are not optimal from an economic point of view, they are sufficient to reveal and demonstrate the effect of blade number on the dynamics of floating VAWTs.

4.3 HAWT Concepts

In this study, a spar-type HAWT with the NREL 5MW wind turbine [76] was used for a comparative study of a spar-type HAWT and VAWT [70, 75] (*Paper 6 and Additional paper 8*). The NREL 5 MW wind turbine is a conventional three-bladed upwind HAWT with variable-speed and variable blade-pitch control [76]. Table 4.5 lists the main specifications of this turbine, and those of the 5 MW Darrieus rotor used by Cheng et al. [70] (*Paper 6*).

The OC3 spar buoy, as described in Jonkman [104], was used to support the NREL 5 MW wind turbine [76]. The spar-type VAWT is described in Section 4.1. A schematic design of the spar-type HAWT and VAWT system

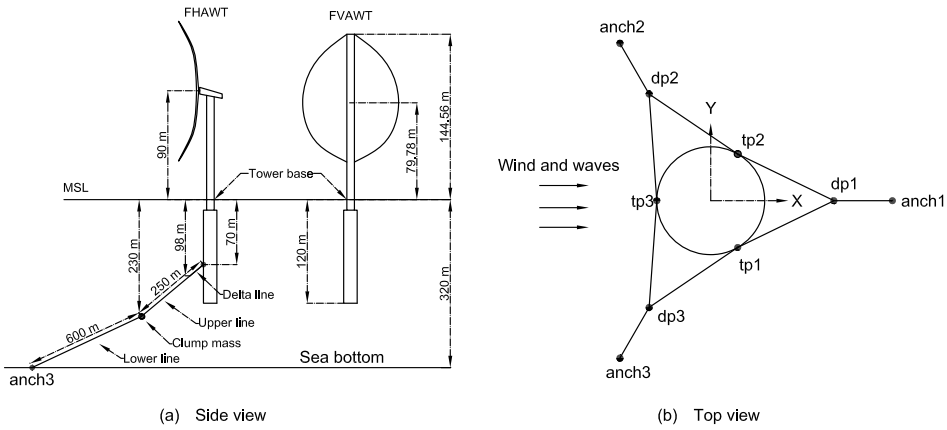

Figure 4.4: Schematic of the spar-type HAWT and VAWT system [70].

is depicted in Figure 4.4. The main properties of the spar HAWT and VAWT system are given in Table 4.6. More detailed geometrical, structural and hydrostatic properties of the spar floaters for the spar HAWT and VAWT are described by Cheng et al. [75].

Table 4.5: Specifications of HAWT and VAWT

Turbines	VAWT	HAWT
Rated power [MW]	5	5
Rotor radius [m]	63.74	63
Rotor height/hub height [m]	129.56	90
Chord [m]	7.45	1.419-4.652
Cut-in, rated, cut-out wind speed [m/s]	5 , 14 , 25	5 , 11.4 , 25
Rated rotor rotational speed [rpm]	5.26	12.1
Nacelle mass [kg]	0	240,000
Rotor mass [kg]	305,044	110,000
Shaft mass/Tower mass [kg]	449,182	249,718
Location of overall CM [m]	(0 , 0 , 75.6)	(-0.2 , 0 , 70.06)

4.4 Environmental Conditions

To evaluate the performance of novel floating VAWT concepts, a realistic environmental condition should be considered. In this thesis, the wind and wave data at the Statfjord site in the northern North Sea was selected. Considering some other conditions, such as current, ice and tidal, is outside the scope of present work.

Table 4.6: Properties of the spar-type HAWT and VAWT system

Floater	Spar VAWT	Spar HAWT
Water depth [m]	320	320
Draft [m]	120	120
Diameter at MWL [m]	6.5	6.5
Platform mass, including ballast [ton]	7308.29	7466.33
Center of mass for platform [m]	(0, 0, -89.76)	(0, 0, -89.92)
Buoyancy in undisplaced position [kN]	80710	80710
Center of buoyancy [m]	(0, 0, -62.07)	(0, 0, -62.07)
Surge/Sway natural period [s]	130.8	130.4
Heave natural period [s]	27.3	31.5
Pitch/Roll natural period [s]	34.5	29.6
Yaw natural period [s]	8.5	8.2

The long term wind and wave data can be described using a joint distribution of the 1-hour mean wind speed at 10 m above sea water level (U_{10}), the significant wave height (H_s), and the spectral peak period (T_p). Based on the wind and wave measurements during 1973-1999, Johannessen et al. [105] proposed a joint probability density distribution as a product of the marginal wind distribution $f_{U_{10}}(u)$, the conditional distribution of H_s given U_{10}, and the conditional distribution of T_p given H_s and U_{10} as follows

$$f_{U_{10}H_sT_p}(u,h,t) = f_{U_{10}}(u) f_{H_s|U_{10}}(h \mid u) f_{T_p|H_sU_{10}}(t \mid h,u) \tag{4.1}$$

Using the environmental data generated by a numerical hindcast model, Li et al. [106] also established another long term distribution model for the wind and wave parameters at five European offshore sites.

The joint probabilistic model can be used to establish a contour surface and thus provide combinations of the weather parameters with a certain return period. In this thesis, the joint distribution function is used to calculate the conditional mean values of H_s and T_p for a given U_{10}, which can be determined from the wind speed U_w at the reference height z_{ref}. A set of environmental conditions at the Statfjord site was selected to simulate the dynamic responses of floating wind turbines, as given in Table 4.7. In this thesis, only normal operating conditions with the wind speed ranging from the cut-in to cut-out were considered.

For turbulent wind conditions, the TurbSim [107] was used to generate the 3D turbulent wind field based on the Kaimal spectral model. The IEC Kaimal model is defined in IEC 61400 [108]. In addition, variation of the mean wind speed with height above the ground, known as wind shear, is significant and also considered using the normal wind profile model proposed

Table 4.7: The turbulent wind and irregular wave condition

	U_w [m/s]	H_s [m]	T_p [s]	T_I [-]
LC1	5	2.10	9.74	0.224
LC2	8	2.55	9.86	0.174
LC3	10	2.88	9.98	0.157
LC4	12	3.24	10.12	0.146
LC5	14	3.62	10.29	0.138
LC6	18	4.44	10.66	0.127
LC7	22	5.32	11.06	0.121
LC8	25	6.02	11.38	0.117

in the IEC 61400 [108]. The power law formulation of wind shear is applied to determine the average wind speed U_z as a function of height z above mean sea level (MSL), as follows

$$U(z) = U_{ref}\left(\frac{z}{z_{ref}}\right)^{\alpha} \tag{4.2}$$

where U_{ref} is the reference wind speed, z_{ref} is the height of the reference wind speed and α is the power law exponent. In this study z_{ref} was set to be 79.78 m above MSL, which is the vertical center of blades of the VAWTs considered. The value of α was chosen to be 0.14 for the floating wind turbines according to IEC 61400-3 [108].

Regarding irregular wave conditions, the long-crested irregular wave was generated using the Joint North Sea Wave Project (JONSWAP) spectrum, which is given by [51]

$$S(\omega) = \frac{\alpha g^2}{\omega^5}\exp\left[-\beta\left(\frac{\omega_p}{\omega}\right)^4\right]\gamma^{\exp\left(\frac{(\omega/\omega_p-1)^2}{2\sigma^2}\right)} \tag{4.3}$$

where

$$\alpha = 5.061\frac{H_s^2}{T_p^4}\left(1 - 0.287\ln(\gamma)\right) \tag{4.4}$$

$$\omega_p = \frac{2\pi}{T_p} \tag{4.5}$$

$$\sigma = \begin{cases} 0.07 & \text{for } \omega < \omega_p \\ 0.09 & \text{for } \omega \geq \omega_p \end{cases} \tag{4.6}$$

in which α is the spectral parameter, β is the form parameter, γ is the peakedness parameter and is limited by $1 \leq \gamma \leq 7$. A typical value of $\gamma = 3.3$ represents a sea state that is not fully developed.

Chapter 5

Dynamic Response Analysis of Floating VAWTs

5.1 General

A variety of studies have been conducted to investigate the dynamic response characteristics of different floating VAWT concepts in the normal operating and fault conditions, as reviewed in Section 1.2.3.

In this chapter, the dynamic response characteristics of several floating VAWT concepts are investigated and demonstrated using fully coupled time domain simulations. It addresses the effect of blade number on the dynamic behavior of floating VAWTs with straight blades (Section 5.2) (*Paper 3*), the dynamic response of a spar, semi-submersible and TLP VAWT with a two-bladed Darrieus rotor (Section 5.3) (*Paper 4*), and the effect of second-order difference-frequency force on the dynamics of a semi-submersible VAWT in misaligned wave-wind conditions (Section 5.4) (*Paper 5*). Lastly, the Section 5.5 (*Paper 6*) presents a comparative study on the dynamic responses of a spar-type HAWT and VAWT.

5.2 Dynamic Analysis of Floating VAWTs with Straight Blades

The number of blades is one of the main concerns when designing a floating VAWT. The effect of the number of blades on the dynamic behavior of floating VAWTs was comprehensively studied by Cheng et al. [23] (*Paper 3*). VAWTs with straight and parallel blades, with identical solidity and with a blade number varying from two to four, were firstly designed using

the AC flow method described in Section 2.3. A generator torque controller was also designed and used to regulate the rotational speed based on the improved control strategy described in Section 3.2.4. These three VAWTs were then adapted to a semi-submersible platform to achieve three floating VAWTs with identical draft, displacement and mooring system. Properties of the rotors and floating VAWT systems are described in Section 4.2. A set of turbulent wind and irregular wave simulations, as given in Table 4.7, were carried out to study the dynamic responses of the three floating VAWTs.

Figure 5.1 shows the mean values and standard deviations of the generator power production, thrust, side force and rotor rotational speed for the three floating VAWTs. It can be found that the mean values in the generator power, thrust, side force and rotor rotational speed of three floating VAWTs are very close to each other for each LC as well. Although the mean side force of the 2-bladed semi VAWT is larger than those of the 3- and 4-bladed semi VAWTs, the absolute value is all small compared to the mean thrust.

Visible differences in Figure 5.1 are observed in the standard deviations, especially in those of the thrust and side force. Such differences are mainly due to the different number of blades. The blade number contributes considerably to the variation of resultant aerodynamic loads acting on the rotor, as illustrated in Figure 5.1 (b) and (c). The standard deviation in the thrust and side force of the 2-bladed semi VAWT is significantly larger than those of the 3- and 4-bladed semi VAWT, since its lift and drag force of each blade reach the maximum and minimum simultaneously, causing the thrust and aerodynamic torque varying from approximate zero to double the mean value.

Moreover, the difference in the standard deviation of the generator power among the three semi VAWTs is much less notable than that of the aerodynamic loads. The standard deviation in the generator power of the 3- and 4-bladed semi VAWTs are very close to each other, while that of the 2-bladed semi VAWT is visibly larger than those of the 3- and 4-bladed semi VAWTs above the rated wind speed.

Neither are the platform motions sensitive to the blade number, due to the compliant catenary mooring system, as demonstrated in Figure 5.2. The mean value of platform motions are mainly induced by the wind loads. The mean surge, pitch and yaw motions increase as wind speeds increase. Moreover, the mean pitch and yaw motions of the 2-bladed semi VAWT are to some extent larger than those of the 3- and 4-bladed semi VAWTs above the rated wind speed. The standard deviations of platform motions are induced by not only the wind loads but also the wave loads. It's obvious

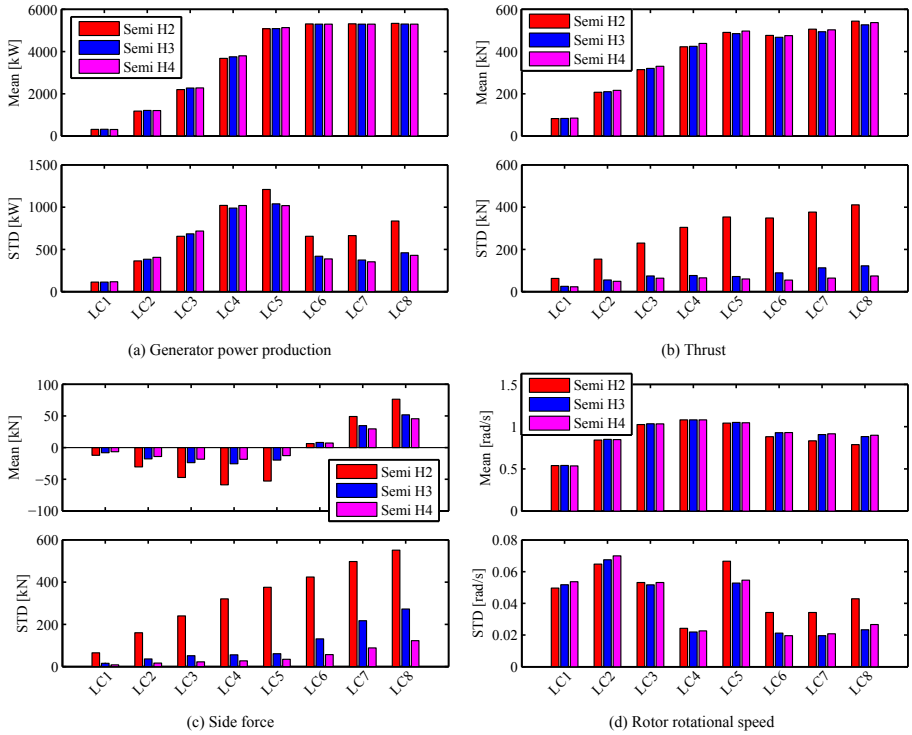

Figure 5.1: The mean value and standard deviation of the (a) generator power production, (b) thrust, (c) side force, and (d) rotor rotational speed of three floating VAWTs (Semi H_i, i-number of blades) in turbulent wind and irregular wave conditions [23].

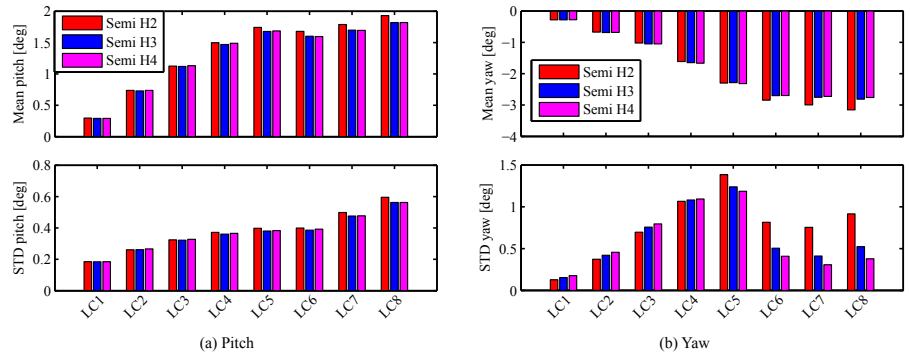

Figure 5.2: The mean value and standard deviation of the pitch and yaw motions of three floating VAWTs in turbulent wind and irregular wave conditions [23].

from Figure 5.2 that the standard deviations of platform motions of the 3- and 4-bladed semi VAWTs are generally very close to each other for each LC. Moreover, the standard deviation of pitch motions of these three floating VAWTs are very close to each other for each LC. However, the 2-bladed semi VAWT gives relatively larger standard deviations in surge, roll and yaw motions at LCs with wind speeds above the rated one.

The effect of blade number on the structural response is of great interest and was studied using the tower base bending moment. Figure 5.3 compares the mean value and standard deviation of the tower base for-aft bending moment M_{FA} and side-side bending moment M_{SS} for the three floating VAWTs. Obviously the discrepancy in the mean value of both M_{FA} and M_{SS} for the three floating VAWTs is fairly small, and is much less notable than that in the standard deviation.

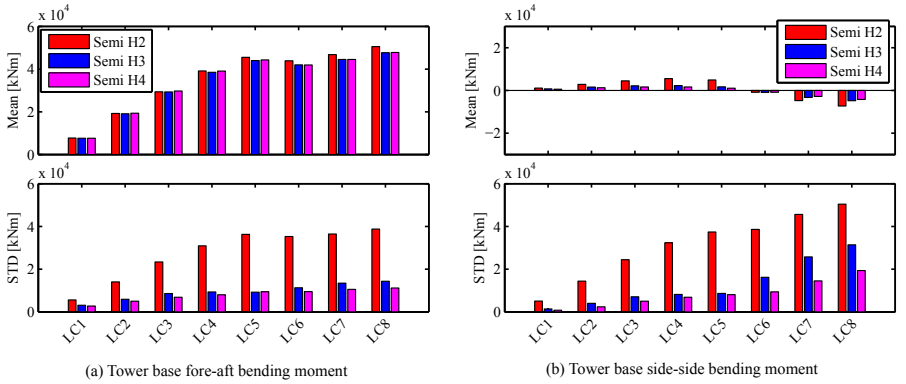

Figure 5.3: The mean value and standard deviation of tower base fore-aft and side-side bending moments of three floating VAWTs in turbulent wind and irregular wave conditions [23].

The 2-bladed semi VAWT gives significantly larger standard deviation than the 3- and 4-bladed semi VAWTs with respect to both the M_{FA} and M_{SS}, as illustrated in Figure 5.3. The ratio of the standard deviation of the 2-bladed semi VAWT to that of the 3-bladed semi VAWT varies from 2.37 to 3.93 for LC2-LC7, while the ratio of the standard deviation of the 4-bladed semi VAWT to that of the 3-bladed semi VAWT remains approximately constant at 0.8. It indicates that increasing blade number from 2 to 3 blades can decrease M_{FA} more significantly than increasing blade number from 3 to 4 blades. Similar conclusion can also be drawn for the M_{FA}. In addition, it is also interesting to see that for the 2-bladed semi VAWT the M_{FA} is smaller than the M_{SS} for all LCs except LC1, and the discrepancy

between M_{FA} and M_{SS} can reach more than 20% at LC7 and LC8. But both 3- and 4-bladed semi VAWT predict to some extent larger M_{FA} than M_{SS} in LCs with wind speed at or below the rated one.

Power spectral analysis can be used to identify the different contributions to the variation of the M_{FA} and M_{SS}, as shown in Figure 5.4. These three floating VAWTs have very close low frequency turbulent wind induced response and wave frequency response, as well as noticeable different responses at the nP (2P, 3P and 4P) frequency. Moreover, the nP response is increasingly dominating, especially in LCs with high wind speeds. For the 2-bladed semi VAWT, it is seen that not only is the 2P response significant but even the 4P response is visible, while only 3P and 4P response is captured for the 3- and 4-bladed semi VAWT, respectively.

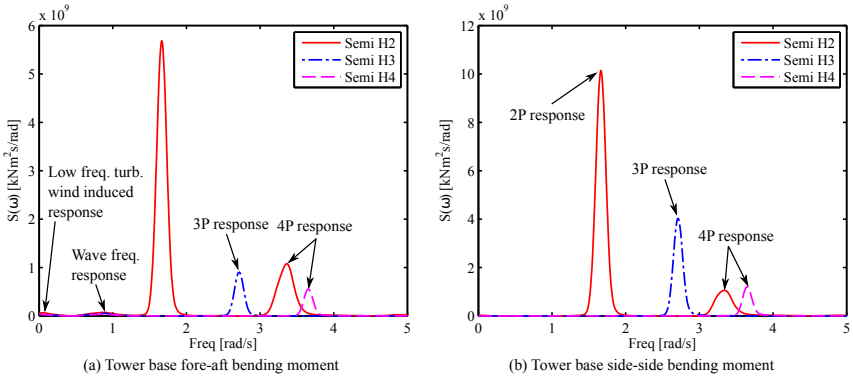

Figure 5.4: Power spectra of the (a) tower base fore-aft bending moment and (b) side-side bending moment of three floating VAWTs in LC7 [23]. LC7 is defined in Table 4.7.

The effect of blade number on the mooring line tension of the three floating VAWTs was also studied. Among the three mooring lines, the mooring line 2 is in line with the wind and wave directions and carries the largest tension when the floating VAWTs are subjected to the wind and wave loads. The tension in mooring line 2 is thus studied. Figure 5.5 shows the mean value and standard deviation of the tension in mooring line 2 of the three floating VAWTs. It can be found that the mean value for each LC is very close to each other for the three floating VAWTs and visible difference is only observed in the standard deviation, especially in LCs with wind speed at or above the rated one. The difference in the standard deviation can be explored by using the power spectra analysis. Generally the power spectral density is dominated by the low frequency turbulent wind induced response,

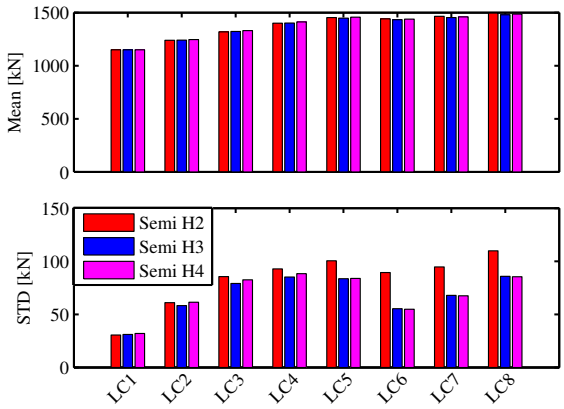

Figure 5.5: The mean value and standard deviation of the tension in mooring line 2 of three floating VAWTs in turbulent wind and irregular wave conditions [23].

and wave frequency response for the three floating VAWTs. For the 2-bladed semi VAWT the 2P response is also very prominent, especially at LCs with high wind speed. In addition, a tiny 3P response is also captured for the 3-bladed semi VAWT in LC7 and LC8. But no 4P response for the 4-bladed semi VAWT is observed for all LCs.

To summarize, the aerodynamic loads and structural responses are strongly dependent on the number of blades. In particular, by increasing the number of blades from two to three reduces the variation in the tower base bending moment more significantly than increasing it from three to four. However, the generator power is not sensitive to the blade number due to the control strategy implemented and neither are the platform motions and tension in mooring lines because of the control strategy and compliant mooring system.

5.3 Dynamic Analysis of a Spar, Semi-submersible and TLP VAWT

The stochastic dynamic responses of a spar, semi-submersible and TLP VAWT concepts [64] (*Paper 4*), as described in Section 4.1, were studied under the turbulent wind and irregular wave conditions, including the generator power production, global platform motion, tower base fore-aft and side-side bending moment and the tensions of the mooring lines. The baseline controller was used during the simulations. Detailed descriptions of load cases used is described by Cheng et al. [64] and also given in Table 4.7.

It should be noted that the stochastic dynamic responses in this section are calculated using the code SIMO-RIFLEX-DMS, but the results are plotted with the mean wind speed as the variable in the abscissa axis for simplicity.

Figure 5.6 shows the mean values of the generator power production of the three floating VAWT concepts. The error bar indicates the standard deviation from the mean value. It can be observed that the mean generator powers increase as the wind speed increases. At rated wind speed of 14 m/s, the mean generator powers slightly exceed the rated power of 5 MW, since the Beddoes-Leishman dynamic stall model is included in the DMS model. The rotor considered can achieve a rated power of 5 MW when excluding the dynamic stall effect. In addition, the mean generator power of the three floating VAWT concepts is very close to each other, except at high wind speeds where the mean generator power of the semi VAWT begins to differ from that of the spar VAWT. The difference results from the different rotational speed and increases as the wind speed increases. The different rotational speed for the three concepts are due to the controller implemented. The controller regulates the rotational speed by adjusting the generator torque, but fails to keep the rotational speed at above rated wind speed exactly constant. The variations of the generator power for the three floating VAWT concepts are very close to each other as well.

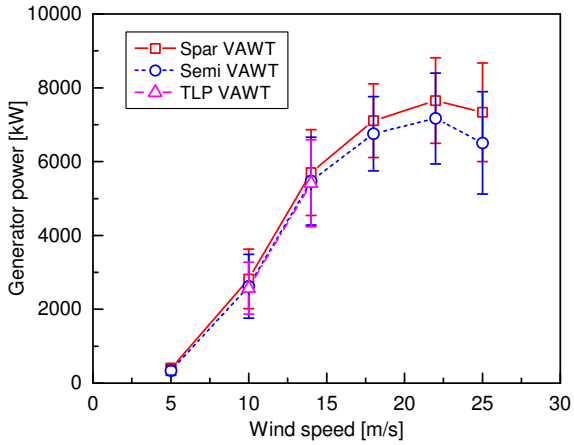

Figure 5.6: Mean power production for the three floating VAWT concepts with error bar indicating the standard deviation from the mean value in the turbulent wind and irregular wave load cases. The load cases are indicated using mean wind speed in the abscissa axis. Results of the TLP VAWT are only given in load cases with wind speeds of 10 and 14 m/s. [64]

The global platform motions of the three floating VAWT concepts present

significant differences. For each load case, the spar VAWT suffers the considerable larger platform motions in surge and pitch. but the standard deviations of the spar VAWT and semi VAWT in pitch motions are very close to each other. Regarding the yaw motion, the mean yaw motions of the three floating VAWT concepts are fairly close. However, the standard deviation of the yaw motion of the semi VAWT is relatively larger than that of the spar VAWT, this is due to the resonant yaw motions excited by the turbulent wind.

Characteristic structural responses for the three floating VAWT concepts are also of great interest. Here both the tower base fore-aft bending moment M_{FA} and side-side bending moment M_{SS} are chosen as the primary structural performance parameters. The tower base was assumed to be located below the bearings between the rotating shaft and the drive train shaft. Since the aerodynamic loads of each blade varies with the azimuthal angle, not only M_{FA} but also M_{SS} have great variations, which is quite different from the horizontal axis wind turbine. These variations of bending moments can cause large stress fluctuations, thus leading to great fatigue damage.

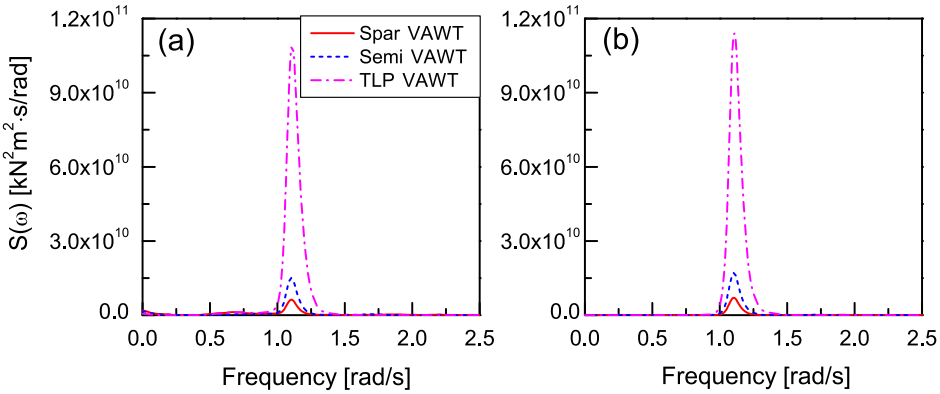

Figure 5.7: Power spectra of tower base (a) fore-aft and (b) side-side bending moment for the three floating VAWT concepts in turbulent wind and irregular wave condition with U_w =14 m/s, H_s=3.62 m, T_p=10.29 s.

Figure 5.7 compares the power spectra of M_{FA} and M_{SS} under the turbulent wind and irregular wave condition. The turbulent winds excite the certain low-frequency response of M_{FA}, but the wind-induced response is much smaller than the 2P response in both M_{FA} and M_{SS}. Furthermore, since the taut tendons cannot absorb the 2P aerodynamic excitations for the TLP VAWT, the 2P responses in M_{FA} and M_{SS} of the spar VAWT and

semi VAWT are much smaller than that of the TLP VAWT, which implies that the catenary mooring system can greatly mitigate the 2P effects on structural dynamic responses. Eigen-frequency analysis has been carried out for this rotor and states that the natural frequencies of the first and second tower base bending modes are far away from the 1P and 2P excitations [44].

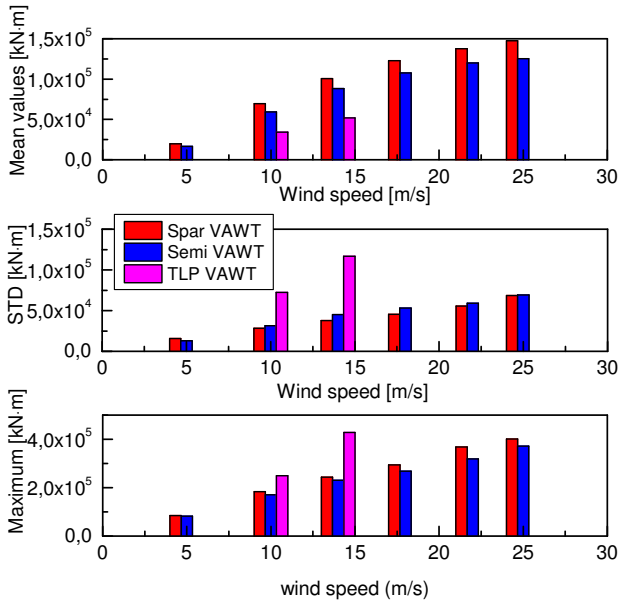

Figure 5.8: Mean values, standard deviations, and maximum values of the tower base fore-aft bending moment for the three floating VAWT concepts. The load cases are indicated using mean wind speed in the abscissa axis. Results of the TLP VAWT are only given in load cases with wind speeds of 10 and 14 m/s.

As a consequence, the standard deviations of M_{FA} and M_{SS} for the spar and semi VAWT are smaller than those of the TLP VAWT, as demonstrated in Figure 5.8. Figure 5.8 compares the mean values and standard deviations of M_{FA} for the three floating VAWT concepts under different environmental conditions. The mean values and standard deviations of M_{FA} increase as the wind speed increases. The mean values of M_{FA} for the spar VAWT and semi-submersible VAWT are much larger than the corresponding standard deviations; on the other hand, the standard deviations of the TLP VAWT are much larger than the mean values. The spar VAWT has the largest mean value of M_{FA} with smallest standard deviation. A similar effect is also observed for M_{SS} for the three floating VAWT concepts.

5.4 Effect of Difference-frequency Force on the Dynamics of a Semi-submersible VAWT in Misaligned Wave-wind Conditions

For moored floating structures, the second order difference-frequency wave force is important for properly simulating the low-frequency wave excitation force and the corresponding global responses. It is therefore of interest to investigate the effect of second order difference-frequency forces on the dynamic responses of a semi-submersible type VAWT. The semi-submersible VAWT considered is a two-bladed 5 MW Darrieus rotor [27] mounted on the OC4 semi-submersible [9], details regarding the properties of the floating wind turbine system is given in Section 4.1.

The load cases used in this study is given in Table 4.7 and by Wang et al. [60]. It should be noted here that the LC2 and LC4 listed in Table 4.7 were not included in this study. Three combinations of hydrodynamic load component were considered as follows

- first order wave excitation force (1st)
- first order wave force and mean drift force (1st + mean drift)
- first order wave force and second order difference-frequency force (1st + full QTF)

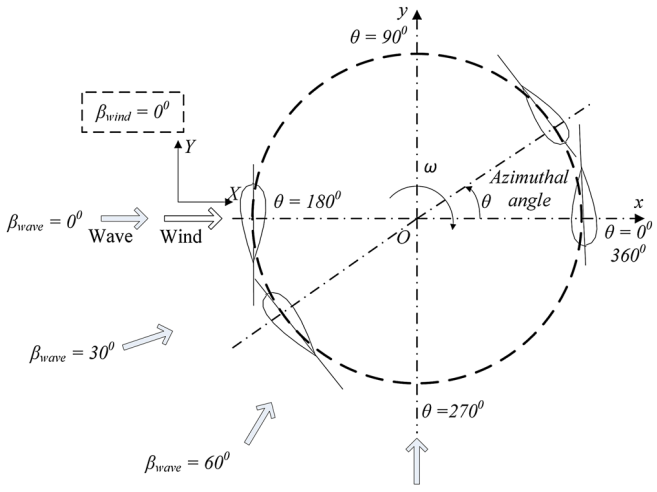

Figure 5.9: A horizontal cross section of the rotor showing the wave direction distribution in misaligned wave-wind conditions [60].

In addition, the wave-wind misalignment was also considered, as depicted in Figure 5.9. Since the wind direction was remained as $\beta_{wind} = 0°$, the wave direction wave was actually a measure of the wave-wind misalignment. For each load case, four wave directions, i.e. β_{wave}= 0°, 30°, 60° and 90°, were simulated considering first order force (1st), first order force and mean drift force (1st + mean drift), and first order force and second order difference-frequency force (1st + full QTF), respectively.

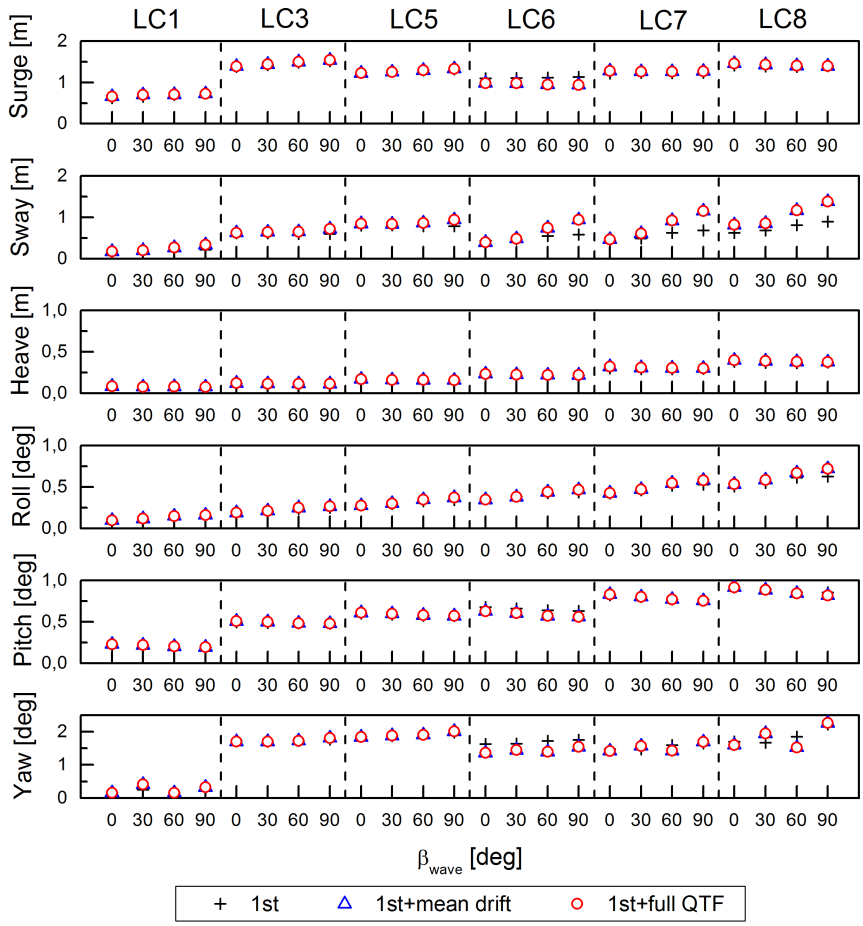

Figure 5.10: Standard deviations of the platform motions as a function of the wave direction β_{wave} for all load cases [60].

Firstly, the effects of second order difference-frequency force and wave-wind misalignment on the platform motions were studied. Since the mean values of platform motions are mainly dominated by wind loads, they are

hardly affected by the wind-wave misalignment. Compared to the mean values, the standard deviations of the platform motions are a little more sensitive to the wave-wind misalignment, as depicted in Figure 5.10. The standard deviation of surge motion increases slowly with increasing β_{wave} in LCs 1, 3 and 5, and decreases slightly with increasing β_{wave} in LCs 6-8. The standard deviation of heave motion almost holds constant for each LC and can be regarded as wave-wind misalignment independent. The standard deviation of pitch motion decreases slowly with increasing β_{wave} for each LC due to the reduction of the component of hydrodynamic loads in surge direction. This decrease in turn causes the increase of the standard deviation of sway and roll motions with increasing β_{wave} and the increase becomes more obvious at higher significant wave height conditions such as LC 6-8. For yaw motion, the standard deviation is dominated by the yaw resonant response.

In addition, spectral analysis shows that as the wave-wind misalignment β_{wave} increases, the low-frequency response increases while the wave-frequency response decreases. The response corresponding to the 2P frequency does not vary with the wave-wind misalignment since they are due to the variation of aerodynamic loads and are thus independent of the misalignment. The increase in the low-frequency response counteracts the reduction in the wave-frequency response, leading to relatively small variation in the standard deviations of surge, heave and pitch motions.

The second order difference-frequency force and the wave-wind misalignment can also affect the structural responses of the semi VAWT. Figure 5.11 presents the mean value, standard deviation and maximum value of the tower base bending moment, including fore-aft bending moment M_{FA} and side-side bending moment M_{SS}, for each load case with different wave-wind misalignment and hydrodynamic load component, respectively. The mean values of M_{FA} and M_{SS} do not strongly depend on the wave-wind misalignment, since the tower base bending moments are primarily caused by the large aerodynamic force acting on the rotor and by the weight of the rotor due to the tower tilt and are thus not affected by the wave-wind misalignment. Unlike the mean value, the wave-wind misalignment has a slight influence on the standard deviations of M_{FA} and M_{SS}. As wave-wind misalignment increases, the standard deviation of M_{SS} decreases slightly while the standard deviation of M_{FA} increases slowly with wave direction in the range of 0° to 60° and then decrease slightly. The maximum values of M_{FA} and M_{SS} vary similarly as the standard deviation when the wave-wind misalignment increases. However, these variations are larger than those of the standard deviation. Therefore, the wave-wind misalignment has relatively

larger influence on the maximum values of M_{FA} and M_{SS} than on the standard deviations of M_{FA} and M_{SS}.

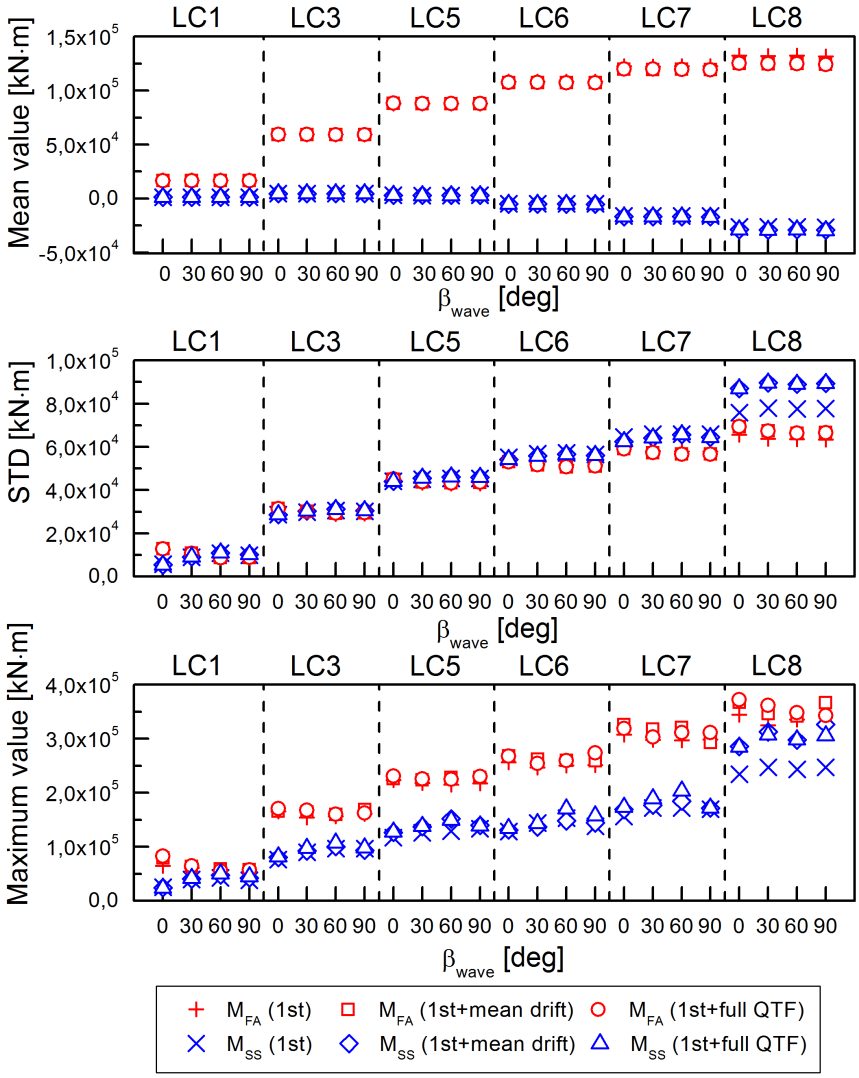

Figure 5.11: Mean value, standard deviation and maximum value of the tower base fore-aft bending moment M_{FA} and side-side bending moment M_{SS} as a function of wave direction β_{wave} for all load cases [60].

5.5 Comparative Study of Spar-type HAWT and VAWT

A comparative study on the dynamics of a spar-type HAWT and VAWT has been conducted to investigate the dynamic response characteristics of each concept by Cheng et al. [75, 70] (*Paper 6 and Additional Paper 8*). The OC3 spar buoy [104] was used to support the NREL 5 MW wind turbine [76] and the DeepWind 5 MW Darrieus rotor [27], respectively. Detailed description of the wind turbines, support structures and mooring systems are given in Section 4.3. The SIMO-RIFLEX-AeroDyn [38] and SIMO-REFLEX-DMS [44] code was used to conduct the fully coupled time domain simulations for the spar HAWT and VAWT, respectively.

Cheng et al. [75] (*Additional Paper 8*) conducted the comparative study using the baseline control strategy, as described in Section 3.2.4, for the spar VAWT. In this comparative study, the wind fields were created with respect to different reference heights for the spar HAWT and VAWT, which implies that a slightly different wind field was used. Moreover, the generator power of the floating VAWT exceeds 5 MW above the rated wind speed and could even reach up to 9 MW. Hence, a more comprehensive comparative study is required by using the same wind field and maintaining almost identical mean generator power production, which is achieved by Cheng et al. [70] (*Paper 6*).

An improved control strategy was proposed and employed to make the comparative study more reasonable by Cheng et al. [70] (*Paper 6*), as described in section 3.2.4. A series of numerical simulations were carried out under identical turbulent wind and irregular wave conditions, as given in Table 4.7.

Figure 5.12 shows the mean values and standard deviations of the generator power and thrust for the spar HAWT and VAWT. At wind speeds above 14 m/s, the mean generator powers of the spar HAWT and VAWT are very close to the rated power of 5 MW. However, the standard deviation of the generator power of the spar VAWT is approximately twice of that of the spar HAWT. For wind speeds below 14 m/s, the mean generator power of the spar HAWT is always much greater than that of the spar VAWT due to the higher power coefficient.

The spar HAWT and VAWT also differ in the platform motions due to the different aerodynamic loads and control strategies. For both the spar HAWT and VAWT, the trends in the mean values of surge, heave and pitch motions are very similar to those of the mean thrust acting on the rotors, since the mean values of the platform motions are mainly related to wind

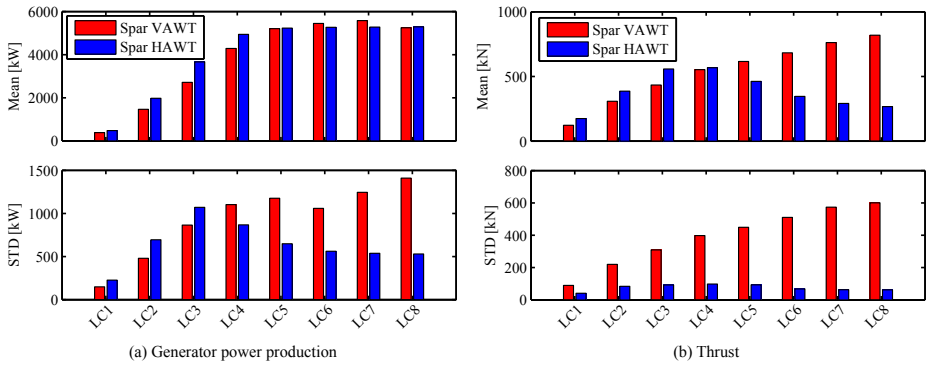

Figure 5.12: Mean values and standard deviations of (a) generator power and (b) thrust for the spar-type HAWT and VAWT under turbulent wind conditions [70].

thrust force. The mean values of the sway, roll and yaw motions of the spar HAWT are very small, because the aerodynamic lateral force and yaw moment are small due to symmetry. However, the spar VAWT has much larger mean values in sway, roll and yaw motions, especially at high wind speed.

The structural responses of the spar HAWT and VAWT exhibit significant differences as well. Figure 5.13 shows the power spectra of the tower base fore-aft and side-side bending moment for the spar HAWT and VAWT in turbulent wind and irregular wave condition with U_w =14 m/s, H_s=3.62 m, T_p=10.29 s. Obviously the response corresponding to the 2P frequency is considerably dominating in the tower base fore-aft and side-side bending moments for the spar VAWT. Moreover, the tower base fore-aft bending moment for the spar VAWT also includes prominent low-frequency turbulent wind induced response and wave frequency response. With respect to the spar HAWT, the tower base fore-aft bending moment consists of significant low-frequency turbulent wind induced response, pitch resonant response and wave frequency response. The pitch resonant response mainly results from the relatively large platform pitch motion. In addition, the tower base of the spar HAWT is mainly affected by the fore-aft bending moment, while the side-to-side bending moment can be neglected.

The tower base of the spar VAWT suffer relatively larger fatigue damage than that of the spar HAWT, as shown in Figure 5.14. A Matlab-based computer program MLife developed by NREL [109] is used to estimate the short-term damage equivalent fatigue loads (DEFLs). The short-term DEFL is a constant-amplitude load that occurs at a fixed mean value and

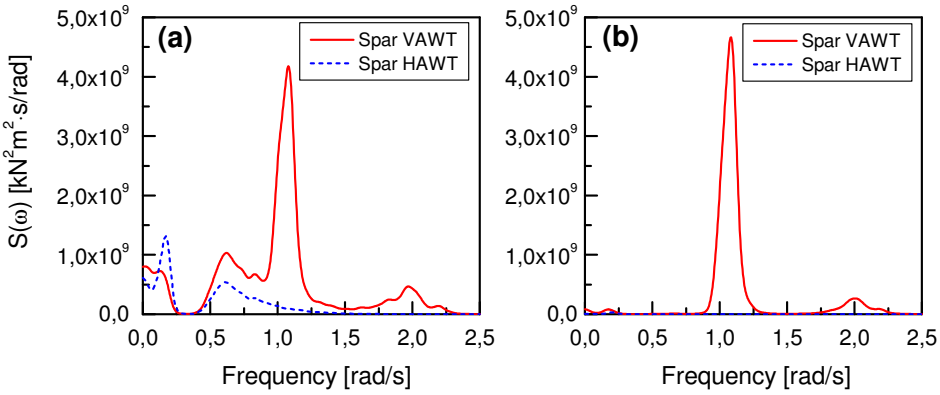

Figure 5.13: Power spectra of the tower base (a) fore-aft bending moment and (b) side-side bending moment for the spar HAWT and VAWT in LC5 with U_w =14 m/s, H_s=3.62 m, T_p=10.29 s [70].

frequency and can produce damage that is equivalent to that of the variable spectrum loads. In this study, a DEFL frequency of 1 Hz was assumed. It can be observed that the DEFL of the fore-aft bending moment for the spar VAWT above the rated wind speed is approximately twice that of the spar HAWT. Moreover, the DEFL of the side-side bending moment for the spar VAWT is more than six times greater than that of the spar HAWT.

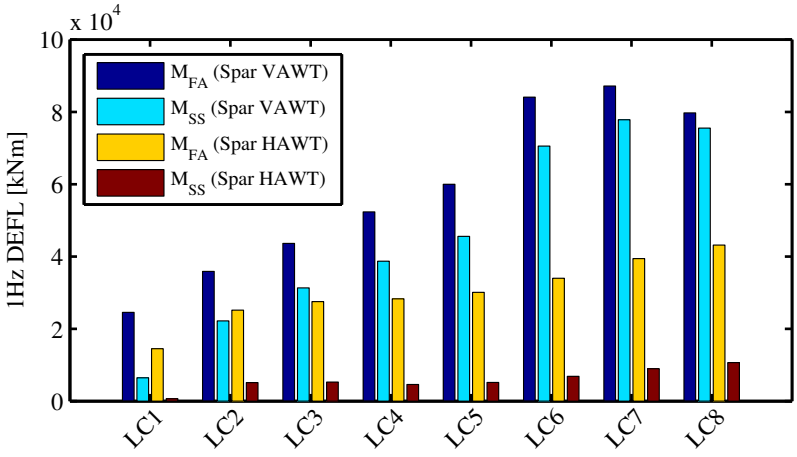

Figure 5.14: 1 Hz damage equivalent fatigue loads (DEFLs) of the tower base fore-aft bending moment (M_{FA}) and side-side bending moment (M_{SS}) for the spar HAWT and VAWT [70].

The spar HAWT and VAWT use identical catenary chain mooring systems with delta lines and clump weights. Each mooring line is composed of two upper delta lines, a upper line, a clump mass and a lower line, as shown in Figure 4.4. The tension in the mooring lines, including the delta lines and lower lines, of the spar HAWT and VAWT are studied. The mean value of the lower line tensions is primarily wind-induced, and the discrepancy in the lower line tensions between the spar HAWT and VAWT is very small compared to the mean value. Due to the large yaw motion experienced by the spar VAWT above the rated wind speed, the mean values of tensions among the six delta lines vary significantly. In addition, the 2P response is observed in the delta lines for the spar VAWT and increases significantly as the wind speed increases. However, despite the prominent 2P response in the delta line tensions, the corresponding 2P response in the lower line tensions is negligible, because the catenary mooring lines can absorb the 2P excitations and alleviate or even dampen out the 2P response in the lower line tensions.

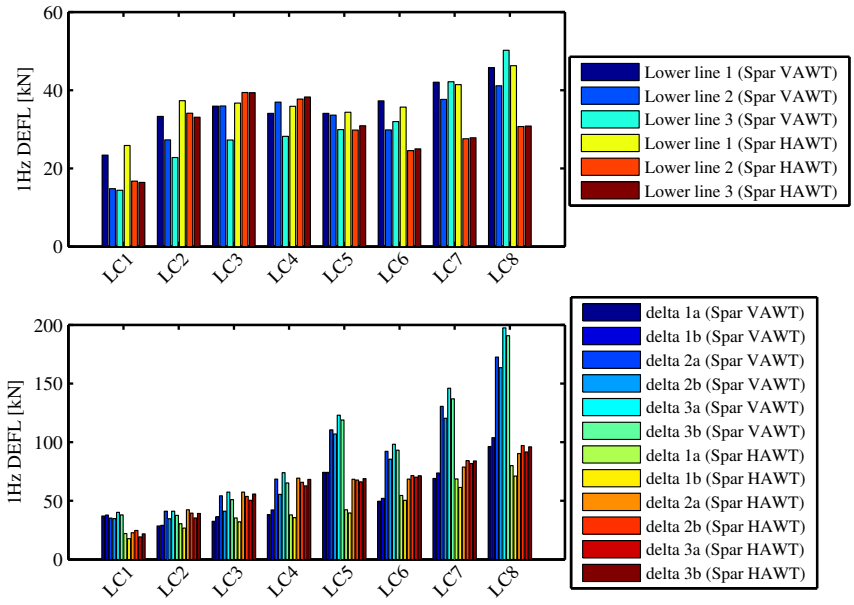

Figure 5.15: 1 Hz damage equivalent fatigue loads (DEFLs) of the tension in the lower lines and delta lines for the spar HAWT and VAWT [70].

Fatigue damages of the lower lines and delta lines are also studied using the MLife code, as the 1 Hz tension DEFLs show in Figure 5.15. The DEFLs of the tension in the lower lines are obviously close to each other for the spar

VAWT and HAWT. However, in the delta lines, the DEFLs of the tension for the spar VAWT are much larger than the spar HAWT in delta lines 2a, 2b, 3a and 3b above the rated wind speed.

Chapter 6

Conclusions and Recommendations for Future Work

This thesis deals with the development, verification and application of fully coupled methods for numerical modeling and dynamic analysis of floating vertical axis wind turbines (VAWTs). An aerodynamic code based on the AC method is developed and validated with experimental data. Then a fully coupled aero-hydro-servo-elastic simulation tool SIMO-RIFLEX-AC is developed and verified, and another fully coupled code SIMO-RIFLEX-DMS is improved as well. Using fully coupled time domain simulations, the dynamic response characteristics of several floating VAWT concepts are investigated and demonstrated. In addition, a comparative study of a spar-type HAWT and VAWT is presented. The final chapter presents the main conclusions, contributions and recommendations for future work.

6.1 Conclusions

The main contributions of the thesis can be summarized as follow:

- The actuator cylinder (AC) flow model, initially developed by Madsen, was further discussed and developed for aerodynamic modeling of floating vertical axis wind turbines (VAWTs). It includes the tangential load term when calculating induced velocities, uses two different approaches to calculate the normal and tangential loads acting on the rotor, and proposes an improved linear solution. The effect of dynamic stall is also considered using the Beddoes-Leishman dynamic

stall model. The developed code is verified to be accurate by a series of comparisons against other numerical models and experimental results. It is found that the effect of including the tangential load term when calculating induced velocities on the aerodynamic loads is very small. The proposed new modified linear solution can improve the power performance compared with the experiment data. Finally, a comparison of the developed AC method and the DMS method was performed and showed that the AC method can predict more accurate aerodynamic loads and power than the DMS method.

- A fully coupled simulation tool, namely SIMO-RIFLEX-AC, was developed and verified for numerical modeling and dynamic analysis of floating VAWTs. Based on the actuator cylinder (AC) flow model, aerodynamic modeling of floating VAWTs was established with consideration of the effects of turbulence, dynamic inflow and dynamic stall. The developed aerodynamic code was then coupled with the code SIMO-RIFLEX to achieve a fully coupled tool, i.e. SIMO-RIFLEX-AC, which can account for the aerodynamic, hydrodynamics, structural dynamics and controller dynamics with high fidelity. A series of code-to-code comparisons with the HAWC2 and SIMO-RIFLEX-DMS code were carried out using a landbased VAWT and a semi VAWT, and revealed that the present code can predict the aerodynamic loads and dynamic responses accurately. Moreover, the code SIMO-RIFLEX-AC can predict more accurate responses than the code SIMO-RIFLEX-DMS, such as the platform motions, tower base bending moments and tension in mooring lines.

- The effect of blade number on the dynamic behavior of floating VAWTs was comprehensively studied in a fully coupled approach. VAWTs with straight and parallel blades, with identical solidity and with a blade number varying from two to four, were firstly designed using the AC method and then adapted to a semi-submersible. A generator torque controller was also designed and used to regulate the rotational speed based on a PI control algorithm. Fully coupled time domain simulations demonstrated that the variation in aerodynamic loads such as the thrust and side force is strongly dependent on the number of blades; consequently the structural response for instance of the tower base bending moments is significantly influenced. In particular, by increasing the number of blades from two to three reduces the variation in the tower base bending moment more significantly than increasing it from three to four. However, the generator power production is not

sensitive to the number of blades due to the control strategy employed, and both the platform motions and tension in mooring lines are also not visibly affected by increasing the number of blades because of the compliant catenary mooring system.

- The dynamic responses of a spar, semi-submersible and TLP VAWT with a two-bladed Darrieus rotor were investigated using fully coupled time domain simulations. Stochastic dynamic response analysis revealed that 2P effects resulting from the 2P aerodynamic loads are prominent in the dynamic responses of these concepts. Due to the compliant catenary mooring systems, the spar and semi-submersible can help to mitigate the 2P effects on structural loads and mooring line tensions as compared to the TLP concept, at the cost of larger platform motions. The TLP is not a good substructure for vertical axis wind turbines unless the cyclic variation of aerodynamic loads is significantly reduced.

- The effect of second-order difference-frequency wave force on the dynamics of a semi-submersible VAWT in misaligned wave-wind conditions was studied. Fully coupled nonlinear time domain simulations demonstrated that the wave-wind misalignment does not significantly affect the mean values of the global responses since the global responses are primarily wind-induced. And the second order difference-frequency force can contribute to a slightly larger mean value. The standard deviations and maximum values of the global responses are slightly more sensitive to the wave-wind misalignment and the second order difference-frequency force, especially at high significant wave height conditions.

- A comparative study on the dynamics of a spar-type HAWT and VAWT was conducted. The OC3 spar buoy was used to support the NREL 5 MW wind turbine and the DeepWind 5 MW Darrieus rotor, respectively. An improved control strategy was proposed for the spar VAWT to maintain the mean generator power approximately constant above the rated wind speed. Fully coupled time domain simulations showed that due to different aerodynamic load characteristics and control strategies, the spar VAWT results in larger mean tower base bending moments and mooring line tensions above the rated wind speed. Because significant 2P aerodynamic loads act on the spar VAWT, the generator power, tower base bending moments and delta line tensions show prominent 2P variation. Consequently the spar VAWT suffers severe fatigue damage at the tower bottom.

6.2 Original Contributions

The main original contribution of this thesis is the development, verification and application of numerical methods for integrated modeling and dynamic analysis of floating VAWTs. It can be summarized as follow:

• *Developing and validating an aerodynamic model for a floating VAWT based on the actuator cylinder flow model*

The actuator cylinder flow model, originally developed by Madsen, was further discussed and improved for a floating VAWT. An aerodynamic code, namely AC, was implemented using the programming language Fortran and validated by comparison with experimental data. It can account for the effects of wind shear and turbulence, dynamic inflow as well as the dynamic stall using the Beddoes-Leishman model.

• *Improving a control strategy of a floating VAWT*

An improved control strategy based on a PI algorithm was proposed to regulate the rotational speed of a floating VAWT. An generator controller was accordingly implemented in Java and coupled with the RIFLEX.

• *Developing and verifying a fully coupled method for numerical modeling and dynamic analysis of a floating VAWT*

A fully coupled simulation tool, namely SIMO-RIFLEX-AC, was developed and verified for numerical modeling and dynamic analysis of a floating VAWT. It integrates an aerodynamic model in AC, a hydrodynamic model in SIMO, a structural model in RIFLEX and a generator torque controller model written in Java, making it capable of accounting for the aerodynamic, hydrodynamics, structural dynamics and controller dynamics with high fidelity. In addition, the dynamic link library (DLL) coupling the RIFLEX and AC was written in Fortran. The generator controller was implemented in Java and coupled with the RIFLEX. The SIMO-RIFLEX-AC code was verified by a series of code-to-code comparisons.

• *Revealing the effect of the number of blades on the dynamics of floating straight-bladed VAWTs*

Three VAWTs with straight and parallel blades, with identical solidity and with a blade number varying from two to four, were designed using the AC method and adapted on a semi-submersible to achieve three floating VAWTs. The effect of the number of blades on the dynamic behavior of floating VAWTs was then studied and demonstrated in a fully coupled way.

• *Comparison of the dynamic behavior of a spar, semi-submersible and TLP VAWT with a two-bladed Darrieus rotor*

The dynamic response characteristics of three floating VAWT concepts with a two-bladed Darrieus rotor mounted on a spar, semi-submersible and TLP floater were studied using fully coupled time domain simulations. They reveal the merits, disadvantages and feasibilities of each concept and can help to resolve the preliminary design trade-off among the three concepts.

• *Demonstrating the effect of difference-frequency force on the dynamics of a semi-submersible VAWT in misaligned wave-wind conditions*

The effects of second-order difference-frequency force and wave-wind misalignment were studied and demonstrated for a semi-submersible VAWT with a two-bladed Darrieus rotor.

• *Comparative study on the dynamics of a spar-type HAWT and VAWT*

A comparative study on the dynamics of a spar-type HAWT with the NREL 5 MW wind turbine and a spar-type VAWT with the DeepWind 5 MW Darrieus rotor was conducted using fully coupled simulations. It captured and demonstrated the different dynamic response characteristics of the floating HAWT and VAWT, and can serve as a basis for their further development.

6.3 Recommendations for Future Work

The following topics are recommended for future work:

• *Validating the fully coupled method by comparison with model tests or field measurements*

The developed fully coupled simulation tool for floating VAWTs has been verified using a series of code-to-code comparisons. Further validation is necessary through comparisons with small-scale model tests, or prototype or full-scale field measurements.

• *Investigating a more advanced control strategy for a floating VAWT*

A generator torque controller based on a PI algorithm has been used and improved in this thesis. A more advanced control strategy is required to better regulate the rotational speed and improve the performance of a floating VAWT.

• *Structural design and optimization of a VAWT*

VAWTs usually suffer severe fatigue problems. A structural design and optimization of the rotor considering the fatigue limit state is of interest.

• *Drivetrain design of a VAWT*

This thesis assumed a direct drive generator for the VAWTs studied. Detailed design of the drivetrain is interesting.

• *Design and optimization of a floating substructure for a VAWT*

The floating substructures considered in this thesis were originally designed to support a HAWT and were slightly adjusted to mount a VAWT. Due to different dynamic response characteristics of a floating HAWT and VAWT, a floating platform is necessary to be designed and optimized for the VAWT.

• *Studying the dynamic response of floating VAWTs considering the parked and fault conditions*

This thesis mainly deals with floating VAWTs in the normal operating conditions, their dynamic behavior in the parked and fault conditions are also of interest.

• *Investigating the dynamic response of a floating VAWT with other promising rotor types*

This thesis mainly deals with floating VAWT concepts with curve and straight blades. Other rotor type, such as the helical-bladed rotor, is promising to reduce the variation in aerodynamic loads and to improve the dynamic behavior of floating VAWT systems. Therefore, dynamic analysis of a floating VAWT with other promising rotor types is of great interest.

• *Comparative study of floating VAWTs with different types of rotors*

The available rotor for a floating VAWT can be H-type, V-type, curved-bladed and helical-bladed. A comparative study on the dynamics of floating VAWTs with different type of rotor is very interesting. It will provide insight into the merits and disadvantages of each rotor type and benefit for further development of floating VAWTs.

• *Investigating a novel combined concept of a floating VAWT and a wave energy converter*

Similar to concepts that combines a floating HAWT with a wave energy concerter, such as the STC (spar-torus-concept), a novel combined concept of a floating VAWT and a wave energy converter is feasible and of interest.

References

[1] Burton T, Jenkins N, Sharpe D, Bossanyi E. *Wind energy handbook*. John Wiley & Sons Ltd: England, 2011.

[2] Manwell JF, McGowan JG, Rogers AL. *Wind Energy Explained: Theory, Design and Application*. John Wiley & Sons Ltd: England, 2009.

[3] Global Wind Energy Council. Global wind statistics 2015 2016.

[4] Jonkman JM. Dynamics of offshore floating wind turbines-model development and verification. *Wind energy* 2009; **12**(5):459–492.

[5] Vijfhuizen W. Design of a wind and wave power barge. PhD thesis, Universities of Glasgow and Strathclyde 2006.

[6] Nielsen FG, Hanson TD, Skaare B. Integrated dynamic analysis of floating offshore wind turbine. *Proceedings of the 25th International Conference on Offshore Mechanics and Arctic Engineering*, 2006.

[7] Karimirad M, Moan T. Wave and wind induced dynamic response of a spar-type offshore wind turbine. *Journal of Waterway, Port, Coastal, and Ocean Engineering* 2012; **138**(1):920, doi:10.1061/(asce)ww.1943-5460.

[8] Fulton G, Malcolm D, Elwany H, Stewart W, Moroz E, Dempster H. Semi-submersible platform and anchor foundation systems for wind turbine support. *Subcontract Report NREL/SR-500-40282*, NREL, Golden, CO, USA 2007.

[9] Robertson A, Jonkman J, Masciola M, Song H, Goupee A, Coulling A, Luan C. Definition of the semi-submersible floating system for phase II of OC4. *Report* 2012.

[10] Roddier D, Cermelli C, Aubault A, Weinstein A. Windfloat: A floating foundation for offshore wind turbines. *Journal of Renewable and Sustainable Energy* 2010; **2**(3):033 104, doi:10.1063/1.3435339.

[11] Kvittem MI, Moan T. Time domain analysis procedures for fatigue assessment of a semi-submersible wind turbine. *Marine Structures* 2015; **40**:38–59, doi:10.1016/j.marstruc.2014.10.009.

[12] Bachynski EE, Moan T. Design considerations for tension leg platform wind turbines. *Marine Structures* 2012; **29**(1):89–114, doi:10.1016/j.marstruc.2012.09.001.

[13] Tracy C. Parametric design of floating wind turbines. PhD thesis, Massachusetts Institute of Technology 2007.

[14] Arapogianni A, Genachte A, Ochagavia RM, Vergara J, Castell D, Tsouroukdissian AR, Korbijn J, Bolleman N, Huera-Huarte F, Schuon F, *et al.*. Deep water: The next step for offshore wind energy. *Report*, European Wind Energy Association (EWEA), Brussels, Belgium 2013.

[15] Smith D. The wind farms of the altamont pass area. *Annual Review of Energy* 1987; **12**(1):145–183.

[16] Paquette J, Barone M. Innovative offshore vertical-axis wind turbine rotor project. *EWEA 2012 Annual Event*, Copenhagen, Denmark, 2012.

[17] Aslam Bhutta MM, Hayat N, Farooq AU, Ali Z, Jamil SR, Hussain Z. Vertical axis wind turbine a review of various configurations and design techniques. *Renewable and Sustainable Energy Reviews* 2012; **16**(4):1926–1939, doi:10.1016/j.rser.2011.12.004.

[18] Paraschivoiu I. *Wind turbine design: with emphasis on Darrieus concept*. Polytechnic International Press.: Montreal, Canada., 2002.

[19] Gipe P. *Wind Energy Basics: A Guide to Home and Community-Scale Wind-Energy Systems*. Chelsea Green Publishing, 2009.

[20] Kinzel M, Mulligan Q, Dabiri JO. Energy exchange in an array of vertical-axis wind turbines. *Journal of Turbulence* ; **13**(38):1–13.

[21] Dabiri JO. Potential order-of-magnitude enhancement of wind farm power density via counter-rotating vertical-axis wind turbine arrays. *Journal of Renewable and Sustainable Energy* ; **3**(4):043 104.

[22] Sutherland HJ, Berg DE, Ashwill TD. A retrospective of vawt technology. *Tech. Report SAND2012-0304*, Sandia National Laboratories, Albuquerque, New Mexico, USA 2012.

[23] Cheng Z, Gao Z, Madsen HA, Moan T. Effect of the number of blades on the dynamics of floating straight-bladed vertical axis wind turbines. *Submitted to Renewable Energy* 2016; .

[24] Wang K, Moan T, Hansen MOL. Stochastic dynamic response analysis of a floating vertical-axis wind turbine with a semi-submersible floater. *Wind Energy* 2016; doi:10.1002/we.1955.

[25] Wang K. Modeling and dynamic analysis of a semi-submersible floating vertical axis wind turbine. PhD thesis, Norwegian University of Science and Technology 2015.

[26] Paulsen US, Borg M, Madsen HA, Pedersen TF, Hattel J, Ritchie E, Ferreira CS, Svendsen H, Berthelsen PA, Smadja C. Outcomes of the deepwind conceptual design. *Energy Procedia* 2015; **80**:329–341, doi:10.1016/j.egypro.2015.11.437.

[27] Vita L. Offshore floating vertical axis wind turbines with rotating platform. Phd thesis, Technical University of Denmark 2011.

[28] `http://www.spinfloat.com/` (accessed on 2016-03-15).

[29] Shires A. Design optimisation of an offshore vertical axis wind turbine. *Proceedings of the ICE-Energy* 2013; **166**(EN1):7–18.

[30] Collu M, Brennan FP, Patel MH. Conceptual design of a floating support structure for an offshore vertical axis wind turbine: the lessons learnt. *Ships and Offshore Structures* ; **9**(1):3–21.

[31] `http://www.inflow-fp7.eu/` (accessed on 2016-03-15).

[32] Akimoto H, Tanaka K, Uzawa K. Floating axis wind turbines for offshore power generation-a conceptual study. *Environmental Research Letters* 2011; **6**(4):044 017, doi:10.1088/1748-9326/6/4/044017.

[33] `http://www.gwind.no/` (accessed on 2016-03-15).

[34] Cahay M, Luquiau E, Smadja C, Silvert F. Use of a vertical wind turbine in an offshore floating wind farm. *Offshore Technology Conference*, Houston, Texas, USA, 2011.

[35] Huijs F, de Bruijn R, Savenije F. Concept design verification of a semi-submersible floating wind turbine using coupled simulations. *Energy Procedia* 2014; **53**:2–12, doi:10.1016/j.egypro.2014.07.210.

[36] Jonkman JM. Dynamics of offshore floating wind turbines-model development and verification. *Wind Energy* 2009; **12**(5):459–492, doi: 10.1002/we.347.

[37] Larsen TJ, Hansen AM. *How 2 HAWC2, the user's manual*. Risø National Laboratory, Technical University of Denmark: Roskilde, Denmark, 2013.

[38] Ormberg H, Bachynski EE. Global analysis of floating wind turbines: Code development, model sensitivity and benchmark study. *Proceedings of the 22th International Offshore and Polar Engineering Conference*, Rhodes, Greece, 2012.

[39] GL Garrad Hassan. Bladed theory manual version 4.4 2013.

[40] Collu M, Borg M, Shires A, Brennan FP. Flovawt: progress on the development of a coupled model of dynamics for floating offshore vertical axis wind turbines. *ASME 2013 32nd International Conference on Ocean, Offshore and Arctic Engineering*, American Society of Mechanical Engineers, 2013.

[41] Antonutti R. Numerical study of floating wind turbine hydro & aeromechanics. PhD thesis, The University of Edinburgh 2015.

[42] Owens BC, Hurtado JE, Paquette JA, Griffith DT, Barone M. Aeroelastic modeling of large off-shore vertical-axis wind turbines: Development of the offshore wind energy simulation toolkit. *Proceedings of the 54th AIAA Structures, Structural Dynamics and Materials Conference*, 2013, doi:10.2514/6.2013-1552.

[43] Larsen TJ, Madsen HA. On the way to reliable aeroelastic load simulation on VAWT's. *Proceedings of EWEA*, 2013.

[44] Wang K, Moan T, Hansen MOL. A method for modeling of floating vertical axis wind turbine. *Proceedings of the 32th International Conference on Ocean, Offshore and Arctic Engineering*, 2013.

[45] Cheng Z, Madsen HA, Gao Z, Moan T. A fully coupled method for numerical modeling and dynamic analysis of floating vertical axis wind turbines. *Submitted to Renewable Energy* 2016; .

[46] Perez T, Fossen TI. A matlab toolbox for parametric identification of radiation-force models of ships and offshore structures. *Modeling, Identification and Control* 2009; **30**(1):1.

[47] Borg M. Offshore floating vertical axis wind turbines: development & application of a coupled model of dynamics. Thesis 2014.

[48] Owens BC, Hurtado JE, Barone M, Paquette JA. An energy preserving time integration method for gyric systems: Development of the offshore wind energy simulation toolkit. *Proceedings of the European Wind Energy Association Conference & Exhibition, EWEA Vienna, Austria*, 2013.

[49] Murray J, Barone M. The development of cactus, a wind and marine turbine performance simulation code. *49th AIAA Aerospace Sciences Meeting. Paper AIAA 2011-47*, 2011.

[50] Fowler MJ, Owens B, Bull D, Goupee AJ, Hurtado J, Griffith DT, Alves M. Hydrodynamic module coupling in the offshore wind energy simulation (owens) toolkit. *ASME 2014 33rd International Conference on Ocean, Offshore and Arctic Engineering*, American Society of Mechanical Engineers, 2014.

[51] MARINTEK. Simo-theory manual version 4.0 2012.

[52] MARINTEK. Riflex theory manual, version 4.0 2012.

[53] Madsen HA. *The Actuator Cylinder: A flow model for vertical axis wind turbines*. Institute of Industrial Constructions and Energy Technology, Aalborg University Centre, 1982.

[54] WAMIT. *WAMIT user manual*. WAMIT INC., 2013.

[55] Ferreira CS, Madsen HA, Barone M, Roscher B, Deglaire P, Arduin I. Comparison of aerodynamic models for vertical axis wind turbines. *Journal of Physics: Conference Series* 2014; **524**(1):012 125.

[56] Cheng Z, Madsen HA, Gao Z, Moan T. Aerodynamic modeling of offshore vertical axis wind turbines using the actuator cylinder method. *Submitted to Energy Procedia* 2016; .

[57] Paulsen US, Pedersen TF, Madsen HA, Enevoldsen K, Nielsen PH, Hattel JH, Zanne L, Battisti L, Brighenti A, Lacaze M. Deepwind-an innovative wind turbine concept for offshore. *European Wind Energy Association (EWEA) Annual Event*, 2011.

[58] Paulsen US, Vita L, Madsen HA, Hattel J, Ritchie E, Leban KM, Berthelsen PA, Carstensen S. 1st deepwind 5 mw baseline design. *Energy Procedia* 2012; **24**:27–35, doi:10.1016/j.egypro.2012.06.083.

[59] Paulsen US, Madsen HA, Hattel JH, Baran I, Nielsen PH. Design optimization of a 5 mw floating offshore vertical-axis wind turbine. *Energy Procedia* 2013; **35**:22–32, doi:10.1016/j.egypro.2013.07.155.

[60] Wang K, Cheng Z, Moan T, Hansen MOL. Effect of difference-frequency forces on the dynamics of a semi-submersible type FVAWT in misaligned wave-wind condition. *Proceedings of the 25th International Ocean and Polar Engineering Conference*, 2015.

[61] Wang K, Hansen MOL, Moan T. Dynamic analysis of a floating vertical axis wind turbine under emergency shutdown using hydrodynamic brake. *Energy Procedia* 2014; **53**:56–69.

[62] Borg M, Collu M. A comparison on the dynamics of a floating vertical axis wind turbine on three different floating support structures. *Energy Procedia* 2014; **53**:268–279, doi:10.1016/j.egypro.2014.07.236.

[63] Borg M, Collu M. Frequency-domain characteristics of aerodynamic loads of offshore floating vertical axis wind turbines. *Applied Energy* 2015; **155**:629–636, doi:10.1016/j.apenergy.2015.06.038.

[64] Cheng Z, Wang K, Gao Z, Moan T. Dynamic response analysis of three floating wind turbine concepts with a two-bladed darrieus rotor. *Journal of Ocean and Wind Energy* 2015; **2**:213–222, doi:10.17736/jowe.2015.jcr33.

[65] Cheng Z, Wang K, Gao Z, Moan T. Dynamic modelling and analysis of three floating wind turbine concepts with vertical axis rotor. *Proceedings of the 25th International Ocean and Polar Engineering Conference*, 2015.

[66] Borg M, Collu M, Brennan FP. Use of a wave energy converter as a motion suppression device for floating wind turbines. *Energy Procedia* 2013; **35**:223–233, doi:10.1016/j.egypro.2013.07.175.

[67] Anagnostopoulou C, Kagemoto H, Sao K, Mizuno A. Concept design and dynamic analyses of a floating vertical-axis wind turbine: case study of power supply to offshore greek islands. *Journal of Ocean Engineering and Marine Energy* ; **2**(1):85–104.

[68] Svendsen HG, Merz KO, Endegnanew AG. Control of floating vertical axis wind turbine. *European Wind Energy Conference and Exhibition*, Copenhagen, Denmark, 2012.

[69] Merz KO, Svendsen HG. A control algorithm for the deepwind floating vertical-axis wind turbine. *Journal of Renewable and Sustainable Energy* 2013; **5**(6):063 136, doi:10.1063/1.4854675.

[70] Cheng Z, Wang K, Gao Z, Moan T. A comparative study on dynamic responses of spar-type floating horizontal and vertical axis wind turbines. *Submitted to Wind Energy* 2016; .

[71] Cheng Z, Moan T, Gao Z. Dynamic response analysis of floating wind turbines with emphasis on vertical axis rotors. *MARE-WINT, New Materials and Reliability in Offshore Wind Turbine Technology*, Ostachowicz W, McGugan M, Hinrichs JUS, Luczac M (eds.), Springer, 2016.

[72] Svendsen HG, Merz KO. Control system for start-up and shut-down of a floating vertical axis wind turbine. *Energy Procedia* 2013; **35**:33–42, doi:10.1016/j.egypro.2013.07.156.

[73] Borg M, Collu M. A comparison between the dynamics of horizontal and vertical axis offshore floating wind turbines. *Philosophical Transactions of the Royal Society of London A: Mathematical, Physical and Engineering Sciences* 2015; **373**(2035):20140 076, doi:10.1098/rsta.2014.0076.

[74] Wang K, Luan C, Moan T, Hansen MOL. Comparative study of a FVAWT and a FHAWT with a semi-submersible floater. *Proceedings of the 24th International Ocean and Polar Engineering Conference*, Busan, South Korea, 2014.

[75] Cheng Z, Wang K, Gao Z, Moan T. Comparative study of spar type floating horizontal and vertical axis wind turbines subjected to constant winds. *Proceedings of EWEA Offshore 2015*, Copenhagen, Denmark, 2015.

[76] Jonkman JM, Butterfield S, Musial W, Scott G. Definition of a 5-mw reference wind turbine for offshore system development. *Tech. Rep. NREL/TP-500-38060*, NREL, Golden, CO, USA 2009.

[77] Templin RJ. Aerodynamic performance theory for the nrc vertical-axis wind turbine. *Technical Report LTR-LA-160*, National Aeronautical Establishment, Ottawa, Ontario, Canada 1974.

[78] Strickland JH. The darrieus turbine: A performance prediction model using multiple streamtubes. *Technical Report SAND75-0430* , Sandia National Laboratories, Albuquerque, N.M. USA 1975.

[79] Madsen HA, Larsen TJ, Paulsen US, Vita L. Implementation of the actuator cylinder flow model in the HAWC2 code for aeroelastic simulations on vertical axis wind turbines. *51st AIAA Aerospace Sciences Meeting including the New Horizons Forum and Aerospace Exposition*, 2013, doi:10.2514/6.2013-913.

[80] Zanon A, Giannattasio P, Simão Ferreira CJ. A vortex panel model for the simulation of the wake flow past a vertical axis wind turbine in dynamic stall. *Wind Energy* 2013; **16**(5):661–680.

[81] Scheurich F, Fletcher TM, Brown RE. Simulating the aerodynamic performance and wake dynamics of a vertical-axis wind turbine. *Wind Energy* 2011; **14**(2):159–177.

[82] Ponta FL, Jacovkis PM. A vortex model for darrieus turbine using finite element techniques. *Renewable energy* 2001; **24**(1):1–18.

[83] Strickland J, Webster B, Nguyen T. A vortex model of the darrieus turbine: an analytical and experimental study. *Journal of Fluids Engineering* 1979; **101**(4):500–505.

[84] Ferreira CS. The near wake of the vawt: 2d and 3d views of the vawt aerodynamics. PhD Thesis, Delft University of Technology 2009.

[85] Ferreira CS, Scheurich F. Demonstrating that power and instantaneous loads are decoupled in a vertical-axis wind turbine. *Wind Energy* 2014; **17**(3):385–396.

[86] Liu W, Xiao Q. Investigation on darrieus type straight blade vertical axis wind turbine with flexible blade. *Ocean Engineering* 2015; **110**:339–356, doi:10.1016/j.oceaneng.2015.10.027.

[87] Kanner S, Persson PO. Validation of a high-order large-eddy simulation solver using a vertical-axis wind turbine. *AIAA Journal* 2016; **54**(1):101–112, doi:10.2514/1.j054138.

[88] Bazilevs Y, Korobenko A, Deng X, Yan J, Kinzel M, Dabiri JO. Fluid-structure interaction modeling of vertical-axis wind turbines. *Journal of Applied Mechanics* 2014; **81**(8):081 006, doi:10.1115/1.4027466.

[89] Castelli MR, Englaro A, Benini E. The darrieus wind turbine: Proposal for a new performance prediction model based on cfd. *Energy* 2011; **36**(8):4919–4934, doi:10.1016/j.energy.2011.05.036.

[90] Borg M, Shires A, Collu M. Offshore floating vertical axis wind turbines, dynamics modelling state of the art. Part I: Aerodynamics. *Renewable and Sustainable Energy Reviews* 2014; **39**:1214–1225, doi:10.1016/j.rser.2014.07.096.

[91] Larsen H. Summary of a vortex theory for the cyclogiro. *Proceedings of the 2nd US National conference on Wind Engineering Research.(1975-8), Colorad State University*, vol. 8, 1975.

[92] Holme O. A contribution to the aerodynamic theory of the vertical-axis wind turbine. *International symposium on wind energy systems*, vol. 1, 1977.

[93] Katz J, Plotkin A. *Low-speed aerodynamics*. Cambridge University Press, 2001.

[94] Wang K, Hansen MOL, Moan T. Model improvements for evaluating the effect of tower tilting on the aerodynamics of a vertical axis wind turbine. *Wind Energy* 2015; **18**:91–110, doi:10.1002/we.1685.

[95] Roscher B. Current aerodynamic models for VAWT and numerical comparison between HAWC2 and U2DiVA. *Special project - EWEM rotor design* 2014.

[96] Leishman JG, Beddoes TS. A semi-empirical model for dynamic stall. *Journal of the American Helicopter Society* ; **34**(3):3–17.

[97] Gupta S, Leishman JG. Dynamic stall modelling of the s809 aerofoil and comparison with experiments. *Wind Energy* 2006; **9**(6):521–547, doi:10.1002/we.200.

[98] Dyachuk E, Goude A, Bernhoff H. Dynamic stall modeling for the conditions of vertical axis wind turbines. *AIAA Journal* 2014; **52**(1):72–81, doi:10.2514/1.j052633.

[99] Luxcey N, Ormberg H, Passano E. Global analysis of a floating wind turbine using an aero-hydro-elastic numerical model: Part 2 benchmark study. *Proceedings of the 30th International Conference on Ocean, Offshore and Arctic Engineering*, 2011.

[100] Ormberg H, Passano E, Luxcey N. Global analysis of a floating wind turbine using an aero-hydro-elastic model: Part 1 code development and case study. *Proceedings of the 30th International Conference on Ocean, Offshore and Arctic Engineering*, 2011.

[101] Cummins WE. The impulse response function and ship motions. *Institut fur schiffbau, universitat hamburg, hamburg* 1962.

[102] Faltinsen OM. *Sea loads on ships and offshore structures*. Cambridge University Press: Cambridge, UK, 1995.

[103] Bachynski EE, Kvittem MI, Luan C, Moan T. Wind-wave misalignment effects on floating wind turbines: Motions and tower load effects. *Journal of Offshore Mechanics and Arctic Engineering* 2014; **136**(4):041 902, doi:10.1115/1.4028028.

[104] Jonkman J. Definition of the floating system for phase IV of OC3. *Tech. Rep. NREL/TP-500-47535*, NREL, Golden, CO, USA 2010.

[105] Johannessen K, Meling TS, Haver S. Joint distribution for wind and waves in the northern north sea. *International Journal of Offshore and Polar Engineering* 2002; **12**(1).

[106] Li L, Gao Z, Moan T. Joint distribution of environmental condition at five european offshore sites for design of combined wind and wave energy devices. *Journal of Offshore Mechanics and Arctic Engineering* 2015; **137**(3):031 901–031 901, doi:10.1115/1.4029842.

[107] Jonkman BJ. Turbsim user's guide: Version 1.50. 2009.

[108] IEC. International standard 61400-1, wind turbines, part 1: Design requirements 2005.

[109] Hayman G. Mlife theory manual for version 1.00 2012.

Appendix A

Appended papers

A.1 Paper 1

Paper 1:
Aerodynamic modeling of floating vertical axis wind turbines using the actuator cylinder flow method.
Zhengshun Cheng, Helge Aagaard Madsen, Zhen Gao, Torgeir Moan
Revision submitted to *Energy Procedia*, 2016

Available online at www.sciencedirect.com

SciVerse ScienceDirect

Energy Procedia 00 (2016) 000–000

Energy Procedia

www.elsevier.com/locate/procedia

13th Deep Sea Offshore Wind R&D Conference, EERA DeepWind'2016, 20-22 January 2016, Trondheim, Norway

Aerodynamic modeling of floating vertical axis wind turbines using the actuator cylinder flow method

Zhengshun Cheng[a,b,c,*], Helge Aagaard Madsen[d], Zhen Gao[a,b,c], Torgeir Moan[a,b,c]

[a]*Department of Marine Technology, Norwegian University of Science and Technology (NTNU), Trondheim, NO-7491, Norway*
[b]*Centre for Ships and Ocean Structures (CeSOS), NTNU, Trondheim, NO-7491, Norway*
[c]*Centre for Autonomous Marine Operations and Systems (AMOS), NTNU, Trondheim, NO-7491, Norway*
[d]*Department of Wind Energy, Technical University of Denmark, Roskilde, 4000, Denmark*

Abstract

Recently the interest in developing vertical axis wind turbines (VAWTs) for offshore application has been increasing. Among the aerodynamic models of VAWTs, double multi-streamtube (DMST) and actuator cylinder (AC) models are two favorable methods for fully coupled modeling and dynamic analysis of floating VAWTs in view of accuracy and computational cost. This paper deals with the development of an aerodynamic code to model floating VAWTs using the AC method developed by Madsen. It includes the tangential load term when calculating induced velocities, addresses two different approaches to calculate the normal and tangential loads acting on the rotor, and proposes a new modified linear solution to correct the linear solution. The effect of dynamic stall is also considered using the Beddoes-Leishman dynamic stall model. The developed code is verified to be accurate by a series of comparisons against other numerical models and experimental results. It is found that the effect of including the tangential load term when calculating induced velocities on the aerodynamic loads is very small. The proposed new modified linear solution can improve the power performance compared with the experiment data. Finally, a comparison of the developed AC method and the DMST method is performed and shows that the AC method can predict more accurate aerodynamic loads and power than the DMST method.

Peer-review under responsibility of SINTEF Energi AS.

Keywords: Floating vertical axis wind turbine; aerodynamic modeling; actuator cylinder flow model; double multi-streamtube model

1. Introduction

During the 1970s and 1980s, vertical axis wind turbines (VAWTs) attracted interests of researchers mainly in USA and Canada and considerable efforts were devoted to investigate and develop the Darrieus VAWTs [9]. Commercial Darrieus VAWTs were also developed by the FloWind Corp. Due to the issues of severe fatigue damage and low power efficiency, VAWTs became less popular than horizontal axis wind turbines (HAWTs). However, as the wind farms are

* Corresponding author. Tel.: +47-73596004 ; fax: +47-73595528.
E-mail address: zhengshun.cheng@ntnu.no

Peer-review under responsibility of SINTEF Energi AS.

moving towards deeper waters where large floating wind turbines will be more economical, floating VAWTs have the potential to reduce the cost compared to floating HAWTs [8] and efforts devoted to investigate floating VAWTs are increasing.

Since Sandia National Laboratories started the study of vertical axis wind turbines in the 1970s, a variety of aerodynamic models have been proposed for VAWTs. These include streamtube models, actuator cylinder (AC) flow model, panel method, vortex method and computational fluid dynamics (CFD) method. The streamtube models are based on the conservation of mass and momentum in a quasi-steady flow. They equate the forces on the rotor blades to the change in the streamwise momentum through the turbine. They can be categorized into three models: single streamtube model (SST) [13], multi-streamtube model (MST) [12] and double multi-streamtube (DMST) [9] model. SST model [13] assumes that the entire rotor represented by an actuator disk is enclosed in one streamtube, MST model [12] extends the SST model by dividing the rotor into a series of adjacent streamtubes and DMST model [9] assumes that the vertical axis wind turbine can be represented by a pair of actuator disks in tandem at each level of the rotor. Up to now, the DMST model has been widely used to estimate the aerodynamic loads on VAWTs.

However, by considering a 2D VAWT rotor, Ferreira et al. [2] compares the different models for VAWTs, including the MST model, DMST model, AC [4] model, U2DiVA using panel model and CACTUS [7] using lifting line model, and reveals that the DMST model seems to be less accurate than the AC, panel and vortex models. An overview of these aerodynamic models can also be found in [11], which considers their complexity, accuracy, computational cost, suitability for optimization and aeroelastic analysis. Due to the considerations of accuracy and computational cost, the AC method seems to be the favorable method that can be used to conduct aero-hydro-servo-elastic time domain simulations of floating VAWTs.

The AC method is a quasi-steady Eulerian model developed by Madsen [4]. The model extends the actuator disc concept to an actuator surface coinciding with the swept area of the 2D VAWT. In the AC model, the normal and tangential forces Q_n and Q_t resulting from the blade forces are applied on the flow as volume force perpendicular and tangential to the rotor plane, respectively, as illustrated in Fig. 1. Thus the velocity induced by the normal and tangential forces Q_n and Q_t can be computed analytically.

The AC method has been implemented in HAWC2 [3] to conduct the fully coupled aero-hydro-servo-elastic time domain simulations of floating VAWTs. It can account for dynamic inflow, structural dynamics, tower shadow and dynamic stall. Paulsen et al. [10] performed a design optimization of the proposed DeepWind concept. An improved design has been obtained with an optimized blade profile with less weight and higher stiffness than the first baseline design.

In this paper, an aerodynamic code is developed using the AC method developed by Madsen [4] to model VAWTs for offshore application. The basic theory of the AC method will firstly be briefly presented. In the developed code, the linear solution of induced velocities will be derived by including the effect of tangential load. The effect of tangential load on the induced velocity was discussed in [5], but was ignored in the implementation of the AC method into HAWC2 [3,6]. Using the AC method, modeling of a VAWT is presented subsequently including the effect of dynamic stall via the Beddoes-Leishman dynamic stall model. Two different approaches are used to calculate the normal and tangential loads acting on the rotor . A series of simulations are conducted to verify the code by comparisons with other numerical models and experimental results . The accuracy of the present code and the effect of tangential load on the induced velocity are addressed. Finally, a comparison of the present AC method and the DMST method is performed.

2. Actuator cylinder flow model

Considering a 2D quasi-static flow problem as shown in Fig. 1, the basic equations are the Euler equation and continuity equation. For simplicity the equations are non-dimensionalized with the basic dimensions R, V_∞ and ρ, which are rotor radius, free stream velocity and flow density, respectively. The velocity components can thus be written as

$$v_x = 1 + w_x \tag{1}$$

$$v_y = w_y \tag{2}$$

where w_x and w_y are local velocities representing the changes in wind speed due to the presence of the VAWT.

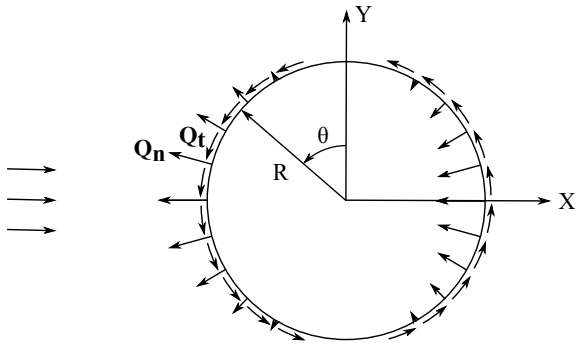

Fig. 1. The actuator cylinder flow model representation [6] of a VAWT with volume forces normal and tangential to the circle. Note that the force direction is from the VAWT onto the flow .

Based on the continuity equation and Euler equation, the velocities w_x and w_y are related to volume forces as well as the normal and tangential loads Q_n and Q_t. The final velocity can be divided into a linear part which is a function of the prescribed normal and tangential loads Q_n and Q_t and a nonlinear part that is a function of the induced forces.

2.1. Linear Solution

The linear solution of the induced velocities can be analytically computed, as given by

$$w_x(f) = -p_f + \int_{-\infty}^{x} f_x dx' \tag{3}$$

$$w_y(f) = -\int_{-\infty}^{x} \frac{\partial p_f}{\partial y} dx' + \int_{-\infty}^{x} f_y dx' \tag{4}$$

where p_f is the pressure given by

$$p_f = \frac{1}{2\pi} \iint \frac{f_x(x-\xi) + f_y(y-\eta)}{(x-\xi)^2 + (y-\eta)^2} d\xi d\eta \tag{5}$$

and the volume forces can be expressed as

$$f_x = -f_n \sin\theta - f_t \cos\theta \tag{6}$$

$$f_y = f_n \cos\theta - f_t \sin\theta \tag{7}$$

in which

$$Q_n(\theta) = \lim_{\epsilon \to 0} \int_{1-\epsilon}^{1+\epsilon} f_n(\theta, r) dr \tag{8}$$

$$Q_t(\theta) = \lim_{\epsilon \to 0} \int_{1-\epsilon}^{1+\epsilon} f_t(\theta, r) dr \tag{9}$$

The integration involved in Eqs. 3 and 4 should be performed item by item throughout the region where the volume forces are different from zero. For the integral part in Eq. 3, since the volume forces are non-zero only along the cylinder, the integral result depends on the position of the calculation point, as shown in Fig. 2. Detailed derivation can refer to the Appendix A.

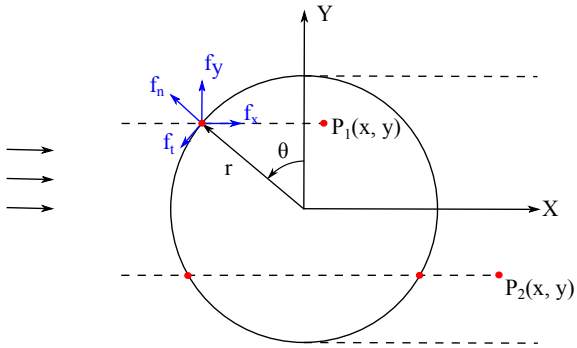

Fig. 2. The actuator cylinder flow model with volume forces

The linear solution of the induced velocities is given as follows

$$\begin{aligned} w_x(f) = &-\frac{1}{2\pi}\int_0^{2\pi} Q_n(\theta)\frac{-(x+\sin\theta)\sin\theta+(y-\cos\theta)\cos\theta}{(x+\sin\theta)^2+(y-\cos\theta)^2}d\theta \\ &-\frac{1}{2\pi}\int_0^{2\pi} Q_t(\theta)\frac{-(x+\sin\theta)\cos\theta-(y-\cos\theta)\sin\theta}{(x+\sin\theta)^2+(y-\cos\theta)^2}d\theta \\ &-(Q_n(\arccos y))^* + (Q_n(-\arccos y))^{**} \\ &-\left(Q_t(\arccos y)\frac{y}{\sqrt{1-y^2}}\right)^* - \left(Q_t(-\arccos y)\frac{y}{\sqrt{1-y^2}}\right)^{**} \end{aligned} \tag{10}$$

$$\begin{aligned} w_y(f) = &-\frac{1}{2\pi}\int_0^{2\pi} Q_n(\theta)\frac{-(x+\sin\theta)\cos\theta-(y-\cos\theta)\sin\theta}{(x+\sin\theta)^2+(y-\cos\theta)^2}d\theta \\ &-\frac{1}{2\pi}\int_0^{2\pi} Q_t(\theta)\frac{(x+\sin\theta)\sin\theta-(y-\cos\theta)\cos\theta}{(x+\sin\theta)^2+(y-\cos\theta)^2}d\theta \end{aligned} \tag{11}$$

where the term marked with $*$ in Eqs. 10 and 11 shall only be added inside the cylinder whereas in the wake behind the cylinder both the term marked with $*$ and $**$ shall be added. Compared with the results in [6], the effect of tangential load on the computed induced velocity is considered here.

Assuming that the loading is piecewise constant, the integral part in Eqs. 10 and 11 can be rewritten as

$$\begin{aligned} w_x = &-\frac{1}{2\pi}\sum_{i=1}^{i=N} Q_{n,i}\int_{\theta_i-\frac{1}{2}\Delta\theta}^{\theta_i+\frac{1}{2}\Delta\theta}\frac{-(x+\sin\theta)\sin\theta+(y-\cos\theta)\cos\theta}{(x+\sin\theta)^2+(y-\cos\theta)^2}d\theta \\ &-\frac{1}{2\pi}\sum_{i=1}^{i=N} Q_{t,i}\int_{\theta_i-\frac{1}{2}\Delta\theta}^{\theta_i+\frac{1}{2}\Delta\theta}\frac{-(x+\sin\theta)\cos\theta-(y-\cos\theta)\sin\theta}{(x+\sin\theta)^2+(y-\cos\theta)^2}d\theta \end{aligned} \tag{12}$$

$$\begin{aligned} w_y = &-\frac{1}{2\pi}\sum_{i=1}^{i=N} Q_{n,i}\int_{\theta_i-\frac{1}{2}\Delta\theta}^{\theta_i+\frac{1}{2}\Delta\theta}\frac{-(x+\sin\theta)\cos\theta-(y-\cos\theta)\sin\theta}{(x+\sin\theta)^2+(y-\cos\theta)^2}d\theta \\ &+\frac{1}{2\pi}\sum_{i=1}^{i=N} Q_{t,i}\int_{\theta_i-\frac{1}{2}\Delta\theta}^{\theta_i+\frac{1}{2}\Delta\theta}\frac{-(x+\sin\theta)\sin\theta+(y-\cos\theta)\cos\theta}{(x+\sin\theta)^2+(y-\cos\theta)^2}d\theta \end{aligned} \tag{13}$$

where N is the total number of calculation points, $\Delta\theta = \frac{2\pi}{N}$ and $\theta_i = \frac{\pi}{N}(2i-1)$ for $i = 1, 2, ..., N$.

Since only induced velocities at the cylinder are of concern, the total velocity solution at calculation point (x_j, y_j) (for $j = 1, 2, ..., N$) on the cylinder can then be rewritten as

$$w_{x,j} = -\frac{1}{2\pi}\left(\sum_{i=1}^{i=N} Q_{n,i}I_{1,i,j} + \sum_{i=1}^{i=N} Q_{t,i}I_{2,i,j}\right) - \left(Q_{n,N+1-j}\right)^* - \left(Q_{t,N+1-j}\frac{y_j}{\sqrt{1-y_j^2}}\right)^* \tag{14}$$

$$w_{y,j} = -\frac{1}{2\pi}\left(\sum_{i=1}^{i=N} Q_{n,i}I_{2,i,j} - \sum_{i=1}^{i=N} Q_{t,i}I_{1,i,j}\right) \tag{15}$$

where the terms marked with $*$ in Eqs. 14 and 15 are only added for $j > \frac{N}{2}$ (the leeward part of the AC with $x_j > 0$). $I_{1,i,j}$ and $I_{2,i,j}$ are influence coefficients in point j influenced by other point i and are given by

$$I_{1,i,j} = \int_{\theta_i-\frac{1}{2}\Delta\theta}^{\theta_i+\frac{1}{2}\Delta\theta} \frac{-\left(x_j+\sin\theta\right)\sin\theta + \left(y_j-\cos\theta\right)\cos\theta}{\left(x_j+\sin\theta\right)^2 + \left(y_j-\cos\theta\right)^2} d\theta \tag{16}$$

$$I_{2,i,j} = \int_{\theta_i-\frac{1}{2}\Delta\theta}^{\theta_i+\frac{1}{2}\Delta\theta} \frac{-\left(x_j+\sin\theta\right)\cos\theta - \left(y_j-\cos\theta\right)\sin\theta}{\left(x_j+\sin\theta\right)^2 + \left(y_j-\cos\theta\right)^2} d\theta \tag{17}$$

in which $x_j = -\sin(j\Delta\theta - \frac{1}{2}\Delta\theta)$, $y_j = \cos(j\Delta\theta - \frac{1}{2}\Delta\theta)$. It can be found that the influence coefficients $I_{1,i,j}$ and $I_{2,i,j}$ are irrespective of time and can thus be integrated once and for all.

2.2. Modified Linear Solution

It's relatively time-consuming to compute the nonlinear solution directly. In order to make the final solution in better agreement with the fully nonlinear solution, a correction is required for the linear solution. Madsen et al. [6] suggested a simple correction by multiplying the velocities from the linear solution w_x and w_y with the factor

$$k_a = \frac{1}{1-a} \tag{18}$$

where the induction factor a is found based on a relationship between the induction a and the average thrust coefficient C_T. A polynomial relationship [3] between C_T and a used in the practical implementation for HAWT's in HAWC2 was adopted, as given in Eq. 19.

$$a = k_3C_T^3 + k_2C_T^2 + k_1C_T + k_0 \tag{19}$$

in which $k_3 = 0.0892074$, $k_2 = 0.0544955$, $k_1 = 0.251163$ and $k_0 = -0.0017077$. This polynomial includes the $C_T = 4a(1-a)$ for $a < 0.5$ as well as the Glauert correction for $a > 0.5$.

However, implementation using the above modified linear solution shows some deviations in the power coefficients at high tip speed ratios, as the results of the code AC3 shown in Fig. 8. This implies that at large tip speed ratio, such a modification can cause large deviations in the power coefficient, thus a new modification that corrects the k_a at high induction factor, which corresponds to large tip speed ratio, is proposed, as follows.

$$k_a = \begin{cases} \frac{1}{1-a}, & (a \le 0.15) \\ \frac{1}{1-a}(0.65 + 0.35\exp\left(-4.5(a-0.15)\right)), & (a > 0.15) \end{cases} \tag{20}$$

in which the empirical parameters are determined by comparing with the experimental data, as illustrated in Fig. 8.

3. Aerodynamic loads on a 2D VAWT

The aerodynamic loads acting on a 2D VAWT according to the AC flow method can be calculated as follows. The local inflow velocity seen at a blade section is computed by adding the free wind speed and the induced velocity and subtracting the velocity due to the motion. Consequently, the relative velocity and angle of attack experienced by the section are found and the corresponding aerodynamic coefficients are determined using a look-up table in terms of the angle of attack. In this way the normal and tangential loads acting on the cylinder can be determined. In this study two approaches are used to determine the normal and tangential loads acting on the rotor, namely:

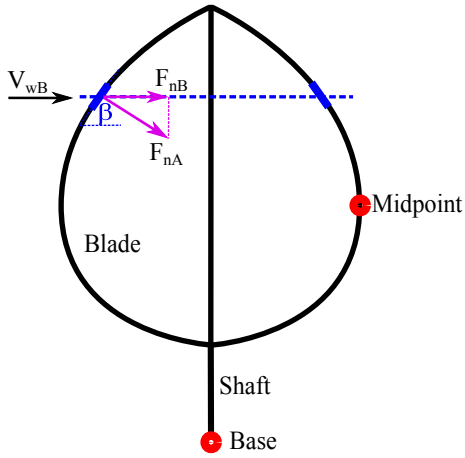

Fig. 3. An illustration of the local element force acting on the blade of a VAWT.

- Approach I:

$$Q_t = \frac{BF_{tB}}{2\pi R\rho V_{wB}^2} \tag{21}$$

$$Q_n = \frac{BF_{nB}}{2\pi R\rho V_{wB}^2} \tag{22}$$

- Approach II:

$$Q_t = \frac{BF_{tA}}{2\pi R\rho V_{wB}^2 \sin(\beta)} \tag{23}$$

$$Q_n = \frac{BF_{nA}}{2\pi R\rho V_{wB}^2 \sin(\beta)} \tag{24}$$

where B is the number of blades, R the radius of the disk considered, β the blade angle with the vertical direction, and V_{wB} the local free wind speed.

Approach I is based on the assumption that the local element considered is parallel to the rotating shaft, while approach II takes into account the inclination of the local element, which can represent more physical phenomena if the blade is curved or helical. The average thrust coefficient used in Eq. 19 can then be computed using Q_n and Q_t.

4. Aerodynamic modeling of a floating VAWT using the AC method

The flow chart of the aerodynamic modeling of a floating VAWT using the AC method is shown in Fig. 4. A swept surface is created when a VAWT rotates. A set of cylinders along the shaft is obtained by dividing the swept surface vertically, and for each cylinder a number of grids coinciding with the swept surface can then be obtained by dividing the cylinder circumferentially. In this sense the flow expansion in the vertical direction is not considered. A typical number of 20-30 cylinders along the shaft and 36 azimuth angles for each cylinder is recommended by [6]. At each time step, the induced velocity coefficients at these grids can be computed based on the AC method described above. Thus the induced velocity at the actual calculation point for each blade can then be determined using an linear interpolation from two nearest grids to the considered calculation point. The effect of dynamic stall is also included using the Beddoes-Leishman dynamic stall model. The effects of wind shear and turbulence if present can be included by the local free wind speed.

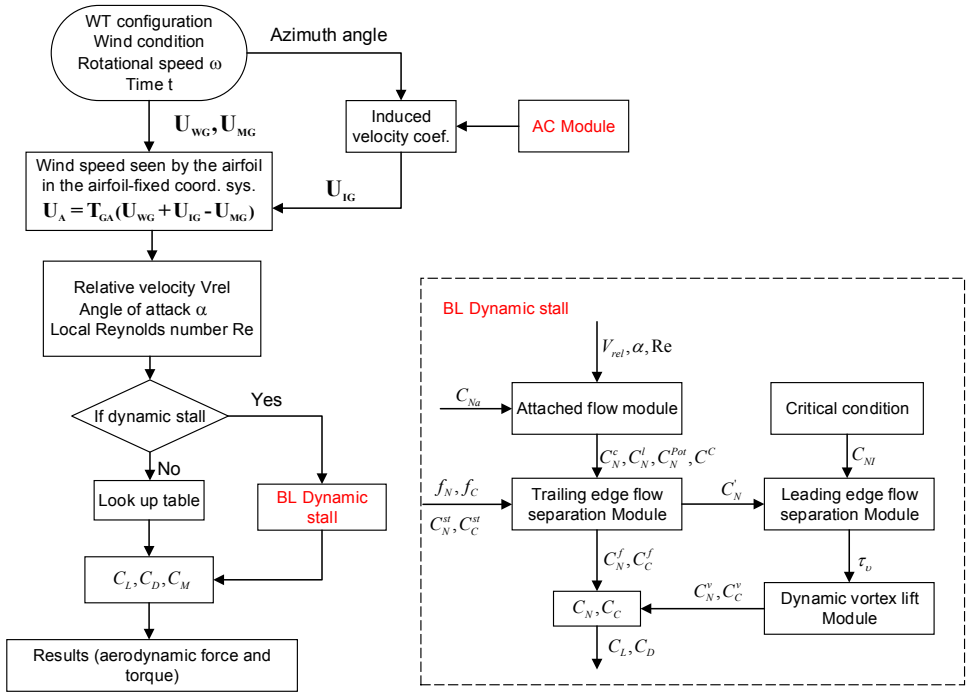

Fig. 4. Flow chart for aerodynamic modeling of a floating VAWT using the AC method. Here $\mathbf{U_{WG}}$, $\mathbf{U_{IG}}$ and $\mathbf{U_{MG}}$ are global wind speed, induced velocity and velocity due to motion, respectively. $\mathbf{T_{GA}}$ is the transform matrix from global coordinate system to the air-foil fixed coordinate system. Other parameters involved can refer to [1].

5. Verifications

An aerodynamic code is developed to model offshore VAWTs using the AC method. In this section, a series of comparisons against numerical models and experimental results are carried out to verify the accuracy of the developed code. Based on the combination of the approaches for the normal and tangential loads, the option for including or neglecting the Q_t term in Eqs. 14 and 15 when calculating the induced velocity, and different modified linear solutions, the AC codes developed can be categorized into AC1, AC2, AC3 and AC4, as given in Table 1.

Table 1. Different AC codes

	Approach for Q_n and Q_t	Q_t term in Eqs. 14 and 15	Modified linear solution
AC1	I	Neglected	Eq. 18
AC2	I	Included	Eq. 18
AC3	II	Included	Eq. 18
AC4	II	Included	Eq. 20

5.1. Verification of the codes AC1 and AC2

The codes AC1 and AC2 compute the aerodynamic loads based on the approach I for the normal and tangential loads. In this study the codes are verified by comparing with the numerical results by Larsen and Madsen [3]. A 5MW

Darrieus rotor with the radius of 64.96 m and height of 130 m was adopted. Various simulations were conducted using the linear solution and modified linear solution. The steady wind with a wind speed of 9 m/s was used and the tip speed ratio λ was set to be 3. The airfoil NACA0015 with the same aerodynamic coefficients were employed in all simulations.

Fig. 5 presents the normal loading Q_n and tangential loading Q_t at the midpoint of the blade (as shown in Fig. 3) along the cylinder periphery when the effect of induced velocities is not considered. Larsen and Madsen [3] carried out the simulations using the AC code and the HAWC2 code, respectively. It shows that these codes agree very well on the normal loading. Regarding the tangential loading, the present AC code agrees well with the result of the HAWC2 code.

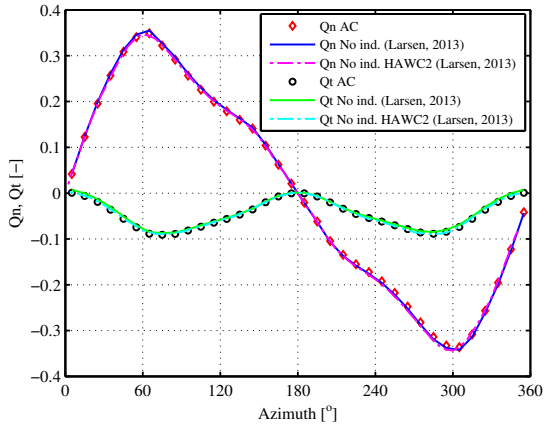

Fig. 5. Normal loading Q_n and tangential loading Q_t at the midpoint of the blade (as shown in Fig. 3) along the cylinder periphery for $\lambda = 3$. The effect of induced velocities is not considered.

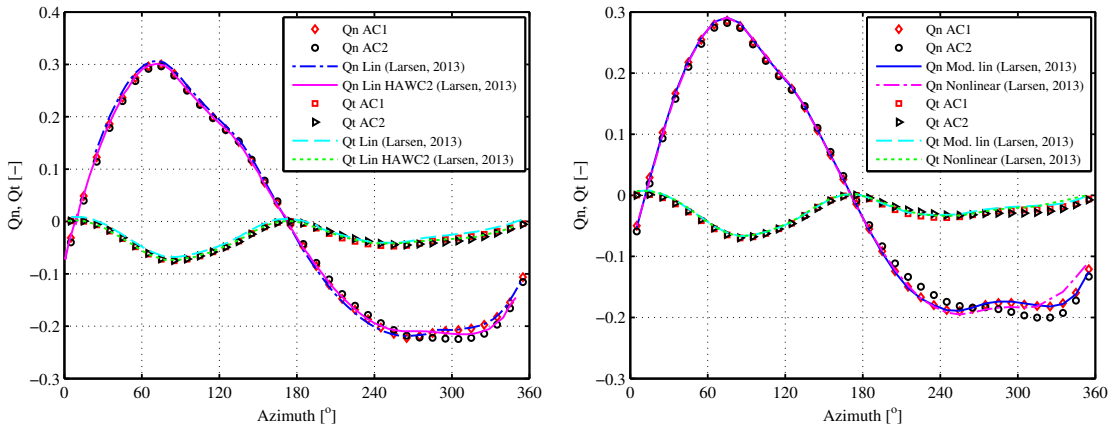

(a) With linear solution (b) With modified linear solution

Fig. 6. Normal loading Q_n and tangential loading Q_t at the midpoint of the blade (as shown in Fig. 3) along the cylinder periphery predicted using the linear solution and modified linear solution for $\lambda = 3$. Differences between the codes AC1 and AC2 can refer to Table 1.

Linear solution is then used to predict the normal and tangential loading on the rotor. Fig. 6(a) demonstrates the normal loading Q_n and tangential loading Q_t at the midpoint of the blade along the cylinder periphery. Here two AC code are applied and the difference between these two AC codes lie in that for the code AC1 the Q_t term in Eqs. 14

and 15 is neglected when calculating the induced velocity. It should also be noted that both the linear solution in the AC by [3] and the implementation of AC method in HAWC2 ignores the Q_t term in Eqs. 14 and 15.

In the windward part, both the normal and tangential loads resulting from AC1, AC2 and the HAWC2 implementation are very close. However, in the leeward part, especially in the vicinity of azimuth angle of 270 ^{o}, those codes present relatively large differences with respect to the normal and tangential loads. The codes AC1 and AC2 predict a little larger tangential load than the HAWC2 implementation. Regarding the codes AC1 and AC2, the AC2 gives a little smaller normal and tangential loads in the first and third quadrants and a little larger normal and tangential loads in the second and fourth quadrants. This is due to the effect of including tangential loads when calculating the induced velocity.

In order to predict the aerodynamic loads accurate at a small computational cost, a modified linear solution proposed by Madsen et al. [6] is used. Fig. 6(b) compares the normal loading Q_n and tangential loading Q_t at the midpoint of the blade along the cylinder periphery using the codes AC1 and AC2. The nonlinear solution considered by Larsen and Madsen [3] neglects the effect of tangential loads when calculating the induced velocity.

The normal load computed by AC1 agrees quite well with that of the modified linear solution by Larsen and Madsen [3]. But the AC1 predicts a little larger tangential loads than the modified linear solution by Larsen and Madsen [3], especially in the downwind part. With respect to the code AC2, deviations between the AC2 and modified linear solution of Larsen and Madsen [3] are both observed in the normal and tangential loads, particularly in the downwind part of the rotor, since the terms of tangential loads are included in AC2 when calculating the induced velocity.

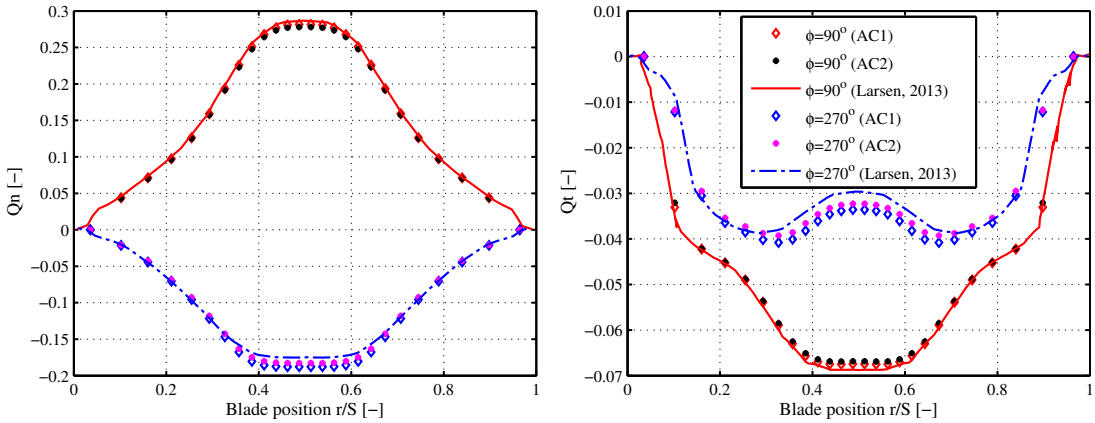

Fig. 7. Distribution of the normal load Q_n and tangential load Q_t as a function of position on the blade at azimuth angle of 90^o and 270^o. Differences between the codes AC1 and AC2 can refer to Table 1.

The above verifications are with respect to the midpoint of the blade. It's also necessary to investigate and verify the distribution of normal and tangential loads along the blade at different azimuth angles, as shown in Fig. 7. At the azimuth angle of 90^o, both the normal and tangential loads predicted by the codes AC1, AC2 and the implementation in HAWC2 by Larsen and Madsen [3] are very close. While at the azimuth angle of 270^o, these codes shows small differences in the middle part of the blade , with the position r/S approximately ranging from 0.3 to 0.7. Moreover, the AC2 gives a little smaller normal and tangential loads than the AC1.

As a whole, the present codes AC1 and AC2 agree well with the results in Larsen and Madsen [3] and can be regarded to be accurate enough to model floating VAWTs.

5.2. *Verification of the codes AC3 and AC4*

The codes AC3 and AC4 calculate the normal and tangential loads using approach II with different method to correct the linear solutions. In this study the codes AC3 and AC4 are verified by comparison with experiment data. Two rotors are considered here, i.e. the 3-bladed Sandia 5 m Darrieus rotor and 2-bladed Sandia 17 m Darrieus rotor. The power coefficient at different tip speed ratio for these two rotors are demonstrated in Fig. 8. It's obvious that at

low tip speed ratio, the codes AC3 and AC4 match well with each other and also agree well with the experimental data; However, at high tip speed ratio, the code AC4 can predict the power accurately while the code AC3 underestimates it. The modified linear solution proposed in this paper can better predict the aerodynamic power.

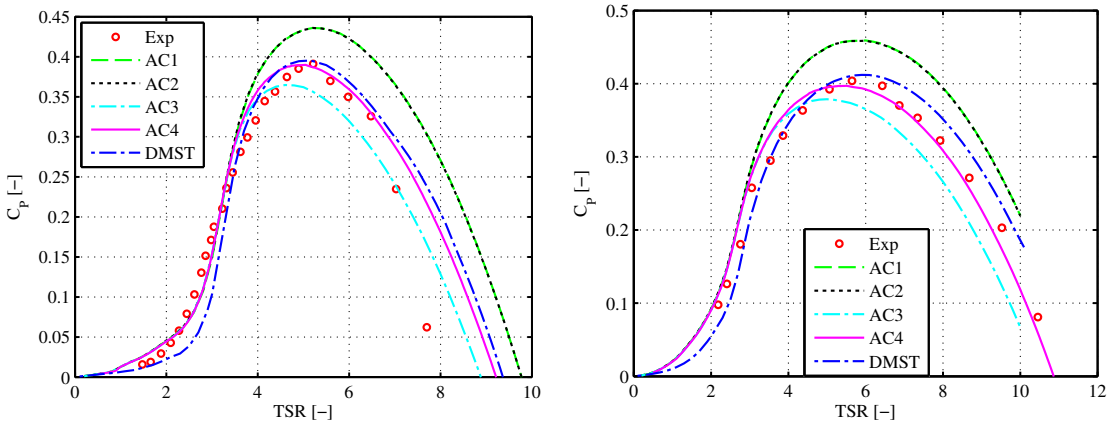

(a) The 3-bladed Sandia 5 m Darrieus rotor

(b) The 2-bladed Sandia 17 m Darrieus rotor

Fig. 8. Comparison of power coefficient curve between simulation model and experimental data. (a): the 3-bladed Sandia 5 m Darrieus rotor at rotational speed of 150 rpm, (b): the 2-bladed Sandia 17 m Darrieus rotor at rotational speed of 50.6 rpm. Differences between the codes AC1, AC2, AC3 and AC4 can refer to Table 1.

6. Comparison of the AC and DMST methods

Fig. 8 also show comparisons between the developed AC methods and the DMST method. It can be found that at a low tip speed ratio, which corresponds to small axial induction factor, the codes AC1, AC2, AC3 and AC4 are very close and can all predict the aerodynamic power accurately; and the DMST method seems to underpredict the aerodynamic power to some extent. At a high tip speed ratio, the AC1, AC2 and DMST codes overestimate the aerodynamic power, whereas the code AC3 underestimates the aerodynamic power.

In order to illustrate the difference between each code, the coefficients of thrust, lateral force and aerodynamic torque of the Sandia 17 m Darrieus rotor are also studied, as shown in Fig. 9. Two representative tip speed ratio are considered here. At a low tip speed ratio, for instance $\lambda = 2.5$, all these codes predict very close aerodynamic torque, but the DMST method differs in thrust and side force from the AC method since it ignores the induction in the cross-flow direction. Moreover, the aforementioned two approaches used to calculate the normal and tangential loads have very small difference at the low tip speed ratio. At a high tip speed ratio, for example $\lambda = 7$, the codes AC1 and AC2 overpredict the thrust and aerodynamic torque significantly, while the code AC3 gives a little smaller thrust and aerodynamic torque than the code AC4. When comparing the results of the codes AC4 and DMST, the DMST method overpredicts a little the aerodynamic torque but underestimates the thrust.

7. Conclusions

This paper deals with the aerodynamic modeling of floating VAWTs using the Actuator Cylinder (AC) method. An aerodynamic code has been developed to calculate the aerodynamic loads acting on the blades of VAWTs considering the shear and turbulent wind as well as the effect of dynamic stall using the Beddoes-Leishman dynamic stall model. Currently, the flow expansion of the induced velocity in the vertical direction is not considered.

The aerodynamic modeling of VAWTs are studied in depth in this paper. Linear solutions of the induced velocities along the cylinder are firstly derived to account for the effect of tangential load. Two different approaches are used to

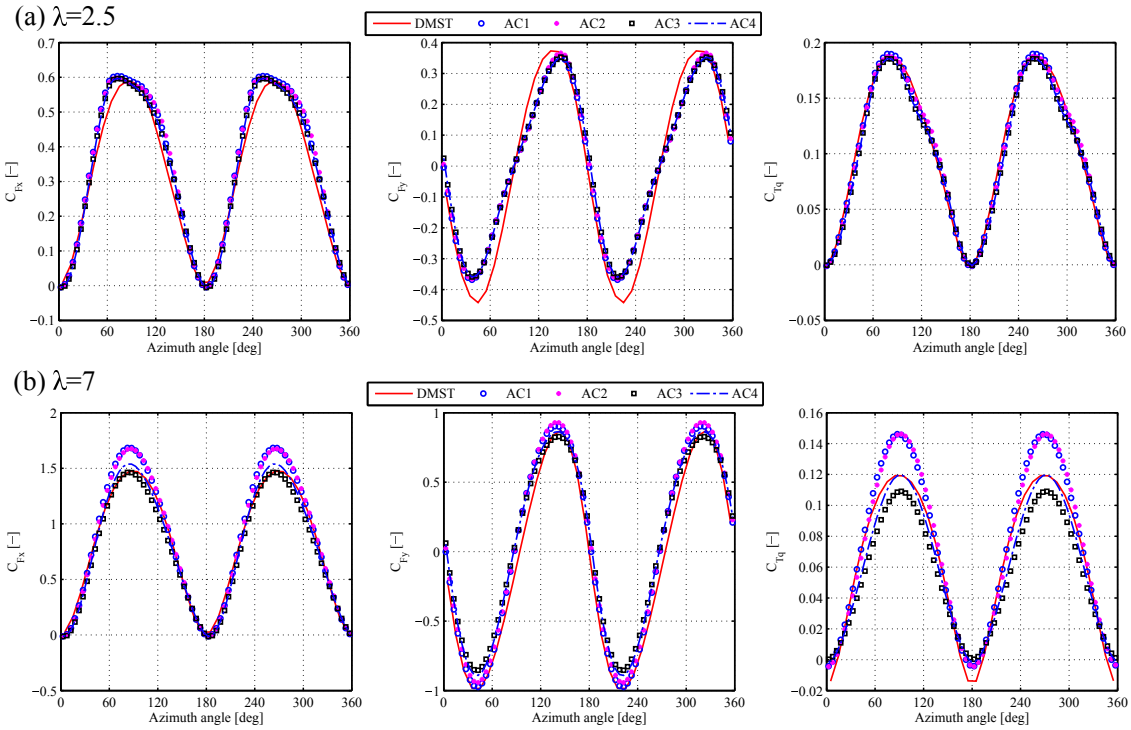

Fig. 9. Coefficients of thrust, side force and torque for the Sandia 17 m Darrieus rotor as a function of the azimuth angle. The effect of dynamic stall is not included. Differences between the codes AC1, AC2, AC3 and AC4 can refer to Table 1.

calculate the normal and tangential loads along the cylinder. Moreover, two different modifications are employed to correct the linear solution of the induced velocities.

The effect of tangential load on the aerodynamic loads when calculating the induced velocities is found to be relatively very small. Calculating the normal and tangential loads using approach II which considers more physical phenomena predicts better aerodynamic loads than approach I. Moreover, the modified linear solution proposed in this study gives very good aerodynamic power prediction compared with experimental data.

In addition, comparative studies of the developed AC codes and the double multi-streamtube (DMST) method are carried out and show that the developed AC method, which includes the tangential load term when calculating the induced velocities, computes the normal and tangential loads using approach II and employs the new modified linear solution, can predict more accurate aerodynamic power and aerodynamic loads than the DMST method.

The developed AC method is found to be accurate for modeling offshore VAWTs. This AC code can be integrated with the computer codes SIMO-RIFLEX to form a fully coupled simulation tool, i.e. SIMO-RIFLEX-AC [1], which is capable of performing the aero-hydro-servo-elastic time-domain analysis for offshore bottom-fixed or floating VAWTs.

Acknowledgments

The authors would like to acknowledge the financial support from the EU FP7 project MARE WINT (project NO. 309395) through the Centre for Ships and Ocean Structures (CeSOS) and Centre for Autonomous Marine Operations and Systems (AMOS) at the Department of Marine Technology, Norwegian University of Science and Technology (NTNU), Trondheim, Norway. The first author would like to thank the Department of Wind Energy for kindly hosting

me and valuable discussions with senior scientist Torben J. Larsen at the Technical University of Denmark, Roskilde, Denmark.

References

[1] Cheng, Z., Madsen, H. A., Gao, Z., Moan, T., 2016. A fully coupled method for numerical modeling and dynamic analysis of floating vertical axis wind turbines. Prepared for possible journal publication.
[2] Ferreira, C. S., Madsen, H. A., Barone, M., Roscher, B., Deglaire, P., Arduin, I., 2014. Comparison of aerodynamic models for vertical axis wind turbines. Journal of Physics: Conference Series 524 (1), 012125.
[3] Larsen, T. J., Madsen, H. A., 2013. On the way to reliable aeroelastic load simulation on VAWT's. In: Proceedings of EWEA.
[4] Madsen, H. A., 1982. The Actuator Cylinder: A flow model for vertical axis wind turbines. Institute of Industrial Constructions and Energy Technology, Aalborg University Centre.
[5] Madsen, H. A., 1983. On the ideal and real energy conversion in a straight bladed vertical axis wind turbine. Institute of Industrial Constructions and Energy Technology, Aalborg University Centre.
[6] Madsen, H. A., Larsen, T. J., Paulsen, U. S., Vita, L., 2013. Implementation of the actuator cylinder flow model in the HAWC2 code for aeroelastic simulations on vertical axis wind turbines. In: 51st AIAA Aerospace Sciences Meeting including the New Horizons Forum and Aerospace Exposition.
[7] Murray, J., Barone, M., 2011. The development of cactus, a wind and marine turbine performance simulation code. In: 49th AIAA Aerospace Sciences Meeting. Paper AIAA 2011-47.
[8] Paquette, J., Barone, M., 2012. Innovative offshore vertical-axis wind turbine rotor project. EWEA 2012 Annual Event.
[9] Paraschivoiu, I., 2002. Wind turbine design: with emphasis on Darrieus concept. Polytechnic International Press., Montreal, Canada.
[10] Paulsen, U. S., Madsen, H. A., Hattel, J. H., Baran, I., Nielsen, P. H., 2013. Design optimization of a 5 mw floating offshore vertical-axis wind turbine. Energy Procedia 35, 22–32.
[11] Roscher, B., 2014. Current aerodynamic models for VAWT and numerical comparison between HAWC2 and U2DiVA. Special project - EWEM rotor design.
[12] Strickland, J. H., 1975. The darrieus turbine: A performance prediction model using multiple streamtubes. Technical Report SAND75-0430 , Sandia National Laboratories, Albuquerque, N.M. USA.
[13] Templin, R. J., 1974. Aerodynamic performance theory for the nrc vertical-axis wind turbine. Technical Report LTR-LA-160, National Aeronautical Establishment, Ottawa, Ontario, Canada.

Appendix A. Linear solution of the AC flow problem

In Eq. 5, let $\xi = -r\sin\theta, \eta = r\cos\theta$, we have

$$\begin{aligned} p_f =& \lim_{\epsilon\to 0}\frac{1}{2\pi}\int_{1-\epsilon}^{1+\epsilon}\int_0^{2\pi}\frac{(-f_n\sin\theta - f_t\cos\theta)(x + r\sin\theta) + (f_n\cos\theta - f_t\sin\theta)(y - r\cos\theta)}{(x + r\sin\theta)^2 + (y - r\cos\theta)^2} r dr d\theta \\ =& \frac{1}{2\pi}\int_0^{2\pi} Q_n(\theta)\frac{-(x+\sin\theta)\sin\theta + (y-\cos\theta)\cos\theta}{(x+\sin\theta)^2 + (y-\cos\theta)^2} d\theta \\ &+ \frac{1}{2\pi}\int_0^{2\pi} Q_t(\theta)\frac{-(x+\sin\theta)\cos\theta - (y-\cos\theta)\sin\theta}{(x+\sin\theta)^2 + (y-\cos\theta)^2} d\theta \end{aligned} \tag{A.1}$$

For the integral part in Eq. 3, since the volume forces are non-zero only along the cylinder, the integral result depends on the position of the calculation point.

- When the calculation point is located inside the cylinder, as the point $P_1(x, y)$ shown in Fig. 2, the integral part can be written as

$$\int_{-\infty}^{x} f_x dx' = \int_{-\infty}^{0} f_x dx'$$

note that $x' = -\sqrt{r^2 - y^2}$, $dx' = -\frac{r}{\sqrt{r^2-y^2}}dr$, and $f_x = -f_n\sin\theta - f_t\cos\theta = -f_n\frac{\sqrt{r^2-y^2}}{r} - f_t\frac{y}{r}$, this yields

$$\begin{aligned}\int_{-\infty}^{x} f_x dx' &= \lim_{\epsilon\to 0}\int_{1+\epsilon}^{1-\epsilon}\left(-f_n\frac{\sqrt{r^2-y^2}}{r}-f_t\frac{y}{r}\right)\left(-\frac{r}{\sqrt{r^2-y^2}}\right)dr\\ &= -\lim_{\epsilon\to 0}\int_{1-\epsilon}^{1+\epsilon}\left(f_n+f_t\frac{y}{\sqrt{r^2-y^2}}\right)dr\\ &= -Q_n(\arccos y)-Q_t(\arccos y)\frac{y}{\sqrt{1-y^2}}\end{aligned} \tag{A.2}$$

- When the calculation point is located at the leeward part of the cylinder, as the point $P_2(x, y)$ shown in Fig. 2, the integral part can be written as

$$\int_{-\infty}^{x} f_x dx' = \int_{-\infty}^{0} f_x dx' + \int_{0}^{x} f_x dx'$$

The first term in the right hand side of the equation has been computed above. For the second term in the right hand side, since $x' > 0$ then $x' = \sqrt{r^2-y^2}$, we have $dx' = \frac{r}{\sqrt{r^2-y^2}}dr$ and $f_x = -f_n\sin\theta - f_t\cos\theta = f_n\frac{\sqrt{r^2-y^2}}{r} - f_t\frac{y}{r}$

$$\begin{aligned}\int_{0}^{x} f_x dx' &= \lim_{\epsilon\to 0}\int_{1-\epsilon}^{1+\epsilon}\left(f_n\frac{\sqrt{r^2-y^2}}{r}-f_t\frac{y}{r}\right)\left(\frac{r}{\sqrt{r^2-y^2}}\right)dr\\ &= \lim_{\epsilon\to 0}\int_{1-\epsilon}^{1+\epsilon}\left(f_n-f_t\frac{y}{\sqrt{r^2-y^2}}\right)dr\\ &= Q_n(-\arccos y)-Q_t(-\arccos y)\frac{y}{\sqrt{1-y^2}}\end{aligned} \tag{A.3}$$

Regarding the integration in Eq. 4, it should be noted that [4]

$$\int_{-\infty}^{x}\frac{\partial p_f}{\partial y}dx' = \frac{1}{2\pi}\iint\frac{-f_y(x-\xi)+f_x(y-\eta)}{(x-\xi)^2+(y-\eta)^2}d\xi d\eta + \int_{-\infty}^{x} f_y dx' \tag{A.4}$$

Therefore,

$$\begin{aligned}w_y(f) &= -\int_{-\infty}^{x}\frac{\partial p_f}{\partial y}dx' + \int_{-\infty}^{x} f_y dx'\\ &= -\frac{1}{2\pi}\iint\frac{-f_y(x-\xi)+f_x(y-\eta)}{(x-\xi)^2+(y-\eta)^2}d\xi d\eta\\ &= -\frac{1}{2\pi}\int_0^{2\pi} Q_n(\theta)\frac{-(x+\sin\theta)\cos\theta-(y-\cos\theta)\sin\theta}{(x+\sin\theta)^2+(y-\cos\theta)^2}d\theta\\ &\quad+\frac{1}{2\pi}\int_0^{2\pi} Q_t(\theta)\frac{-(x+\sin\theta)\sin\theta+(y-\cos\theta)\cos\theta}{(x+\sin\theta)^2+(y-\cos\theta)^2}d\theta\end{aligned} \tag{A.5}$$

In this way, the integration in Eqs. 3 and 4 can be conducted and the linear solution of the velocities can be obtained.

A.2 Paper 2

Paper 2:
A fully coupled method for numerical modeling and dynamic analysis of floating vertical axis wind turbines.
Zhengshun Cheng, Helge Aagaard Madsen, Zhen Gao, Torgeir Moan
Submitted to *Renewable Energy*, 2016

A fully coupled method for numerical modeling and dynamic analysis of floating vertical axis wind turbines

Zhengshun Cheng [*1, 2, 3], Helge Aagaard Madsen[4], Zhen Gao[1, 2, 3], and Torgeir Moan[1, 2, 3]

[1]Department of Marine Technology, Norwegian University of Science and Technology (NTNU), Trondheim, NO-7491, Norway
[2]Centre for Ships and Ocean Structures (CeSOS), NTNU, Trondheim, NO-7491, Norway
[3]Centre for Autonomous Marine Operations and Systems (AMOS), NTNU, Trondheim, NO-7491, Norway
[4]Department of Wind Energy, Technical University of Denmark, Roskilde, 4000, Denmark

April 5, 2016

Abstract

Offshore wind energy is one of the most promising renewable energy resources and an increasing interest arises to develop floating vertical axis wind turbines (VAWTs), which have the potential of achieving more than 20% cost of energy reduction. Assessment of the performance of floating VAWTs requires sophisticated fully coupled aero-hydro-servo-elastic simulation tools, which are currently limited. This paper aims to develop a fully integrated simulation tool for floating VAWTs. Based on the actuator cylinder (AC) flow model, aerodynamic modeling of floating VAWTs is established with consideration of the effects of turbulence, dynamic inflow and dynamic stall. The developed aerodynamic code is then coupled with the code SIMO-RIFLEX to achieve a fully coupled tool, i.e. SIMO-RIFLEX-AC, which can account for the aerodynamic, hydrodynamics, structural dynamics and controller dynamics with high fidelity. A series of code-to-code comparisons with the codes HAWC2 and SIMO-RIFLEX-DMS are carried out using a landbased VAWT and a semi VAWT, and reveal that the present code can predict the aerodynamic loads and dynamic responses accurately. Moreover, the code SIMO-RIFLEX-AC can predict more accurate responses than the code SIMO-RIFLEX-DMS, such as the platform motions, tower base bending moments and tension in mooring lines.

Key words: Floating vertical axis wind turbine; fully coupled method; aero-hydro-servo-elastic; actuator cylinder flow model

[*]Corresponding author. Email address: zhengshun.cheng@ntnu.no Tel.:+47-7359 6004; fax: +47-7359 5528.

1 Introduction

During the 1970s and 1980s, a substantial amount of researches were conducted to develop the vertical axis wind turbines (VAWTs), particularly in the United States and Canada. The largest onshore VAWT, the Éole Darrieus wind turbine, was built in 1986 at Québec, Canada. Commercial development of VAWTs was made in the United States during the 1980s by FloWind Ltd. However, due to fatigue problems within the bearings and blades, VAWTs lost the ground relative to the horizontal axis wind turbines (HAWTs).

In recent years, offshore wind farms are moving towards deeper waters and the interest in the development of floating VAWTs has been resurging. Compared with floating HAWTs, floating VAWTs have lower centers of gravity, are independent of wind direction, can provide reduced machine complexity and have the potential of achieving more than 20% cost of energy reductions (Paquette and Barone, 2012). Moreover, floating platform can help to mitigate the fatigue damage suffered by the onshore VAWTs (Wang et al., 2015b). In addition, floating VAWTs are more suitable for deployment as wind farms than floating HAWTs. Thus, more and more efforts are devoted to the development of floating VAWTs. In order to asses the technical feasibility of floating VAWTs, a fully coupled simulation tool is required. However, currently the simulation tools which are capable of performing fully coupled analysis of floating VAWTs are very limited, due to the difficulty of predicting the aerodynamic loads accurately at a small computational cost.

Since Sandia National Laboratories started the study of VAWTs in the 1970s, a variety of aerodynamic models have been used to predict aerodynamic loads acting on the rotor for VAWTs. These include multi-streamtube model, double multi-streamtube (DMS) model, actuator cylinder (AC) flow model, panel method, vortex method and computational fluid dynamics (CFD) method. A comprehensive overview of these models can refer to Borg et al. (2014).

Among these models, currently the DMS model has been widely used to estimate the aerodynamic loads on VAWTs. The DMS is also adopted in several available fully coupled simulation tools, including the SIMO-RIFLEX-DMS developed in NTNU (Wang et al., 2013), FloVAWT developed in Cranfield University (Collu et al., 2013) and OWENS by Sandia National Laboratories (Owens et al., 2013). The Simo-Riflex-DMS code was developed by Wang et al. (2013) to perform the fully coupled non-linear aero-hydro-servo-elastic simulations for floating VAWTs. This code is based on the SIMO-RIFLEX code which has been extensively used and validated for offshore structures subjected to wave loads. It can account for the turbulent wind inflow, aerodynamics, hydrodynamics, control dynamics, structural mechanics and mooring line dynamics. The aerodynamic loads are calculated using the DMS model with the Beddoes-Leishman dynamic stall model. To provide a simplified coupled dynamics design tool to the use in the preliminary design stages of floating VAWTs, Collu et al. (2013) from Cranfield University developed FloVAWT (Floating Vertical Axis Wind Turbines) code. The DMS model with Gormont-Berg dynamic stall is used in the aerodynamic model. Main drawbacks of this code are that the dynamic mooring model, structural dynamics and control dynamic are missing. Sandia National Laboratories developed the OWENS (Offshore Wind ENergy Simulation) toolkit (Owens et al., 2013) aiming at establishing a robust and flexible finite element framework and VAWT mesh generation utility, coupled with a modular interface that allows users to integrate easily with existing codes, such as aerodynamic and hydrodynamic codes.

However, by considering a 2D VAWT rotor, Ferreira et al. (2014) compares the different models used to model the VAWT, including the multi-streamtube model, the DMS model, the AC model, a 2D potential flow panel

model, a 3D unsteady lifting line model and a 2D conformal mapping unsteady vortex model. The comparison reveals that the DMS model proves to be fundamentally incorrect in the prediction of the effect of changing the fixed pitch angle, and that the AC model shows a good agreement with the panel and vortex models. Moreover, Roscher (2014) compares these models with respect to complexity, accuracy, computational cost, suitability for optimization and aeroelastic analysis. Due to the consideration of accuracy and computational cost, the AC model is the favorable method that can be used for aero-hydro-servo-elastic time domain simulations for floating VAWTs.

The AC model is originally developed by Madsen (1982) in his PhD study. The AC model has been implemented in HAWC2 (Madsen et al., 2013; Larsen and Madsen, 2013) to conduct the fully coupled aero-hydro-servo-elastic time domain simulations for floating VAWTs. It can account for dynamic inflow, structural dynamics, tower shadow and dynamic stall. Paulsen et al. (2013) performed a design optimization of the proposed DeepWind concept. An improved design has been obtained with an optimized blade profile with less weight and higher stiffness than the 1st baseline design.

In the present study an aerodynamic code is to be developed using the AC model. Induction calculation using the AC method is firstly described. Latter aerodynamic modeling of floating VAWTs is established with consideration of the effects of dynamic stall, turbulent and dynamic inflow. Then this aerodynamic code is to be coupled with SIMO-RIFLEX to achieve a fully coupled aero-hydro-servo-elastic simulation tool with high fidelity. Using a landbased VAWT and a semi VAWT, a series of numerical simulations are carried out to verify the fully coupled code.

2 Aerodynamic Modeling of floating VAWTs

When a VAWT rotates, each calculation point along the blade creates a cross section which is a cylinder perpendicular to the shaft. The swept surface created by the VAWT can then be divided approximately into a number of vertically stacked cylinders with finite height and with a radius coinciding with the rotor radius at the actual position along the shaft. Therefore the complex 3D flow problem is condensed into a number of 2D actuator cylinder flow problems. For each cylinder, the AC method, developed by Madsen (1982), is used to find out the induced velocity.

In this section, the aerodynamic modeling of floating VAWTs using the AC method is presented, as the flow chart illustrated in Figure 1. The effects of wind shear, turbulence, dynamic stall and dynamic inflow are also taken into account in the present implementation.

2.1 Aerodynamic loads on a 2D VAWT

For each calculation point in the local airfoil coordinate system , the local inflow velocity $\mathbf{V_A}$ seen at a blade section can be determined from

$$\mathbf{V_A} = \mathbf{T_{GA}} \left(\mathbf{V_{WG}} + \mathbf{V_{IG}} - \mathbf{V_{MG}} \right) \tag{1}$$

where $\mathbf{T_{GA}}$ is a transformation matrix from global to airfoil-fixed coordinate system. The global inflow velocity $\mathbf{V_G}$ seen at a blade section is the vector sum of the free wind speed $\mathbf{V_{WG}}$, the induced velocity $\mathbf{V_{IG}}$ and subtracting the velocity due to the motion $\mathbf{V_{MG}}$. $\mathbf{V_{MG}}$ is comprised of the blade rotation, the translational and rotational velocity

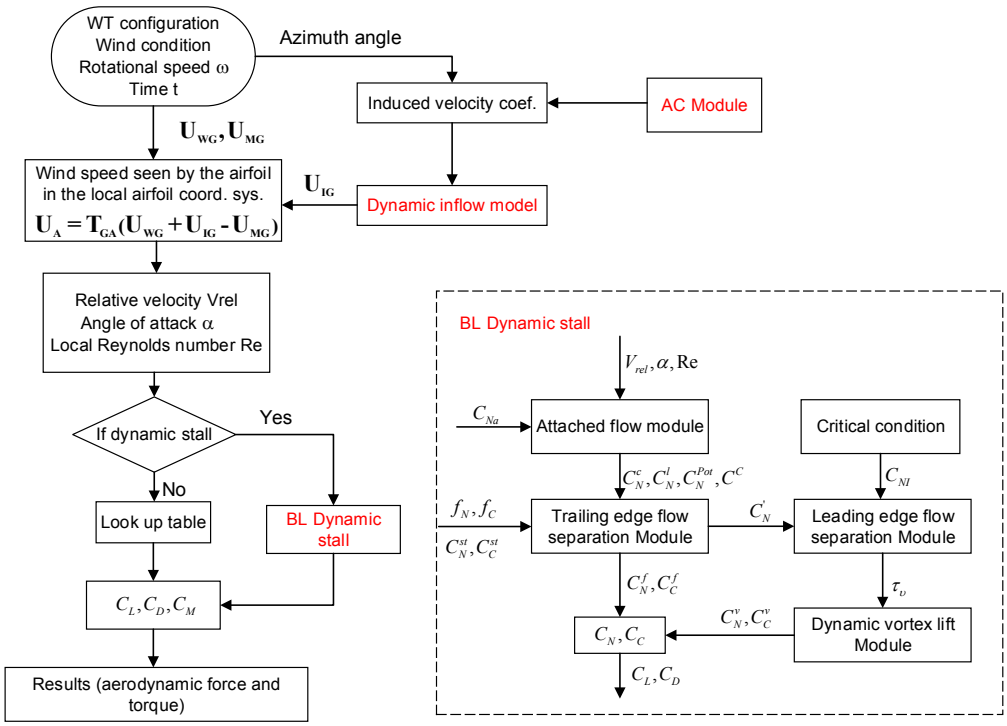

Figure 1: Flow chart of modeling of a floating VAWT using AC method. The models of dynamic inflow and dynamic stall are included.

from the platform and the velocity due to the elastic deformation of the blades. The induced velocity $\mathbf{V_{IG}}$ can be calculated using the AC method by assuming a 2D quasi-static flow problem, which is described latter.

Therefore, a 2D look-up table giving the relationship between the coefficients C_l, C_d and the angle of attack α is used to compute the aerodynamic lift and drag force, as well as the tangential load F_{tA} and normal load F_{nA} acting on the local element. In the AC method, the tangential and normal loads are non-dimensionalized as follows (Cheng et al., 2016)

$$Q_t = -\frac{BF_{tA}}{2\pi R\rho V_{wB}^2 \sin(\beta)} \tag{2}$$

$$Q_n = \frac{BF_{nA}}{2\pi R\rho V_{wB}^2 \sin(\beta)} \tag{3}$$

where B is the number of blades, ρ the air density, R the radius of the disk considered, β the blade angle with the vertical direction, and V_{wB} the local free wind speed.

2.2 Actuator Cylinder Flow Model

The AC method is a quasi-steady Eulerian model. The model extends the actuator disc concept to an actuator surface coinciding with the swept area of the 2D VAWT. In the AC model, the normal and tangential forces Q_n and Q_t resulting from the blade forces are applied on the flow as volume force perpendicular and tangential to the rotor plane, respectively, as illustrated in Figure 2. Thus the induced velocities w_x and w_y are related to volume forces as well as the normal and tangential loads Q_n and Q_t based on the Euler equation and continuity equation. In this way, the final velocity can be divided into a linear part which is a function of the prescribed normal and tangential loads Q_n and Q_t and a nonlinear part that is a function of the induced forces. Detailed derivations regarding this 2D quasi-static flow problem can refer to Madsen et al. (2013).

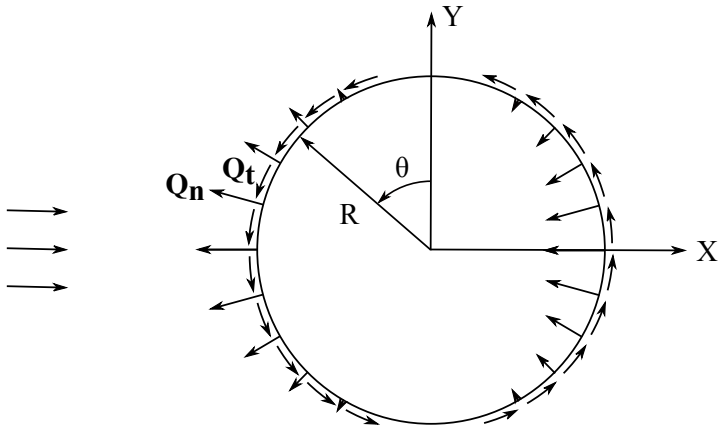

Figure 2: The actuator cylinder flow model representation of a VAWT with volume forces normal and tangential to the circle. Note that the force direction is from the VAWT noto the flow. (Madsen et al., 2013)

2.2.1 Linear solution

The linear solution of the induced velocities can be analytically computed, which is given by Cheng et al. (2016) as follows.

$$
\begin{aligned}
w_x = &-\frac{1}{2\pi}\int_0^{2\pi} Q_n(\theta)\frac{-(x+\sin\theta)\sin\theta+(y-\cos\theta)\cos\theta}{(x+\sin\theta)^2+(y-\cos\theta)^2}d\theta \\
&-\frac{1}{2\pi}\int_0^{2\pi} Q_t(\theta)\frac{-(x+\sin\theta)\cos\theta-(y-\cos\theta)\sin\theta}{(x+\sin\theta)^2+(y-\cos\theta)^2}d\theta \\
&-(Q_n(\arccos y))^* + (Q_n(-\arccos y))^{**} \\
&-\left(Q_t(\arccos y)\frac{y}{\sqrt{1-y^2}}\right)^* - \left(Q_t(-\arccos y)\frac{y}{\sqrt{1-y^2}}\right)^{**}
\end{aligned}
\tag{4}
$$

$$
\begin{aligned}
w_y = &-\frac{1}{2\pi}\int_0^{2\pi} Q_n(\theta)\frac{-(x+\sin\theta)\cos\theta-(y-\cos\theta)\sin\theta}{(x+\sin\theta)^2+(y-\cos\theta)^2}d\theta \\
&-\frac{1}{2\pi}\int_0^{2\pi} Q_t(\theta)\frac{(x+\sin\theta)\sin\theta-(y-\cos\theta)\cos\theta}{(x+\sin\theta)^2+(y-\cos\theta)^2}d\theta
\end{aligned} \tag{5}
$$

where θ is the azimuth angle, the term marked with $*$ in Eq. 4 shall only be added inside the cylinder whereas in the wake behind the cylinder both the term marked with $*$ and $**$ shall be added. Compared with the results in Madsen et al. (2013), the effect of tangential load on the computed induced velocity is considered here.

Assuming that the loading is piecewise constant, the integral part in Eqs. 4 and 5 can be rewritten as

$$
\begin{aligned}
w_x = &-\frac{1}{2\pi}\sum_{i=1}^{i=N} Q_{n,i}\int_{\theta_i-\frac{1}{2}\Delta\theta}^{\theta_i+\frac{1}{2}\Delta\theta}\frac{-(x+\sin\theta)\sin\theta+(y-\cos\theta)\cos\theta}{(x+\sin\theta)^2+(y-\cos\theta)^2}d\theta \\
&-\frac{1}{2\pi}\sum_{i=1}^{i=N} Q_{t,i}\int_{\theta_i-\frac{1}{2}\Delta\theta}^{\theta_i+\frac{1}{2}\Delta\theta}\frac{-(x+\sin\theta)\cos\theta-(y-\cos\theta)\sin\theta}{(x+\sin\theta)^2+(y-\cos\theta)^2}d\theta
\end{aligned} \tag{6}
$$

$$
\begin{aligned}
w_y = &-\frac{1}{2\pi}\sum_{i=1}^{i=N} Q_{n,i}\int_{\theta_i-\frac{1}{2}\Delta\theta}^{\theta_i+\frac{1}{2}\Delta\theta}\frac{-(x+\sin\theta)\cos\theta-(y-\cos\theta)\sin\theta}{(x+\sin\theta)^2+(y-\cos\theta)^2}d\theta \\
&+\frac{1}{2\pi}\sum_{i=1}^{i=N} Q_{t,i}\int_{\theta_i-\frac{1}{2}\Delta\theta}^{\theta_i+\frac{1}{2}\Delta\theta}\frac{-(x+\sin\theta)\sin\theta+(y-\cos\theta)\cos\theta}{(x+\sin\theta)^2+(y-\cos\theta)^2}d\theta
\end{aligned} \tag{7}
$$

where N is the total number of calculation points, $\Delta\theta = \frac{2\pi}{N}$ and $\theta_i = \frac{\pi}{N}(2i-1)$ for $i = 1, 2, ..., N$.

Since only induced velocities at the cylinder are of concern, the total velocity solution at the calculation point (x_j, y_j) (for $j = 1, 2, ..., N$) on the cylinder can then be rewritten as

$$
w_{x,j} = -\frac{1}{2\pi}\left(\sum_{i=1}^{i=N} Q_{n,i}I_{1,i,j} + \sum_{i=1}^{i=N} Q_{t,i}I_{2,i,j}\right) - \left(Q_{n,N+1-j}\right)^* - \left(Q_{t,N+1-j}\frac{y_j}{\sqrt{1-y_j^2}}\right)^* \tag{8}
$$

$$
w_{y,j} = -\frac{1}{2\pi}\left(\sum_{i=1}^{i=N} Q_{n,i}I_{2,i,j} - \sum_{i=1}^{i=N} Q_{t,i}I_{1,i,j}\right) \tag{9}
$$

where the terms marked with $*$ in Eqs. 8 and 9 are only added for $j > \frac{N}{2}$ (the leeward part of the AC with $x_j > 0$). $I_{1,i,j}$ and $I_{2,i,j}$ are influence coefficients at point j influenced by other point i and are given by

$$
I_{1,i,j} = \int_{\theta_i-\frac{1}{2}\Delta\theta}^{\theta_i+\frac{1}{2}\Delta\theta}\frac{-\left(x_j+\sin\theta\right)\sin\theta+\left(y_j-\cos\theta\right)\cos\theta}{\left(x_j+\sin\theta\right)^2+\left(y_j-\cos\theta\right)^2}d\theta \tag{10}
$$

$$
I_{2,i,j} = \int_{\theta_i-\frac{1}{2}\Delta\theta}^{\theta_i+\frac{1}{2}\Delta\theta}\frac{-\left(x_j+\sin\theta\right)\cos\theta-\left(y_j-\cos\theta\right)\sin\theta}{\left(x_j+\sin\theta\right)^2+\left(y_j-\cos\theta\right)^2}d\theta \tag{11}
$$

in which $x_j = -\sin(j\Delta\theta - \frac{1}{2}\Delta\theta)$, $y_j = \cos(j\Delta\theta - \frac{1}{2}\Delta\theta)$. It can be found that the influence coefficients $I_{1,i,j}$ and $I_{2,i,j}$ are irrespective of time and can thus be integrated once and for all.

2.2.2 Modified linear solution

It's to some extent time-consuming to compute the nonlinear solution directly. In order to make the final solution in better agreement with the fully nonlinear solution, a correction is required for the linear solution. A simple correction (Madsen et al., 2013) is suggested by multiplying the velocities from the linear solution w_x and w_y with a factor k_a that is related to the axial induction factor. However, Cheng et al. (2016) stated that the correction proposed by Madsen et al. (2013) can give some deviation in the power coefficient at high tip speed ratios when comparing with experiments. Thus a new modification which corrects the k_a at a high induction factor, which corresponds to a large tip speed ratio, is proposed by Cheng et al. (2016).

$$k_a = \begin{cases} \frac{1}{1-a}, & (a \leq 0.15) \\ \frac{1}{1-a}(1 - 0.35\,(1 - \exp\,(-4.5(a - 0.15)))), & (a > 0.15) \end{cases} \tag{12}$$

where the induction factor a is found based on a relationship between the induction a and the average thrust coefficient C_T.

2.3 Wind inflow

The effects of wind shear and turbulence can be included in the local free wind speed. The wind inflow can be determined using the hub height wind file, full field wind file and user-defined wind file. For the turbulent wind inflow, the three dimensional turbulent wind fields are generated using the NREL's TurbSim program (Jonkman, 2009).

2.4 Dynamic stall model

In this work, the Beddoes-Leishman dynamic stall model is used to predict the VAWT's aerodynamic loads. It is a semi-empirical model which can represent the physical phenomenon to a certain extent through a superposition of separate indicial functions. The Beddoes-Leishman model is original developed to simulate the dynamic stall effect on the helicopter (Leishman and Beddoes, 1989). The adaptation of this model has been studied for HAWTs by Gupta and Leishman (2006) and VAWTs by Dyachuk et al. (2014).

The Beddoes-Leishman model consists of three parts: unsteady attached flow, unsteady separated flow and dynamic vortex lift. In the unsteady attached flow regime, the aerodynamic loads are comprised of a circulatory component related to the change of the angle of attack and an impulsive component related to the change rate of the angle of attack and pitch moment. Thus the total normal force coefficient C_N under the attached flow condition can be written as

$$C_N = C_N^C + C_N^I \tag{13}$$

where C_N^C and C_N^I are the circulatory and impulsive normal force coefficients, respectively. The unsteady chordwise force coefficient C_C is based on the circulatory component of C_N.

The calculated attached flow response is then modified due to the flow separation on the low-pressure side of the airfoil. The unsteady separate flow usually includes leading edge separation and trailing edge separation. The effective separation point is related to the normal force coefficient and the chordwise force coefficient according to

the Kirchhoff theory and calculated using static data. An empirically derived first order lag is then applied to the movement of the effective separation point to account for the time lag in movement of the separation point during unsteady conditions. The final main component of the model represents the vortex buildup and shedding that occurs during the dynamic stall. The vortex lift contribution is empirically modeled as an excess circulation in the vicinity of the airfoil using the difference between the attached flow C_N and the unsteady non-linear value from the Kirchhoff relationship. Therefore, the total loading on the airfoil is obtained by summing all of the aforementioned components.

Several modifications are implemented to adapt the Beddoes-Leishman model for VAWT applications, as described in the AeroDyn theory manual (Moriarty and Hansen, 2005). The model is capable of producing aerodynamic force coefficients over the entire range of possible angles of attack. To ensure proper regeneration of coefficients, two effective separation point tables are used, one for the normal force coefficient and one for the chordwise force coefficient. Moreover, the sign of the effective separation point is saved with the value of the parameter. Due to the effect of vortex component, the chordwise force coefficient is modified by adding one additional term from the vortex lift in the same manner as the circulatory component of C_N, as follows (Wang et al., 2015b)

$$C_C = C_{Na}\left(\alpha_e - \alpha_0\right)\alpha_e\sqrt{f_C''} + C_N^v\alpha_e\left(1-\tau_v\right) \tag{14}$$

where α_e is the effective angle of attack, α_0 is the zero-lift angle, C_{Na} is the normal force coefficient curve slope, f_C'' is the dynamic separation point function, C_N^v is the normal force coefficient from the vortex lift contribution and τ_v is the non-dimensional parameter to track the position of the vortex across the airfoil. Finally, the lift coefficient and drag coefficient are calculated from C_N and C_C by force resolution as

$$C_L = C_N\cos\left(\alpha\right) + C_C\sin\left(\alpha\right) \tag{15}$$

$$C_D = C_N\sin\left(\alpha\right) - C_C\cos\left(\alpha\right) + C_{d0} \tag{16}$$

where C_{d0} is the minimum drag coefficient corresponding to the zero angle of attack.

The integration of the Beddoes-Leishman dynamic stall model into the AC model in the time domain is shown in the flow chart in Figure 1. At each time step, the calculated relative velocity and the angle of attack are inputs into the Beddoes-Leishman dynamic stall model. By including the dynamic stall effect the normal force coefficient and the chordwise force coefficient are corrected and the lift coefficient and drag coefficient are thus obtained.

2.5 Dynamic inflow model

The induced velocities calculated using the AC method are based on a steady state equilibrium without time. However, the mass flow through the rotor is substantial. In order to account for the time delay before the induced velocities are in equilibrium with the aerodynamic loads, a dynamic flow model should be applied.

Currently there is none sophisticated dynamic flow models for VAWTs. The dynamic flow model proposed by Larsen and Madsen (2013) is employed here. The dynamic inflow is modeled using a low pass filtering of the calculated steady state induced velocities, which is in a similar way as for a horizontal axis wind turbine. Here two first-order filters are coupled in parallel with weighted functions to model the near wake and far wake effects respectively. Assuming that the induced velocity in a previous step is denoted y_{n-1}, and the raw signal of induced

velocity in the current step is denoted q, then the filtered induced velocities due to the near wake and far wake can be written as

$$y_{nw} = y_{n-1} \exp\left(-\frac{\Delta T}{\tau_{nw}}\right) + q\left(1 - \exp\left(-\frac{\Delta T}{\tau_{nw}}\right)\right) \tag{17}$$

$$y_{fw} = y_{n-1} \exp\left(-\frac{\Delta T}{\tau_{fw}}\right) + q\left(1 - \exp\left(-\frac{\Delta T}{\tau_{fw}}\right)\right) \tag{18}$$

where ΔT is the constant time step. τ_{nw} and τ_{fw} are time constants for the near wake filter and far wake filter, respectively. The time constant is non-dimensionalized with respect to the rotor radius and the average wake velocity $\tau = \tau^* \frac{R}{V_{wake}}$, in which the non-dimensional time constant τ^* is set to be approximately 0.5 and 2 for the near wake filter and far wake filter, respectively. Applying a weighed factor of 0.6 for the near wake filter and 0.4 for the far wake filter, the final filtered induced velocity is given as

$$y_n = 0.6 y_{nw} + 0.4 y_{fw} \tag{19}$$

3 Development of a fully coupled simulation tool

The developed AC model is then coupled with SIMO-RIFLEX to achieve a fully coupled simulation tool for evaluating the performance of floating VAWT systems. The codes SIMO(MARINTEK, 2012b) and RIFLEX(MARINTEK, 2012a) were developed by MARINTEK and widely used in the offshore oil and gas industry. The SIMO-RIFLEX wind turbine module has previously been verified (Luxcey et al., 2011; Ormberg et al., 2011). The code SIMO-RIFLEX-AC can account for the turbulent wind inflow, aerodynamics, hydrodynamics, structural dynamics and control dynamics. This coupled code, as illustrated in Figure 3, integrates three computer codes. SIMO computes the rigid body hydrodynamic forces and moments on the hull (MARINTEK, 2012b) ; RIFLEX serves as a nonlinear finite element solver and provides the links to an external controller and the code AC (MARINTEK, 2012a); AC calculates the aerodynamic loads on the blades. The external controller, which is written in Java, is used to regulate the rotor rotational speed for VAWTs with fixed blade pitch. This combination provides a comprehensive aero-hydro-servo-elastic simulation tool with well-known aerodynamics, sophisticated hydrodynamics, a stable nonlinear finite element solver, and user-defined control logic.

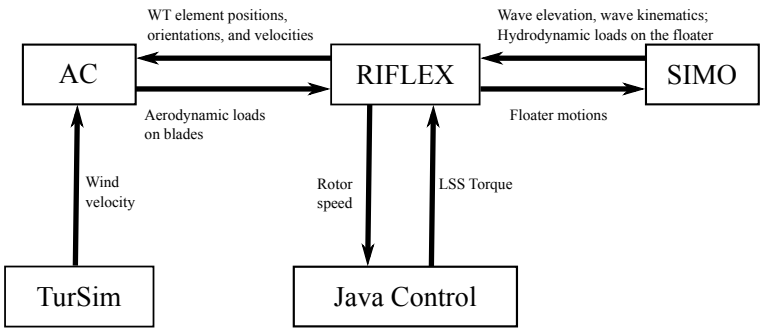

Figure 3: Overview of the fully coupled simulation tool SIMO-RIFLEX-AC

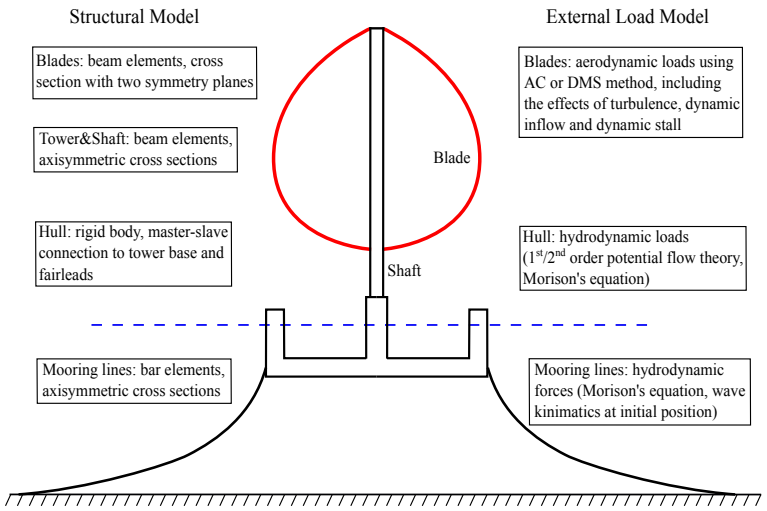

Figure 4: The structural model and external force model of a floating VAWT.

A floating VAWT system is usually comprised of a rotor harvesting wind energy, a floater supporting the rotor and a mooring system keeping the floater in position. Figure 4 shows the structural model and external load model of a floating VAWT system in the coupled code SIMO-RIFLEX-AC. The blades, shaft, tower and mooring lines are modeled using the nonlinear flexible finite elements while the floating platform is considered as a rigid body. The dynamics of the floating platform is represented using the equation of motion proposed by Cummins (1962)

$$(\mathbf{M}+\mathbf{A}_\infty)\ddot{\mathbf{x}}(t)+\int_{-\infty}^{\infty}\kappa(t-\tau)\,\dot{\mathbf{x}}(t)\,d\tau+(\mathbf{K_m}(\mathbf{x},t)+\mathbf{K_h})\,\mathbf{x}(t)=\mathbf{F_{exc}}(\mathbf{x},\dot{\mathbf{x}},t) \tag{20}$$

where $\mathbf{M}$ is the mass matrix of the floating system, $\mathbf{A}_\infty$ is the added mass matrix at infinite frequencies, $\mathbf{x}$, $\dot{\mathbf{x}}$ and $\ddot{\mathbf{x}}$ are the displacement, velocity and acceleration of the platform, respectively. $\kappa(t-\tau)$ is the retardation function which represents the fluid memory effect. $\mathbf{K_h}$ is the hydrostatic restoring matrix and $\mathbf{K_m}$ is the nonlinear restoring matrix from the mooring system. $\mathbf{F_{exc}}$ is the excitation forces which includes the Froude-Krylov force $\mathbf{F^{FK}}$, diffraction force $\mathbf{F^D}$, aerodynamic force $\mathbf{F^{Aero}}$ and viscous force $\mathbf{F^{Drag}}$.

$$\mathbf{F_{exc}}(\mathbf{x},\dot{\mathbf{x}},t)=\mathbf{F^{FK}}(t)+\mathbf{F^D}(t)+\mathbf{F^{Aero}}(\mathbf{x},\dot{\mathbf{x}},t)+\mathbf{F^{Drag}}(\dot{\mathbf{x}},t) \tag{21}$$

The aerodynamic force $\mathbf{F^{Aero}}$ is computed in the AC model and transfered from the rotor to the generator. While the hydrodynamic loads involved in Eqs. 20 and 21 are calculated in SIMO (MARINTEK, 2012b). At each time step, the dynamic equilibrium equations of the rotor, platform and mooring lines are solved in RIFLEX and the rotor rotational speed is regulated through the external controller. Then the platform motions are transfered to SIMO to update the hydrodynamic loads, while the positions, velocities and accelerations of the blade elements are transfered to the AC model to update the aerodynamic loads.

3.1 Aerodynamic model

The aerodynamic model, i.e. AC, has been comprehensively described above. It accounts for the effects of variation in the Reynolds number, wind shear and turbulence, dynamic stall and dynamic inflow. The induced velocity is computed based on the AC method. The Beddoes-Leishman dynamic stall model is implemented to predict the aerodynamic loads more accurately.

3.2 Hydrodynamic model

The hydrodynamic loads are computed using a combination of the potential flow theory and Morison's equation. The hydrostatic restoring coefficients are computed on the basis of the mean position of the structure. For large volume structures, the first-order potential flow theory gives the wave excitation force by solving a diffraction problem and provides the added mass and potential damping by solving a radiation problem. The added mass, radiation damping are then applied in the time domain using the convolution technique (Faltinsen, 1995).

When the second-order wave force becomes important for structures with natural frequencies that either very low or near twice the wave frequency, the second-order potential flow theory is applied to account for the mean drift, difference-frequency and sum-frequency wave forces. If applicable, the Newman approximation, which is based on the solution of the first-order potential flow theory, can be adopted to represent the difference-frequency wave force. Otherwise, the quadratic transfer function (QTF) should be used for the difference-frequency and sum-frequency wave forces. Moreover, the third-order wave force can also be included if, for instance, the effect of ringing response is relevant.

Regarding the slender structures where the diameter D is small compared to the wavelength λ (roughly, $\frac{D}{\lambda} < \frac{1}{5}$), the Morison equation is applied to calculate the inertial load and viscous drag load (Faltinsen, 1995). The transverse hydrodynamic force per unit length is given by

$$dF = \rho_w \pi \frac{D^2}{4} \dot{u_w} + \rho_w \pi C_a \frac{D^2}{4} (\dot{u_w} - \dot{u_b}) + \frac{1}{2} \rho_w C_d D (u_w - u_b) |u_w - u_b| \tag{22}$$

where ρ_w is the water density, u_w is the transverse wave particle velocity, u_b is the local transverse body velocity, and C_a and C_d are the added mass and quadratic drag coefficients, respectively. In addition, viscous forces on large volume structures can also be incorporated through the Morison's equation by considering only the quadratic viscous drag term in Eq. 22.

3.3 Structural model

In the structural model, the blades are modeled as flexible beam elements with two symmetric planes to differ the flapwise stiffness and edgewise stiffness. The tower and shaft are modeled as axisymmetric beam elements while the mooring lines are considered as nonlinear bar element. A very short tower close to the tower base is used to connect the rotating shaft and floater through a flexible joint. The electric torque from the generator is applied at this joint to regulate the rotational speed according to the prescribed control strategy. Moreover, master-slave connections are applied to integrate the motions between the tower base and fairleads.

Therefore, the dynamic equilibrium of the whole floating VAWT system can be expressed as the following

equation by assuming a linear elastic material,

$$\mathbf{M_g}\ddot{\mathbf{r}} + \mathbf{B_g}\dot{\mathbf{r}} + \mathbf{K_g}\mathbf{r} = \mathbf{R^E}(\mathbf{r}, \dot{\mathbf{r}}, t) \tag{23}$$

where $\mathbf{M_g}$, $\mathbf{B_g}$ and $\mathbf{K_g}$ are the global mass, damping and stiffness matrices, respectively. r, $\dot{r}$ and $\ddot{r}$ are the system displacement, velocity and acceleration vectors, respectively. The structural damping here is specified using the Rayleigh damping, which is a linear combination of the mass $\mathbf{M_g}$, and stiffness $\mathbf{K_g}$ matrices as in the following equation.

$$\mathbf{B_g} = \alpha_1 \mathbf{M_g} + \alpha_2 \mathbf{K_g} \tag{24}$$

In which α_1 and α_2 are the mass and stiffness proportional coefficients, respectively. In RIFLEX, the dynamic equilibrium equations can be solved in the time domain using the Newmark-β numerical integration ($\beta = 0.256$, $\gamma = 0.505$).

3.4 Control strategy

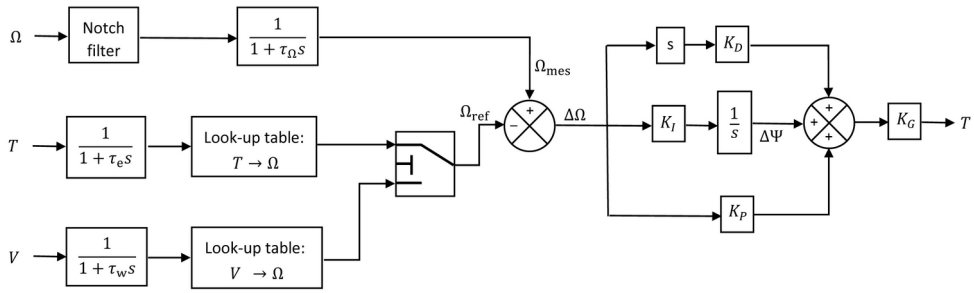

Figure 5: The generator torque control algorithm for a floating VAWT based on a PID architecture.

In the previous study, two control strategies were used to enable the variable-speed and fixed-pitch operations of a floating VAWT system (Cheng et al., 2015b). The architecture of the generator torque controller is shown in Figure 5. The generator rotational speed and electric torque are measured and low-pass filtered. The controller aims to minimize the error between the measured and filtered rotational speed Ω_{mes} and the reference rotational speed Ω_{ref},

$$\Delta\Omega = \Omega_{mes} - \Omega_{ref} \tag{25}$$

in which the reference rotational speed Ω_{ref} is defined as a function of the measured wind speed $\widehat{V}$ and the measured and low-pass filtered electric torque $\widehat{T}$. The rotational speed error $\Delta\Omega$ is then fed through the proportional, integral and derivative paths to obtain an updated value of the required electric torque, as follows,

$$T(t) = K_G\left(K_P\Delta\Omega(t) + K_I\int_0^t \Delta\Omega(\tau)d\tau + K_D\frac{d}{dt}\Delta\Omega(t)\right) \tag{26}$$

in which K_G is the generator stiffness, and K_P, K_I and K_D are the proportional, integral and derivative gains, respectively.

Figure 6 presents the relationship between the reference rotational speed and the wind speed for a typical floating VAWT. According to the operating conditions, it can be divided into three regions, as highlighted in Figure 6. In region I where wind speeds ranges from V_{in} to V_{Ω_N}, the rotor operates at the optimal tip speed ratio so as to achieve the highest power coefficient. In region II, the rotor operates at a moderate tip speed ratio and holds the rotational speed constant at the rated rotational speed. The control targets in region I and II aim to maximize the power capture and at the same time keeps the rotational speed not larger than the rated one.

However, the control targets in region III shift to limit the aerodynamic loads acting on the rotor by limiting the rotational speed. In this case, the rotor rotates at relatively low tip speed ratios and two control strategies, i.e. the baseline controller and improved controller, are considered here, as illustrated in Figure 6. This baseline controller is capable of maximizing the power capture for wind speeds below V_{Ω_N} and maintaining the rotational speed for wind speeds above V_{Ω_N}, while the improved controller aims to maximize the power capture for wind speeds below V_N and maintaining the power capture approximately constant for the above rated wind speeds.

In addition, a notch filter is implemented in the controller to isolate the electric torque from the variation of aerodynamic loads. For turbulent wind conditions the wind speed is measured and low-pass filtered.

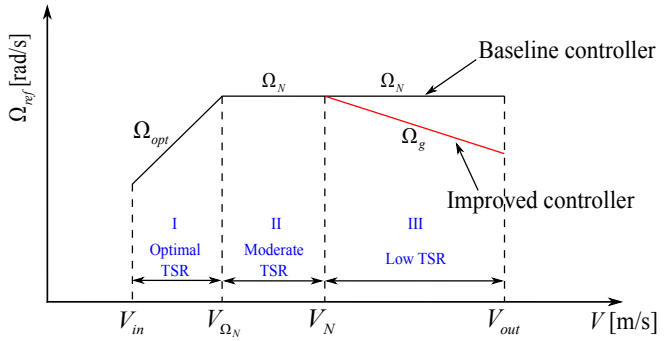

Figure 6: The relationship between the reference rotor rotational speed and the wind speed for the baseline and improved controllers. V_{in}, V_N and $V_{out}$are the cut-in, rated, and cut-out wind speed, respectively; V_{Ω_N} is the wind speed for the rated rotational speed; Ω_N is the rated rotational speed; Ω_{opt} is the optimal rotational speed that can maximize the power capture; Ω_g is the rotational speed that can hold the mean generator power approximately constant.

4 Verification of the fully coupled simulation tool

4.1 Wind turbine models

In this study, two wind turbine models, one landbased VAWT and one floating VAWT as depicted in Figure 7, are used to verify the code SIMO-RIFLEX-AC. The landbased VAWT considered is the 5MW Darrieus rotor developed in the DeepWind project (Vita, 2011). The rotor is comprised of two blades and one rotating tower that spans from the top to the bottom which is connected to the generator. Main specifications of this rotor are summarized in Table 1. The generator considered here is assumed to be placed at the tower base.

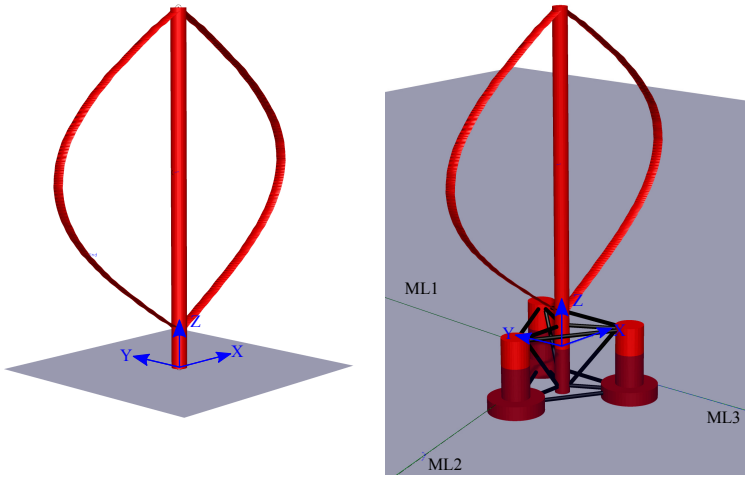

Figure 7: The landbased VAWT and semi VAWT concepts.

Table 1: Specifications of the Darrieus 5 MW wind turbine

Rated power [MW]	5
Rotor radius [m]	63.74
Rotor height, root-to-root [m]	129.56
Chord length [m]	7.45
Airfoil [-]	NACA0018
Cut-in, rated, cut-out wind speed [m/s]	5 , 14 , 25
Rated rotor rotational speed [rpm]	5.26
Total mass, including rotor, shaft and tower [kg]	754,226
Location of overall CM [m]	(0 , 0 , 75.6)

Table 2: Properties of the semi-submersible VAWT system

Water depth [m]	200
Draft [m]	20
Diameter at mean water level [m]	12.0/6.5
Platform mass, including ballast and generator [ton]	13353.7
Center of mass for platform [m]	(0, 0, -13.42)
Buoyancy in undisplaced position [kN]	139816
Center of buoyancy [m]	(0, 0, -13.15)
Surge/Sway natural period [s]	114.0
Heave natural period [s]	17.1
Roll/Pitch natural period [s]	31.0
Yaw natural period [s]	79.7

A floating VAWT concept with a semi-submersible platform supporting the 5MW Darrieus rotor is also used to verify the code SIMO-RIFLEX-AC. This concept is proposed by Wang et al. (2013) and comprehensively studied using the code SIMO-RIFLEX-DMS (Cheng et al., 2015a; Wang, 2015; Wang et al., 2015a). The semi-submersible platform considered was originally designed to support the NREL 5 MW wind turbine (Jonkman et al., 2009) in the water depth of 200 m. Here reasonable modifications are made on the platform to support the 5 MW Darrieus rotor, such as adjusting the ballast of the semi. Details regarding the adjustment can refer to Cheng et al. (2015a). Properties related to the floating VAWT system are given in Table 2. The natural periods of rigid body motions for the floating system were estimated by conducting free decay tests (Cheng et al., 2015a).

The code SIMO-RIFLEX has been widely used and validated in the offshore oil and gas industry. Regarding the present floating wind turbine model, several verifications with respect to the structural dynamics and hydrodynamics have been carried out in the previous studies. Wang et al. (2013) investigated the first 10 natural frequencies and corresponding eigen modes of the landbased VAWT using both RIFLEX and Abaqus. The Lanczos's method is used in these two analyses. It is found that RIFLEX agrees quite well with Abaqus. Cheng et al. (2015a) studied the response amplitude operators (RAOs) of the semi VAWT subjected to wave loads using both the regular wave technique and white noise technique. The white noise technique predicts all RAOs accurately except at the resonant frequency of each mode.

In the following, verification of the code SIMO-RIFLEX-AC is to be conducted by comparison with the codes SIMO-RIFLEX-DMS and HAWC2 using the landbased VAWT and semi VAWT.

4.2 Load cases

A series of load cases were defined to verify the code SIMO-RIFLEX-AC, as given in table 3. LC1 is the steady wind condition and is used to verify the aerodynamic loads calculated using different codes. LC2 and LC3 are the steady wind and irregular wave condition, and the turbulent wind and irregular wave condition, respectively. The wind and wave are correlated and directionally aligned. They were used to verify the dynamic responses of the floating wind turbine system subjected to wind and wave loads.

Table 3: Definition of load cases

	U_W [m/s]	H_S [m]	T_P [s]	T_I [-]	Wave Cond.	Sim. Length [s]
LC1.1	8	-	-	0	-	800
LC1.2	14	-	-	0	-	800
LC1.3	18	-	-	0	-	800
LC2.1	8	2.55	9.86	0	Irreg. wave	3600
LC2.2	14	3.62	10.29	0	Irreg. wave	3600
LC2.3	18	4.44	10.66	0	Irreg. wave	3600
LC3.1	8	2.55	9.86	0.17	Irreg. wave	3600
LC3.2	14	3.62	10.29	0.13	Irreg. wave	3600
LC3.3	18	4.44	10.66	0.12	Irreg. wave	3600

For steady wind conditions, the normal wind profile (NWP) was applied, in which the wind profile $U(z)$ is the average wind speed as a function of height z above mean sea level (MSL), and is given by the following power law

$$U(z) = U_{ref}\left(\frac{z}{z_{ref}}\right)^{\alpha} \tag{27}$$

where U_{ref} is the reference wind speed, z_{ref} is the height of reference wind speed and α is the power law exponent. In this study z_{ref} is set to be 79.78 m, which is the vertical center of blades above MSL. The value of α was chosen to be 0.14 for the floating wind turbines according to IEC 61400-3 (IEC, 2005). For turbulent wind conditions, the TurbSim was used to generate the three dimensional turbulent wind field according to the Kaimal turbulence model for IEC Class C. Regarding the irregular wave conditions, the irregular wave history was generated using the JONSWAP wave model. The significant wave height and peak period were set based on their correlation with wind speed for the Statfjord site in the northern North Sea (Johannessen et al., 2002).

4.3 Verification using the landbased VAWT

The landbased VAWT is firstly used to study the capability of the code SIMO-RIFLEX-AC to calculate the aerodynamic loads accurately. Three fully coupled aero-hydro-servo-elastic codes are considered here, i.e. SIMO-RIFLEX-DMS, SIMO-RIFLEX-AC and HAWC2. The code SIMO-RIFLEX-DMS calculates the aerodynamic loads using the DMS method with the Beddoes-Leishman dynamic stall model. While the HAWC2 computes the aerodynamic loads using the AC method with the Stig Øye dynamic stall model. An overview of the capability of these three codes are demonstrated in table 4.

Table 4: Description of three codes

	SIMO-RIFLEX-DMS	SIMO-RIFLEX-AC	HAWC2
Aerodynamics (aero)	DMS+BL DS	AC+BL DS	AC+Stig Øye DS
Hydrodynamics (hydro)	Airy + PF + ME	Airy + PF + ME	Airy + ME
Structural dynamics (elastic)	FEM	FEM	MB
Control system (servo)	UD DLL	UD DLL	UD DLL

DMS: Double multi-streamtube; AC: Actuator cylinder; DS: Dynamic stall; BL: Beddoes-Leishman; Airy: Airy wave theory; PF: Potential flow; ME: Morison's equation; FEM: Finite element method; MB: Multi-body system; UD DLL: user defined external dynamic link library

LC1 with steady wind is carried out using each code for the landbased VAWT, respectively. LC1.1, LC1.2 and LC1.3 are three representative operational conditions with a wind speed that is below, equal to and above the rated wind speed, respectively. The corresponding typical tip speed ratios are 4.39, 2.51 and 1.95. The adaptation of the Beddoes-Leishman dynamic stall model has been studied for VAWTs by Dyachuk et al. (2014), However, dynamic stall model implemented in HAWC2 is developed for HAWTs and does not seem to work reliably for VAWTs (Verelst et al., 2015), the simulations of the landbased VAWT are thus carried out without considering the effect of dynamic stall. Time histories of the rotor rotational speed, thrust, side force and aerodynamic torque calculated using the three codes are compared, as illustrated in Figure 8 -9.

For the considered two-bladed rotor, the aerodynamic loads vary periodically from approximate zero to double the mean value. These periodic aerodynamic loads cause the periodic variation in the rotor rotational speed. Due to the robust controller implemented, the amplitude of this variation is very small compared to the mean value. It is

thus assumed that the small variation in the rotor rotational speed does not affect the aerodynamic loads, including the thrust and aerodynamic torque.

For load cases with low tip speed ratio such as LC1.2 and LC1.3, these three codes agree well with each other in the thrust and aerodynamic torque. This can be observed in Figure 8, which shows the thrust force, side force and aerodynamic torque computed using these three codes when ignoring the effect of dynamic stall. However, at load cases with relatively high tip speed ratio such as LC1.1, these three codes present notable differences in terms of the thrust force, side force and aerodynamic torque, as shown in Figure 9. When neglecting the effect of dynamic stall, HAWC2 predicts a smaller thrust and aerodynamic torque than the codes SIMO-RIFLEX-AC and SIMO-RIFLEX-DMS. Moreover, the thrusts computed using SIMO-RIFLEX-AC and SIMO-RIFLEX-DMS are very close to each other. In addition, the peak values of the aerodynamic torque predicted using SIMO-RIFLEX-AC and SIMO-RIFLEX-DMS are very close and much larger than that by HAWC2. And HAWC2 predicts a valley value of aerodynamic torque that is much larger than zero.

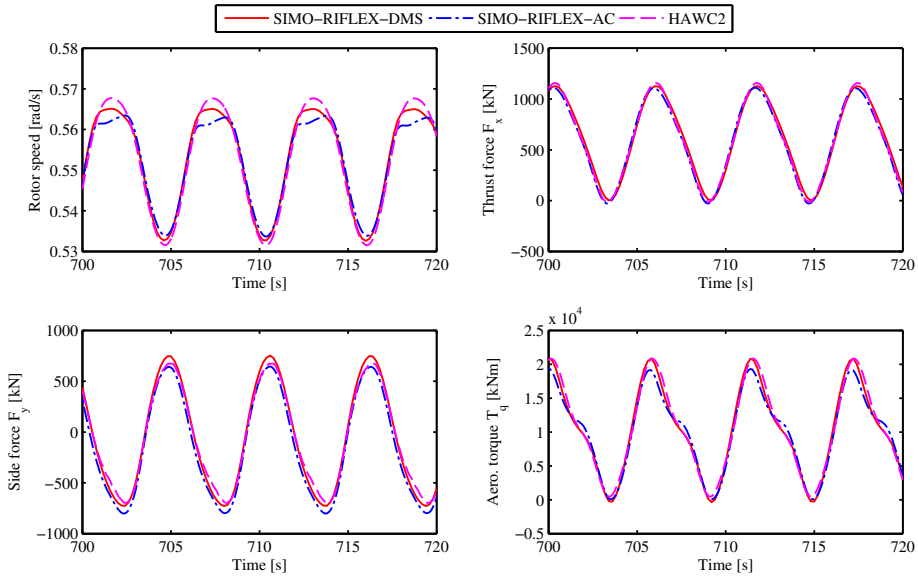

Figure 8: Comparison of the rotational speed, thrust, side force and aerodynamic torque of the landbased VAWT using three codes without considering the effect of dynamic stall in LC1.2 .

In order to reveal the essential reasons that result in the different resultant aerodynamic loads, the normal load and tangential load acting on the blade element are studied, as shown in Figure 10 and 11. Figure 10 shows the time history of blade normal and tangential loads at the midpont of the blade simulated using the codes SIMO-RIFLEX-AC and HAWC2. it's obvious that the negative normal loads differ notably. The possible reason for this deviation is that the code SIMO-RIFLEX-AC accounts for the tangential term when calculating the induced velocity, while HAWC2 ignores it. It has been shown in Cheng et al. (2016) that including the tangential term when calculating the induced velocity can modify the behavior of normal loads in the downwind part as depicted in Figure 10, which corresponds to negative normal loads.

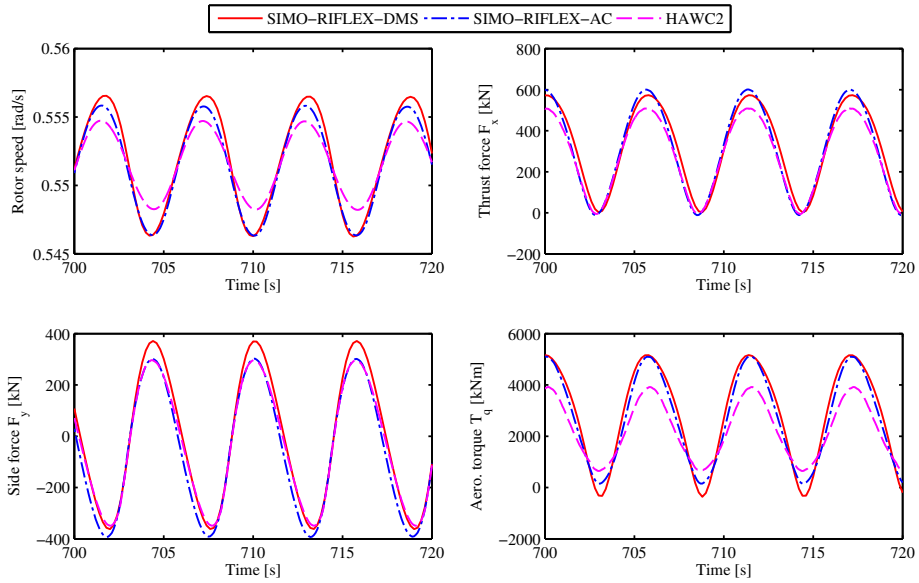

Figure 9: Comparison of the rotational speed, thrust, side force and aerodynamic torque of the landbased VAWT using three codes without considering the effect of dynamic stall in LC1.1.

In Figure 11, the distribution of the normal and tangential loads along the blade are demonstrated when the rotor encounters the largest and smallest aerodynamic torque, which are denoted as peak and valley, respectively. It can be observed that the distribution of the normal and tangential loads along the blade are not smooth, showing a large number of small peaks. This is due to the blade elasticity considered in the present study. The blade deforms when the blade suffers from the aerodynamic loads, consequently the inclination of the elements within the blade is not very continuous and has some peaks, which ultimately results in the small peaks in the distribution of loads along the blades. The codes SIMO-RIFLEX-AC and HAWC2 differs in the normal and, especially, tangential loads. It's the tangential force that mainly contributes to the aerodynamic torque, consequently the aerodynamic torque differs a lot. The distributions of normal and tangential loads are not symmetric because of the wind shear and blade elasticity. Moreover, the part with the position r/S approximately ranging from 0.35 to 0.85 is the main contribution for the tangential load.

4.4 Verification using the semi VAWT

In this section, the semi VAWT is used to verifiy the capability of the code SIMO-RIFLEX-AC. Only the code SIMO-RIFLEX-DMS is considered, since it models the hydrodynamics, structural mechanics and controller dynamics in the same way as the code SIMO-RIFLEX-AC. This verification starts from the steady wind only LCs.

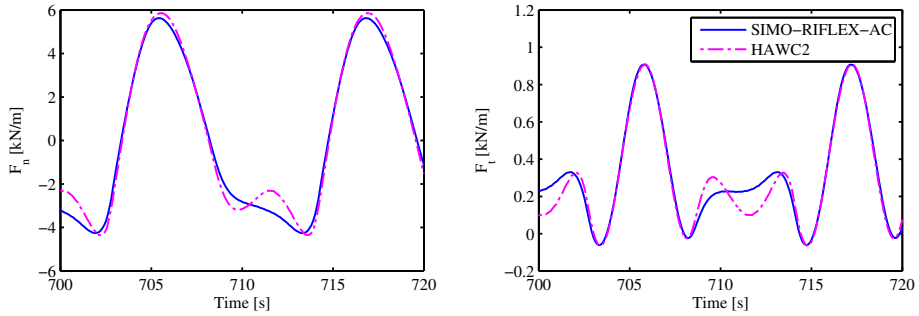

Figure 10: Comparison of simulated blade forces in normal and tangential direction at midpoint of the blade using SIMO-RIFFLEX-AC and HAWC2 in LC1.1, the effect of dynamic stall is not considered.

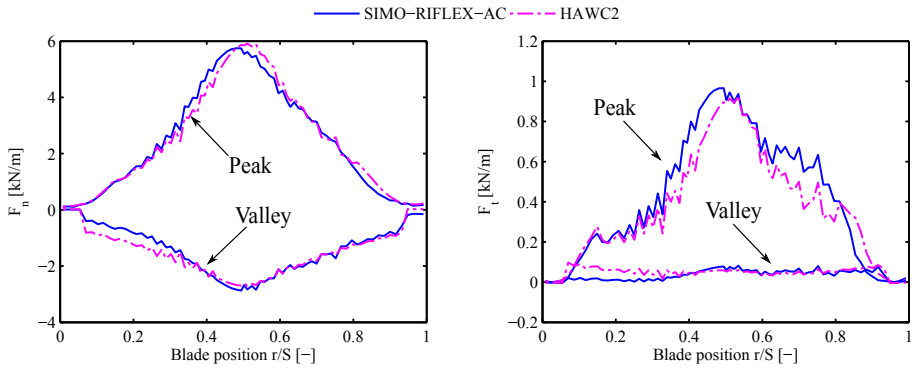

Figure 11: Distribution of the normal and tangential forces along the blade at the peak and valley value of aerodynamic torque using SIMO-RIFFLEX-AC and HAWC2 in LC1.1, the effect of dynamic stall is not considered.

4.4.1 Steady wind cases

LC1 with steady wind is firstly carried out for the semi VAWT using the codes SIMO-RIFLEX-AC and SIMO-RIFLEX-DMS. It aims to investigate the capability of SIMO-RIFLEX-AC to predict the wind-induced responses, including the platform motions, structural responses and wind turbine performance.

Figure 12 shows the mean values and standard deviations of the generator power, thrust, side force and aerodynamic torque acting on the semi VAWT in LC1. The mean values of the thrust predicted using SIMO-RIFLEX-AC are a little smaller than those by SIMO-RIFLEX-DMS. But SIMO-RIFLEX-AC gives a little larger standard deviation of thrust in LC1.1, which corresponds to load cases with high tip speed ratios. SIMO-RIFLEX-AC also predicts a little larger mean aerodynamic torque in LC1.3. Visible difference lies in the mean value of side force, especially in LC1.1 where SIMO-RIFLEX-AC gives a negative side force while SIMO-RIFLEX-DMS predicts almost zero side force. These differences result from three possible reasons: one is that AC method predicts smaller aerodynamic loads than the DMS method; another one is that the DMS method essentially neglects the lateral induction, which has some influence on the side force. The last one is that the code SIMO-RIFLEX-DMS assumes that the rotor always holds upright even though the tower is inclined due to the roll or pitch motions of the platform, since Wang et al. (2015b) stated that the effect of tower tilt on the aerodynamic coefficients of the rotor studied is considered negligible up to a tilt angle of 10°. In addition, the code SIMO-RIFLEX-DMS does not account for the effect of dynamic inflow.

In LC1, the platform motions are wind-induced and present similar trends as the aerodynamic loads, as illustrated in Figure 13. The code SIMO-RIFLEX-AC predicts smaller mean values in surge, heave, pitch and yaw motions than the code SIMO-RIFLEX-DMS. However, the sway and roll motions show notable differences since these two codes predict significant different mean values in the side force. Similar trends are also find in the structural responses, such as the tower base fore-aft bending moment M_{FA} and side-side bending moment M_{SS}. The code SIMO-RIFLEX-AC gives a little smaller values in the mean value and standard deviation of M_{FA}, and the standard deviation of M_{SS}. In addition, the mean value of M_{SS} is significantly different.

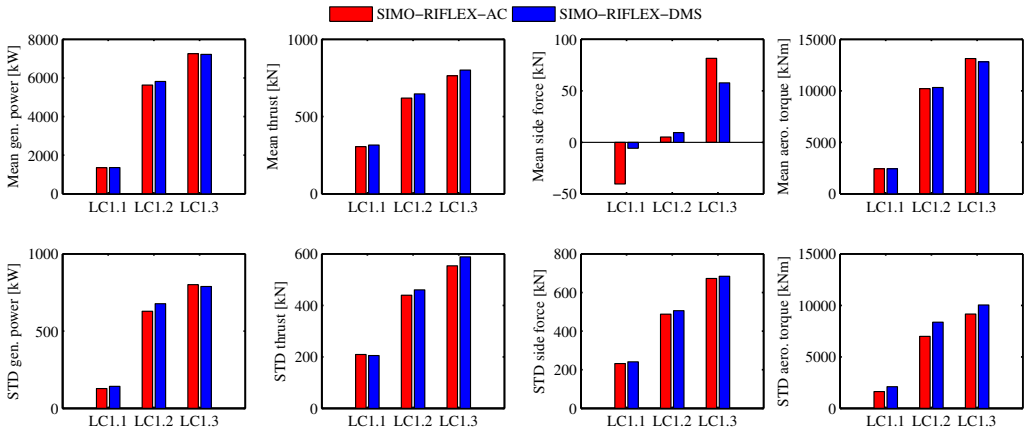

Figure 12: Mean values and standard deviations of the generator power, aerodynamic thrust, side force and torque acting on the semi VAWT in LC1.

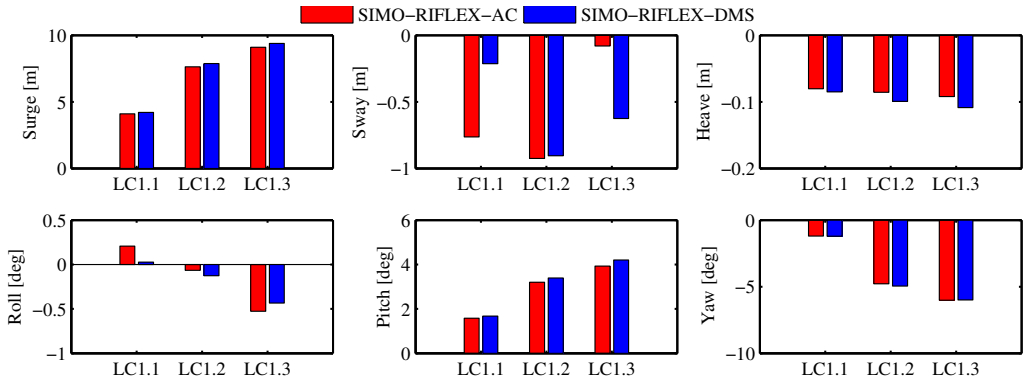

Figure 13: Mean values of platform motions of the semi VAWT in LC1 .

4.4.2 Combined wind and wave cases

The combined wind and wave cases, i.e. the LC2 and LC3, are then used to verify the capability of the code SIMO-RIFLEX-AC to capture the stochastic variations of the dynamic responses. Identical wind and wave time series are used for the codes SIMO-RIFLEX-DMS and SIMO-RIFLEX-AC.

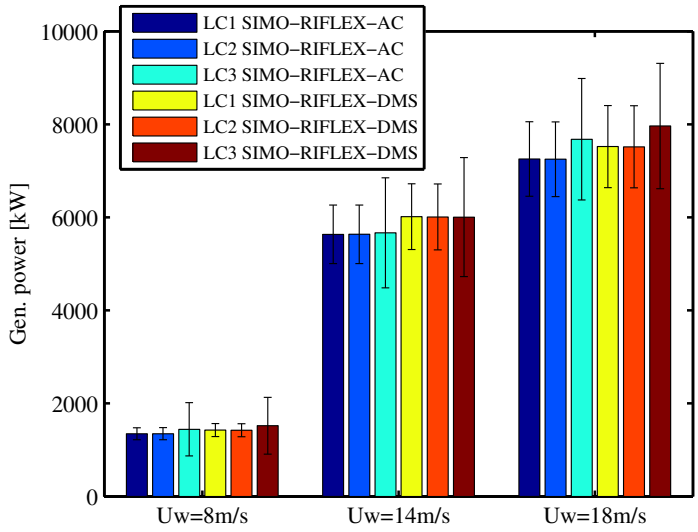

Figure 14: Mean value and standard deviation of the generator power for the semi VAWT in LC1, LC2 and LC3. The error bar indicates the standard deviation from the mean value.

Figure 14 compares the mean values of the generator power for the semi VAWT in LC1, LC2 and LC3 with the error bar indicating the standard deviation. It can be found that at a certain mean wind speed, LC1 and LC2 gives very close mean value and standard deviation in the generator power for both codes, which implies that wave loads have slight influence on the generator power. Moreover, in LC3 the mean value and standard deviation of the

generator power all increase to some extent than the steady wind cases LC1 and LC2. In addition, the code SIMO-RIFLEX-AC predicts smaller mean values of the generator power than the code SIMO-RIFLEX-DMS while the standard deviation estimated by these two codes are very close.

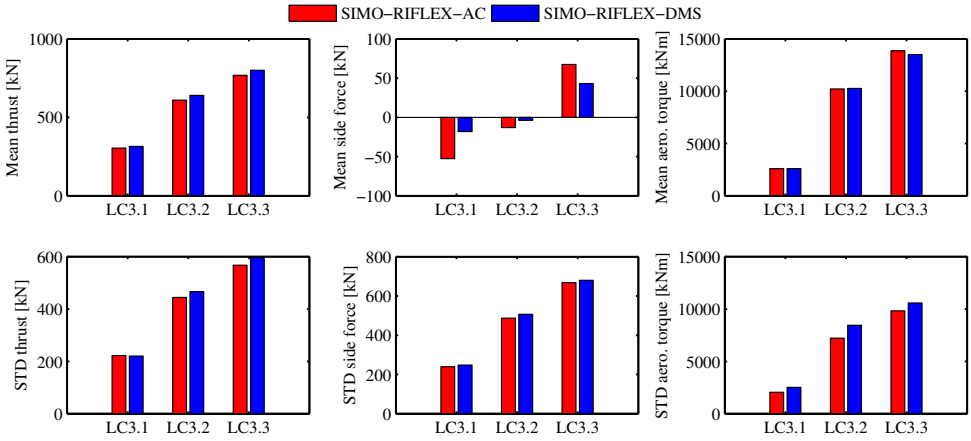

Figure 15: Mean value and standard deviation of the aerodynamic thrust, side force and torque for the semi VAWT in LC3

In Figure 15, the mean value and standard deviation of the aerodynamic thrust, side force and torque are shown for the semi VAWT in LC3 with turbulent wind and irregular waves. The trends observed in Figure 15 are quite similar as those in Figure 12. Due to the wind turbulence, there is a shift in the mean value of the side force compared with the steady wind only cases.

Rigid body motions of the semi VAWT are also of concern. The mean values and standard deviations of the platform motions are shown in Figure 16. The mean values of the platform motions are quite close to the mean values in the steady wind only conditions, since the mean value of these platform motions are highly dependent on wind loads.

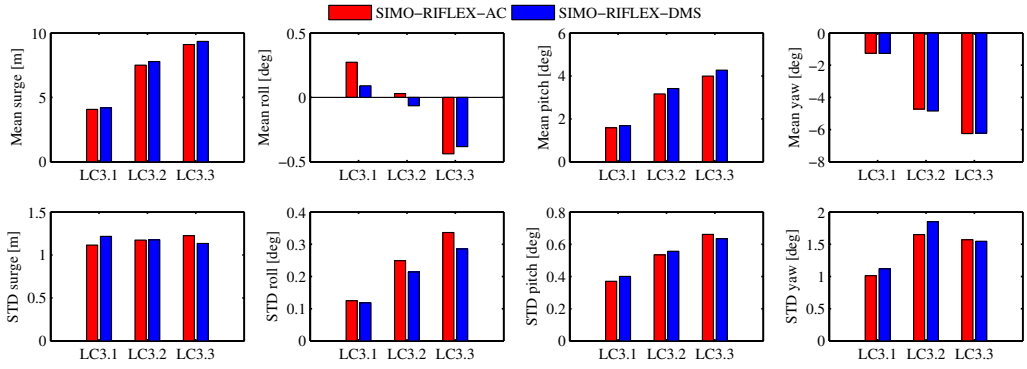

Figure 16: Mean value and standard deviation of the surge, roll, pitch and yaw motions of the semi VAWT in LC3

Though the standard deviation of the thrust given by the code SIMO-RIFLEX-AC is smaller than those given

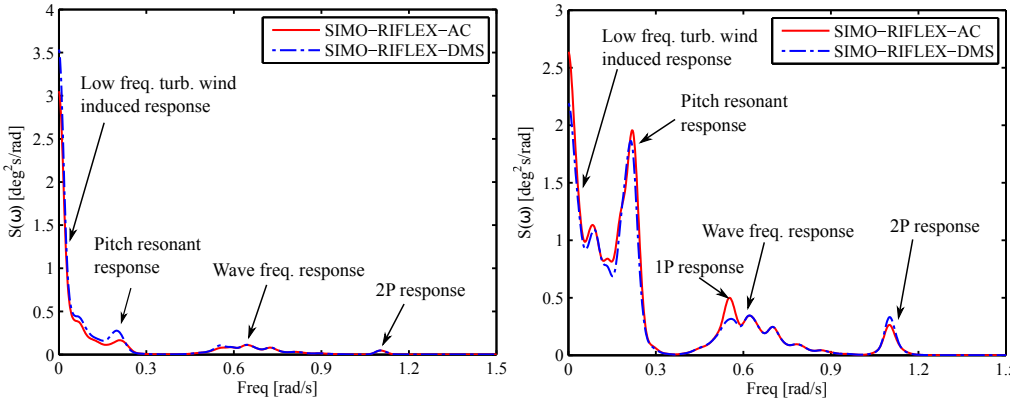

(a) LC3.1: U_W = 8 m/s, H_S = 2.55 m, T_P = 9.86 s (b) LC3.3: U_W = 18 m/s, H_S = 4.44 m, T_P = 10.66 s

Figure 17: Power spectra of the pitch motion of the semi VAWT in (a) LC3.1 and (b) LC3.3

by the code SIMO-RIFLEX-DMS, the code SIMO-RIFLEX-AC gives a smaller standard deviation of surge and pitch motions in LC3.1 and LC3.2, but predicts a little larger in LC3.3. This is due to the fact that the code SIMO-RIFLEX-DMS omits the effect of tower tilt when calculating the aerodynamic loads. However, as the wind speed increases, the effect of tower tilt on aerodynamic loads as well as platform motions becomes more important. This can also be observed using the power spectrum analysis, as the power spectra of pitch motions demonstrated in Figure 17. The wave frequency response predicted by these two codes agrees very well. Visible differences are found in the low frequency region, which is mainly induced by the low frequency turbulent wind. When the wind speed is relatively small, the effect of tower tilt on platform motion is very small, the low frequency response given by the code SIMO-RIFLEX-DMS is larger due to the larger aerodynamic loads predicted by the DMS method, as shown in Figure 17(a). However, as the wind speed becomes larger, which causes the larger platform pitch motion, the effect of tower tilt becomes more significant and gives larger low frequency response.

Moreover, the code SIMO-RIFLEX-AC predicts larger standard deviation of roll motion in LC3 than the code SIMO-RIFLEX-DMS. Power spectral analysis of roll in LC3.2, as illustrated in Figure 18, reveals that the code SIMO-RIFLEX-DMS contributes a little bigger 2P response, whereas the low frequency turbulent wind induced response is much smaller than that given by the code SIMO-RIFLEX-AC. A small 1P response is captured by both codes as well. With respect to the yaw motion, the responses are dominated by the yaw resonant response and low frequency turbulent wind induced response. In LC3.1 and LC3.2, the yaw resonant responses given by the code SIMO-RIFLEX-DMS are much larger than those by the code SIMO-RIFLEX-AC, the corresponding standard deviations of yaw motion are thus also bigger. However, in LC3.3 the code SIMO-RIFLEX-AC gives a little larger standard deviation of yaw motion, power spectral analysis shows that in LC3.3 the yaw resonant response predicted by the two codes are comparable while the code SIMO-RIFLEX-AC gives a little larger low frequency turbulent wind induced yaw motion.

For floating wind turbines, the tower base bending moment is caused by the large aerodynamic force acting on the rotor and by the weight of the rotor due to the tower tilt. The codes SIMO-RIFLEX-AC and SIMO-RIFLEX-

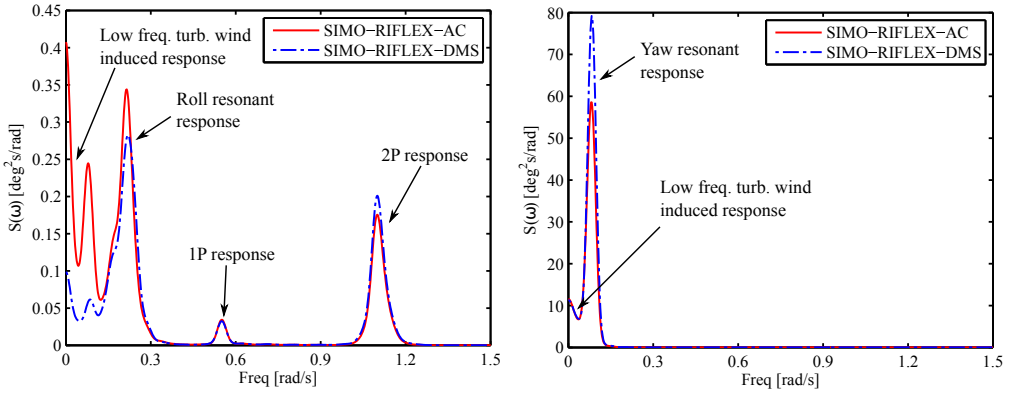

(a) Roll in LC3.2: U_W = 14 m/s, H_S = 3.62 m, T_P = 10.29 s (b) Yaw in LC3.2: U_W = 14 m/s, H_S = 3.62 m, T_P = 10.29 s

Figure 18: Power spectra of the roll and yaw motions of the semi VAWT in LC3.2. (a) roll motion, (b) yaw motion.

DMS predict different aerodynamic loads and tower tilt angle, consequently the tower base bending moments are different. Figure 19 gives the mean value and standard deviation of the tower base fore-aft bending moment M_{FA} and side-side bending moment M_{SS}. The code SIMO-RIFLEX-AC gives a little smaller values than the code SIMO-RIFLEX-DMS in the mean value and standard deviation of M_{FA}. The percentage difference of the mean value of the M_{FA} between the codes SIMO-RIFLEX-AC and SIMO-RIFLEX-DMS is 6.5%, 8.0% and 6.9% for the LC3.1, LC3.2 and LC3.3, respectively. Regarding the M_{SS}, the mean value of M_{SS} is significantly different. Moreover, the percentage difference of the standard deviation of the M_{SS} between the codes SIMO-RIFLEX-AC and SIMO-RIFLEX-DMS is 6.7%, 7.8% and 6.4%, respectively. This also implies that the code SIMO-RIFLEX-DMS can over estimate the fatigue damage.

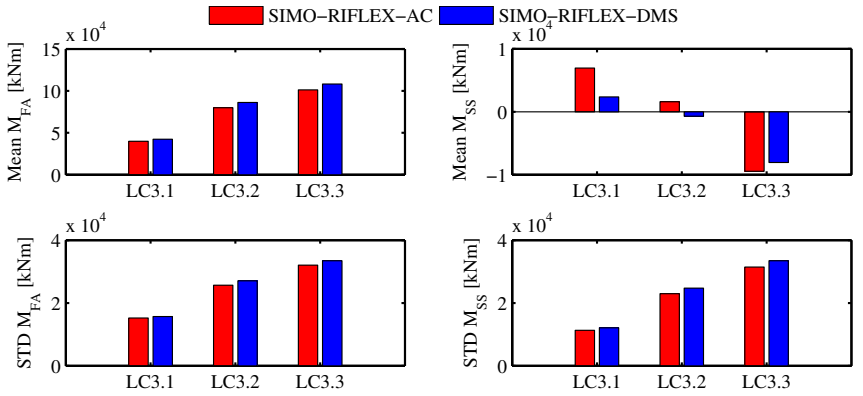

Figure 19: Mean values and standard deviations of tower base fore-aft bending moment M_{FA} and side-side bending moment M_{SS} of the semi VAWT in LC3

Power spectrum analyses of the M_{FA} and M_{SS} are also performed, as depicted in Figure 20. It can be observed that the wave frequency response computed using these two codes matches very well with each other. Visible

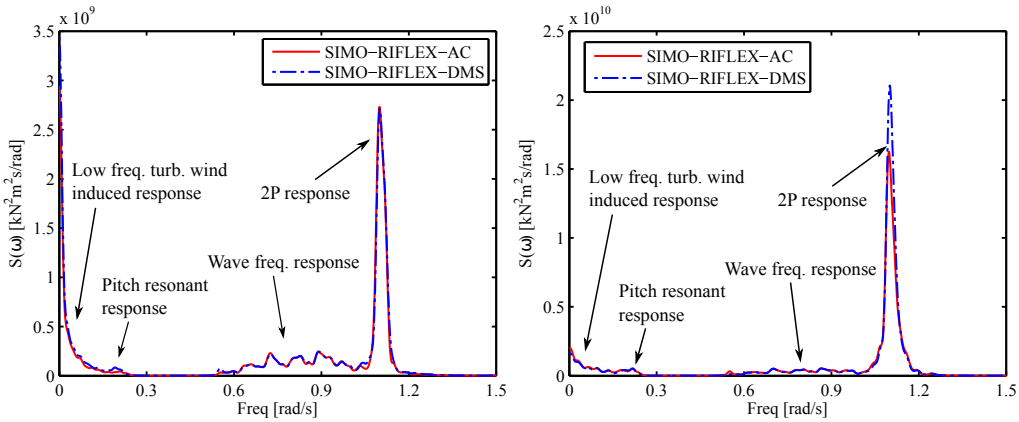

(a) LC3.1: U_W = 8 m/s, H_S = 2.55 m, T_P = 9.86 s (b) LC3.3: U_W = 18 m/s, H_S = 4.44 m, T_P = 10.66 s

Figure 20: Power spectra of tower base fore-aft bending moment for the semi VAWT in (a) LC3.1 and (b) LC3.3

differences result from the low frequency turbulent wind induced response and, especially, the 2P response. The responses of M_{FA} are mainly dominated by the wind loads and the contribution of 2P response increases dramatically as the mean wind speed increases. In LC3.1, the code SIMO-RIFLEX-AC gives a little larger peak in the 2P response, but also a much smaller low frequency turbulent wind induced response, as shown in Figure 20(a). As a result, the standard deviation of the M_{FA} predicted by the code SIMO-RIFLEX-AC is smaller than that by the code SIMO-RIFLEX-DMS. However, when it comes to LC3.3, the 2P response predicted by the code SIMO-RIFLEX-DMS is otherwise much larger. With respect to the responses of the M_{SS}, the 2P response is extremely dominating and the code SIMO-RIFLEX-DMS alway overestimates the standard deviation of the M_{SS}.

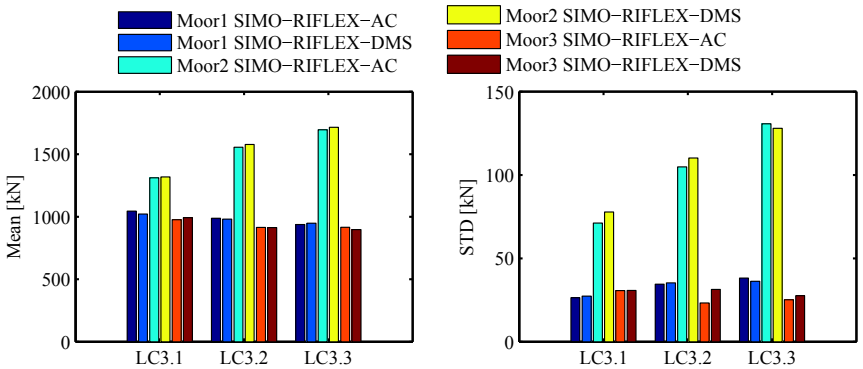

Figure 21: Mean values and standard deviations of tension in mooring lines for the semi VAWT in LC3

Three catenary mooring lines are used to keep the platform in position, as depicted in Figure 7. Among them the mooring line 2 is deployed with direction aligned with the incoming wind. Therefore the mooring line 2 carries the largest tension with respect to both the mean value and the standard deviation, as shown in Figure 21. Due to the yaw motion, the tension in the mooring line 1 is also larger than that in the mooring line 3. Considering the

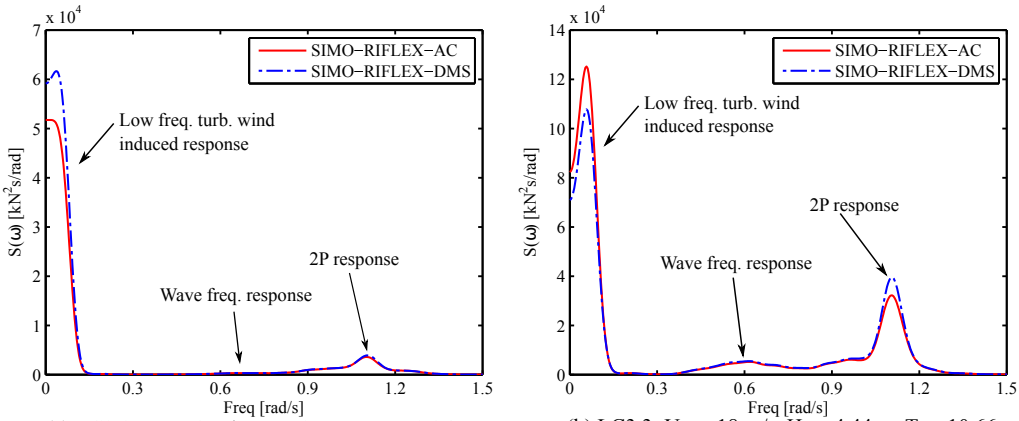

(a) LC3.1: U_W = 8 m/s, H_S = 2.55 m, T_P = 9.86 s (b) LC3.3: U_W = 18 m/s, H_S = 4.44 m, T_P = 10.66 s

Figure 22: Power spectra of tension in mooring line 2 for the semi VAWT in (a) LC3.1 and (b) LC3.3

mooring line 2, the code SIMO-RIFLEX-AC predicts a smaller mean value of tension in LC3. Moreover, it also gives smaller standard deviations in LC3.1 and LC3.2, however in LC3.3 the code SIMO-RIFLEX-AC predicts a little larger standard deviation of tension in mooring line 2. Power spectral analysis of the tension shows that the wave frequency response matches very well for these two code, but the total response is dominated by the low frequency turbulent wind induced response and the 2P response, which are both related to the aerodynamic loads. In LC3.1 and LC3.2, the code SIMO-RIFLEX-AC gives smaller low frequency response, whereas it predicts relatively larger low frequency response in LC3.3.

5 Conclusions

This paper deals with the development and verification of a fully coupled method for modeling and dynamic analysis of floating vertical axis wind turbines. Based on the AC flow model, an aerodynamic code, i.e. AC, is developed and then coupled with the code SIMO-RIFLEX to achieve a fully integrated simulation tool to evaluate the performance of floating VAWT systems. The code SIMO-RIFLEX-AC can account for the turbulent wind inflow, aerodynamics, hydrodynamics, structural dynamics and control dynamics.

Details regarding the induction calculation in the AC model is firstly described in this paper. When calculating the linear induced velocities, contributions from not only the normal load but also the tangential load are taken into account. A new modified linear solution is proposed to better correct the linear solution. Using the AC method, aerodynamic modeling of floating VAWTs is established with consideration of the effects of wind shear, turbulence and dynamic inflow. The Beddoes-Leishman dynamic stall model is also implemented to account for the unsteady aerodynamic effect.

The developed aerodynamic code is then coupled with SIMO-RIFLEX to achieve a fully coupled aero-hydro-servo-elastic simulation tool, i.e. SIMO-RIFLEX-AC. It calculates the 1st and 2nd order hydrodynamic loads using potential flow theory and viscous force using the Morison's equation. The blades, tower, shaft and mooring

lines are modeled using flexible finite element and solved using the Newmark-β method. Also implemented is a controller that can enable variable-speed fixed-pitch operation.

Finally the developed code SIMO-RIFLEX-AC is verified by a series of code-to-code comparisons. Both a landbased VAWT and a semi VAWT are considered. Using the landbased VAWT, the code SIMO-RIFLEX-AC is verified by comparison with the codes SIMO-RIFLEX-DMS and HAWC2. It shows that the code SIMO-RIFLEX-DMS overestimates the side force and aerodynamic torque, especially at load cases with relatively high tip speed ratio. At load cases with low tip speed ratio, these three codes agree well with each other. Considering the semi VAWT, the code SIMO-RIFLEX-AC is verified with the code SIMO-RIFLEX-DMS. Comparative study reveals that these two code give relatively close dynamic responses. Moreover, because of neglecting the effect of tower tilt and the essential characteristics of the DMS method, the code SIMO-RIFLEX-DMS over-predicts the surge, heave and pitch motions, the tower base fore-aft bending moment and the tension in mooring line 2. At load cases with high tip speed ratio, it also overpredicts the aerodynamic torque, the generator power, as well as the yaw motion. In addition, the code SIMO-RIFLEX-DMS can also overestimate the fatigue damage at the tower base.

Acknowledgment

The authors would like to acknowledge the financial support from the EU FP7 project MARE WINT (project NO. 309395) through the Centre for Ships and Ocean Structures (CeSOS) and Centre for Autonomous Marine Operations and Systems (AMOS) at the Department of Marine Technology, Norwegian University of Science and Technology (NTNU), Trondheim, Norway. The first author would like to thank the Department of Wind Energy for kindly hosting me and valuable discussions with senior scientist Torben J. Larsen at the Technical University of Denmark, Roskilde, Denmark. The first author would also appreciate the kindly help on the coupling between the codes RIFLEX and AC from Dr. Erin Bachynski at MARINTEK and Dr. Kai Wang at Aker Solutions.

References

M. Borg, A. Shires, and M. Collu. Offshore floating vertical axis wind turbines, dynamics modelling state of the art. part i: Aerodynamics. *Renewable and Sustainable Energy Reviews*, 2014. doi: 10.1016/j.rser.2014.07.096.

Z. Cheng, K. Wang, Z. Gao, and T. Moan. Dynamic response analysis of three floating wind turbine concepts with a two-bladed darrieus rotor. *Journal of Ocean and Wind Energy*, 2:213–222, 2015a. doi: 10.17736/jowe.2015.jcr33.

Z. Cheng, K. Wang, Z. Gao, and T. Moan. A comparative study on dynamic responses of spar-type floating horizontal and vertical axis wind turbines. *Submitted for journal publication*, 2015b.

Z. Cheng, H. A. Madsen, Z. Gao, and T. Moan. Aerodynamic modeling of offshore vertical axis wind turbines using the actuator cylinder method. *Energy Procedia (submitted)*, 2016.

M. Collu, M. Borg, A. Shires, and F. P. Brennan. Flovawt: progress on the development of a coupled model of dynamics for floating offshore vertical axis wind turbines. In *Proceedings of the ASME 2013 32nd International Conference on Ocean, Offshore and Arctic Engineering*, 2013.

W. E. Cummins. The impulse response function and ship motions. Institut fur schiffbau, universitat hamburg, hamburg, 1962.

E. Dyachuk, A. Goude, and H. Bernhoff. Dynamic stall modeling for the conditions of vertical axis wind turbines. *AIAA Journal*, 52(1):72–81, 2014. doi: 10.2514/1.j052633.

O. M. Faltinsen. *Sea loads on ships and offshore structures*. Cambridge University Press, Cambridge, UK, 1995.

C. S. Ferreira, H. A. Madsen, M. Barone, B. Roscher, P. Deglaire, and I. Arduin. Comparison of aerodynamic models for vertical axis wind turbines. *Journal of Physics: Conference Series*, 524(1):012125, 2014.

S. Gupta and J. G. Leishman. Dynamic stall modelling of the s809 aerofoil and comparison with experiments. *Wind Energy*, 9(6):521–547, 2006. doi: 10.1002/we.200.

IEC. International standard 61400-1, wind turbines, part 1: Design requirements, 2005.

K. Johannessen, T. S. Meling, and S. Haver. Joint distribution for wind and waves in the northern north sea. *International Journal of Offshore and Polar Engineering*, 12(1), 2002.

B. J. Jonkman. Turbsim user's guide: Version 1.50., 2009.

J. M. Jonkman, S. Butterfield, W. Musial, and G. Scott. Definition of a 5-mw reference wind turbine for offshore system development. Tech. Rep. NREL/TP-500-38060, NREL, Golden, CO, USA, 2009.

T. J. Larsen and H. A. Madsen. On the way to reliable aeroelastic load simulation on VAWT's. In *Proceedings of EWEA*, 2013.

J. G. Leishman and T. S. Beddoes. A semi-empirical model for dynamic stall. *Journal of the American Helicopter Society*, 34(3):3–17, 1989. doi: 10.4050/JAHS.34.3.

N. Luxcey, H. Ormberg, and E. Passano. Global analysis of a floating wind turbine using an aero-hydro-elastic numerical model: Part 2 benchmark study. In *Proceedings of the 30th International Conference on Ocean, Offshore and Arctic Engineering*, 2011.

H. A. Madsen. *The Actuator Cylinder: A flow model for vertical axis wind turbines*. Institute of Industrial Constructions and Energy Technology, Aalborg University Centre, 1982.

H. A. Madsen, T. J. Larsen, U. S. Paulsen, and L. Vita. Implementation of the actuator cylinder flow model in the HAWC2 code for aeroelastic simulations on vertical axis wind turbines. In *51st AIAA Aerospace Sciences Meeting including the New Horizons Forum and Aerospace Exposition*, 2013. doi: 10.2514/6.2013-913.

MARINTEK. Rifelx theory manual, version 4.0, 2012a.

MARINTEK. Simo-theory manual version 4.0, 2012b.

P. J. Moriarty and A. C. Hansen. AeroDyn theory manual, NREL/TP-500-36881, 2005.

H. Ormberg, E. Passano, and N. Luxcey. Global analysis of a floating wind turbine using an aero-hydro-elastic model: Part 1 code development and case study. In *Proceedings of the 30th International Conference on Ocean, Offshore and Arctic Engineering*, 2011.

B. C. Owens, J. E. Hurtado, J. A. Paquette, D. T. Griffith, and M. Barone. Aeroelastic modeling of large offshore vertical-axis wind turbines: development of the offshore wind energy simulation toolkit. In *Proceedings of the 54th AIAA Structures, Structural Dynamics and Materials Conference*, 2013.

J. Paquette and M. Barone. Innovative offshore vertical-axis wind turbine rotor project. *EWEA 2012 Annual Event*, 2012.

U. S. Paulsen, H. A. Madsen, J. H. Hattel, I. Baran, and P. H. Nielsen. Design optimization of a 5 mw floating offshore vertical-axis wind turbine. *Energy Procedia*, 35:22–32, 2013. doi: 10.1016/j.egypro.2013.07.155.

B. Roscher. Current aerodynamic models for VAWT and numerical comparison between HAWC2 and U2DiVA. Special project - EWEM rotor design, 2014.

D. Verelst, H. A. Madsen, M. Borg, U. S. Paulsen, H. G. Svendsen, and P. A. Berthelsen. integrated simulation challenges with the deepwind floating vertical axis wind turbine. *Energy Procedia*, 80:321–328, 2015.

L. Vita. *Offshore Floating Vertical Axis Wind Turbines with Rotating Platform*. Phd thesis, Technical University of Denmark, 2011.

K. Wang. *Modeling and dynamic analysis of a semi-submersible floating vertical axis wind turbine*. PhD thesis, Norwegian University of Science and Technology, 2015.

K. Wang, T. Moan, and M. O. L. Hansen. A method for modeling of floating vertical axis wind turbine. In *Proceedings of the 32th International Conference on Ocean, Offshore and Arctic Engineering*, 2013.

K. Wang, Z. Cheng, T. Moan, and M. O. L. Hansen. Effect of difference-frequency forces on the dynamics of a semi-submersible type FVAWT in misaligned wave-wind condition. In *Proceedings of the 25th International Ocean and Polar Engineering Conference*, 2015a.

K. Wang, M. O. L. Hansen, and T. Moan. Model improvements for evaluating the effect of tower tilting on the aerodynamics of a vertical axis wind turbine. *Wind Energy*, 18:91–110, 2015b. doi: 10.1002/we.1685.

A.3 Paper 3

Paper 3:
Effect of the number of blades on the dynamics of floating straight-bladed vertical axis wind turbines.
Zhengshun Cheng, Helge Aagaard Madsen, Zhen Gao, Torgeir Moan
Submitted to *Renewable Energy*, 2016

Effect of the number of blades on the dynamics of floating straight-bladed vertical axis wind turbines

Zhengshun Cheng [*1,2,3], Helge Aagaard Madsen[4], Zhen Gao[1,2,3], and Torgeir Moan[1,2,3]

[1]Department of Marine Technology, Norwegian University of Science and Technology (NTNU), Trondheim, NO-7491, Norway
[2]Centre for Ships and Ocean Structures (CeSOS), NTNU, Trondheim, NO-7491, Norway
[3]Centre for Autonomous Marine Operations and Systems (AMOS), NTNU, Trondheim, NO-7491, Norway
[4]Department of Wind Energy, Technical University of Denmark, Roskilde, 4000, Denmark

April 5, 2016

Abstract

Floating vertical axis wind turbines (VAWTs) are promising solutions for exploiting the wind energy resource in deep waters due to their potential cost-of-energy reduction. The number of blades is one of the main concerns when designing a VAWT for offshore application. In this paper, the effect of blade number on the performance of VAWTs and dynamic behavior of floating VAWTs was comprehensively studied in a fully coupled aero-hydro-servo-elastic way. Three VAWTs with straight and parallel blades, with identical solidity and with a blade number varying from two to four, were designed using the actuator cylinder method and adapted to a semi-submersible platform. A generator torque controller was also designed based on a PI control algorithm. Time domain simulations demonstrated that the aerodynamic loads and structural responses are strongly dependent on the number of blades. In particular, by increasing the number of blades from two to three reduces the variation in the tower base bending moment more significantly than increasing it from three to four. However, the blade number does not significantly affect the generator power production due to the control strategy employed, and the platform motions and tension in mooring lines because of the compliant catenary mooring system.

Key words: Floating vertical axis wind turbine; straight blades; number of blades; aero-hydro-servo-elastic; dynamic response

[*]Corresponding author. Email address: zhengshun.cheng@ntnu.no Tel.:+47-7359 6004; fax: +47-7359 5528.

1 Introduction

In the last decades, offshore wind turbine installations are experiencing a rapid growth in shallow waters due to the increasing demand on renewable energy production. Most wind turbines deployed are bottom-fixed horizontal axis wind turbines (HAWTs) due to their commercial success onshore or near-shore. However, offshore wind farms are moving towards deeper waters where floating wind turbines are required in countries such as the Japan, United States and United Kingdom. Floating HAWTs are now beening widely studied and prototypes have been developed and tested, such as the Hywind demo in Norway, the WindFloat demo in Portugal and the floating wind turbines off the Fukushima coast of northeast Japan.

Floating vertical axis wind turbines (VAWTs) are also a promising alternative to harvest wind energy in deeper waters. Compared with floating HAWTs, floating VAWTs have lower centers of gravity, are independent of wind direction, can provide reduced machine complexity and have the potential of achieving more than 20% cost of energy reductions (Paquette and Barone, 2012). Moreover, floating substructures can help to mitigate the fatigue damages that are suffered by landbased VAWTs (Wang et al., 2016). In addition, floating VAWTs are more suitable for deploying as wind farms than floating HAWTs (Dabiri, 2011). Thus, increasing efforts are devoted to the development of floating VAWTs, and currently several floating VAWT concepts have been proposed, including the DeepWind (Vita, 2011), VertiWind (Cahay et al., 2011) and Aerogenerator X (Collu et al., 2014) concepts.

Floating VAWTs can be categorized according to the blade configuration, such as the straight-bladed VAWT, curve-bladed VAWT, helical-bladed VAWT and V-shaped VAWT. A number of studies have been conducted for the straigh-bladed and curved-bladed floating VAWTs to investigate their dynamic response characteristics. Based on a 5 MW two-bladed Darrieus rotor designed in the DeepWind project (Vita, 2011), Wang et al. (2013) proposed a floating VAWT concept with this rotor mounted on a semi-submersible platform. Fully coupled aero-hydro-servo-elastic simulations were carried out to investigate the stochastic dynamic responses (Wang et al., 2016), effects of second order difference-frequency forces and wind-wave misalignment (Wang et al., 2015), and emergency shutdown process with consideration of faults (Wang et al., 2014). Using the semi-submersible VAWT concept proposed by Wang et al. (2013), Borg and Collu (2015) studied the aerodynamic characteristics of a floating VAWT in the frequency domain. Moreover, the dynamic response characteristic of three floating VAWT concepts with this two-bladed Darrieus rotor mounted on a spar, semi and TLP floater are investigated by Cheng et al. (2015b), and for the spar-type VAWT, a comparative study with the spar-type HAWT is performed to demonstrate the merits and disadvantages in the dynamic responses for each concept (Cheng et al., 2015a). In addition, dynamic analysis of floating VAWT concepts with straight blades are also conducted. Borg et al. (2013) used a wave energy converter as a motion suppression device for a floating VAWT with a two-bladed H-type rotor mounted on a semi-submersible. Anagnostopoulou Anagnostopoulou et al. (2015) performed the concept design and dynamic analyses of a floating VAWT with a three-bladed rotor mounted on a semi-submersible for power supply to offshore Greek islands; however, the wind loads acting on the rotor is very simplified in this study.

The aforementioned dynamic analysis of floating VAWTs considered the curve-bladed rotor with two blades, and the straight-bladed rotor with two or three blades. Significant 2P (two per revolution) effects are revealed and demonstrated for the two-bladed floating VAWTs. As a matter of fact, choosing the number of blades is an important issue when designing a VAWT for offshore application with given blade type, since the number of blades may significantly affect the aerodynamic performance of VAWTs and dynamic response characteristics of

floating VAWT systems. The effect of the number of blades on the aerodynamic performance of VAWTs with straight-bladed and curve-bladed blades has been numerically and experimentally studied by several researchers. Considering a set of curve-bladed VAWTs with constant solidity and different blade number that varies from one to four, the impact of the number of blades on the aerodynamic loads was numerically estimated by Bedon et al. (2015) based on the double multiple streamtube method. The considered VAWT was originally developed in the DeepWind project (Vita, 2011), which was mounted on a floating platform. Li et al. (2015) evaluated the effect of blade number on the aerodynamic forces on a straight-bladed VAWT using the wind tunnel experiment. Considering the number of blades varying from two to five, the tangential and normal forces were quantitatively studied as a function of azimuth angle. However, these studies only discuss the effect of the number of blades from the aerodynamic point of view and do not reveal its potential impact on the dynamic responses of floating VAWTs in a fully coupled way. These dynamic responses include the generator power production, platform motions, structural loads and tension in mooring lines etc. To which extent these dynamic responses could be influenced by the number of blades for floating VAWTs is still unknown and of great interest.

This study aims to demonstrate the effect of the number of blades on the dynamic responses of floating VAWTs by a series of fully coupled time domain simulations. Firstly, three straight-bladed VAWTs with identical solidity and different number of blades are designed using the actuator cylinder flow method. The number of blades varies from two to four. A generator torque controller is also designed based on the control strategy established by Cheng et al. (2016b). These three VAWTs are then adapted to a semi-submersible platform to achieve three floating VAWTs. Using the fully coupled code SIMO-RIFLEX-AC (Cheng et al., 2016b), a series of load cases are conducted to identify the floating VAWT systems and to illustrate the discrepancy in the dynamic responses of these three floating VAWTs. This study systematically demonstrates the effect of the number of blades on the dynamic responses of floating VAWTs and can serve as a basis for the design of floating VAWTs.

2 Methodology

In this study, an aerodynamic code based on the actuator cylinder (AC) flow model, initially developed by Madsen (1982) and implemented and modified by Cheng et al. (2016a), was used to design three straight-bladed VAWTs and a corresponding generator-torque controller. Compared with the conventional double multi-streamtube method (Paraschivoiu, 2002), the AC method predicts more accurate aerodynamic loads with similar computational efficiency (Ferreira et al., 2014; Cheng et al., 2016a). The code SIMO-RIFLEX-AC developed by Cheng et al. (2016b) was later used to conduct fully coupled aero-hydro-servo-elastic time domain simulations. The relevant theories for the AC and SIMO-RIFLEX-AC code are briefly summarized in this section.

2.1 Actuator cylinder flow method

The AC method is a 2D quasi-steady flow model proposed by Madsen (1982). The model extends the actuator disc concept to an actuator surface coinciding with the swept area of the 2D VAWT. In the AC model, the normal and tangential forces resulting from the blade forces are applied on the flow as volume force perpendicular and tangential to the rotor plane, respectively. The induced velocities are thus related to the volume force based on the continuity equation and Euler equation. The induced velocity can be divided into a linear part and a nonlinear part;

the linear part can be computed analytically given the normal and tangential loads. However, it's to some extent time-consuming to compute the nonlinear solution directly. A simple correction is therefore introduced to make the final solution in better agreement with the fully nonlinear solution.

The developed AC code (Cheng et al., 2016a) includes the effect of normal and tangential loads when calculating the induced velocity, uses a more physical approach to represent the normal and tangential loads and a new modified linear solution. The effect of dynamic stall was also incorporated using the Beddoes-Leishman model. The AC code was validated by comparison with other numerical models and experimental data and was found to be accurate (Cheng et al., 2016a).

2.2 Fully coupled numerical method

The developed AC code (Cheng et al., 2016a) was integrated with the SIMO (MARINTEK, 2012b) and RIFLEX (MARINTEK, 2012a) codes to achieve a fully coupled aero-hydro-servo-elastic code, namely SIMO-RIFLEX-AC (Cheng et al., 2016b), for numerical modeling and dynamic analysis of floating VAWTs. The SIMO (MARINTEK, 2012b) and RIFLEX (MARINTEK, 2012a) codes were developed by MARINTEK and have been widely used in the offshore oil and gas industry. The SIMO-RIFLEX-AC code is capable of accounting for the turbulent wind inflow, aerodynamics, hydrodynamics, structural dynamics, control system dynamics and mooring line dynamics. It integrates three computer codes: SIMO (MARINTEK, 2012b) computes the hydrodynamic loads acting on the platform hull; RIFLEX (MARINTEK, 2012a) models the blades, tower, shaft, struts and mooring lines using flexible finite elements and provides links to an external controller and AC; and AC calculates the aerodynamic loads acting on the blades. Moreover, a generator torque controller based on the proportional-integral (PI) control algorithm is implemented to regulate the rotor rotational speed. The SIMO-RIFLEX-AC code has been verified by a series of numerical comparisons with the codes HAWC2 and SIMO-RIFLEX-DMS (Cheng et al., 2016b).

In this study, a semi-submersible supporting straight-bladed VAWTs was studied. The aerodynamic loads acting on the blades were calculated based on the AC method as described above, and the effect of the wind shear and turbulence, dynamic inflow and dynamic stall was all taken into account. But the effect of the tip loss, tower shadow as well as the drag forces on the struts and tower was neglected.

The hydrodynamic loads acting on the semi-submersible hull was represented using a combination of potential flow and Morison's equation. Added mass, radiation damping and first order wave excitation forces were obtained from a potential flow model and applied in the time domain using the convolution technique (Faltinsen, 1995). Additional viscous damping on the hull was included using the Morison's formula. Morison's formula was also applied to the brace and mooring lines that were not included in the potential flow model.

In the structural model, the semi-submersible including the braces were represented as a rigid body; the blades, struts, tower and shaft were modeled using nonlinear beam elements; and the mooring lines were considered as nonlinear bar elements. A very short tower close to the tower base was used to connect the rotating shaft and semi through a flexible joint. The dynamic equilibrium equations were solved in the time domain using the Newmark-β integration method ($\beta = 0.256$, $\gamma = 0.505$). Structural damping was included through global proportional Rayleigh damping terms for all beam elements.

3 Floating VAWT models

3.1 Design of straight bladed VAWTs

Considering a straight bladed VAWT with a radius of R and height of h, the power can be expressed as (Brusca et al., 2014)

$$P = \frac{1}{2}\rho U_w^3 (2Rh) C_p \tag{1}$$

where ρ is the air density, U_w is the wind speed, and C_p is the power coefficient. For a specific airfoil type, the power coefficient C_p is a function of the tip speed ratio λ, rotor solidity σ and Reynolds number Re, which are defined as follows.

$$\lambda = \frac{\omega R}{U_w} \tag{2}$$

$$\sigma = \frac{Bc}{R} \tag{3}$$

$$Re = \frac{cV_{rel}}{\nu} \tag{4}$$

in which B is the blade number, c is the chord length, ν is the kinematic air viscosity, and V_{rel} is the relative velocity seen by the airfoil. Assuming the aspect ratio γ is given by $\gamma = h/R$, therefore the power can be rewritten as

$$P = \frac{\rho\omega^3 R^5 \gamma C_p(\lambda, \sigma, Re)}{\lambda^3} \tag{5}$$

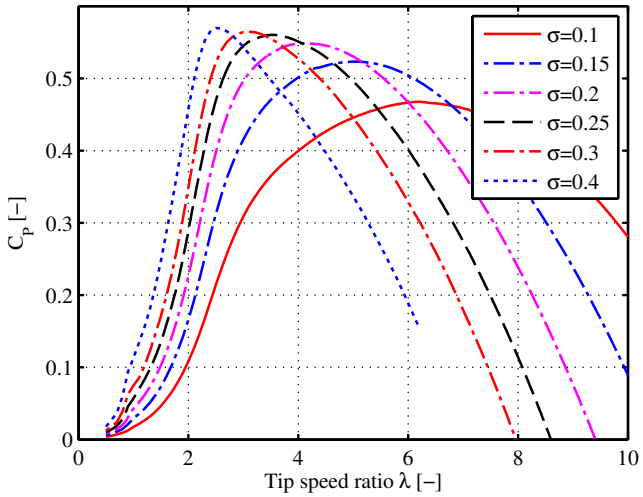

Figure 1: Power coefficient of a VAWT with straight blades and symmetric airfoil NACA 0018 at high Reynolds number of $8 \sim 10 \times 10^6$ for different rotor solidity $\sigma = \frac{Bc}{R}$.

In this study three 5MW VAWTs with straight blades and the NACA 0018 airfoil, as shown in Figure 2, were designed. Eq. 5 shows that the power coefficient C_p is one of the crucial parameters and should be firstly

determined. Large megawatt VAWTs usually operate at very high Reynolds number. Figure 1 shows the power coefficient C_p plotted against the tip speed ratio λ as a function of rotor solidity σ for the NACA 0018 airfoil at Reynolds number of $8 \sim 10 \times 10^6$. It should be noted here that the Reynolds number experienced by the airfoil at a specific position along the blade varies periodically when the rotor rotates. In this study it is assumed that such variation in the Reynolds number will not cause much changes in the corresponding lift and drag coefficients for the NACA 0018. Due to the consideration of solidity and power coefficient of large megawatt VAWTs in reality, the solidity of $\sigma = 0.20$ is chosen, which has a $C_{pmax} = 0.50$ corresponding to $\lambda = 3.0$.

Assuming that the rated wind speed is 14.0 m/s and the aspect ratio is set to be 2.05, three optimal designs for a rated power of 5.3 MW are given in Table 1. The height of tower top, i.e. the vertical center of blades, is assumed to be 79.78 m. The aerodynamic power is estimated considering the wind shear with a power coefficient of 0.14 according to the IEC 61400-3 (IEC, 2005). In the design process, the chord length is reduced with increasing number of blades so as to keep the solidity constant. This can also cause a change in Reynolds number and thus affect the lift and drag coefficients, but the impact on the total aerodynamic loads and power is assumed to be small. In addition, despite the same solidity number, the mean thrust coefficients have small variation because of the different number of blades. Since the modified linear solution in the AC method is sensitive to the mean thrust coefficient, the computed rated power does therefore show small deviation from the value of 5.3 MW.

Table 1: Main parameters of the designed VAWTs

	H2	H3	H4
Rated power [MW]	5.21	5.30	5.35
Blade number [-]	2	3	4
Rotor radius [m]	39.0	39.0	39.0
Height [m]	80.0	80.0	80.0
Chord length [m]	4.05	2.7	2.03
Tower top height [m]	79.78	79.78	79.78
Aerofoil section	NACA 0018	NACA 0018	NACA 0018
Cut-in, rated and cut-out wind speed [m/s]	5.0, 14.0, 25.0	5.0, 14.0, 25.0	5.0, 14.0, 25.0
Rated rotational speed [rad/s]	1.08	1.08	1.08

3.2 Description of landbased and floating VAWT models

In this study, three straight-bladed floating VAWTs with a semi-submersible floater are considered. For the straight-bladed rotors, the structural properties of the blades, struts, tower and shaft were determined on the basis of the Deepwind rotor (Vita, 2011), which was a 5 MW Darrieus rotor. The blades of the designed straight-bladed rotors and Deepwind rotor both used the same NACA 0018 airfoil, but they differed in the chord length. It was thus assumed that the structural properties of the blades, such as the mass per unit length, axial and bending stiffness, are related to a length scale that is determined using the chord length. In this study, the blades, instead of struts, are our concern. To avoid large deformation in the blades at high wind load conditions, the stiffness of the blades and struts was increased. The stiffness of the tower and shaft remained the same as the Deepwind design. Actually in a realistic design, the struts might be different from the present ones and additional struts, as the dash line shown in Figure 2, could be constructed. The mass properties of the three rotors are given in Table 2.

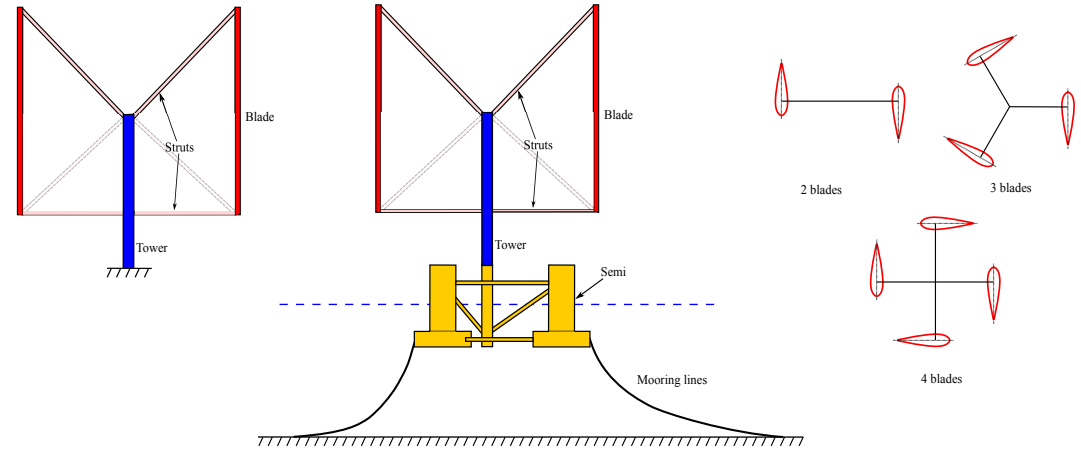

(a) Straight-bladed landbased VAWTs (b) Straight-bladed floating VAWTs (c) Top view of the blades

Figure 2: The landbased and floating straight-bladed VAWTs with different number of blades.

The OC4 semi-submersible (Robertson et al., 2012) , which was originally designed to support the NREL 5 MW wind turbine (Jonkman et al., 2009), was used to support the three straight-bladed VAWTs. The considered water depth was assumed to be 200 m. The same semi-submersible was used to support the 5 MW Darrieus Deepwind rotor and studied by Cheng et al. (2015b) and Wang et al. (2016). Due to the difference in the rotor mass, the ballast of the semi-submersible was adjusted to maintain the same draft and displacement when supporting three different VAWTs. Properties of the three floating VAWT systems are given in Table 2. More details about the semi-submersible and catenary mooring system are given by Robertson et al. (2012). The generator was assumed to be located at the tower base and its mass was incorporated in the platform mass. Since the difference in the rotor mass between the NREL 5 MW wind turbine and three designed rotors is small compared to the displacement of the semi-submersible, it is therefore assumed that such modification will not significantly affect the hydrostatic and hydrodynamic performance of each floater.

Table 2: Properties of the floating VAWT systems

	Semi H2	Semi H3	Semi H4
Water depth [m]	200	200	200
Draft [m]	20	20	20
Diameter at mean water line [m]	12.0/6.5	12.0/6.5	12.0/6.5
Rotor mass, including blades, struts, tower and shaft [ton]	350.1	315.3	287.7
Center of mass for rotor [m]	(0, 0, 51.03)	(0, 0, 48.14)	(0, 0, 45.34)
Platform mass, including ballast and generator [ton]	13761.3	13796.1	13823.7
Center of mass for platform [m]	(0, 0, -13.44)	(0, 0, -13.43)	(0, 0, -13.43)
Buoyancy at the equilibrium position [kN]	139816	139816	139816
Center of buoyancy [m]	(0, 0, -13.15)	(0, 0, -13.15)	(0, 0, -13.15)

Although the structural properties of rotors and the substructure is not optimal from an economic point of view,

they are sufficient to demonstrate and reveal the effect of the number of blades on the dynamics of floating VAWTs.

3.3 Control strategy for the landbased and floating VAWTs

In this section, a generator-torque controller is designed for the above VAWTs. Cheng et al. (2016b) demonstrated the typical relationship between the reference rotational speed and wind speed for a typical floating VAWT system and identified two control strategies, namely the baseline controller and improved controller, in terms of the target in region above the rated wind speed. Herein the improved controller was adopted.

Considering the 3-bladed VAWT, the rotor power is plotted against the rotational speed as a function of wind speed, as shown in Figure 3. For wind speeds below the rated wind speed, the designed rotational speed is determined by maximizing the power capture. Regarding wind speeds ranging from 5-10.5 m/s, the rotational speed is chosen to make the rotor operating at the optimal tip speed ratio. Moreover for wind speeds ranging from 10.5-14 m/s, the rotational speed is set to be the rated rotational speed. Therefore the optimized curve rotational speed can be obtained for wind speeds below the rated one.

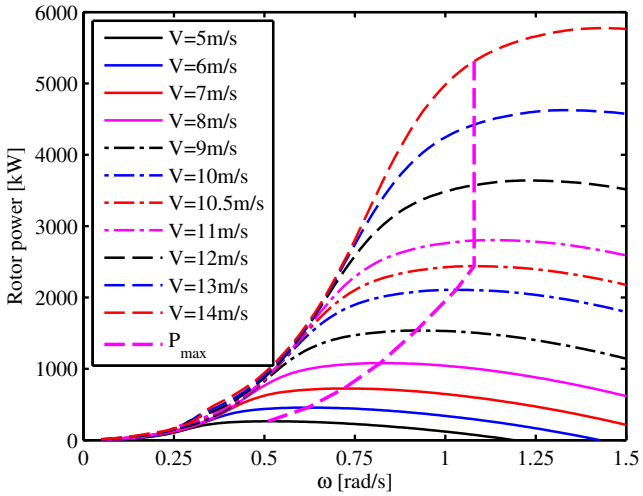

Figure 3: The mean aerodynamic power as a function of the rotational speed and wind speed.

With respect to wind speeds above the rated one, the improved controller that maintains the mean rotor power approximately constant is applied. Given a wind speed, the desirable rotational speed is computed to make the mean aerodynamic power achieve a prescribed value, for instance 5.3 MW in this study. In this way the designed rotational speed is obtained as a function of wind speed as demonstrated in Figure 4.

In the implementation of the controller, the generator rotational speed and electric torque are measured and low-pass filtered. The controller aims to minimize the error between the measured and filtered rotational speed Ω_{mea} and the reference rotational speed Ω_{ref},

$$\Delta\Omega = \Omega_{mea} - \Omega_{ref} \tag{6}$$

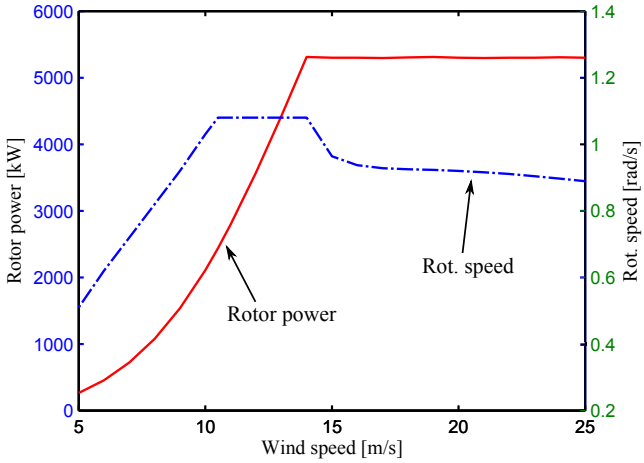

Figure 4: The mean rotor power and rotational speed as a function of wind speed for the improved control strategy.

in which the reference rotational speed Ω_{ref} is determined on the basis of a look-up table showing the relationship of the filtered electric torque and reference rotational speed for wind speeds below the rated one; while for wind speed above the rated one, it is determined according to a look-up table of the low-pass filtered wind speed and reference rotational speed.

The rotational speed error $\Delta\Omega$ is then fed through the proportional, integral and derivative paths to obtain an updated value of the required electric torque, as follows,

$$T(t) = K_G\left(K_P\Delta\Omega(t) + K_I\int_0^t \Delta\Omega(\tau)d\tau + K_D\frac{d}{dt}\Delta\Omega(t)\right) \tag{7}$$

in which K_G is the generator stiffness, and K_P, K_I and K_D are the proportional, integral and derivative gains, respectively. In this study, the value of K_G, K_P, K_I and K_D were determined with reference to the controller developed by Merz and Svendsen (2013) for the DeepWind 5MW Darrieus rotor.

The aforementioned controller is determined using the 3-bladed VAWT. It is also applicable to the 2- and 4-bladed VAWTs, as illustrated in Figure 6. Figure 6 shows the mean value of the generator power production of three equivalent landbased VAWTs and three floating VAWTs considered in the steady wind conditions. Description of the landbased and floating VAWTs can refer to section 3.2. Obviously all the mean generator power of the three rotors follow the pre-calculated power curve very well. Therefore, the designed controller was applied for the VAWTs in all simulations.

4 Load cases and environmental conditions

A series of load cases (LCs) were defined for the floating VAWT system and used in the time domain simulations, as given in Tables 3 and 4. LC1 and LC2 are free decay and white noise wave cases, respectively. They are used to identify the three floating VAWT systems and capture the difference in terms of natural periods of rigid

body motions and response amplitude operators (RAOs). Those differences should be small in order to reveal the essential effect of the number of blades on the dynamics of floating VAWTs. LC3 and LC4 are the steady wind only cases and the turbulent wind and irregular wave cases, respectively. The wind and wave are correlated and directionally aligned. They are used to study the effect of the number of blades on the dynamics of floating VAWTs.

Table 3: Load cases: free decay and white noise

Load cases (LCs)		Response	Wind Cond.	Wave Cond.
LC1	Decay	Decay (Surge, heave, pitch and yaw)	-	Calm water
LC2	White noise	RAO	-	White noise

Table 4: Load cases: wind and wave cases

	U_W [m/s]	H_S [m]	T_P [s]	T_I [-]	Wave Cond.	Simulation Length [s] *
LC3.1	5	-	-	0	-	800
LC3.2	8	-	-	0	-	800
LC3.3	10	-	-	0	-	800
LC3.4	12	-	-	0	-	800
LC3.5	14	-	-	0	-	800
LC3.6	18	-	-	0	-	800
LC3.7	22	-	-	0	-	800
LC3.8	25	-	-	0	-	800
LC4.1	5	2.10	9.74	0.224	Irreg. wave	3600
LC4.2	8	2.55	9.86	0.174	Irreg. wave	3600
LC4.3	10	2.88	9.98	0.157	Irreg. wave	3600
LC4.4	12	3.24	10.12	0.146	Irreg. wave	3600
LC4.5	14	3.62	10.29	0.138	Irreg. wave	3600
LC4.6	18	4.44	10.66	0.127	Irreg. wave	3600
LC4.7	22	5.32	11.06	0.121	Irreg. wave	3600
LC4.8	25	6.02	11.38	0.117	Irreg. wave	3600

* Net simulation time for stochastic wave and wind conditions, i.e. removal of transient start-up.

The normal wind profile (NWP) was applied in the steady wind conditions, in which the wind profile is the average wind speed as a function of height z above mean sea level (MSL) and is given as follows

$$U(z) = U_{ref}\left(\frac{z}{z_{ref}}\right)^{\alpha} \tag{8}$$

where U_{ref} is the reference wind speed, z_{ref} is the height of reference wind speed and α is the power law exponent. In this study z_{ref} was set to be 79.78 m, which is the vertical center of blades above MSL. The value of α was chosen to be 0.14 for the floating wind turbines according to IEC 61400-3 (IEC, 2005). For turbulent wind conditions, the TurbSim (Jonkman, 2009) was used to generate the three dimensional turbulent wind field according to the Kaimal turbulence model for IEC Class C. Regarding the irregular wave conditions, the irregular wave history was generated using the JONSWAP wave model. The significant wave height and peak period were set based on their

correlation with wind speed for the Statfjord site in the northern North Sea (Johannessen et al., 2002).

In the turbulent wind and irregular wave LCs, each simulation lasted 4600 s and corresponded to a one-hour dynamic analysis, since the first 1000 s was removed to eliminate the start-up transient effects. Five identical and independent one-hour simulations with different seeds for the turbulent wind and irregular waves were carried out for each LC to reduce the stochastic variations. The mean value and standard deviation of the dynamic responses were obtained by averaging the mean values and standard deviations of five one-hour ensembles.

5 Results and discussions

5.1 Identification of the properties of floating VAWT systems

A series of numerical simulations were carried out to identify the floating VAWT systems, including the eigen-frequencies of equivalent landbased VAWTs, the natural periods of rigid-body motions of floating VAWTs and the RAOs of floating VAWTs subject to wave loads.

The eigen-frequencies and corresponding eigen modes of the equivalent landbased VAWTs were estimated using the code SIMO-RIFLEX-AC. The eigenvalue problems were solved using the Lanczos' method. The rotors were assumed to be parked and the effects of aerodynamic loads and rotation on the eigen-frequencies and eigen-modes were not considered here. The results show that the two lowest eigen-frequencies of the 2-, 3- and 4-bladed rotors are located outside of the corresponding 2P, 3P and 4P regions, respectively, which indicates that the resonant modes of the rotor will not be excited during the normal operation.

Free decay tests in calm water were carried out using the code SIMO-RIFLEX-AC to estimate the natural periods of rigid body motions for the three floating VAWTs. In the free decay tests, the wind turbines were parked in the position as shown in Figure 2 and were not subjected to the aerodynamic loads. Here the influence of the rotor azimuth angle when parked on the pitch and roll natural periods was neglected since the influence was very small. The results are given in Table 5. These three floating VAWTs have identical draft and displacement and employ the same mooring system, the natural periods in surge, sway and heave motions are thus almost the same. In addition, since the three floating VAWTs have nearly the same rotor masses and the rotor masses are small compared to the displacement, the natural periods in pitch, roll and yaw motions are also close to each other.

Table 5: Natural periods of rigid body motions for the three floating VAWTs

	Semi H2	Semi H3	Semi H4
Surge/Sway [s]	113.15	113.15	113.15
Heave [s]	17.04	17.04	17.04
Pitch/Roll [s]	21.17	20.68	20.32
Yaw [s]	80.38	80.44	80.49

The RAOs of floating VAWTs were estimated using the white noise technique. Cheng et al. (2015b) stated that the white noise technique can capture the natural frequency of rigid-body motions precisely and predict all RAOs accurately except at the resonant frequency of each mode. The white noise waves were created using the fast Fourier transform (FFT) with a frequency interval $\Delta\omega$=0.005 rad/s. In the white noise simulations, the wind turbines were parked as in the free decay tests. The surge and pitch RAOs of the three floating VAWTs are shown

in Figure 5. It can be observed that the natural periods captured by the white noise technique agree well with those from the free decay tests. Moreover, the surge and heave RAOs for the three floating VAWTs agree very well over a wide range of frequencies; while visible discrepancy lies in the pitch RAO, especially at the pitch resonant frequency. This is due to the different moment of inertia in pitch of the three floating VAWTs. When adapting the three rotors with different mass to the semi, the ballast of the semi was adjusted to achieve the same draft and displacement for the three floating VAWTs. Consequently, the moments of inertia in pitch and roll of the three floating VAWTs differ, and the pitch natural frequency and pitch resonant response exhibit slight differences.

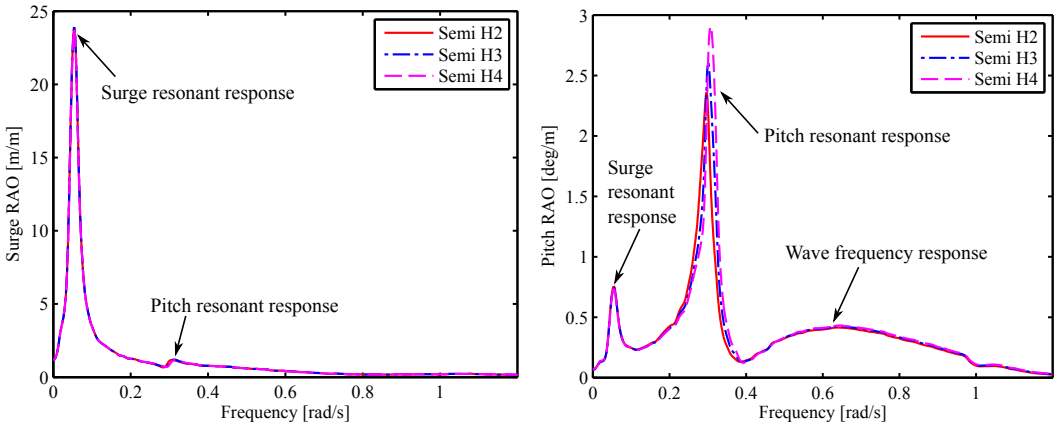

Figure 5: Surge and pitch RAOs of the three floating VAWTs for wave loads.

5.2 Steady wind conditions

The steady wind LCs were used to verify the robustness of the designed controller, and to illustrate the difference between landbased and floating straight-bladed VAWTs with different number of blades.

The robustness of the controller has been investigated and shown in Figure 6. The landbased and floating VAWTs can all achieve the pre-calculated power curve at a given wind speed. Figure 6 also presents the mean thrust of the landbased and floating VAWTs. An example of the time history of the thrust and side force acting on the rotor for the three floating VAWTs are shown in Figure 7. In general the mean thrust of the landbased and floating VAWTs are close to each other, and the small difference, especially in high wind speeds, is mainly due to two possible reasons: one is that the effect of dynamic stall on the airfoil is not identical for the 2-, 3- and 4-bladed VAWTs when operating at relatively low tip speed ratios. This can cause discrepancy in the mean value of the resultant forces. Another reason is that when the VAWTs rotate, not only the aerodynamic loads vary, so do the rotational speed and the generator torque used to regulate the rotational speed, as illustrated in Figure 7. The generator controller responds a little differently to the variation of rotational speed for VAWTs with different number of blades.

In addition, the 2-bladed VAWT exhibits much more significant variation in the thrust and side force compared to the 3- and 4-bladed VAWTs, since its lift and drag forces of each blade reach the maximum and minimum

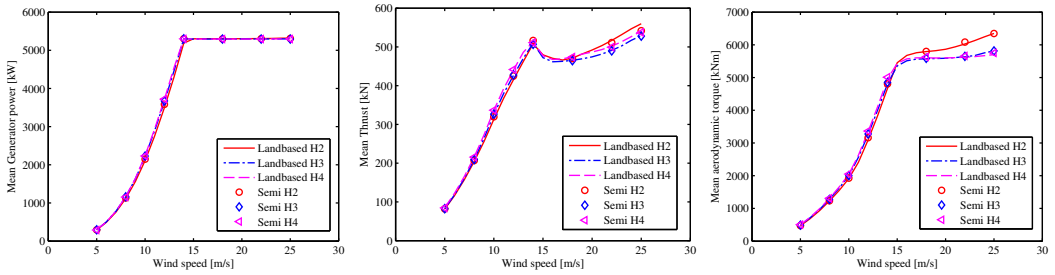

Figure 6: The mean value of the generator power, thrust and aerodynamic torque of the landbased and floating VAWTs with the improved controller.

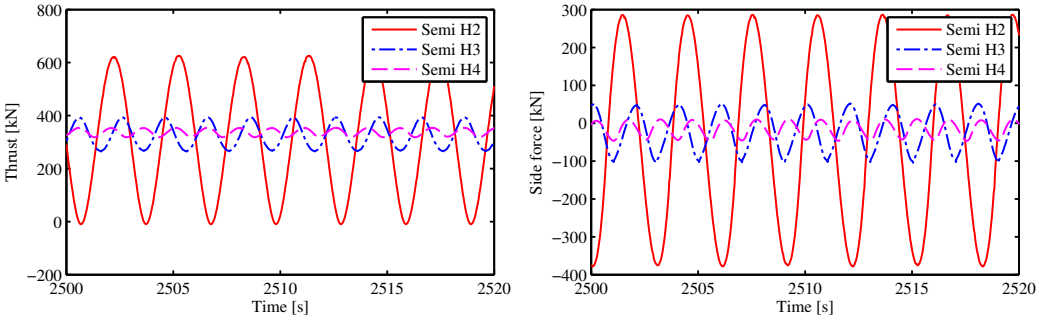

Figure 7: Time history of the thrust and side forces acting on the three floating VAWTs in the steady wind condition with a wind speed of 10 m/s.

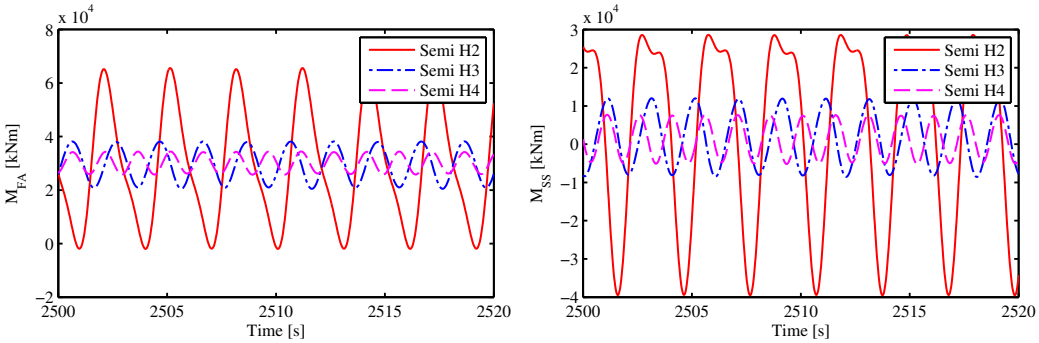

Figure 8: Time history of the tower base fore-aft and side-side bending moments of the three floating VAWTs in the steady wind condition with a wind speed of 10 m/s.

simultaneously, causing the thrust and aerodynamic torque varying from approximate zero to double the mean value. Consequently, the induced structural responses, for instance the tower base fore-aft and side-side bending moments, vary considerably, and the fluctuation of the 2-bladed VAWT is much more notable than that of the 3- and 4-bladed VAWTs . This can be observed in Figures 7 and 8.

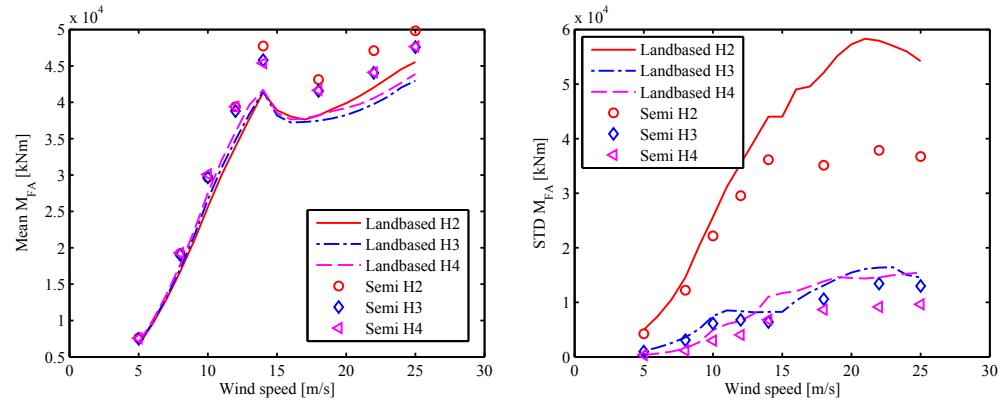

(a) Tower base fore-aft bending moment

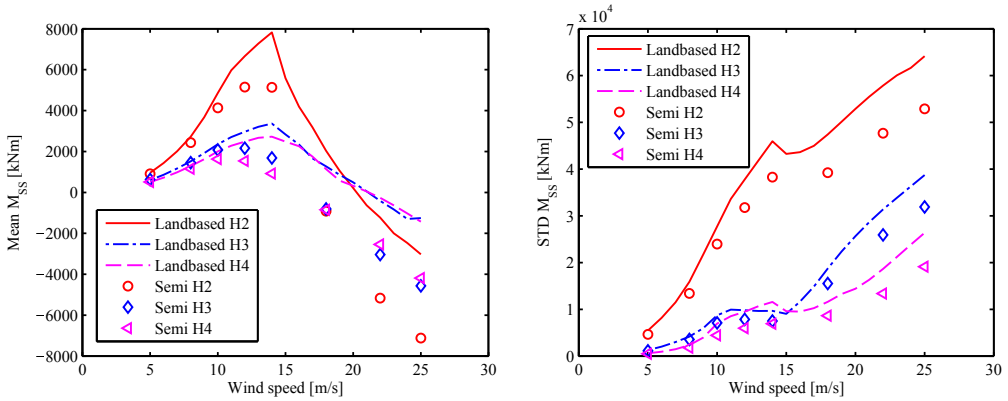

(b) Tower base side-side bending moment

Figure 9: The mean value and standard deviation of tower base fore-aft and side-side bending moments of the landbased and floating VAWTs in steady wind conditions.

Figure 9 further compares the mean value and standard deviation of the tower base fore-aft and side-side bending moment of the landbased and floating VAWTs in the steady wind conditions. Compared to the landbased VAWTs, the floating VAWTs give relatively larger mean value in the fore-aft bending moment, especially at high wind speeds, due to the contribution from the tower weight and platform's pitch motions. In contrast, the landbased VAWTs give larger mean value in the side-side bending moment than the floating ones. Regarding the standard deviation, both the fore-aft and side-side bending moment of the floating VAWTs are smaller than those of the landbased VAWTs. For the 2-bladed semi VAWT, the standard deviation of the fore-aft bending moment can

reduce up to approximately 40% compared to the landbased one. It implies that the floating substructure with compliant catenary mooring systems can help to mitigate the variation in structural responses at the cost of some pitch motion. This is also demonstrated in the turbulent wind and irregular wave simulations. In addition, the 3- and 4-bladed VAWTs present much smaller standard deviations in the tower base fore-aft and side-side bending moment than the 2-bladed VAWT.

5.3 Turbulent wind and irregular wave conditions

In the turbulent wind and irregular wave conditions, several stochastic dynamic responses of the three floating VAWTs are studied, such as the wind turbine performance, platform motions, tower base bending moments and tension in mooring lines.

5.3.1 Wind turbine performance

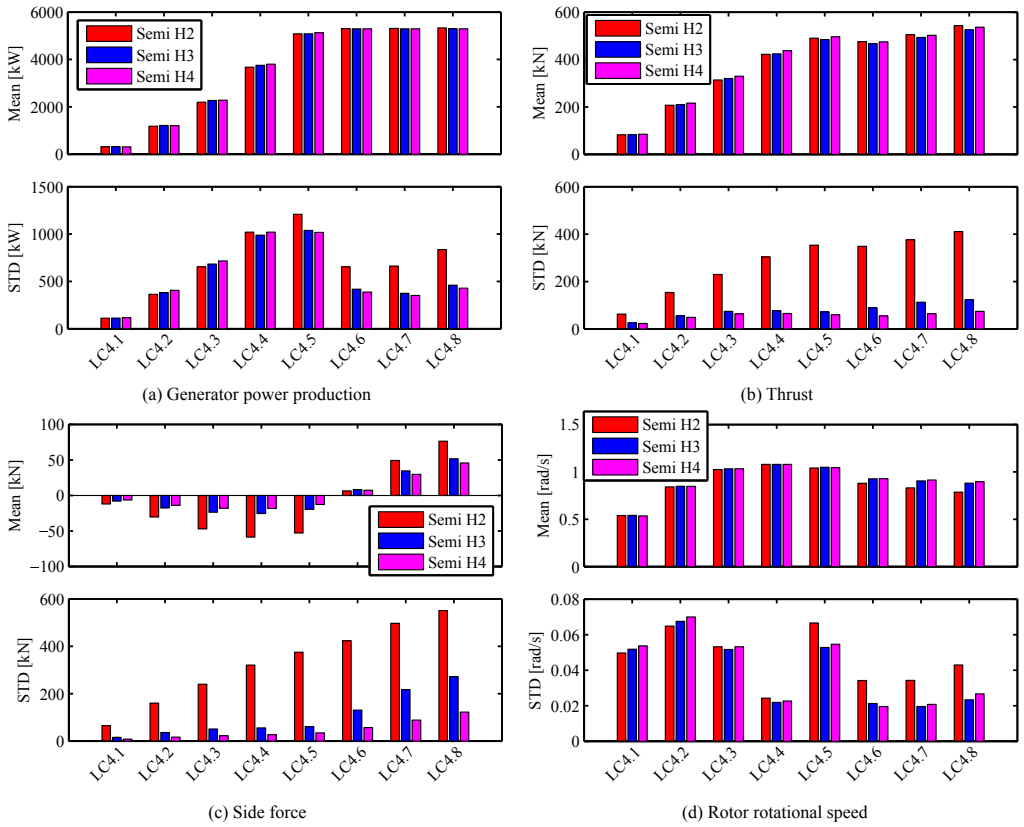

Figure 10: The mean value and standard deviation of the (a) generator power production, (b) thrust, (c) side force, and (d) rotor rotational speed of three floating VAWTs in LC4 with turbulent wind and irregular wave conditions.

Figure 10 shows the mean values and standard deviations of the generator power production, thrust, side force and rotor rotational speed for the three floating VAWTs in LC4. It can be found that the mean generator power production remains approximately constant above the rated wind speed (LC4.5) because of the robust controller implemented. For each LC, the difference in mean generator power among the three floating VAWTs is also very small. In addition, the mean values in the thrust and rotor rotational speed of three floating VAWTs are very close to each other for each LC as well. Although the mean side force of the 2-bladed semi VAWT is larger than those of the 3- and 4-bladed semi VAWTs, the absolute value is all small compared to the mean thrust.

Visible differences in Figure 10 are observed in the standard deviations, especially in those of the thrust and side force. Such discrepancies are mainly due to the different number of blades. The blade number contributes considerably to the variation of resultant aerodynamic loads acting on the rotor, as illustrated in Figure 10 (b) and (c). The standard deviation in the thrust of the 2-bladed semi VAWT is more than three times larger than that of the 3-bladed semi VAWTs at above the wind speed of 10 m/s (LC4.3). For wind speeds ranging from the cut-in (LC4.1) to rated (LC4.5) one, the standard deviation in thrust of the 4-bladed semi VAWT is more than 80% of that of the 3-bladed semi VAWT. Regarding the side force, the 2-bladed semi VAWT gives more than four times larger standard deviation than the 3-bladed one at below the rated wind speed (LC4.5), while the standard deviation of the side force for the 4-bladed semi VAWT is approximately half of that of the 3-bladed one.

Similar to the thrust and side force, the aerodynamic torque varies significantly, especially for the 2-bladed semi VAWT. However, the fluctuation in the generator torque is relatively small compared to that of the aerodynamic torque, due to the adjustment of the controller. Consequently, the variation in the generator power is relatively small as well, as the standard deviation of the generator power shown in Figure 10. Moreover, the difference in the standard deviation of the generator power among the three semi VAWTs is much less notable than that of the aerodynamic loads. The standard deviation in the generator power of the 3- and 4-bladed semi VAWTs are very close to each other, while that of the 2-bladed semi VAWT is visibly larger than those of the 3- and 4-bladed semi VAWTs above the rated wind speed. As a whole, the generator power is not sensitive to the blade number due to the control strategy implemented.

5.3.2 Global platform motions

For the Darrieus type floating VAWTs, the mean value of platform motions are mainly induced by the wind loads (Cheng et al., 2015b), this also applies to the straight-bladed floating VAWTs considered in this study, as shown in Figure 11. For all three floating VAWTs, the trends in the surge and pitch motions follow that of the thrust, while the trends in the roll and yaw motions follow that of the side force and generator torque, respectively. These three floating VAWTs have very close mean values in the aerodynamic loads, as a result their mean values in the platform motions are close to each other as well. The mean motions in surge, pitch and yaw increase as wind speeds increase. Moreover, the mean pitch and yaw motions of the 2-bladed semi VAWT are to some extent larger than those of the 3- and 4-bladed semi VAWTs above the rated wind speed.

The standard deviation of platform motions are induced by not only the wind loads but also the wave loads. It's obvious from Figure 11 that the standard deviation of platform motions of the 3- and 4-bladed semi VAWTs are generally very close to each other for each LCs. Moreover, the standard deviation of pitch motions of these three floating VAWTs are very close to each other for each LCs. However, the 2-bladed semi VAWT gives relatively

larger standard deviations in surge, roll and yaw motions at LCs with wind speeds above the rated one.

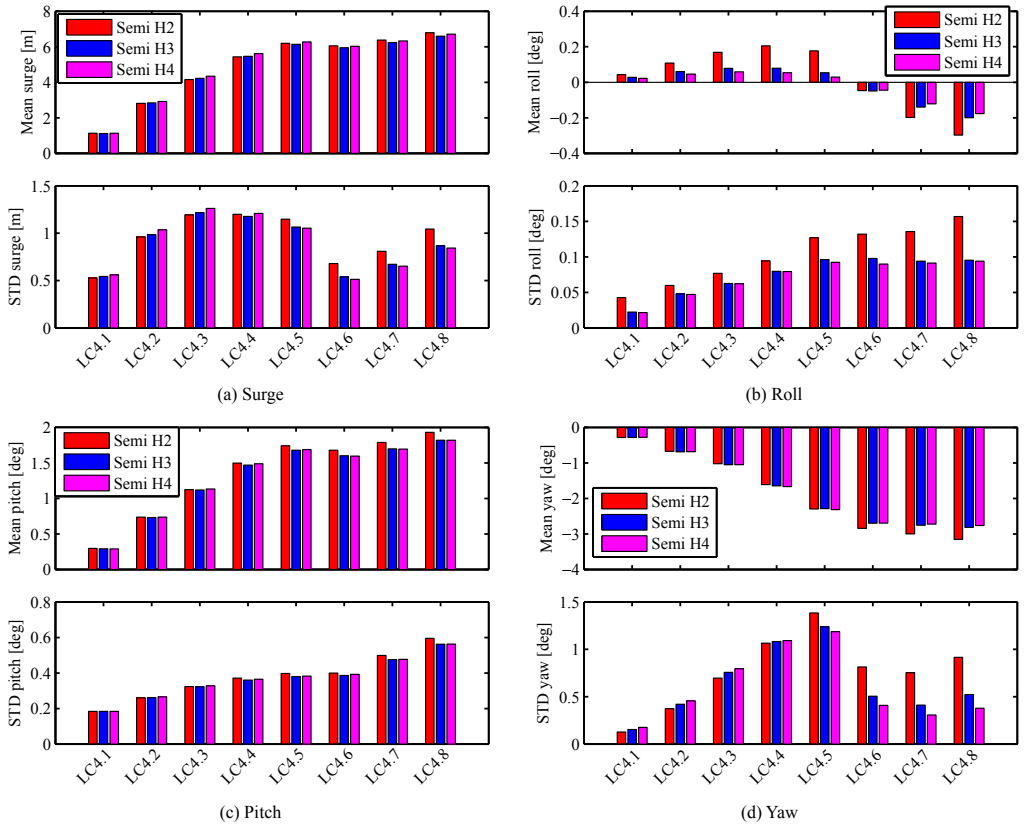

Figure 11: The mean values and standard deviations of the surge, roll, pitch and yaw motions of three floating VAWTs in LC4 with turbulent wind and irregular wave conditions.

Power spectral analysis was carried out to identify different contributions from the wind or wave for each mode in each LC. Since it has been stated in section 5.1 that these three floating VAWTs have almost identical RAOs in surge and heave motions when subjected to wave loads, the discrepancy in the standard deviation of surge motions are mainly caused by the wind loads. Figure 12 presents the power spectra of surge motions in LC4.2 and LC4.7. The wave frequency response of these three floating VAWTs are identical and the difference in responses locates at the surge resonant frequency. The 2-bladed semi VAWT has a little smaller surge resonant response at LCs with wind speeds below the rated one, while it holds a little larger surge resonant response at LCs with wind speeds above the rated one. Moreover, no 2P, 3P or 4P response is observed in the power spectra of surge motions for the 2-, 3- and 4-bladed semi VAWT, respectively. In addition, the severer the sea state is, the more the wave loads contribute to the surge power spectra.

Power spectra of pitch motions in Figure 13 (b) reveal that the contributions are from the low turbulent wind induced response, pitch resonant response and wave frequency response. In very severe sea state such as LC4.7

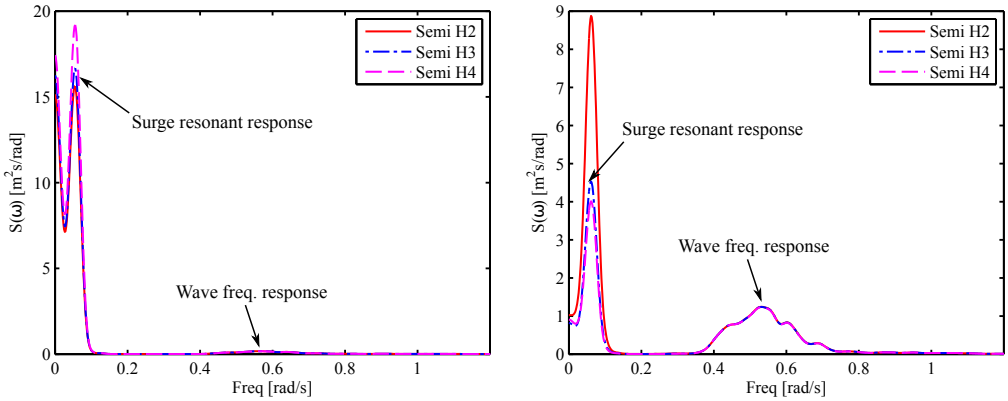

(a) LC4.2: Uw=8m/s, Hs=2.55m, Tp=9.74s (b) LC4.7: Uw=22m/s, Hs=5.32m, Tp=11.06s

Figure 12: Power spectra of the surge motion of three floating VAWTs in (a) LC4.2 and (b) LC4.7.

and LC4.8, a very small 2P response is also observed only for the 2-bladed semi VAWT. Due to the identical RAOs in the range of wave frequency, the wave frequency pitch response is also almost identical for these three floating VAWTs. Moreover, Pitch response with contribution from wave loads increases as the sea state becomes more severer, which is similar as the surge response. Regarding the power spectra of roll motions, not only is a notable 2P response observed for the 2-bladed semi VAWT, but also a very small 3P response is captured for the 3-bladed semi VAWT. However, no 4P response is identified for the 4-bladed semi VAWT.

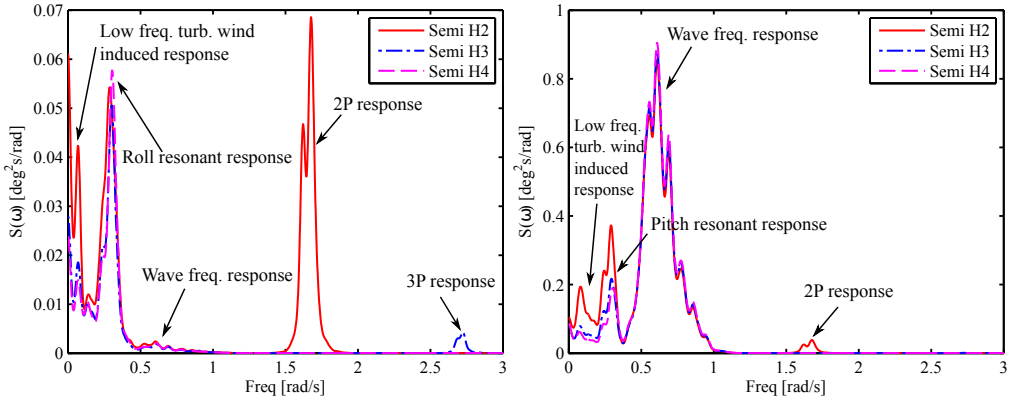

(a) Roll in LC4.7: Uw=22m/s, Hs=5.32m, Tp=11.06s (b) Pitch in LC4.7: Uw=22m/s, Hs=5.32m, Tp=11.06s

Figure 13: Power spectra of the (a) roll motion and (b) pitch motion of three floating VAWTs in LC 4.7.

The power spectra of yaw motions are mainly dominated by the low turbulent wind induced response and yaw resonant response, as shown in Figure 14. At LCs with wind speeds below the rated one, the 4-bladed semi VAWT gives a litter larger yaw resonant response; while it presents much smaller yaw resonant response at LCs with wind speeds above the rated one.

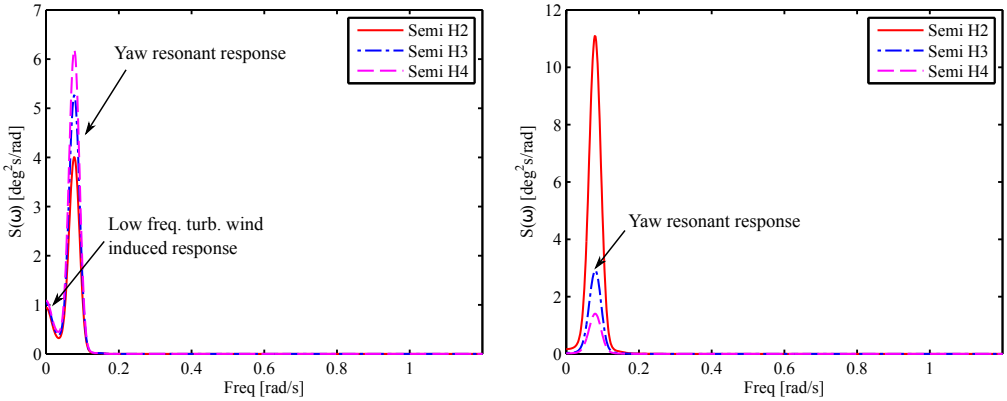

(a) LC4.2: Uw=8m/s, Hs=2.55m, Tp=9.74s

(b) LC4.7: Uw=22m/s, Hs=5.32m, Tp=11.06s

Figure 14: Power spectra of the yaw motion of three floating VAWTs in (a) LC4.2 and (b) LC4.7.

5.3.3 Tower base bending moments

It is of great interest to study the effect of blade number on the structural response. In this study the tower base bending moment was considered. The tower base bending moment is usually caused by the aerodynamic loads acting on the rotor as well as by the weight of the rotor due to the platform's pitch and roll motions.

Figure 15 compares the mean value and standard deviation of the tower base for-aft bending moment M_{FA} and side-side bending moment M_{SS} for the three floating VAWTs in LC4. Obviously the discrepancy in the mean value of both M_{FA} and M_{SS} for the three floating VAWTs is fairly small, and is much less notable than that in the standard deviation. This is due to two possible reasons: one is that the mean value of the aerodynamic loads acting on the rotor is very close to each other, and the torque arm resulting in the tower base bending moments is almost identical. Another reason is that these three floating VAWTs slightly differ in the rotor mass, and in the mean value of the pitch and roll motions of the platform since the pitch and roll motions are mainly wind-induced.

The 2-bladed semi VAWT gives significantly larger standard deviation than the 3- and 4-bladed semi VAWTs with respect to both the M_{FA} and M_{SS}, as illustrated in Figure 15. The ratio of the standard deviation of the 2-bladed semi VAWT to that of the 3-bladed semi VAWT varies from 2.37 to 3.93 for LC4.2-LC4.7, while the ratio of the standard deviation of the 4-bladed semi VAWT to that of the 3-bladed semi VAWT remains approximately constant at 0.8. It indicates that increasing blade number from 2 to 3 blades can decrease M_{FA} more significantly than increasing blade number from 3 to 4 blades. Similar conclusion can also be drawn for the M_{FA}. In addition, it is also interesting to see that for the 2-bladed semi VAWT the M_{FA} is smaller than the M_{SS} for all LCs except LC4.1, and the discrepancy between M_{FA} and M_{SS} can reach more than 20% at LC4.7 and LC4.8. But both 3- and 4-bladed semi VAWT predict to some extent larger M_{FA} than M_{SS} in LCs with wind speed at or below the rated one.

Power spectral analysis can be used to identify the different contributions to the variation of the M_{FA} and M_{SS}, as shown in Figure 16. These three floating VAWTs have very close low frequency turbulent wind induced response and wave frequency response, as well as noticeable different responses at the nP (2P, 3P and 4P) frequency.

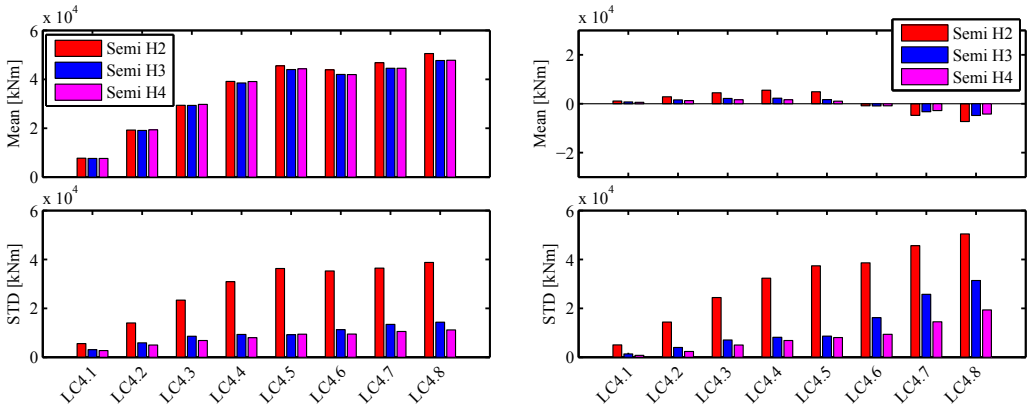

(a) Tower base fore-aft bending moment

(b) Tower base side-side bending moment

Figure 15: The mean value and standard deviation of tower base fore-aft and side-side bending moments of three floating VAWTs in LC4 with turbulent wind and irregular wave conditions.

Moreover, the nP response is increasingly dominating, especially in LCs with high wind speeds. For the 2-bladed semi VAWT, it is seen that not only is the 2P response significant but even the 4P response is visible, while only 3P and 4P response is captured for the 3- and 4-bladed semi VAWT, respectively.

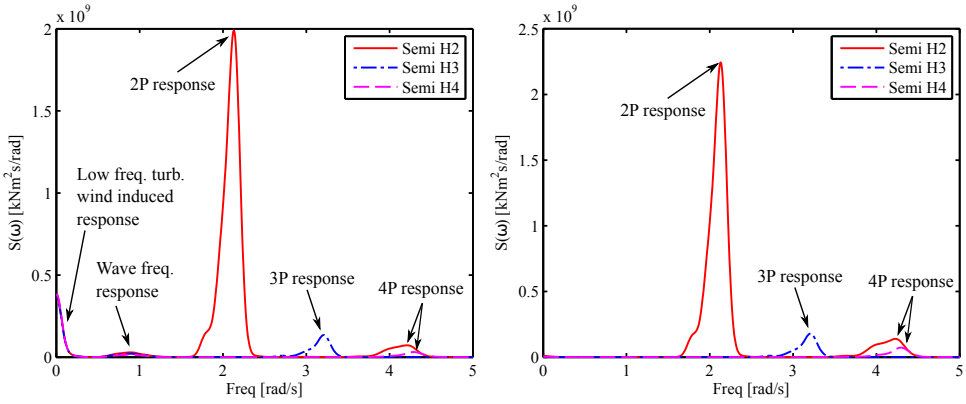

(a) Tower base fore-aft bending moment

(b) Tower base side-side bending moment

Figure 16: Power spectra of the (a) tower base fore-aft bending moment and (b) side-side bending moment of three floating VAWTs in LC4.3

5.3.4 Tension in mooring lines

Identical catenary mooring systems with three mooring lines were use to keep the three floating VAWTs in position. The layout of the mooring system is given by Robertson et al. (2012). Among the three mooring lines, the mooring line 2 is in line with the wind and wave directions and carries the largest tension when the floating VAWTs are

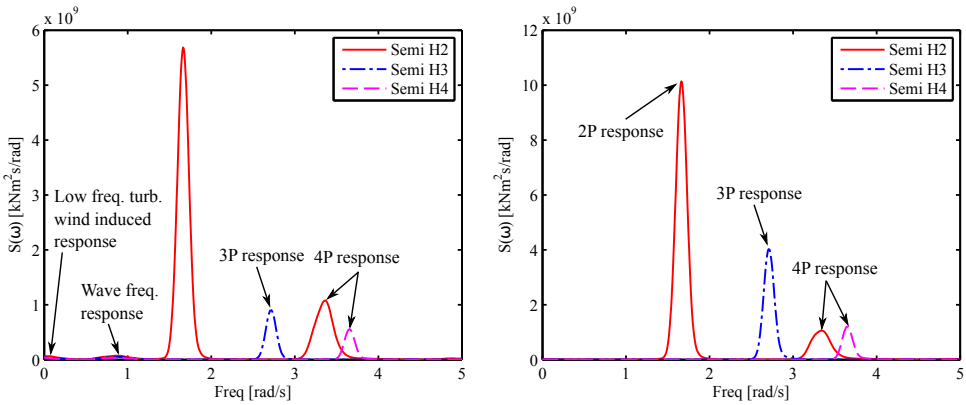

Figure 17: Power spectra of the (a) tower base fore-aft bending moment and (b) side-side bending moment of three floating VAWTs in LC4.7

subjected to the wind and wave loads. The tension in mooring line 2 is thus studied.

Figure 18 shows the mean value and standard deviation of the tension in mooring line 2 of the three floating VAWTs in LC4. It can be found that the mean value for each LC is very close to each other for the three floating VAWTs and visible difference is only observed in the standard deviation, especially in LCs with wind speed at or above the rated one. Moreover, the standard deviation is relatively small compared with the mean value, implying that the present mooring system could be sufficient even in survival conditions.

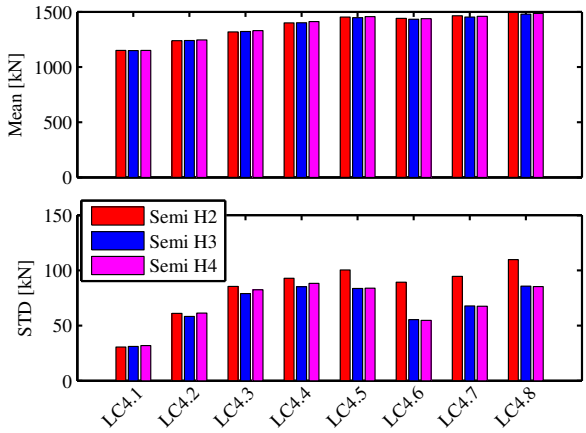

Figure 18: The mean value and standard deviation of the tension in mooring line 2 of three floating VAWTs in LC4 with turbulent wind and irregular wave conditions.

The difference in the standard deviation can be explored by using the power spectra analysis. Figure 19 gives the power spectra of tension in mooring line 2 of the three floating VAWTs for LC4.3 and LC4.7. Generally the

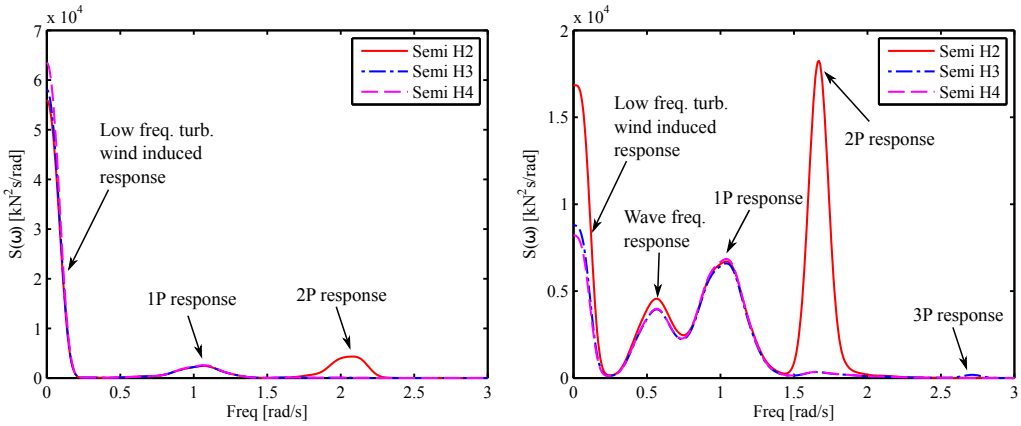

(a) LC4.3: Uw=10 m/s, Hs=2.88 m, Tp=9.98 s

(b) LC4.7: Uw=22 m/s, Hs=5.32 m, Tp=11.06 s

Figure 19: Power spectra of the tension in mooring line 2 of three floating VAWTs in (a) LC4.3 and (b) LC4.7.

power spectral density is dominated by the low frequency turbulent wind induced response and 1P response for the three floating VAWTs; and the wave frequency response also becomes dominating at LCs with high significant wave height. For the 2-bladed semi VAWT the 2P response is also very prominent, especially at LCs with high wind speed. In addition, a tiny 3P response is also captured for the 3-bladed semi VAWT in LC4.7 and LC4.8. But no 4P response for the 4-bladed semi VAWT is observed for all LCs. In LC4.2 to LC4.4, the 2-bladed semi VAWT gives the largest standard deviation of tension in mooring line 2 because of the 2P response; while in LC4.5 to LC4.8, not only considerably large 2P response but also the low frequency turbulent wind induced response contribute to the standard deviation, causing it much larger compared to those of the 3- and 4-bladed semi VAWTs.

6 Conclusions

This study deals with the effect of the number of blades on the dynamic behavior of floating vertical axis wind turbines (VAWTs) with straight parallel blades. Three straight-bladed VAWTs with identical solidity and with a blade number ranging from two to four were aerodynamically designed using the actuator cylinder flow method. These three VAWTs were then adapted to a semi-submersible platform to establish three floating straight-bladed VAWTs, which have identical draft and displacement and use the same mooring system. A generator torque controller was also designed and used to regulate the rotational speed based on a proportional-integral (PI) control algorithm.

The dynamic response of the floating VAWTs was then computed based on a series of load cases using the fully coupled aero-hydro-servo-elastic simulation tool SIMO-RIFLEX-AC. The floating VAWT systems were firstly identified using the eigen-frequency analysis, free decay tests and white noise wave simulations. The natural periods of rigid-body motions and response amplitude operators (RAOs) in surge, pitch and heave are all close to each other for the three floating VAWTs.

Steady wind simulations capture the effect of the number of blades on the structural responses of the landbased

and floating VAWTs. Floating substructures with a compliant mooring system can help to alleviate the variations in the structural responses, for instance in the tower base fore-aft and side-side bending moment. The tower base fore-aft bending moment, especially for the 2-bladed semi VAWT, can be greatly reduced above the rated wind speed, compared to that of the corresponding equivalent landbased one.

The impact of the number of blades is further studied using the turbulent wind and irregular wave simulations. Stochastic dynamic response analysis shows that the variation of aerodynamic loads such as the thrust and side force are strongly dependent on the number of blades; consequently the standard deviation of structural responses for instance the tower base bending moment is significantly influenced. Moreover, increasing the number of blades from two to three can decrease the variation in the tower base bending moment significantly whereas increasing from three to four blades has limited additional effect. However, the generator power production is not sensitive to the number of blades due to the control strategy used. Moreover, neither the platform motions nor mooring line tension are very sensitive to the number of blades either because of the compliant catenary mooring system.

As a whole, this study demonstrates the effect of the number of blades on the dynamic behavior of floating VAWTs using a fully coupled aero-hydro-servo-elastic approach and will serve as a basis for the preliminary design trade-offs with respect to the number of blades for floating VAWTs.

Acknowledgement

The authors would like to acknowledge the financial support from the EU FP7 project MARE WINT (project NO. 309395) and Research Council of Norway through the Centre for Ships and Ocean Structures (CeSOS) and Centre for Autonomous Marine Operations and Systems (AMOS) at the Department of Marine Technology, Norwegian University of Science and Technology (NTNU), Trondheim, Norway.

References

Anagnostopoulou, C., Kagemoto, H., Sao, K., Mizuno, A., 2015. Concept design and dynamic analyses of a floating vertical-axis wind turbine: case study of power supply to offshore greek islands. Journal of Ocean Engineering and Marine Energy 2 (1), 85–104.

Bedon, G., Schmidt Paulsen, U., Aagaard Madsen, H., Belloni, F., Raciti Castelli, M., Benini, E., 2015. Computational assessment of the deepwind aerodynamic performance with different blade and airfoil configurations. Applied Energy.

Borg, M., Collu, M., 2015. Frequency-domain characteristics of aerodynamic loads of offshore floating vertical axis wind turbines. Applied Energy 155, 629–636.

Borg, M., Collu, M., Brennan, F. P., 2013. Use of a wave energy converter as a motion suppression device for floating wind turbines. Energy Procedia 35, 223–233.

Brusca, S., Lanzafame, R., Messina, M., 2014. Design of a vertical-axis wind turbine: how the aspect ratio affects the turbine's performance. International Journal of Energy and Environmental Engineering 5 (4), 333–340.

Cahay, M., Luquiau, E., Smadja, C., Silvert, F., 2011. Use of a vertical wind turbine in an offshore floating wind farm. In: Offshore Technology Conference. Houston, Texas, USA.

Cheng, Z., Madsen, H. A., Gao, Z., Moan, T., 2016a. Aerodynamic modeling of offshore vertical axis wind turbines using the actuator cylinder method. Submitted to Energy Procedia.

Cheng, Z., Madsen, H. A., Gao, Z., Moan, T., 2016b. A fully coupled method for numerical modeling and dynamic analysis of floating vertical axis wind turbines. Submitted to Renewable Energy.

Cheng, Z., Wang, K., Gao, Z., Moan, T., 2015a. A comparative study on dynamic responses of spar-type floating horizontal and vertical axis wind turbines. Submitted to Wind Energy.

Cheng, Z., Wang, K., Gao, Z., Moan, T., 2015b. Dynamic response analysis of three floating wind turbine concepts with a two-bladed darrieus rotor. Journal of Ocean and Wind Energy 2, 213–222.

Collu, M., Brennan, F. P., Patel, M. H., 2014. Conceptual design of a floating support structure for an offshore vertical axis wind turbine: the lessons learnt. Ships and Offshore Structures 9 (1), 3–21.

Dabiri, J. O., 2011. Potential order-of-magnitude enhancement of wind farm power density via counter-rotating vertical-axis wind turbine arrays. Journal of Renewable and Sustainable Energy 3 (4), 043104.

Faltinsen, O. M., 1995. Sea loads on ships and offshore structures. Cambridge University Press, Cambridge, UK.

Ferreira, C. S., Madsen, H. A., Barone, M., Roscher, B., Deglaire, P., Arduin, I., 2014. Comparison of aerodynamic models for vertical axis wind turbines. Journal of Physics: Conference Series 524 (1), 012125.

IEC, 2005. International standard 61400-1, wind turbines, part 1: Design requirements.

Johannessen, K., Meling, T. S., Haver, S., 2002. Joint distribution for wind and waves in the northern north sea. International Journal of Offshore and Polar Engineering 12 (1).

Jonkman, B. J., 2009. Turbsim user's guide: Version 1.50.

Jonkman, J. M., Butterfield, S., Musial, W., Scott, G., 2009. Definition of a 5-mw reference wind turbine for offshore system development. Tech. Rep. NREL/TP-500-38060, NREL, Golden, CO, USA.

Li, Q., Maeda, T., Kamada, Y., Murata, J., Furukawa, K., Yamamoto, M., 2015. Effect of number of blades on aerodynamic forces on a straight-bladed vertical axis wind turbine. Energy 90, 784–795.

Madsen, H. A., 1982. The Actuator Cylinder: A flow model for vertical axis wind turbines. Institute of Industrial Constructions and Energy Technology, Aalborg University Centre.

MARINTEK, 2012a. Riflex theory manual, version 4.0.

MARINTEK, 2012b. Simo-theory manual version 4.0.

Merz, K. O., Svendsen, H. G., 2013. A control algorithm for the deepwind floating vertical-axis wind turbine. Journal of Renewable and Sustainable Energy 5 (6), 063136.

Paquette, J., Barone, M., 2012. Innovative offshore vertical-axis wind turbine rotor project. In: EWEA 2012 Annual Event. Copenhagen, Denmark.

Paraschivoiu, I., 2002. Wind turbine design: with emphasis on Darrieus concept. Polytechnic International Press., Montreal, Canada.

Robertson, A., Jonkman, J., Masciola, M., Song, H., Goupee, A., Coulling, A., Luan, C., 2012. Definition of the semi-submersible floating system for phase II of OC4. Report.

Vita, L., 2011. Offshore floating vertical axis wind turbines with rotating platform. Phd thesis, Technical University of Denmark.

Wang, K., Cheng, Z., Moan, T., Hansen, M. O. L., 2015. Effect of difference-frequency forces on the dynamics of a semi-submersible type FVAWT in misaligned wave-wind condition. In: Proceedings of the 25th International Ocean and Polar Engineering Conference.

Wang, K., Hansen, M. O. L., Moan, T., 2014. Dynamic analysis of a floating vertical axis wind turbine under emergency shutdown using hydrodynamic brake. Energy Procedia 53, 56–69.

Wang, K., Moan, T., Hansen, M. O. L., 2013. A method for modeling of floating vertical axis wind turbine. In: Proceedings of the 32th International Conference on Ocean, Offshore and Arctic Engineering.

Wang, K., Moan, T., Hansen, M. O. L., 2016. Stochastic dynamic response analysis of a floating vertical-axis wind turbine with a semi-submersible floater. Wind Energy.

A.4 Paper 4

Paper 4:

Dynamic response analysis of three floating wind turbine concepts with a two-bladed Darrieus rotor.

Zhengshun Cheng, Kai Wang, Zhen Gao, Torgeir Moan

Published in *Journal of Ocean and Wind Energy*, 2:213-222, 2015, DOI: 10.17736/jowe.2015.jcr33

Journal of Ocean and Wind Energy (ISSN 2310-3604)
Copyright © by The International Society of Offshore and Polar Engineers
Vol. 2, No. 4, November 2015, pp. 213–222; http://dx.doi.org/10.17736/jowe.2015.jcr33
http://www.isope.org/publications/publications.htm

Dynamic Response Analysis of Three Floating Wind Turbine Concepts with a Two-Bladed Darrieus Rotor

Zhengshun Cheng*
Department of Marine Technology, Norwegian University of Science and Technology
Trondheim, Norway

Kai Wang
Centre for Ships and Ocean Structures, Norwegian University of Science and Technology
Trondheim, Norway

Zhen Gao
Department of Marine Technology, Norwegian University of Science and Technology
Trondheim, Norway

Torgeir Moan
Centre for Autonomous Marine Operations and Systems (AMOS)
Norwegian University of Science and Technology, Trondheim, Norway

Recently, interest in the development of floating vertical axis wind turbines (FVAWTs) has been increasing, since FVAWTs might prove to be one of the optimal configurations in deep waters. In this study, a FVAWT with a 5 MW Darrieus rotor was used as the reference wind turbine and was mounted on three different floating support structures: the OC3 spar buoy, the OC4 semi-submersible, and a tension leg platform (TLP). Fully coupled nonlinear time domain simulations using the code SIMO-RIFLEX-DMS were conducted. A series of load cases with turbulent wind and irregular waves was carried out to investigate the dynamic responses of these three FVAWT concepts by estimating the generator power production, the platform motions, the tower base bending moments, and the mooring line loads. For the spar, semi-submersible, and TLP FVAWT concepts, twice-per-revolution (2P) effects resulting from the 2P aerodynamic loads are prominent in the dynamic responses of these concepts. Because of the compliant catenary mooring systems, the spar and the semi-submersible can help to mitigate the 2P effects on structural loads and mooring line tensions as compared to the TLP concept, at the cost of larger platform motions. The TLP is not a good substructure for a vertical axis wind turbine unless the cyclic variation of aerodynamic loads is significantly reduced.

INTRODUCTION

During the 1970s and 1980s, considerable efforts were devoted to investigate and develop Darrieus vertical axis wind turbines (VAWTs), mainly in the USA and Canada (Paraschivoiu, 2002). Commercial Darrieus VAWTs were also developed by the FloWind Corporation. Unfortunately, after the bankruptcy of the FloWind Corporation and the termination of VAWT research sponsored by the U.S. Department of Energy, VAWTs lost ground to the horizontal axis wind turbines (HAWTs) that are predominant today. However, as wind farms are moving toward deeper waters where large floating wind turbines will be more economical, this may change, since the cost of installation and maintenance will become relatively more important.

As a matter of fact, floating vertical axis wind turbines (FVAWTs) have several advantages over floating horizontal axis wind turbines (FHAWTs), such as lower centers of gravity, wind direction independence, and lower costs. Paquette and Barone (2012) indicated that FVAWTs have the potential of achieving more than 20% of the cost of energy reductions compared with FHAWTs. Moreover, FVAWTs are more suitable for deployment as wind farms compared to FHAWTs. The wake of a pair of counter-rotating H-rotors can dissipate much more quickly than that of FHAWTs, allowing them to be packed closer (Kinzel et al., 2012). The average power generated by a pair of H-rotors at all azimuth angles is higher than that of an isolated turbine (Dabiri, 2011), implying that the conversion efficiency of VAWTs can be improved. In addition, other efforts on comparative study of HAWTs and VAWTs have also been made by several researchers to reveal the merits and feasibilities of each concept, including Paraschivoiu (2002), Islam et al. (2013), and Jamieson (2011). Borg et al. (2014) compared VAWTs with HAWTs in technology, conversion efficiency, upscaling, fatigue, machinery position, etc. Wang et al. (2014) conducted a comparative study of a FVAWT with a 5 MW Darrieus rotor (Vita, 2011) and a FHAWT with the NREL 5 MW wind turbine (Jonkman et al., 2009), both mounted on the OC4 semi-submersible platform (Robertson et al., 2012).

For these reasons, interest in FVAWTs is resurging, and various FVAWT concepts are being proposed, including the DeepWind concept (Paulsen et al., 2011), VertiWind concept (Cahay et al., 2011), etc. Similar to those of the FHAWTs, the substructures for the FVAWT concepts can also be classified into the spar, semi-submersible, and tension leg platform (TLP) types in terms of how they achieve static stability. A semi-submersible type FVAWT

*ISOPE Member.
Received March 23, 2015; revised manuscript received by the editors August 14, 2015. The original version was submitted directly to the Journal.
KEY WORDS: Floating vertical axis wind turbine, dynamic analysis, spar; semi-submersible, tension leg platform.

with a 5 MW Darrieus rotor mounted on the OC4 DeepCwind semi-submersible (Robertson et al., 2012) was proposed and analyzed by Wang et al. (2013). A spar-type FVAWT with the same rotor placed on the OC3 Hywind spar buoy (Jonkman, 2010) was also put forward by Borg and Collu (2014) and Cheng et al. (2015). Fully coupled aero-hydro-servo-elastic dynamic simulations were carried out for the FVAWTs. State-of-the-art limited comparative studies on different FVAWT concepts have been conducted. Borg and Collu (2014) performed preliminary investigations of the dynamic responses of FVAWTs with the spar, semi-submersible, and TLP floaters; however, the yaw of the spar and the surge and sway of the TLP were disabled during the simulations. Moreover, the structural elasticity and variable speed control were not taken into account.

To better understand the performance and benefit of FVAWTs, the current work compares the dynamic response characteristics of three FVAWT concepts. A 5 MW Darrieus rotor was mounted on three platforms: the OC3 Hywind spar (Jonkman, 2010), the OC4 DeepCwind semi-submersible (Robertson et al., 2012), and a TLP design by Bachynski and Moan (2012). Fully coupled time domain simulations were carried out using the SIMO-RIFLEX-DMS code, which is an aero-hydro-servo-elastic computational code. A number of load cases (LCs) were carried out to study the dynamic responses of the three FVAWT concepts. Motions, tower base bending moments, and mooring line tensions were calculated and compared. The results reveal the merits, disadvantages, and feasibilities of each FVAWT concept and will help to resolve preliminary design trade-offs among the three FVAWT concepts.

FLOATING WIND TURBINE MODELS

Three floating support structures were studied here: a spar, a semi-submersible, and a TLP, as depicted in Fig. 1 and listed in Table 2. The concepts were used to support a 5 MW Darrieus rotor, which is the baseline design developed in the DeepWind project (Vita, 2011). The rotor is comprised of two blades and one rotating tower that spans from the top to the bottom, which is connected to the generator. The main specifications of this rotor are summarized in Table 1. The generator considered here was assumed to be placed at the tower base, and the generator mass was incorporated in the platform hull mass.

The concepts were originally designed to support the NREL 5 MW wind turbine (Jonkman et al., 2009). The concepts were considered in the water depth where they were designed, ranging from 150 m for the TLP to 200 m for the semi-submersible to 320 m for the spar. Here reasonable modifications were made to each platform to support the 5 MW Darrieus rotor, such as adjusting the ballast of the spar and the semi-submersible, and the tendon pre-tension of the TLP. For each platform, the draft

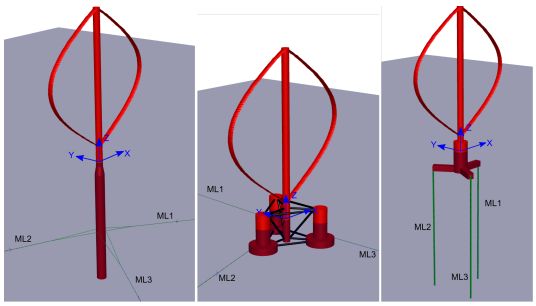

Fig. 1 Three FVAWT concepts: spar, semi-submersible, and TLP

Rated power [MW]	5
Rotor height, root to root [m]	129.56
Rotor radius [m]	63.74
Chord length [m]	7.45
Airfoil section	NACA 0018
Cut-in, rated, cut-out wind speed [m/s]	5, 14, 25
Rated rotational speed [rpm]	5.26
Total mass, incl. rotor and tower [kg]	754,226
Center of mass [m]	(0, 0, 75.6)

Table 1 Specifications of the Darrieus 5 MW wind turbine

Floater	Spar	Semi	TLP
Water depth [m]	320	200	150
Draft [m]	120	20	22
Waterline diameter [m]	6.5	12.0/6.5	14.0
Hull mass, including ballast and generator [ton]	7,308.3	13,353.7	2,771.9
CM location below MSL [m]	−89.76	−13.42	−15.38
Displacement [m^3]	8,027	13,919	5,655
CB location below MSL [m]	−62.06	−13.15	−14.20
Moment of inertia in roll about global x-axis [ton·m^2]	6.362×10^7	9.159×10^6	9.871×10^5
Moment of inertia in pitch about global y-axis [ton·m^2]	6.362×10^7	9.159×10^6	9.871×10^5
Moment of inertia in yaw about platform centerline [ton·m^2]	1.588×10^5	1.209×10^7	2.288×10^5

Table 2 Properties of the three floating platforms; MSL, mean sea level; CM, center of mass; CB, center of buoyancy

and displacement were maintained the same as the original one. Since the difference in mass between the 5 MW Darrieus rotor and the NREL 5 MW wind turbine was small compared to the displacements of the three concepts, it was assumed that such modifications would not alter the hydrostatic performance of each platform significantly, which was verified by the following simulations. After these modifications, these substructures supporting the 5 MW Darrieus rotor may not be optimal from an economical point of view, but they are sufficient to demonstrate the inherent motion and structural response characteristics of each concept.

Spar Structure

The spar platform studied here was the OC3 Hywind hull, as described by Jonkman (2010). The spar consists of two cylindrical regions connected by a linearly tapered conical region. The heavy ballast located at the bottom provides good stability and restoring stiffness, thus limiting the platform pitch and roll motion in wind and waves. A catenary chain mooring system with delta lines and clump weights was applied to approximate the horizontal restoring stiffness, as described by Jonkman (2010); a schematic layout of the mooring system is illustrated by Karimirad and Moan (2012). Because of the difference in mass between the Darrieus rotor and the NREL 5 MW wind turbine, the ballast was adjusted to retain the same draft and displacement specified for the spar FHAWT, leading to changes in the hull mass, center of gravity, and moment of inertia, as highlighted in Table 2. The moments of inertia are calculated with respect to the origin of the global coordinate system, as shown in Fig. 1.

Semi-Submersible Structure

The semi-submersible platform considered here was the OC4 DeepCwind semi-submersible, as defined by Robertson et al.

(2012). The semi-submersible is composed of three offset columns, three pontoons, a central column, and braces. The rotor is located on the central column. Braces are used to connect all of the columns as an integrated body. Three catenary mooring lines are attached to the three offset columns to provide horizontal restoring stiffness. Good stability is achieved by the large waterplane area moment of inertia to limit the pitch and roll motion in wind and waves. The ballast was also adjusted to maintain the same draft and displacement as that of the semi-submersible FHAWT described by Robertson et al. (2012).

Tension Leg Structure

The TLP model considered here was a design by Bachynski and Moan (2012), which is identical to the TLPWT 3. The TLP model consists of one large central column, which contributes to approximately 60% of the displacement, and three pontoons. The stability is obtained by three tendons to limit the global motions in wind and waves. Because of the tendon pre-tension, the hull mass, including ballast and generator, is approximately one-half of that corresponding to the displacement, as shown in Table 2. Here the same draft and displacement as the TLP FHAWT were also maintained for the TLP FVAWT by changing the tendon pretension from 8,262 kN to 7,450.9 kN.

METHODOLOGY

Numerical simulations were carried out in order to investigate the dynamic responses of the FVAWTs. The code SIMO-RIFLEX-DMS, developed by Wang et al. (2013; 2015a), was used to conduct the fully coupled nonlinear time domain simulations. It can account for the turbulent wind inflow, aerodynamics, hydrodynamics, control dynamics, structural mechanics, and mooring line dynamics. Three computer codes are integrated in the code SIMO-RIFLEX-DMS. SIMO computes the rigid body hydrodynamic forces and moments on the hull (MARINTEK, 2012a); RIFLEX represents the blades, tower, shaft, and mooring lines as nonlinear bar or beam elements and provides the links to an external controller and DMS (MARINTEK, 2012b); and DMS calculates the aerodynamic loads on the rotor. The generator torque controller was written in Java, which is able to maximize the power capture below the rated operating point and keep the rotational speed constant above the rated operating point. The SIMO-RIFLEX wind turbine module has previously been verified (Luxcey et al., 2011; Ormberg et al., 2011), and the code SIMO-RIFLEX-DMS was verified in Wang et al. (2013).

The aerodynamic loads on the rotor were calculated according to the double multi-streamtube (DMS) theory (Paraschivoiu, 2002). The DMS model accounted for the effect of variation in the Reynolds number and incorporated the effect of dynamic stall by using the Beddoes–Leishman dynamic stall model. In the DMS model, the relative velocity seen at a blade section is the vector sum of the free wind speed and the induced velocity, subtracting the velocity due to the motion. The velocity of the motion is comprised of the blade rotation, the translational and rotational velocities of the platform, and the elastic deformation of the blades. The aerodynamic code DMS is validated by comparison with experimental results (Wang et al., 2015a).

The hydrodynamic model of each concept included a combination of potential flow and Morison's equation. Added mass, radiation damping, and first order wave forces were obtained from a potential flow model and applied in the time domain using the convolution technique (Faltinsen, 1995). Additional viscous forces on large volume structures were incorporated through Morison's equation. The Morison equation was also applied to slender elements that were not included in the potential flow model. Morison coefficients in the hydrodynamic model are those used by Bachynski et al. (2014). In addition to the first-order and viscous hydrodynamic forces, second-order wave forces were also considered for the spar, semi-submersible, and TLP, respectively. For the spar hull, the mean wave drift forces were applied, and Newman's approximation was used to estimate the second-order difference-frequency wave excitation forces. Regarding the semi-submersible platform, the second-order difference-frequency wave excitation force was considered, using the full quadratic transfer function (QTF). The effect of second-order difference-frequency force on the dynamic responses of this semi-submersible FVAWT in misaligned wind–wave conditions was studied by Wang et al. (2015c). With respect to the TLP FVAWT, second-order difference-frequency wave excitation forces using Newman's approximation and sum-frequency wave excitation forces using the full QTF were applied.

Regarding the structural model of each concept, the platform hull was considered as a rigid body. The tower, blades, and shaft were modeled by using beam elements; the catenary mooring lines of the spar and semi-submersible were represented by using bar elements; and the tendons for the TLP were modeled by using beam elements and connecting joints.

LOAD CASES (LCs) AND ENVIRONMENTAL CONDITIONS

A series of load cases (LCs) was defined to perform the comparative study for the three FVAWT concepts, as summarized in Tables 3 and 4. In LC1, free decay tests in surge, heave, pitch, and yaw were carried out to assess the natural periods. In LC2, both the unidirectional white noise test and a number of regular wave tests were conducted to estimate the response amplitude operators (RAOs) of the FVAWTs. In LC3 are six conditions with correlated and directionally aligned wind and waves.

The three-dimensional turbulent wind fields were generated by using the National Renewable Energy Laboratory's (NREL's) TurbSim program (Jonkman, 2009) according to the Kaimal turbulence model for IEC Class C. Both the normal wind profile (NWP) and normal turbulence model (NTM) were applied. Regarding the NWP condition, the wind profile $U(z)$ is the aver-

	Load cases (LCs)	Response	Wind	Waves
LC1	Decay	Decay	–	Calm water
LC2.1	White noise	RAO	–	White noise
LC2.2	Regular waves	RAO	–	Regular waves

Table 3 Load cases (LCs): decay, white noise, and regular wave conditions

LC	U_w [m/s]	H_s [m]	T_p [s]	Turb. model	Sim. len. [s]
LC3.1	5	2.10	9.74	NTM	3,600
LC3.2	10	2.88	9.98	NTM	3,600
LC3.3	14	3.62	10.29	NTM	3,600
LC3.4	18	4.44	10.66	NTM	3,600
LC3.5	22	5.32	11.06	NTM	3,600
LC3.6	25	6.02	11.38	NTM	3,600

Table 4 Load cases (LCs): combined wind and wave conditions; NTM, normal turbulence model; Sim. len., simulation length

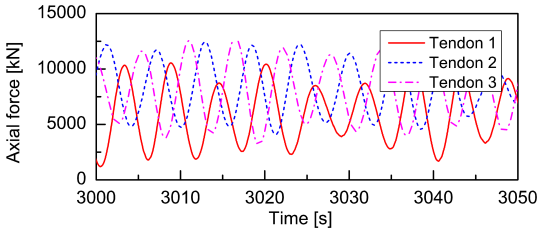

Fig. 2 Time history of the tendon axial forces for the TLP FVAWT in LC3.3 with $U_w = 14$ m/s, $H_s = 3.62$ m, and $T_p = 10.29$ s

age wind speed as a function of height z above the mean sea level (MSL) and is given by the power law as follows:

$$U(z) = U_{\text{ref}}(z/z_{\text{ref}})^{\alpha} \tag{1}$$

where U_{ref} is the reference wind speed, z_{ref} is the height of the reference wind speed, and α is the power law exponent. The value of z_{ref} was set to 79.78 m (the vertical center of the blades) above the MSL. The value of α was chosen to be 0.14 for the floating wind turbines according to IEC 61400-3 (IEC, 2009). The mean wind speed U_w given in Table 4 is the reference wind speed at the vertical center of the blades. The JONSWAP wave model was used to generate the wave history. The significant wave height H_s and peak period T_p were set in accordance with the correlation with wind speed for the Statfjord site in the northern North Sea (Johannessen et al., 2002).

For the combined wind and wave simulations, each simulation lasted 4,600 s and corresponded to a one-hour dynamic analysis, since the first 1,000 s were removed to eliminate the start-up transient effects. Five identical and independent one-hour simulations with different seeds for the turbulent wind and irregular waves were carried out for each LC to reduce the stochastic variations. It should be noted here that only LC3.2 and LC3.3 were conducted for the TLP FVAWT, since negative tendon axial forces will arise for large wind speeds. One possible reason for such negative tendon tension is due to the reduction of tendon pre-tension, but the primary reason is due to the essential characteristics of aerodynamic loads acting on the rotor. The aerodynamic loads are always periodic and are varying with large amplitude, which induce a twice-per-revolution (2P) response in platform motions and thus cause large variation of tension in the tendon, as demonstrated in Fig. 6. Figure 2 also presents the time history of the tendon axial force for the TLP FVAWT in LC3.3. Large variations are observed in the tendon axial forces with period equal to the 2P period. These variations increase with increasing mean wind speed and give rise to negative axial forces, which is unrealistic.

RESULTS AND DISCUSSIONS

Free Decay Tests

The three floaters considered here are originally designed to support the NREL 5 MW baseline wind turbine. When they are used to support the 5 MW Darrieus rotor, modifications such as adjusting the ballast for the spar and the semi-submersible or reducing the tendon pre-tension for the TLP have been made to maintain the same draft and displacement as the original ones. Such modifications can lead to changes in the natural periods in the global motions. The natural periods of the three FVAWT concepts are given in Table 5. Free decay tests in calm water were carried out to estimate the natural periods. In the free decay tests, the wind turbine was parked with the rotor plane parallel to the x-axis of the global coordinate system, as demonstrated in Fig. 1, and no aerodynamic loads acted on the rotor.

Floater	Spar	Semi	TLP
Surge/Sway [s]	130.8	114.0	45.3
Heave [s]	27.3	17.1	0.6
Roll/Pitch [s]	34.5	31.0	4.5/4.9
Yaw [s]	8.5	79.7	19.3

Table 5 Natural periods of the three FVAWT concepts obtained by free decay tests

In surge and sway, the spar and the semi-submersible have very large natural periods because of the relatively small surge and sway restoring stiffness of the catenary mooring system employed. In heave, the natural periods of the spar and the TLP are located outside the upper and lower limits of ocean wave periods, respectively, while the natural period of the semi-submersible is well within the wave excitation range, indicating that significant heave motion for the semi-submersible can be excited. In roll and pitch, the natural periods of these three platforms are also well situated outside the wave periods, implying that the wave-induced pitch motion will be small. In addition, for the TLP FVAWT, due to the rotor orientation, the rotor contributes a lot to the roll/pitch moments of inertia and causes different roll and pitch natural periods. Since the yaw natural period of the spar is well within the wave period, the spar FVAWT may experience significant yaw motion.

Response Amplitude Operators (RAOs) for Wave Loads

The hydrodynamic performance of the three floating concepts can be characterized by response amplitude operators (RAOs). The RAOs can be obtained through unidirectional white noise simulations or a number of regular wave simulations. In the present study, both white noise simulations and regular wave simulations were performed. The white noise waves were generated using fast Fourier transform (FFT) with a frequency interval $\Delta\omega = 0.005$ rad/s. The surge and pitch RAOs are presented in Figs. 3 and 4, respectively. The white noise simulation technology captures almost the same natural frequencies as those obtained by the free decay tests. It also predicts all RAOs accurately except at the resonant frequency of each mode. Since the center of gravity of the spar FVAWT is approximately 73.5 m below MSL, there is

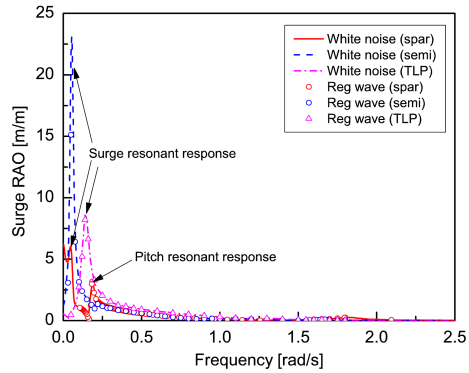

Fig. 3 Surge RAO of the three FVAWT concepts

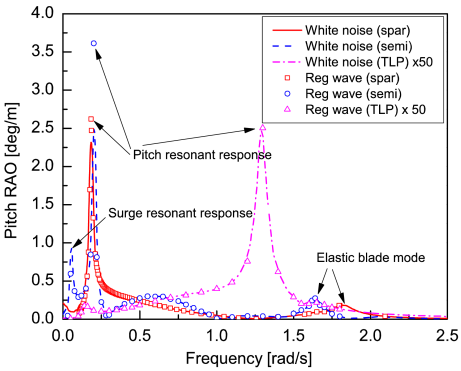

Fig. 4 Pitch RAO of the three FVAWT concepts; the pitch RAO of the TLP FVAWT is multiplied by 50.

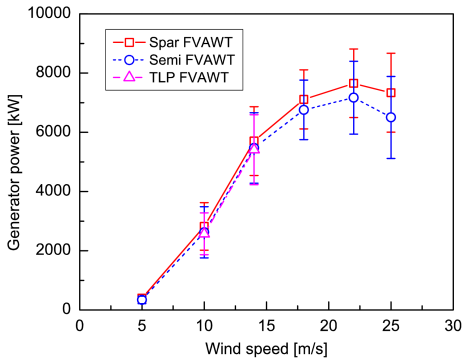

Fig. 5 Mean power production for the three FVAWT concepts with error bar indicating the standard deviation from the mean value

a close coupling between surge and pitch, resulting in relatively large surge RAOs at the pitch natural frequency, as illustrated in Fig. 3. As given in Table 5 and demonstrated in Figs. 3 and 4, the natural frequencies of surge and pitch for the spar FVAWT and the semi-submersible FVAWT are very close to each other. In addition, the semi-submersible FVAWT has much larger RAOs at both surge and pitch resonant frequencies than the spar FVAWT. Regarding the TLP FVAWT, it only exhibits large surge RAOs in the vicinity of the surge natural frequency, and the pitch RAOs are very close to zero as a result of the tensioned tendons.

During the present simulations, the structural elasticity of the curved blades and the tower were taken into account. Peaks corresponding to the elastic blade flatwise mode are thus observed in the pitch RAO for the spar FVAWT and the semi-submersible FVAWT, as presented in Fig. 4. The first 10 eigenmodes of the onshore VAWT have been discussed by Wang et al. (2013). It is obvious that the first blade flatwise frequency and the frequencies corresponding to these two peaks for the spar FVAWT and the semi-submersible FVAWT do not exactly coincide. These discrepancies come from the differences in mass and restoring coefficients of the floating platforms, which cause a small shift in the first blade flatwise frequency as compared to the onshore VAWT.

Generator Power Performance

The stochastic dynamic responses of the three FVAWT concepts are studied under the turbulent wind and irregular wave conditions, including the generator power production, global platform motion, tower base fore-aft and side-to-side bending moment, and the tensions of the mooring lines. For each case of each FVAWT model, five identical and independent one-hour simulations were performed; the mean value and standard deviation of the dynamic responses were obtained by averaging the mean values and standard deviations of five one-hour ensembles.

Figure 5 shows the generator power production of the three FVAWT concepts under the turbulent wind and irregular wave conditions. Hereinafter, the results are plotted with the mean wind speed as the variable along the abscissa axis for simplicity. The power curve is based on the mean generator power production with the error bar showing the standard deviation from the mean value. The mean generator powers of the three FVAWT concepts increase as the wind speed increases. At rated wind speed of 14 m/s, the mean generator powers slightly exceed the rated power of 5 MW, since the Beddoes–Leishman dynamic stall model is included in the DMS model. The controller implemented is designed to keep the rotational speed constant when the rated operating point is reached; the mean generator powers are therefore increasing at above rated wind speeds. The effects of this nonconstant power production at above rated wind speeds on the grid can be reduced when the FVAWTs are operated as wind farms. Moreover, a more robust controller will be developed in the future to improve the generator power performance for the FVAWT.

In addition, the mean generator powers of the three FVAWT concepts are very close to each other, except at high wind speeds where the mean generator power of the semi-submersible FVAWT begins to differ from that of the spar FVAWT. The difference results from the different rotational speed and increases as the wind speed increases. The different rotational speed for the three concepts is due to the fact that the controller implemented in the present study is not very robust: it fails to keep the rotational speed at above rated wind speed exactly constant. The variations of the generator power for the three FVAWT concepts are very close to each other as well.

Platform Motions

Because of the differences in structural and hydrodynamic properties and in mooring systems, the three FVAWT concepts present different global motions. The platform motions are defined in the global coordinate system with the z-axis along the tower and the x-axis parallel to the wind direction, as depicted in Fig. 1. Power spectra analysis with frequency smoothing using a Parzen window function was used to analyze the time series of global motions. Figure 6 shows the power spectrum of surge, roll, pitch, and yaw motions for the three FVAWT concepts under the turbulent wind and irregular wave conditions with $U_w = 14$ m/s, $H_s = 3.62$ m, and $T_p = 10.29$ s, respectively. The responses corresponding to the 2P frequency are observed for each FVAWT. The 2P frequency arises from the characteristic of aerodynamic loads acting on the two-blade VAWT. Since the rotating axis is not parallel to the wind direction, the angle of attack of each blade varies with the azimuth angle of the shaft, leading to the variation of resulting aerodynamic loads within one revolution. For a two-blade FVAWT, the resultant aerodynamic forces and torque vary twice per revolution and thus give rise to the 2P frequency responses. The semi-submersible FVAWT has larger 2P responses in pitch and roll motions, while the spar FVAWT has large 2P responses in surge and sway motions. These 2P responses increase as the wind speed increases.

Because of the taut mooring system, the spectrum of motions for the TLP FVAWT is much smaller than that of the spar FVAWT and the semi-submersible FVAWT. The surge motions of the three FVAWTs are dominated by the low-frequency responses due to the turbulent wind and surge resonant responses. The wave frequency surge responses are larger than the corresponding 2P responses. The spar FVAWT has much larger wind-induced surge motion, as well as the 2P responses, while the TLP FVAWT has larger wave-frequency surge responses. The spectrum of sway motion differs from the surge spectrum since the wind-induced sway responses of the semi-submersible FVAWT are otherwise much larger than those of the spar FVAWT, though the low-frequency wind-induced sway responses are both dominating. For the semi-submersible FVAWT, the wind-induced surge and sway are the same order of magnitude, which means that the misaligned wind and wave are of interest, as has been studied by Wang et al. (2015b). The heave spectrum of the three FVAWTs is mainly wave-frequency dominated.

The spectrum of pitch motions is very similar to that of the surge motion, as the wind-induced responses and the pitch resonant responses are more dominating. The semi-submersible FVAWT has larger wave frequency response and 2P responses in pitch than the spar FVAWT, but the pitch motion of the spar FVAWT is otherwise larger due to the dominating wind-induced responses in the turbulent wind conditions, as shown in Fig. 6c. The pitch response of the TLP FVAWT is much smaller than the others. Not only the 2P roll response but also the 1P roll response can be observed for the semi-submersible FVAWT, as illustrated in Fig. 6b. The wind-induced roll responses are very small, which differs from the sway responses. Regarding the yaw motion, the yaw responses are also dominated by the turbulent wind-induced yaw responses for the three FVAWTs. The yaw motion of the semi-submersible FVAWT is significantly magnified under the turbulent wind condition because the turbulent wind excites the yaw resonant response. For the spar FVAWT and the TLP FVAWT, the 2P yaw response is more prominent than for the semi-submersible FVAWT; this is a consequence of the mooring system used.

Figure 7 compares the mean values and standard deviations of the global motions of the three FVAWT concepts under the turbulent wind and irregular wave conditions. Here only the results of surge, pitch, and yaw motion are presented. The error bar indicates the standard deviation from the mean value. The mean values of the global motion increase as the wind speed increases, since the mean values are mainly wind-induced. For the TLP FVAWT, as a result of the tensioned tendons, the vertical motions including the roll, pitch, and heave are close to zero, and the surge and sway are also much smaller than those of the spar FVAWT and the semi-submersible FVAWT. For the spar FVAWT and the semi-submersible FVAWT, the spar FVAWT presents larger mean pitch motion due to the smaller pitch restoring coefficient, but the standard deviations are very close to each other. Since the center of gravity of the spar FVAWT is 73.5 m below MSL, which is much larger than that of the semi-submersible FVAWT, the mean value and standard deviation of surge motion for the spar FVAWT are therefore significantly larger: the mean surge motion reaches 35.20 m under LC3.6. Similar results can be observed for the mean values of roll and sway motions for the spar FVAWT and the semi-submersible FVAWT. Though the mean values of each global motion in surge, sway, pitch, and roll illustrate significant discrepancies for the three FVAWT concepts, the mean yaw motions are fairly close, as shown in Fig. 7c. In addition, the standard deviation of yaw of the semi-submersible FVAWT is much larger than that of the spar FVAWT; this is because the resonant yaw motions are excited by the turbulent wind.

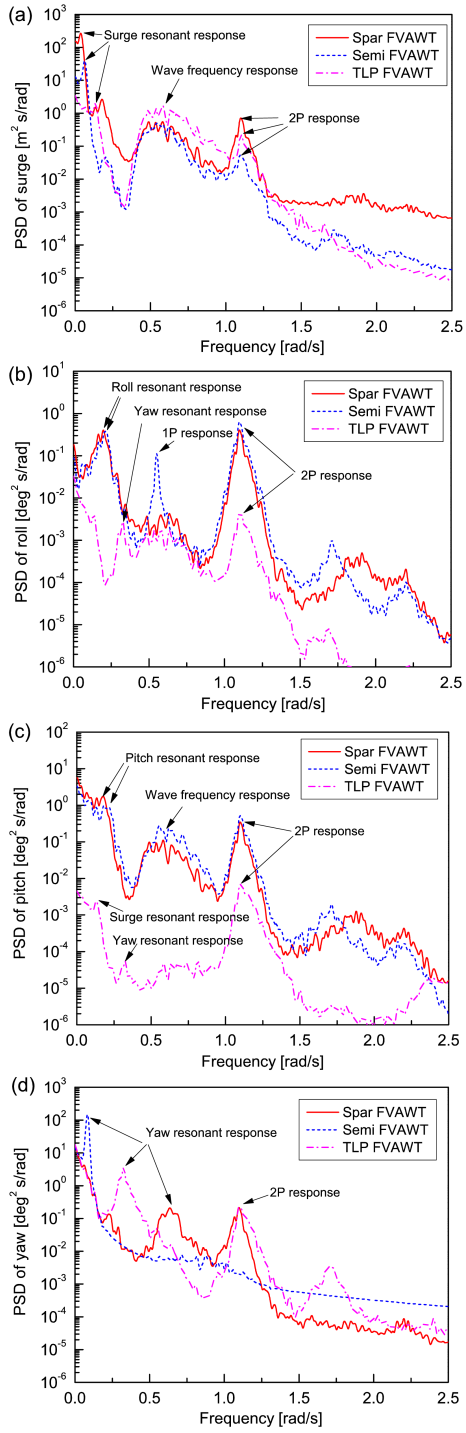

Fig. 6 Power spectra of (a) surge, (b) roll, (c) pitch, and (d) yaw motions for the three FVAWT concepts in LC3.3 with $U_w =$ 14 m/s, $H_s = 3.62$ m, and $T_p = 10.29$ s; different scales are used along the abscissa axis and ordinate axis.

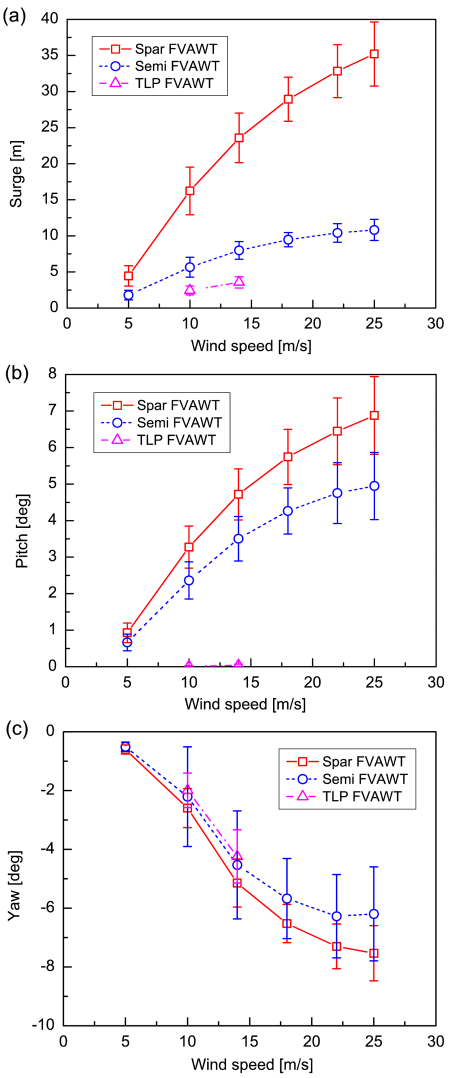

Fig. 7 Mean values of (a) surge, (b) pitch, and (c) yaw motions for the three FVAWT concepts with error bar indicating the standard deviation; there are no results for TLP FVAWT at LC4 through LC6.

Tower Base Bending Moment

Here the tower base was assumed to be located below the bearings between the rotating shaft and the drivetrain shaft. The tower base bending moment is caused by the large aerodynamic force acting on the rotor and by the weight of the rotor due to the tower tilt. Even under the same environmental condition, the three FVAWT concepts demonstrate significant differences in platform motions, leading to discrepancies in the tower base bending moment. Here both the tower base fore-aft bending moment M_{FA} and side-to-side bending moment M_{SS} are chosen as the primary structural performance parameters. Since the aerodynamic loads of each blade vary with the azimuthal angle, not only M_{FA} but also M_{SS} have great variations, which is quite different from

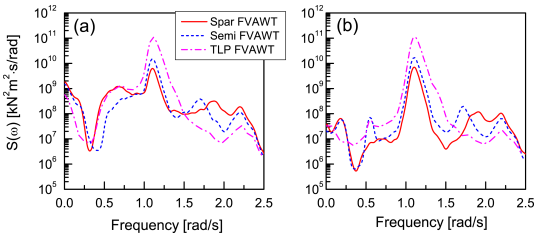

Fig. 8 Power spectra of (a) tower base fore-aft bending moment and (b) tower base side-to-side bending moment for the three FVAWT concepts in LC3.3 with $U_w = 14$ m/s, $H_s = 3.62$ m, and $T_p = 10.29$ s

the HAWT. These variations of bending moments can cause large stress fluctuations, thus leading to great fatigue damage.

Figure 8 compares the power spectra of M_{FA} and M_{SS} under the turbulent wind and irregular wave conditions. The turbulent winds excite the certain low-frequency response of M_{FA}, but the wind-induced response is much smaller than the 2P response in both M_{FA} and M_{SS}. Furthermore, since the taut tendons cannot absorb the 2P aerodynamic excitations for the TLP FVAWT, the 2P responses in M_{FA} and M_{SS} of the spar FVAWT and the semi-submersible FVAWT are much smaller than those of the TLP FVAWT, which implies that the catenary mooring system can greatly mitigate the 2P effects on structural dynamic responses. As a consequence, the standard deviations of M_{FA} and M_{SS} for the spar FVAWT and the semi-submersible FVAWT are smaller than those of the TLP FVAWT, as shown in Fig. 9. Figure 9 compares the mean values and standard deviations of M_{FA} for the three FVAWT concepts under different environmental conditions. The mean values and standard deviations of M_{FA} increase as the wind speed increases. The mean values of M_{FA} for the spar FVAWT and the semi-submersible FVAWT are much larger than the corresponding standard deviations; on the other hand, the standard deviations of the TLP FVAWT are much larger than the mean

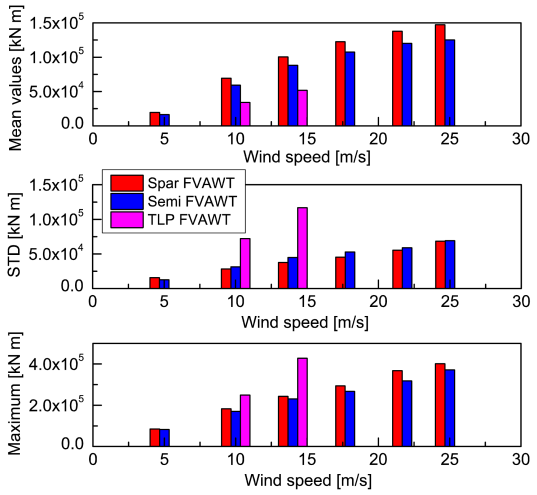

Fig. 9 Mean values, standard deviations, and maximum values of the tower base fore-aft bending moment for the three FVAWT concepts; there are no results for TLP FVAWT at LC4 through LC6.

values. The spar FVAWT has the largest mean value of M_{FA} with smallest standard deviation. A similar effect is also observed for M_{SS} for the three FVAWT concepts.

Mooring Line Tension

The mooring system is used to keep the platform in position. Because of the large aerodynamic excitations at high wind speeds, the FVAWT may experience large global motion, especially the yaw motion, as shown in Fig. 7c. The three FVAWT concepts used different mooring systems, as depicted in Fig. 1. The TLP FVAWT employed the three pre-tension tendons, which results in large 2P variation of tension in the tendons, as demonstrated in Fig. 2. The TLP is a desirable supporting structure choice when the variations of the aerodynamic loads acting on the rotor are reduced significantly. This can be achieved by increasing the blade number or using a helical blade (Cahay et al., 2011). One chain mooring system with delta lines and clump weights was applied for the spar FVAWT, and one catenary mooring system was adopted by the semi-submersible FVAWT. In the present study, the mooring line tensions at the fairlead were studied; Fig. 10 presents the power spectrum of the tension of mooring line 2 for the semi-submersible and TLP FVAWTs and delta line 2a for the spar FVAWT under turbulent wind and irregular wave conditions. The mooring lines in the global coordinate system are specified in Fig. 1 for three FVAWT concepts, respectively.

The power spectral density (PSD) of the tension of the TLP FVAWT is approximately three orders of magnitude higher than that of the semi-submersible FVAWT and the spar FVAWT, since the variations of tendon tensions are too large as compared to the other two. For the spar and semi-submersible FVAWTs, the turbulent wind-induced response of the tension of mooring line is dominating, and the contributions from the wave frequency response and 2P response increase as the significant wave height and wind speed increase. Additionally, for the spar FVAWT, the delta line tensions always remain positive, meaning that the current mooring system is acceptable for the operational condition. Moreover, the mean value, standard deviation, and maximum values of the semi-submersible FVAWT are all larger than those of the spar FVAWT, as shown in Fig. 11.

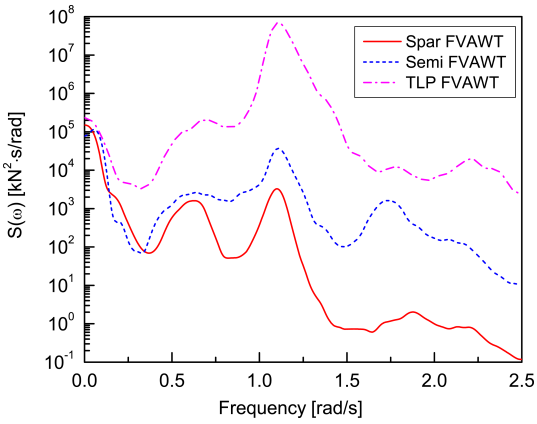

Fig. 10 Power spectrum of the tension in delta line 2a for the spar FVAWT and mooring line 2 for the semi-submersible and TLP FVAWTs in LC3.3 with $U_w = 14$ m/s, $H_s = 3.62$ m, and $T_p = 10.29$ s

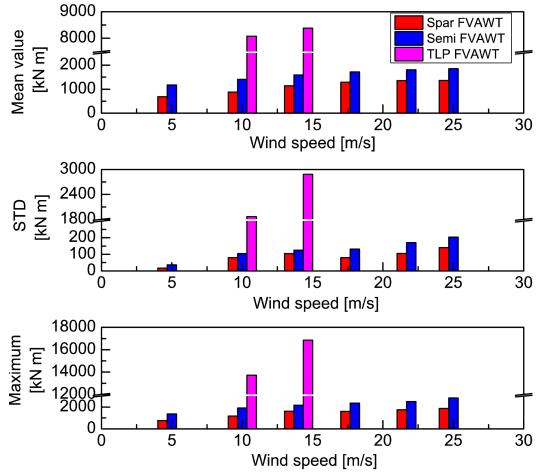

Fig. 11 Mean values, standard deviations, and maximum values of the tension in delta line 2a for the spar FVAWT and mooring line 2 for the semi-submersible and TLP FVAWTs; there are no results for TLP FVAWT at LC4 through LC6.

CONCLUSIONS

The present paper deals with a comparative study of the dynamic responses of three FVAWT concepts with a two-bladed Darrieus rotor. The OC3 spar, the OC4 semi-submersible, and a TLP, which were originally designed to support the NREL 5 MW wind turbine, were taken as the floating platform to support a 5 MW Darrieus rotor. Fully coupled time domain simulations were carried out using the SIMO-RIFLEX-DMS code. A series of load cases with turbulent wind and irregular waves was defined to investigate global stochastic dynamic responses of the three FVAWT concepts, including the generator power production, the platform motions, the tower base bending moment, and the tensions of mooring lines.

Both the mean values and the standard deviations of the generator power production for the three FVAWTs are very close, except that differences in mean power between the spar FVAWT and the semi-submersible FVAWT arise due to the different rotor rotational speeds. For the three FVAWTs, the motion of surge, pitch, and yaw are mainly due to the low-frequency turbulent wind loads, and the responses corresponding to the 2P frequency are observed for each motion. The spar FVAWT suffers the largest mean value and standard deviation of motions in surge, pitch, and yaw. The semi-submersible FVAWT displays the best global motion performance. Though the three FVAWTs experience severe yaw motion, especially at high wind speed, the yaw motion of the semi-submersible FVAWT is mainly caused by the wind-induced yaw resonant response. Attention should be paid to the yaw natural period when designing a semi-submersible for FVAWTs.

Significant 2P effects can be observed in the responses of the tower base bending moments for the three FVAWTs. These 2P responses can cause great fatigue damage and should be reduced, e.g., by damping. The slack mooring lines can mitigate the 2P effects since they are more efficient at absorbing the 2P aerodynamic excitations. In addition, the 2P variations in the aerodynamic loads can be relieved by increasing the number of blades, using helical blades, or adopting more advanced control strategy despite the increasing costs. Large variations of axial force also

exist in the tendons of the TLP FVAWT because of the 2P aerodynamic loads. Unless these variations are significantly reduced, the TLP is not a very good supporting structure. The present mooring system with clump weight and delta lines for the spar FVAWT can only work well for the operational condition that a new mooring system is required when extreme condition analysis is carried out. Both the mooring line tensions for the semi-submersible FVAWT and the delta line tensions for the spar FVAWT show an obvious 2P response, but they are much smaller than those for the TLP FVAWT.

Although the three floating platforms are originally designed to support the NREL 5 MW wind turbine, the present study aims to reveal the dynamic response characteristics of each FVAWT concept. The results can help to resolve preliminary design tradeoffs among the three FVAWT concepts and will serve as a basis for further developments of each FVAWT concept.

ACKNOWLEDGEMENTS

The authors would like to acknowledge the financial support from the EU FP7 project MARE WINT (Project no 309395) through the Centre for Ships and Ocean Structures at the Department of Marine Technology, Norwegian University of Science and Technology, Trondheim, Norway. The first author would also like to thank Dr. Erin Bachynski from MARINTEK for providing the TLP model and kind help with using the simulation codes.

REFERENCES

Bachynski, EE, and Moan, T (2012). "Design Considerations for Tension Leg Platform Wind Turbines," *Mar Struct*, 29(1), 89–114. http://dx.doi.org/10.1016/j.marstruc.2012.09.001.

Bachynski, EE, Kvittem, MI, Luan, C, and Moan, T (2014). "Wind–Wave Misalignment Effects on Floating Wind Turbines: Motions and Tower Load Effects," *J Offshore Mech Arct Eng*, 136(4), 041902. http://dx.doi.org/10.1115/1.4028028.

Borg, M, and Collu, M (2014). "A Comparison on the Dynamics of a Floating Vertical Axis Wind Turbine on Three Different Floating Support Structures," *Energy Procedia*, 53, 268–279. http://dx.doi.org/10.1016/j.egypro.2014.07.236.

Borg, M, Shires, A, and Collu, M (2014). "Offshore Floating Vertical Axis Wind Turbines, Dynamics Modelling State of the Art. Part I: Aerodynamics," *Renewable Sustainable Energy Rev*, 39, 1214–1225. http://dx.doi.org/10.1016/j.rser.2014.07.096.

Cahay, M, Luquiau, E, Smadja, C, and Silvert, F (2011). "Use of a Vertical Wind Turbine in an Offshore Floating Wind Farm," *Offshore Technol Conf*, Houston, TX, USA, OTC-21705-MS. http://dx.doi.org/10.4043/21705-MS.

Cheng, Z, Wang, K, Gao, Z, and Moan, T (2015). "Comparative Study of Spar Type Floating Horizontal and Vertical Axis Wind Turbines Subjected to Constant Winds," Presented at: *Eur Wind Energy Assoc Offshore 2015*, Copenhagen, Denmark, EWEA.

Dabiri, JO (2011). "Potential Order-of-Magnitude Enhancement of Wind Farm Power Density via Counter-Rotating Vertical-Axis Wind Turbine Arrays," *J Renewable Sustainable Energy*, 3(4), 043104. http://dx.doi.org/10.1063/1.3608170.

Faltinsen, OM (1995). *Sea Loads on Ships and Offshore Structures*, Cambridge University Press, Cambridge, UK, 340 pp.

IEC (2009). *Wind Turbines, Part 3: Design Requirements for Offshore Wind Turbines,* International Standard 61400-3, International Electrochemical Commission, Geneva, Switzerland.

Islam, MR, Mekhilef, S, and Saidur, R (2013). "Progress and Recent Trends of Wind Energy Technology," *Renewable Sustainable Energy Rev*, 21, 456–468. http://dx.doi.org/10.1016/j.rser.2013.01.007.

Jamieson, P (2011). *Innovation in Wind Turbine Design*, John Wiley & Sons, 316 pp.

Johannessen, K, Meling, TS, and Haver, S (2002). "Joint Distribution for Wind and Waves in the Northern North Sea," *Int J Offshore Polar Eng*, ISOPE, 12(1), 1–8.

Jonkman, BJ (2009). *TurbSim User's Guide: Version 1.50*, Technical Report NREL/TP-500-46198, National Renewable Energy Laboratory, Golden, CO, USA.

Jonkman, J (2010). *Definition of the Floating System for Phase IV of OC3*, Technical Report NREL/TP-500-47535, National Renewable Energy Laboratory, Golden, CO, USA.

Jonkman, JM, Butterfield, S, Musial, W, and Scott, G (2009). *Definition of a 5-MW Reference Wind Turbine for Offshore System Development*, Technical Report NREL/TP-500-38060, National Renewable Energy Laboratory, Golden, CO, USA.

Karimirad, M, and Moan, T (2012). "Wave and Wind Induced Dynamic Response of a Spar-Type Offshore Wind Turbine," *J Waterw Port Coastal Ocean Eng*, 138(1), 9–20. http://dx.doi.org/10.1061/(ASCE)WW.1943-5460.0000087.

Kinzel, M, Mulligan, Q, and Dabiri, JO (2012). "Energy Exchange in an Array of Vertical-Axis Wind Turbines," *J Turbul*, 13(38), 1–13. http://dx.doi.org/10.1080/14685248.2012.712698.

Luxcey, N, Ormberg, H, and Passano, E (2011). "Global Analysis of a Floating Wind Turbine Using an Aero-Hydro-Elastic Numerical Model: Part 2 - Benchmark Study," *Proc 30th Int Conf Ocean Offshore Arct Eng*, Rotterdam, Netherlands, ASME, 5, 819–827. http://dx.doi.org/10.1115/OMAE2011-50088.

MARINTEK (2012a). *SIMO-Theory Manual, Version 4.0*.

MARINTEK (2012b). *RIFLEX Theory Manual, Version 4.0*.

Ormberg, H, Passano, E, and Luxcey, N (2011). "Global Analysis of a Floating Wind Turbine Using an Aero-Hydro-Elastic Model: Part 1 - Code Development and Case Study," *Proc 30th Int Conf Ocean Offshore Arct Eng*, Rotterdam, Netherlands, ASME, 5, 837–847. http://dx.doi.org/10.1115/OMAE2011-50114.

Paquette, J, and Barone, M (2012). "Innovative Offshore Vertical-Axis Wind Turbine Rotor Project," Presented at: *Eur Wind Energy Assoc 2012 Annual Event*, Copenhagen, Denmark, EWEA.

Paraschivoiu, I (2002). *Wind Turbine Design: With Emphasis on Darrieus Concept*, Polytechnic International Press, 438 pp.

Paulsen, US, et al. (2011). "DeepWind: An Innovative Wind Turbine Concept for Offshore," Presented at: *Eur Wind Energy Assoc 2011 Annual Event*, Brussels, Belgium, EWEA.

Robertson, A, et al. (2012). *Definition of the Semisubmersible Floating System for Phase II of OC4*, Technical Report NREL/TP-5000-6060, National Renewable Energy Laboratory, Golden, CO, USA.

Vita, L (2011). *Offshore Floating Vertical Axis Wind Turbines with Rotating Platform*, PhD Thesis, Technical University of Denmark, Røskilde, Denmark.

Wang, K, Hansen, MOL, and Moan, T (2015a). "Model Improvements for Evaluating the Effect of Tower Tilting on the Aerody-

namics of a Vertical Axis Wind Turbine," *Wind Energy*, 18(1), 91–110. http://dx.doi.org/10.1002/we.1685.

Wang, K, Moan, T, and Hansen, MOL (2013). "A Method for Modeling of Floating Vertical Axis Wind Turbine," *Proc 32nd Int Conf Ocean Offshore Arct Eng*, Nantes, France, V008T09A016. http://dx.doi.org/10.1115/OMAE2013-10289.

Wang, K, Moan, T, and Hansen, MOL (2015b). "Stochastic Dynamic Response Analysis of a Floating Vertical Axis Wind Turbine with a Semi-Submersible Floater," *Wind Energy*, (submitted).

Wang, K, Cheng, Z, Moan, T, and Hansen, MOL (2015c). "Effect of Difference-Frequency Forces on the Dynamics of a Semi-Submersible Type FVAWT in Misaligned Wave–Wind Condition," *Proc 25th Int Ocean Polar Eng Conf*, Kona, HI, USA, ISOPE, 1, 517–524.

Wang, K, Luan, C, Moan, T, and Hansen, MOL (2014). "Comparative Study of a FVAWT and a FHAWT with a Semi-Submersible Floater," *Proc 24th Int Ocean Polar Eng Conf*, Busan, Korea, ISOPE, 1, 302–310.

A.5 Paper 5

Paper 5:

Effect of difference-frequency forces on the dynamics of a semi-submersible type FVAWT in misaligned wave-wind condition.

Zhengshun Cheng, Kai Wang, Zhen Gao, Torgeir Moan

Published in *Proceedings of the Twenty-fifth (2015) International Ocean and Polar Engineering Conference*, Kona, Big Island, Hawaii, USA, June 21-26, 2015

Effect of Difference-frequency Forces on the Dynamics of a Semi-submersible Type FVAWT in Misaligned Wave-wind Condition

Kai Wang[1,3], Zhengshun Cheng[1,2], Torgeir Moan[1,4], Martin Otto Laver Hansen[1,5]

1 CeSOS, NTNU, Trondheim, Norway
2 Department of Marine Technology, NTNU, Trondheim, Norway
3 NOWITECH, NTNU, Trondheim, Norway
4 AMOS, NTNU, Trondheim, Norway
5 DTU Wind Energy, Lyngby, Denmark

ABSTRACT

With increasing interests in the development of offshore floating vertical axis wind turbines (FVAWTs), a large amount of studies on the FVAWTs have been conducted. This paper focuses on evaluating the effect of second-order difference-frequency force on the dynamics of a 5 MW FVAWT in misaligned wave-wind condition. The studied FVAWT is composed of a 5 MW Darrieus rotor, a semi-submersible floater and a catenary mooring system. Fully coupled nonlinear time domain simulations were conducted using the state-of-art code Simo-Riflex-DMS. Several misaligned wave-wind conditions were selected to investigate the global dynamic responses of the FVAWT, such as the platform motions, structural responses and mooring line tensions. It has been found that the wave-wind misalignment does not significantly affect the mean values of the global responses since the global responses are primarily wind-induced. And the second order difference-frequency force can contribute to a slightly larger mean value. The standard deviations and maximum values of the global responses are slightly more sensitive to the wave-wind misalignment and the second order difference-frequency force, especially at high significant wave height conditions.

KEY WORDS: Floating vertical axis wind turbine; difference-frequency force; wave-wind misalignment; dynamic responses.

INTRODUCTION

Floating vertical-axis wind turbines (FVAWTs) provide the potential for utilizing offshore wind resources in moderate and deep water due to their economical installation and maintenance. Increasing interest in the development of the FVAWTs has been stimulated covering different aspects, such as development of coupled models, proposal of novel concepts, extensive dynamics analysis, comparative study between the FVAWTs and the floating horizontal axis wind turbines (FHAWTs) and so on. Sandia National Laboratories obtained a research grant from the U.S. Department of Energy to investigate the feasibility of VAWTs for offshore deployment in 2011 (Sutherland et al., 2012). One of the objectives was to investigate the cost-competitiveness of a multi-MW FVAWT through a series of design studies. A preliminary feasibility study has showed that a potential of over 20% cost-of-energy (COE) reduction could be achieved through application of VAWT rotor technology in the offshore wind energy (Paquette and Barone, 2012). Up to now, several FVAWT concepts have been proposed by different research institutions and industries. These FVAWTs consist of VAWTs, supporting platforms and mooring systems, which are very similar to those used for FHAWTs. Some examples of proposed concepts include DeepWind (Vita, 2011), VertiWind (Cahay et al., 2011), Aerogenerator X (Wind Power Limited & Grimshaw) , "floating tilted axis" (Akimoto et al., 2011) concepts.

In order to evaluate these FVAWT concepts, a model should be developed to represent the aerodynamic, hydrodynamic, structural dynamic and control systems for a FVAWT in a fully coupled manner. The available simulation tools to model the FVAWTs in a fully-coupled way are limited, but are emerging. A simplified method for the analysis of the aerodynamic loads for the DeepWind concept under turbulent wind and platform motion was created by Merz (2012), but only the surge displacement of the FVAWT was considered by applying a simple mass-spring-damper model. Furthermore, this method was extended by including the hydrodynamic calculations based on Morison formula and focused on the investigation of a control algorithm for the DeepWind FVAWT (Merz and Svendsen, 2013; Svendsen and Merz, 2013; Svendsen et al., 2012). Sandia National Laboratory is developing the Offshore Wind ENergy Simulation (OWENS) toolkit (Fowler et al., 2014; Owens et al., 2013a; Owens et al., 2013b) aiming at establishing a robust and flexible finite element framework and VAWT mesh generation utility. It can also be coupled with a modular interface that allows users to integrate easily with existing codes, such as aerodynamic and hydrodynamic codes. Further developments are being made by using the two-way coupled aerodynamics model that receives blade deformations and performs aeroelastic calculations, by integrating a nonlinear mooring module and by adding other necessary features. The HAWC2, a state-of-the-art aero-hydro-servo-elastic code used for FHAWTs, has been developed to calculate the responses of a FVAWT in the time domain for the DeepWind Project (Vita, 2011). However, wave loads in the existing HAWC2 are calculated using the Morison formula, which is well suitable for slender structures such as spar floater. Therefore, HAWC2 is still not suitable for FVAWTs with a semi-submersible floater. Based on the Simo-Riflex code which has been extensively used and validated for offshore structures subjected to wave loads, the Simo-Riflex-DMS

code (Wang et al., 2013) has been developed as a nonlinear aero-hydro-servo-elastic simulation tool for modeling FVAWTs. This simulation tool integrates models of the wind inflow, aerodynamics, hydrodynamics, structural dynamics and controller dynamics, and carries out the simulations in a fully coupled manner in the time domain. The development of this simulation tool provides approaches of high fidelity of analysis for FVAWTs. A comparison of this code and the FloWind code (Collu et al., 2013) has been carried out to assess the effect of different models used in the simulation tools. This comparative study (Borg et al., 2014c) identified significant difference in the calculated responses due to different dynamic modelling of the mooring lines and the controller, and it also discussed the needs for further development. However, other aspects in modeling also need to be addressed. One of these aspects is the modeling of the flexibility of the blades and the rotating shaft which has not been considered. The rotor was assumed to be rigid, and the stochastic nature of the response has not been addressed in the comparison.

Using these developed simulation tools for FVAWTs, some researches have been performed. A research group at the Technical University of Denmark (DTU) has performed a design optimization of the proposed DeepWind concept (Paulsen et al., 2013). An improved design has been obtained with an optimized blade profile with less weight and higher stiffness than the 1st baseline design. Based on a developing simulation tool named as FloVAWT, Borg et al. presented a review of the dynamic modeling of FVAWTs (Borg et al., 2014a; Borg et al., 2014b), used a wave energy converter as a motion suppression device for floating wind turbines (Borg et al., 2013) and further performed a comparison on the dynamics of FVAWTs with three different floating support structures (Borg and Collu, 2014). Using the Simo-Riflex-DMS code, a series of studies on a 5MW semisubmersible FVAWT have been performed with the emphasis on the stochastic dynamic response analyses of the studied FVAWT under different environmental conditions (Wang et al., 2015) as well as a comparative study of a FVAWT and a FHAWT (Wang et al., 2014b). Additionally, emergency shutdown process of the FVAWT with consideration of fault is investigated based on a novel hydrodynamic brake (Wang et al., 2014a).

It is also of great interest to take into account effect of wave-wind misalignment on the dynamic response of the FVAWT. In general, large misalignments occur at lower wind speeds while small misalignments occur at higher wind speeds (Fischer et al., 2011). Based on observations in the North Sea, it is common to reach 30 degrees of misalignment, but misalignments greater than 60 degrees occur less than 5% of the time (Kühn, 2001). Therefore, misalignment effects on four different FHAWTs were investigated in conditions of up to 90 degrees of misalignment between the wind and wave directions by Bachynski et al. (2014), whereas Barj et al. (2014) conducted a study on the effect of wind-wave misalignment in the loads analysis of a spar floating wind turbine for all angles between wind and wave directions. As for the FVAWTs, the effect of wind-wave misalignment on the global motions and structural responses in selected operational conditions has been investigated (Wang et al., 2015) by only considering the first-order force. Increased global motions, except the pitch mode, are observed in the misaligned conditions. The tower base bending moments and the mooring line tension are found not to depend strongly on the wave directions due to the large contribution from the 2P load variation. The effect of the wind-wave misalignment is not significant when compared to the amplitude of the wind loads. However, the second-order wave forces have not been considered. Therefore, this paper focuses on the effect of the mean drift and difference-frequency wave forces on dynamic response in the misaligned wave and wind conditions. Including the difference-frequency wave forces, the effect of wind-wave misalignment becomes more apparent when compared with cases with the first-order wave forces only.

FLOATING WIND TURBINE MODELS

The FVAWT used in this study was a 5 MW Darrieus VAWT mounted on a semi-submersible floater with three catenary mooring lines, as shown in Fig. 1. The Darrieus rotor is composed of two blades and one rotating shaft which spans from the top to the bottom where the generator is connected. The rotor is derived from the DeepWind project in the FP7 European program (Vita, 2011). Main specifications of the rotor are given in Table 1. A direct drive generator is assumed to be placed at tower base, so the gearbox is not considered in the model and the mass of the generator is integrated into the total mass of the platform.

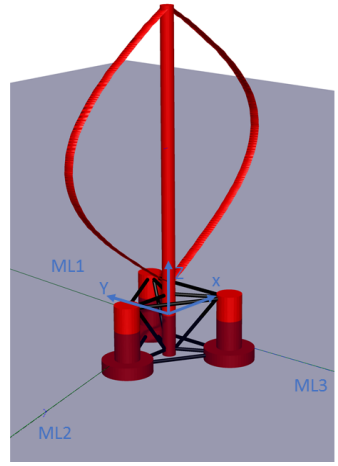

Fig. 1. Schematic view of the FVAWT concept

Table 1. Specifications of the Darrieus 5MW wind turbine

Rated power	5 MW
Rotor height, root-to-root	129.56 m
Rotor radius	63.74 m
Chord length	7.45 m
Airfoil section	NACA0018
Cut-in, rated, cut-out wind speed	5 m/s, 14 m/s, 25 m/s
Rated rotational speed	5.26 rpm
Total mass, including rotor and tower	754226 kg
Center of mass	(0 m, 0 m, 75.6 m)

The semi-submersible floater is composed of three offset columns, three pontoons, a central column and braces. The rotor is supported by the central column. The columns and pontoons are connected by braces to form an integrated body. Three catenary mooring lines are attached to the three offset columns to provide horizontal restoring stiffness. Sufficient restoring stiffness is ensured by the large second moment of water line area to limit the roll and pitch motions under various wave and wind conditions. The semi-submersible floater and the mooring system were originally developed for the DeepCwind project and are also used to support a 5 MW HAWT in Phase II of the Offshore Code

Comparison Collaboration Continuation (OC4) project. When compared to the FHAWT in the OC4 project, the FVAWT uses the 5 MW Darrieus rotor instead of the NREL 5 MW wind turbine. Since the 5 MW Darrieus rotor is heavier than the NREL 5 MW wind turbine, the ballast of the FVAWT is adjusted to maintain the same draft and displacement as the FHAWT. The properties of the FVAWT are summarized in Table 2. The platform motions are calculated with respect to the global coordinate system, as shown in Fig. 1. Free decay tests have been carried out for this FVAWT to assess the natural periods in Wang et al. (2014b).

Table 2. Properties of the FVAWT with a semi-submersible floater

Water depth [m]	200
Draft [m]	20
Waterline diameter [m]	12.0/6.5
Hull mass, including ballast and generator [ton]	13353.7
CM location below MSL [m]	-13.42
Displacement [m^3]	13919
CB location below MSL [m]	-13.15
Natural period in surge/sway [s]	114.0
Natural period in heave [s]	17.1
Natural period in roll/pitch [s]	31.0
Natural period in yaw [s]	79.7

METHODOLOGY

Fully Coupled Analysis Tool

A fully coupled simulation tool Simo-Riflex-DMS was developed to study the dynamic behavior of a FVAWT in the time domain. It integrated several separate models to account for the wind inflow, aerodynamics, hydrodynamics, structural dynamics and controller dynamics. Three computer codes were coupled: Simo calculated the rigid body hydrodynamic forces and moments on the floater; Riflex modeled the blades, tower, shaft and mooring system as flexible finite elements, as well as provided the link to the DMS code and external controller; the DMS code computed the aerodynamic loads on the blades using an external aerodynamic module based on the Double Multi-Streamtube (DMS) theory. The generator torque characteristic was written in Java. The hydrodynamic loads were calculated at the actual displaced position of the floater. This combination produces a comprehensive aero-hydro-servo-elastic simulation tool with sophisticated hydrodynamics, stable nonlinear finite element solver, well-known aerodynamics and user-defined controller. The Simo-Riflex wind turbine module has previously been verified (Luxcey et al., 2011; Ormberg et al., 2011), and the Simo-Riflex-DMS code has been presented and verified in Wang et al. (2013).

Second-order Difference-frequency Wave-diffraction Force Formulation

For moored floating structures, the second order difference-frequency wave force is important for properly simulating the low-frequency wave excitation force and the corresponding global responses. It is therefore of interest to investigate the effect of second order difference-frequency forces on the dynamic responses of a FVAWT with the semi-submersible considered. The formulation of the second order difference-frequency force implemented in the current simulation tool is briefly outlined in the following.

The time varing wave surface elevation $h(\mathrm{t})$ can be written as the sum of its wave frequency components as follows

$$h(\mathrm{t}) = \mathrm{Re}\sum_{n=1}^{N} a_n e^{i\omega_n t} \tag{1}$$

where N is the number of frequency components, ω_n and a_n are the n^{th} wave component frequency and complex-valued amplitude including phase, t is time and i is the imaginary unity. Then, the second order difference frequency wave force $F_j^D(t)$ can be computed as

$$F_j^D(t) = \mathrm{Re}\sum_{n=1}^{N}\sum_{m=1}^{N} a_n a_m^* D_{nm}^{(j)} e^{i(\omega_n-\omega_m)t} \tag{2}$$

where $D_{nm}^{(j)}$ is the complex difference-frequency quatratic transfer function (QTF) for the j^{th} degree of freedom and the superscipt * denotes the complex conjugate. The second order difference frequency force can be decomposed into time constant part (mean-drift force) and time varing part (slowly-varying force). The mean drift force $F_j^M(t)$ can be obtained by setting m=n in Eq. (2) as the following

$$F_j^M(t) = \sum_{n=1}^{N} |a_n|^2 D_{nn}^{(j)} \tag{3}$$

In the present study, the mean drift force and the second order force with full QTF are taken into account, respectively. A convergence study was carried out to assess the accuracy of the computed QTF. Two meshes, as given in Table 3, were employed to calculate the mean drift force and QTF. Fig. 2 compares the difference-frequency surge force QTF at the surge resonance difference-frequency (i.e. $\omega_n - \omega_m = \pm\omega_1$, in which ω_1 is the surge natural frequency) for the two meshes. It can be observed that in the wave-frequency range of 0.3 -1.2 rad/s, the difference in the difference-frequency surge force between the two meshes are very small. The results corresponding to mesh 1 are thus considered to be accurate and will be used in the following analysis.

Table 3. Meshes of the semi hull and free surface

	Semi hull	Free surface
Mesh 1	7980	6000
Mesh 2	4320	4650

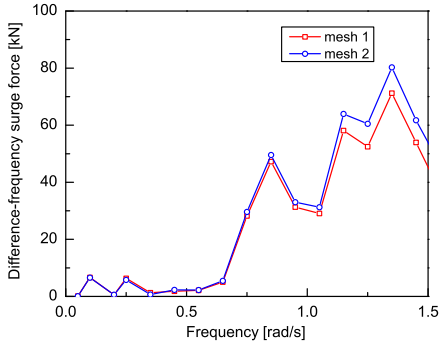

Fig. 2. Comparison of the difference-frequency surge QTF at the surge resonance difference-frequency for two meshes.

LOAD CASES

Six load cases (LCs) with misaligned wave-wind conditions were defined to perform coupled time domain simulation for the FVAWT, as given in Table 4. The three dimensional turbulent wind fields were generated using the NREL's TurbSim program (Jonkman, 2009) according to the Kaimal turbulence model for IEC Class C. Both the normal wind profile (NWP) and normal turbulence model (NTM) was applied. Regarding the NWP condition, the wind profile $U(z)$ is the average wind speed as a function of height z above the mean sea level (MSL), and is given by the power law as follows

$$U(z) = U_{\text{ref}}(z/z_{\text{ref}})^{\alpha} \quad (4)$$

where U_{ref} is the reference wind speed, z_{ref} the height of reference wind speed and α the power law exponent. The value of z_{ref} was set equal to 79.78 m (vertical center of the blades) above the MSL. The value of α was chosen to be 0.14 for the floating wind turbines according to IEC 61400-3 (IEC, 2009). The mean wind speed U_w given in Table 4 is the reference wind speed at the vertical center of the blades. The JONSWAP wave spectrum was used to generate the wave history. The significant wave height (H_s) and peak period (T_p) were set in accordance with the correlation with wind speed for the Statfjord site in the northern North Sea (Johannessen et al., 2002).

Table 4. Load case - combined wind and wave conditions

LC	U_w [m/s]	H_s [m]	T_p [s]	Turb. Model	Sim. Len. [s]
LC1	5	2.10	9.74	NTM	4600
LC2	10	2.88	9.98	NTM	4600
LC3	14	3.62	10.29	NTM	4600
LC4	18	4.44	10.66	NTM	4600
LC5	22	5.32	11.06	NTM	4600
LC6	25	6.02	11.38	NTM	4600

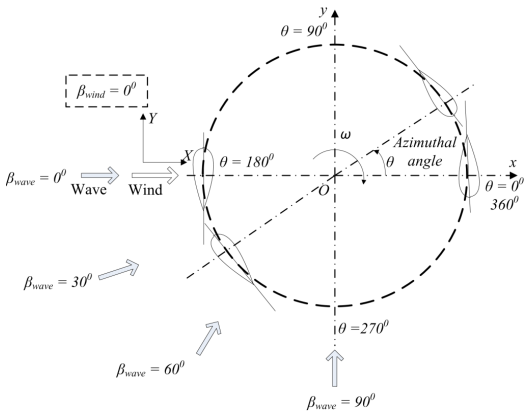

Fig. 3. A horizontal cross section of the rotor showing the wave direction distribution in misaligned wave-wind conditions.

Fig. 3 depicts the configuration of the wave and wind directions. Since the wind direction was remained as β_{wind}= 0º, the wave direction β_{wave} was actually a measure of the wave-wind misalignment. For each load case, four wave directions, i.e. β_{wave}= 0º, 30º, 60º and 90º, were simulated considering first order force (1st), first order force and mean drift force (1st + mean drift), and first order force and second order difference-frequency force (1st + full QTF), respectively. Each simulation lasted 4600 s and corresponded to a one-hour dynamic analysis, since the first 1000 s was removed to eliminate the start-up transient effects. For each LC and each wave direction, five identical and independent one-hour simulations with different seeds for the turbulent winds and irregular waves were carried out to reduce the stochastic variation. The mean value and standard deviation of the dynamic responses were obtained by averaging the mean values and standard deviation of five 1-h ensembles.

RESULTS and DISCUSSIONS

Platform Motion

Firstly, the effect of second order difference-frequency force and wave-wind misalignment on the platform motions were studied. Fig. 4 and 5 shows the mean value and standard deviation of the platform motions under different load cases, respectively.

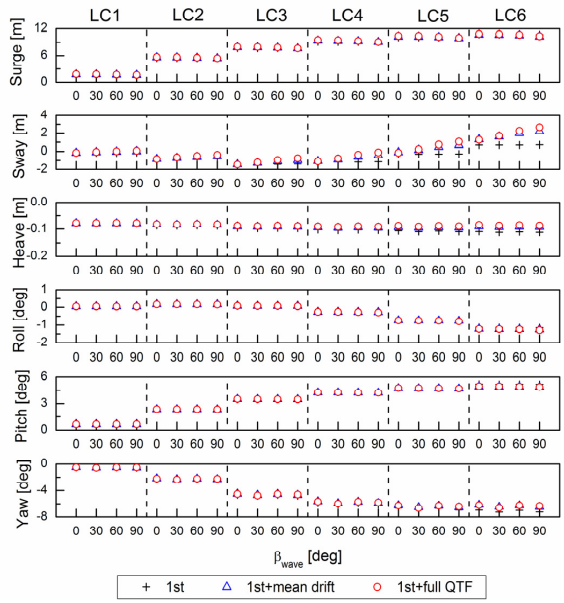

Fig. 4. Mean values of the platform motions as a function of the wave direction β_{wave} for all load cases. Here 1st indicates the first order force.

The mean values of the platform motions depend on the aerodynamic loads acting on the rotor, the hydrodynamic loads on the platform and the mooring line tensions on the fairleads. It can be found that the mean values of the platform motions are not significantly affected by the wave-wind misalignment and the second order difference-frequency force, except the sway and yaw motions in LCs with large significant wave height. Since the aerodynamic loads are much larger than the corresponding hydrodynamic loads, the mean values of the platform motions are mainly wind induced. Furthermore, the mean values of surge and pitch motions are also much larger than those of sway and roll motions, respectively, as shown in Fig. 4.

The mean values of the platform motions are a little larger when considering the mean drift force or second order difference-frequency force. The hydrodynamic loads acting on the platform hull, braces, columns and mooring lines will vary with changing wave direction and

will increase with increasing significant wave height. Under more severe wave conditions in LC 4-6, these hydrodynamic loads greatly contribute to the mean values of the sway and yaw motions and thus cause different mean values in sway and yaw motions. These discrepancies increase when the mean drift force or second order difference frequency force are taken into account.

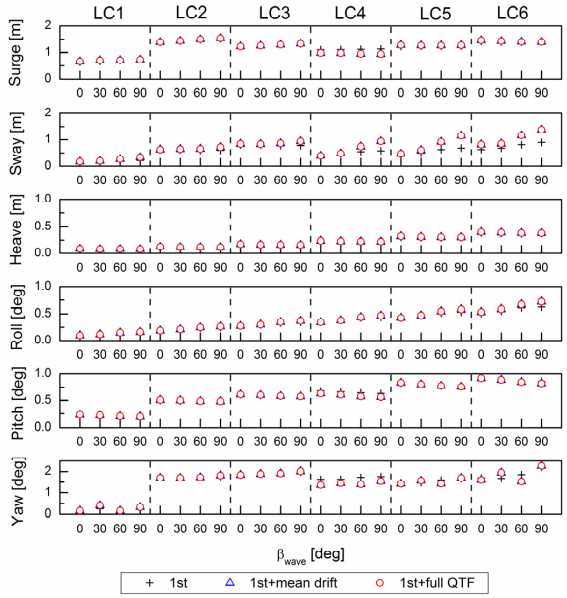

Fig. 5. Standard deviations of the platform motions as a function of the wave direction β_{wave} for all load cases.

When compared to the mean values, the standard deviations of the platform motions are a little more sensitive to the wave-wind misalignment, as depicted in Fig. 5. This can also be clearly observed from the power spectra of platform motions, for instance the power spectrum of pitch motion in LC 3 in Fig. 6. Here both first order excitation force and second order difference-frequency force are considered. It shows that as the wave-wind misalignment β_{wave} increases, the low-frequency response increases while the wave-frequency response decreases. The response corresponding to the 2P frequency does not vary with the wave-wind misalignment since they are due to the variation of aerodynamic loads and are thus independent of the misalignment. The increase in the low-frequency response counteracts the reduction in the wave-frequency response, leading to relatively small variation in the standard deviations of surge, heave and pitch motions. The standard deviation of surge motion increases slowly with increasing β_{wave} in LC 1-3, and decreases slightly with increasing β_{wave} in LC 4-6. The standard deviation of heave motion almost holds constant for each LC and can be regarded as wave-wind misalignment indepenent. The standard deviation of pitch motion decreases slowly with increasing β_{wave} for each LC due to the reduction of the component of hydrodynamic loads in surge direction. This decrease in turn causes the increase of the standard deviation of sway and roll motions with increasing β_{wave} and the increase becomes more obvious at higher significant wave height conditions such as LC 4-6. For yaw motion, the standard deviation is dominated by the yaw resonant response, as illustrated in Fig. 7. When β_{wave}= 0º or 60 º, i.e. the wave direction is parallel to the pontoon, the wave-frequency yaw response is very close to zero and much smaller than those when β_{wave}= 30º or 90 º.

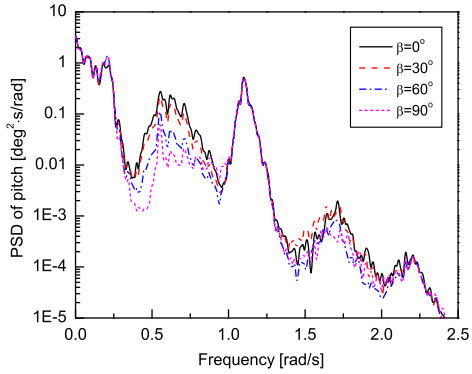

Fig. 6. Power spectra of pitch motions for the semi FVAWT with consideration of full QTF at different wave direction in LC 3.

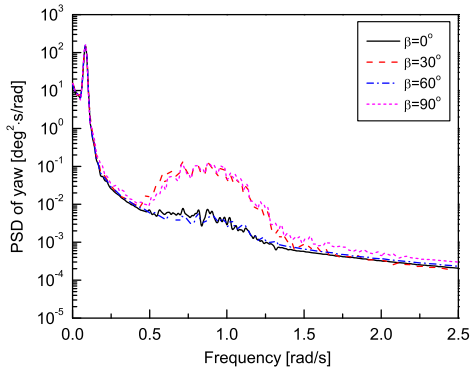

Fig. 7. Power spectra of yaw motions for the semi FVAWT with consideration of full QTF at different wave direction in LC 3.

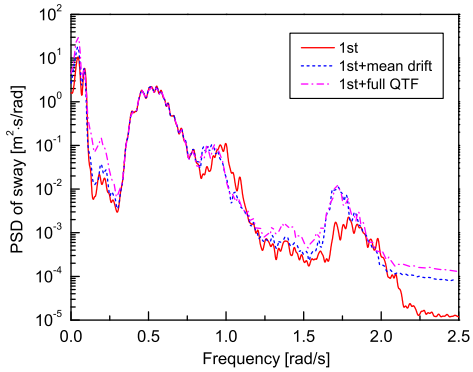

Fig. 8. Power spectra of sway motions for the semi FVAWT with wave direction of 90 degree in LC 6 under different consideration of hydrodynamic loads.

Fig. 5 also compares the standard deviation of platforms when considering first order force, first order force and mean drift force, and first order force and second order difference-frequency force, respectively. As illustrated in Fig. 5, the second order difference-

frequency force has slight influence on the standard deviation of surge, heave, roll and pitch motions. For sway and yaw motions, the second order difference-frequency force contributes to some extent to the standard deviation. Fig. 8 demonstrates the power spectra of sway motions in LC 6 with β_{wave}= 90º and by considering first order force, first order force and mean drift force, and first order force and second order difference-frequency force, respectively. It can be found that the wave-frequency responses are almost identical under difference wave load conditions. However, the second order difference-frequency force and mean drift force cause larger low-frequency sway and roll resonant responses, as shown in Fig. 8. Furthermore, the sway and roll resonant responses due to the second order difference-frequency force are much larger than those because of mean drift force.

Tower Base Bending Moment

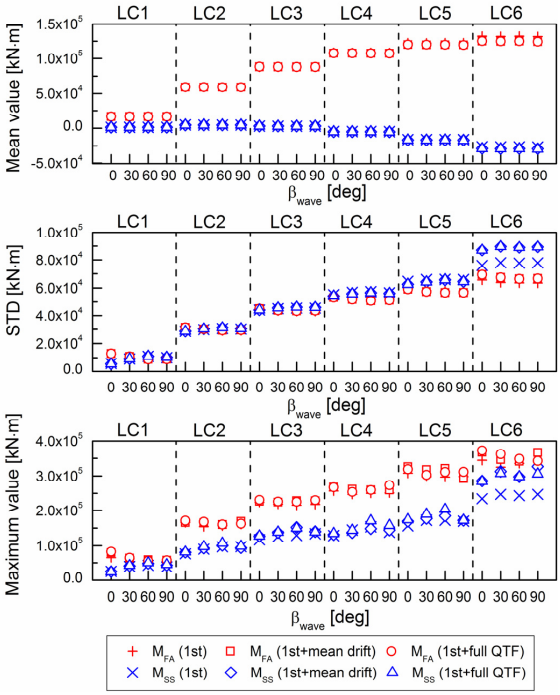

Fig. 9. Mean value, standard deviation and maximum value of the tower base fore-aft bending moment M_{FA} and side-to-side bending moment M_{SS} as a function of wave direction β_{wave} for all load cases.

The second order difference-frequency force and the wave-wind misalignment can also affect the structural responses of the FVAWT. Fig. 9 presents the mean value, standard deviation and maximum value of the the tower base bending moment, including fore-aft bending moment M_{FA} and side-to-side bending moment M_{SS}, for each load case with different wave-wind misalignment and hydrodynamic load component, respectively. The effects of wave-wind misalignment are firstly investigated by considering the cases with the first order force and second order difference-frequency force (1st+full QTF). As shown in Fig. 9, the mean values of M_{FA} and M_{SS} do not strongly depend on the wave-wind misalignment, since the tower base bending moments are primarily caused by the large aerodyanmic force acting on the rotor and by the weight of the rotor due to the tower tilt and are thus not affected by the wave-wind misalignment. Unlike the mean value, the wave-wind misalignment has a slight influence on the standard deviations of M_{FA} and M_{SS}. As wave-wind misalignment increases, the standard deviation of M_{SS} decreases slightly while the standard deviation of M_{FA} increases slowly with wave direction in the range of 0º to 60 º and then decrease slightly. The maximum values of M_{FA} and M_{SS} vary similarly as the standard deviation when the wave-wind misalignment increases. However, these variations are larger than those for the standard deviation. Therefore, the wave-wind misalignment has relatively larger influence on the maximum values of M_{FA} and M_{SS} than on the standard deviations of M_{FA} and M_{SS}. In addition, the effects of wave-wind misalignment can be more clearly observed by power spectrum analysis, as shown in Fig. 10. When β_{wave}= 0º, the responses of M_{FA} and M_{SS} are dominated by the response corresponding to the 2P frequency. As the wave-wind misalignment increases, these 2P responses decrease, and increasing responses corresponding to the elastic blade frequency are excited.

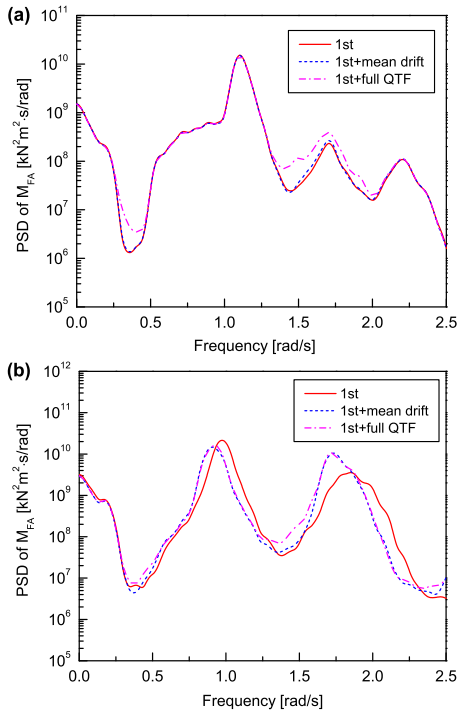

Fig. 10. power spectrum of the tower base fore-aft bending moment M_{FA} under different consideration of hydrodynamic loads. (a) β_{wave}= 0º in LC 3 (b) β_{wave}= 90º in LC 6.

Fig. 9 also demonstrates the effects of second order difference-frequency force on the tower base bending moments M_{FA} and M_{SS}. Second order difference-frequency force slightly affects the mean values of M_{FA} and M_{SS}. However, the standard deviations of the tower base bending moments, especially M_{SS} at higher significant wave height such as LC6, depend on the second order difference-frequency force. Fig. 10 (b) compares the power spectrum of M_{FA} with β_{wave}= 90º in LC 6 under different hydrodynamic loads. it is found that when the second order difference-frequency force is taken into consideration, the 2P response becomes smaller and much larger response corresponding to the elastic blade frequency is excited. As a result, the second order

difference-frequency force causes much larger standard deviation of M_{FA} at higher significant wave height.

Mooring Line Tension

Fig. 11 shows the mean values, standard deviations and maximum values of the tensions in mooring line for each load case. among the mean value, standard deviation and maximum value, the largest tension is all found in mooring line 2, which is deployed along the wind direction as shown in Fig. 1. Moreover, the mean values of mooring line tensions are much larger than the standard deviations.

By considering the cases with the first order force and second order difference-frequency force (1st+full QTF), the influences of wave-wind misalignment are discussed. As the mean values of the tower base bending moment, the mean values of mooring line tension remain almost the same and are not affected by the wave-wind misalignment, this is because the mean values are primarily determined by the wind loads. The standard deviations of the tensions in mooring line are slightly sensitive to the wave-wind misalignment. With increasing wave-wind misalignment, the standard deviation of tension in mooring line 2 decreases while those in mooring line 1 and 3 increase. The maximum value shows the same trend as the standard deviation when the wave-wind misalignment increase.

In addition, the second order difference-frequency force slightly increases the standard deviation and maximum value of the tensions in mooring line. And these increases are more obvious in wave-wind aligned conditions with high significant wave height such as LC6.

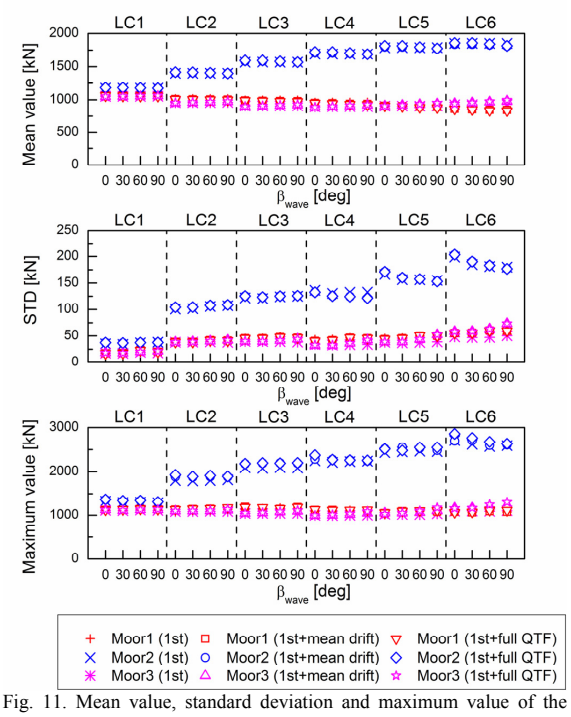

Fig. 11. Mean value, standard deviation and maximum value of the tension in mooring line 1, 2 and 3 as a function of wave direction β_{wave} for all load cases.

CONCLUSIONS

The present paper deals with the effect of second order difference-frequency force on the dynamic responses of a 5 MW FVAWT in wave-wind misalignment condition. The FVAWT considered is a 5 MW Darrieus rotor mounted on a semi-submersible floater and is subjected to various misalgned turbulent wind and irregular wave conditions. The platform motions, structural responses and mooring line tensions of the FVAWT are calculated using time domain simulations based on a fully coupled nonlinear model.

The mean values of the platform motions are not affected by the wave-wind misalignment, except the sway motion in LCs with high wind speed. The standard deviations of the platform motions are slightly sensitive to the wave-wind misalignment. The mean values of the plarform motions are a little larger when considering the mean drift force or second order difference frequency force. Moreover, the second order difference-frequency forces have slight influence on the standard deviation of surge, heave, roll and pitch motions. For sway and yaw motions, the second order difference-frequency force contributes to some extent to the standard deviation.

The mean values of tower base bending moments M_{FA} and M_{SS} do not strongly depend on the wave-wind misalignment . However, the wave-wind misalignment has a slight influence on the standard deviations of M_{FA} and M_{SS}. With increasing wave-wind misalignment, the standard deviation of M_{SS} decreases slightly while the standard deviation of M_{FA} increases slowly with wave direction in the range of 0º to 60 º and then decreases slightly. The maximum values of M_{FA} and M_{SS} vary similarily as the standard deviation when the wave-wind misalignment increases. The second order difference-frequency force slightly affects the mean values of M_{FA} and M_{SS}. However, the standard deviations of the tower base bending moment, especially M_{SS} at higher significant wave height, depend on the second order difference-frequency force.

The mean values of mooring line tensions are not affected by the wave-wind misalignment since they are mainly wind-induced. In contrast, the standard deviations and maximum values of mooring line tensions are slightly sensitive to the wave-wind misalignment in LCs with high wind speed and significant wave height. In addition, the second order difference-frequency force causes increases in the standard deviations and maximum values of the mooring line tensions.

ACKNOWLEDGEMENTS

The first author would like to acknowledge the financial support from the Research Council of Norway through NOWITECH and the Centre for Ships and Ocean Structures at the Department of Marine Technology, Norwegian University of Science and Technology, Trondheim, Norway. The second author would like to acknowledge the financial support from the EU FP7 project MARE WINT (project no 309395) through the Centre for Ships and Ocean Structures at the Department of Marine Technology, Norwegian University of Science and Technology, Trondheim, Norway.

REFERENCES

"10MW Aerogenerator X © Wind Power Limited & Grimshaw at http://vimeo.com/13654447.

Akimoto, H, Tanaka, K, and Uzawa, K (2011). "Floating axis wind turbines for offshore power generation—a conceptual study," *Environmental Research Letters*, *6*(4), 044017.

Bachynski, EE, Kvittem, MI, Luan, C, and Moan, T (2014). "Wind-Wave Misalignment Effects on Floating Wind Turbines: Motions

and Tower Load Effects," *Journal of Offshore Mechanics and Arctic Engineering*, *136*(4), 041902.

Barj, L, Stewart, S, Stewart, G, Lackner, M, Jonkman, J, Robertson, A, and Matha, D (2014). "Wind/Wave Misalignment in the Loads Analysis of a Floating Offshore Wind Turbine," in *AIAA SciTech 2014*, National Harbor, Maryland, USA.

Borg, M, and Collu, M (2014). "A Comparison on the Dynamics of a Floating Vertical Axis Wind Turbine on Three Different Floating Support Structures," *Energy Procedia*, *53*, 268-279.

Borg, M, Collu, M, and Brennan, FP (2013). "Use of a Wave Energy Converter as a Motion Suppression Device for Floating Wind Turbines," *Energy Procedia*, *35*, 223-233.

Borg, M, Shires, A, and Collu, M (2014a). "Offshore floating vertical axis wind turbines, dynamics modelling state of the art. part I: Aerodynamics," *Renewable and Sustainable Energy Reviews*.

Borg, M, Collu, M, and Kolios, A (2014b). "Offshore floating vertical axis wind turbines, dynamics modelling state of the art. Part II: Mooring line and structural dynamics," *Renewable and Sustainable Energy Reviews*.

Borg, M, Wang, K, Collu, M, and Moan, T (2014c). "A Comparison of Two Coupled Model of Dynamics for Offshore Floating Vertical Axis Wind Turbines (VAWT)," *Proceedings of the 33rd International Conference on Ocean, Offshore and Arctic Engineering, OMAE2014-23301*, San Francisco, California, USA.

Cahay, M, Luquiau, E, Smadja, C, and Silvert, F (2011). "Use of a vertical wind turbine in an offshore floating wind farm," *Offshore Technology Conference*, Houston, Texas, USA.

Collu, M, Borg, M, Shires, A, and Brennan, FP (2013). "FloVAWT: progress on the development of a coupled model of dynamics for floating offshore vertical axis wind turbines," *ASME 2013 32nd International Conference on Ocean, Offshore and Arctic Engineering*, American Society of Mechanical Engineers.

Fischer, T, Rainey, P, Bossanyi, E, and Kühn, M (2011). "Study on control concepts suitable for mitigation of loads from misaligned wind and waves on offshore wind turbines supported on monopiles," *Wind Engineering*, *35*(5), 561-574.

Fowler, MJ, Owens, B, Bull, D, Goupee, AJ, Hurtado, J, Griffith, DT, and Alves, M (2014). "Hydrodynamic Module Coupling in the Offshore Wind Energy Simulation (OWENS) Toolkit," *ASME 2014 33rd International Conference on Ocean, Offshore and Arctic Engineering*, American Society of Mechanical Engineers.

IEC (2009). "International Standard 61400-3, Wind turbines, Part 3: Design requirements for offshore wind turbines.

Johannessen, K, Meling, TS, and Haver, S (2002). "Joint distribution for wind and waves in the northern north sea," *International Journal of Offshore and Polar Engineering*, *12*(1).

Jonkman, BJ (2009). TurbSim user's guide: Version 1.50. , Tech. Rep. NREL/TP-500-46198, NREL, Golden, CO, USA.

Kühn, MJ (2001). Dynamics and design optimisation of offshore wind energy conversion systems, PhD thesis, Delft University of Technology, Delft, Netherlands.

Luxcey, N, Ormberg, H, and Passano, E (2011). "Global analysis of a floating wind turbine using an aero-hydro-elastic numerical model. Part 2: Benchmark study," in *Offshore Mechanics and Arctic Engineering Conference*, Rotterdam, The Netherlands.

Merz, KO (2012). "A Method for Analysis of VAWT Aerodynamic Loads under Turbulent Wind and Platform Motion," *Energy Procedia*, *24*, 44-51.

Merz, KO, and Svendsen, HG (2013). "A control algorithm for the deepwind floating vertical-axis wind turbine," *Journal of Renewable and Sustainable Energy*, *5*(6), 063136.

Ormberg, H, Passano, E, and Luxcey, N (2011). "Global analysis of a floating wind turbine using an aero-hydroelastic model. Part 1: Code development and case study," *Offshore Mechanics and Arctic Engineering Conference*, Rotterdam, The Netherlands.

Owens, B, Hurtado, J, Barone, M, and Paquette, J (2013a). "An energy preserving time integration method for gyric systems: development of the offshore wind energy simulation toolkit," *Proceedings of the European Wind Energy Association Conference & Exhibition*.

Owens, BC, Hurtado, JE, Barone, M, Griffith, D, and Paquette, J (2013b). "Aeroelastic modeling of large offshore vertical-axis wind turbines: development of the offshore wind energy simulation toolkit," *Proceedings of the 54th AIAA Structures, Structural Dynamics and Materials Conference*.

Paquette, J, and Barone, M (2012). "Innovative offshore vertical-axis wind turbine rotor project," *EWEA 2012 Annual Event*.

Paulsen, US, Madsen, HA, Hattel, JH, Baran, I, and Nielsen, PH (2013). "Design optimization of a 5 MW floating offshore vertical-axis wind turbine," *Energy Procedia*, *35*, 22-32.

Sutherland, HJ, Berg, DE, and Ashwill, TD (2012). "A retrospective of VAWT technology," *Sandia Report, SAND2012*, *304*.

Svendsen, HG, and Merz, KO (2013). "Control System for Start-up and Shut-down of a Floating Vertical Axis Wind Turbine," *Energy Procedia*, *35*, 33-42.

Svendsen, HG, Merz, KO, and Endegnanew, AG (2012). "Control of floating vertical axis wind turbine," *European Wind Energy Conference and Exhibition*, Copenhagen, Denmark.

Vita, L (2011). Offshore Floating Vertical Axis Wind Turbines with Rotating Platform, National Laboratory for Sustainable Energy, DTU.

Wang, K, Moan, T, and Hansen, MOL (2013). "A method for modeling of floating vertical axis wind turbine," *Proceedings of the 32th International Conference on Ocean, Offshore and Arctic Engineering*, OMAE2013-10289, Nantes, France.

Wang, K, Hansen, MOL, and Moan, T (2014a). "Dynamic analysis of a floating vertical axis wind turbine under emergency shutdown using hydrodynamic brake," *Energy Procedia*, *53*(C), 56-69.

Wang, K, Moan, T, and Hansen, MOL (2015). "Stochastic dynamic response analysis of a floating vertical axis wind turbine with a semi-submersible floater," *Wind Energy*, *(submitted)*.

Wang, K, Luan, C, Moan, T, and Hansen, MOL (2014b). "Comparative Study of a FVAWT and a FHAWT with a Semi-submersible Floater," *Proceedings of the 24th International Ocean and Polar Engineering Conference*, Busan, Korea.

A.6 Paper 6

Paper 6:

A comparative study on dynamic responses of spar-type floating horizontal and vertical axis wind turbines.

Zhengshun Cheng, Kai Wang, Zhen Gao, Torgeir Moan

Revision submitted to *Wind Energy*, 2016

A comparative study on dynamic responses of spar-type floating horizontal and vertical axis wind turbines

Zhengshun Cheng *[1,2,4], Kai Wang[2,3], Zhen Gao[1,2,4], and Torgeir Moan[1,2,4]

[1]Department of Marine Technology, Norwegian University of Science and Technology, Trondheim, Norway
[2]Centre for Ships and Ocean Structures, Norwegian University of Science and Technology, Trondheim, Norway
[3]NOWITECH, Norwegian University of Science and Technology, Trondheim, Norway
[4]Centre for Autonomous Marine Operations and Systems, Norwegian University of Science and Technology, Trondheim, Norway

Abstract

Interest in the exploitation of offshore wind resources using floating wind turbines has increased. Commercial development of floating horizontal axis wind turbines (FHAWTs) is emerging due to their commercial success in onshore and near-shore areas. Floating vertical axis wind turbines (FVAWTs) are also promising due to their low installation and maintenance costs. Therefore, a comparative study on the dynamic responses of FHAWTs and FVAWTs is of great interest. In the present study, a FHAWT employing the NREL 5 MW wind turbine and a FVAWT employing a Darrieus rotor, both mounted on the OC3 spar buoy, were considered. An improved control strategy was introduced for FVAWTs to achieve an approximately constant mean generator power for the above rated wind speeds. Fully coupled time domain simulations were carried out using identical, directional aligned and correlated wind and wave conditions. Due to different aerodynamic load characteristics and control strategies, the FVAWT results in larger mean tower base bending moments and mooring line tensions above the rated wind speed. Because significant two-per-revolution (2P) aerodynamic loads act on the FVAWT, the generator power, tower base bending moments and delta line tensions show prominent 2P variation. Consequently the FVAWT suffers from severe fatigue damage at the tower bottom. However, the dynamic performance of the FVAWT could be improved by increasing the number of blades , using helical blades or employing a more advanced control strategy, which requires additional research.

Key words: floating wind turbine; horizontal axis; vertical axis; dynamic response; comparative study.

*Email: zhengshun.cheng@ntnu.no

1 Introduction

In recent years, offshore wind technology has been rapidly developing with a total global installed capacity of 8.771 GW by the end of 2014 (Global Wind Energy Council, 2015). Currently, most commercial wind farms are deployed in waters that are shallower than 50 m by using bottom-fixed supporting structures such as monopile, tripod or jacket. However, floating wind turbines are more desirable in deeper water sites, especially in the North Sea, Japan, South Korea, USA and China. Due to their commercial success onshore and near shore, floating horizontal axis wind turbines (FHAWTs) are widely used and studied with different supporting structures, including spar (Karimirad and Moan, 2012, 2011), TLP (Bachynski and Moan, 2012) and semi-submersible (Kvittem et al., 2012; Roddier et al., 2010) structures. Moreover, commercial development projects for FHAWTs are emerging, including the Kincardine and Buchan Deep projects in Scotland, the WindFloat Pacific project in the USA, and the Fukushima Forward project in Japan.

Floating vertical axis wind turbines (FVAWTs) are a very promising alternative for offshore application. Compared with FHAWTs, FVAWTs have lower centers of gravity, are independent of wind direction, and can provide reduced machine complexity. Consequently, FVAWTs may have lower operations and maintenance, support structure design, installation, and electrical infrastructure costs. Paquette and Barone (2012) indicated the potential of achieving more than 20% cost of energy (COE) reductions by using FVAWTs. Moreover, FVAWTs are more suitable for deployment on wind farms than FHAWTs. The wake generated by a pair of counter-rotating H-rotors can dissipate more quickly than the wake generated by FHAWTs, allowing them to be installed in parks with smaller separations (Kinzel et al., 2012). The average power generated by a pair of H-rotors at all azimuth angles is higher than that of an isolated turbine (Dabiri, 2011), implying that the conversion efficiency of VAWTs can be improved.

Thus, the development of FVAWTs increased and several FVAWT concepts have recently been proposed, including the DeepWind (Paulsen et al., 2015) , VertiWind (Cahay et al., 2011), Aerogenerator X (Shires, 2013; Collu et al., 2014) , and floating tilted axis (Akimoto et al., 2011) concepts. Similar to the FHAWTs, the substructures supporting the FVAWTs can be categorized as spar, semi-submersible and TLP types. A FVAWT concept with a 5 MW Darrieus rotor mounted on a semi-submersible was proposed by Wang et al. (2013), and fully coupled aero-hydro-servo-elastic simulations were carried out with emphasis on stochastic dynamic responses (Wang et al., 2016), the effects of second order difference-frequency forces and wind-wave misalignment (Wang et al., 2015a), and the emergency shutdown process with consideration of faults (Wang et al., 2014a). Dynamic response analyses were conducted for the three FVAWTs (Cheng et al., 2015b) with a 5 MW Darrieus rotor mounted on the OC3 spar buoy, the OC4 semi-submersible and a TLP designed by Bachynski and Moan (2012) by using fully coupled nonlinear time domain simulations.

Therefore it is of interest to perform comparative studies to reveal the merits and feasibilities of FHAWTs and FVAWTs. Paraschivoiu (2002) discussed the merits and disadvantages of HAWTs and VAWTs and investigated their rotor performances and support foundation loads. Eriksson et al. (2008) evaluated three different wind turbine concepts, including HAWTs and two different VAWTs with H-rotor and Darrieus rotor respectively. The comparative study emphasized the design, aerodynamic performance, type of control system, environmental impacts, noise, and manufacturing, operation and maintenance costs of these turbines. Islam et al. (2013) compared HAWTs and VAWTs regarding their footprints and highlighted the fish-schooling concept for VAWT farms. Borg et al. (2014) compared VAWTs

with HAWTs by considering aspects of technology, conversion efficiency, upscaling, fatigue, machinery position, extreme conditions and packing factors. However, the aforementioned comparisons are limited to onshore wind turbines and lack integrated dynamic response analysis.

Recently, these comparative studies were extended to floating wind turbines by several researchers. Borg and Collu (2015) further carried out a preliminary comparison between the FHAWT and FVAWT based on prime principles with emphasis on the aerodynamic forces and their impact on the static and dynamic responses. But limited comparison regarding the dynamic behavior was conducted and no controller was included for the FVAWT. Wang et al. (2014b) performed a comparative study of a FVAWT with a 5 MW Darrieus rotor and a FHAWT with the NREL 5 MW wind turbine (Jonkman et al., 2009), which were both mounted on the OC4 semi-submersible (Robertson et al., 2012). Fully coupled nonlinear simulations were carried out to investigate the dynamic responses of the FHAWT and FVAWT. Cheng et al. (2015a) studied the same rotors with OC3 spar buoys (Jonkman, 2010) subjected to constant wind. However, the wind fields were created with respect to different reference heights for the FHAWT and FVAWT,which implies that a slightly different wind field was used. Moreover, the generator power of the FVAWT exceeds 5 MW above the rated wind speed and could even reach up to 9 MW. Thus, the FHAWT and FVAWT considered in the previous comparative studies were different regarding their generator power production above the rated wind speed. Additional comparative studies of FHAWTs and FVAWTs in the same wind and wave conditions and with the same rated power, supporting platform and mooring system are needed.

In the present study, the control strategy for FVAWTs is improved to achieve an approximately constant mean generator power above the rated wind speed, which was set as 5 MW (the same as that of the FHAWT). Based on the improved controller for the FVAWT, this comparison was further extended to floating wind turbines by considering the OC3 spar floater supporting the NREL 5 MW wind turbine and a 5 MW Darrieus rotor, respectively. The ballast of the spar platform supporting the FVAWT was adjusted to retain the same draft and displacement as that of the FHAWT. A series of correlated and directionally aligned turbulent wind and wave were carried out to investigate the wind turbine performance, platform motion, structural response and mooring line tension for each floating wind turbine. This comparative study captures and demonstrates the different characteristics of these floating wind turbines and allows for detailed assessments of FHAWTs and FVAWTs.

2 Methodology

2.1 Floating Wind Turbine Models

A floating wind turbine system is usually composed of a rotor to harvest wind energy, a floating platform to support the rotor and a mooring system to hold the floater in position. The studied FHAWT and FVAWT were considered in water with a depth of 320 m, as depicted in Figure 1. The OC3 spar buoy used for the FHAWT is described in Jonkman (2010) and was used to support the NREL 5 MW wind turbine, which is a traditional three-bladed upwind HAWT (Jonkman et al., 2009). Good stability is guaranteed by the heavy ballast located at the bottom, which limits the platform pitch and roll motions under the wind and wave condition. The horizontal restoring stiffness is provided by the mooring system, as shown in Figure 1. A catenary chain mooring system with delta lines and clump weights was applied

so as to increase the yaw stiffness to resist the aerodynamic yaw moment.

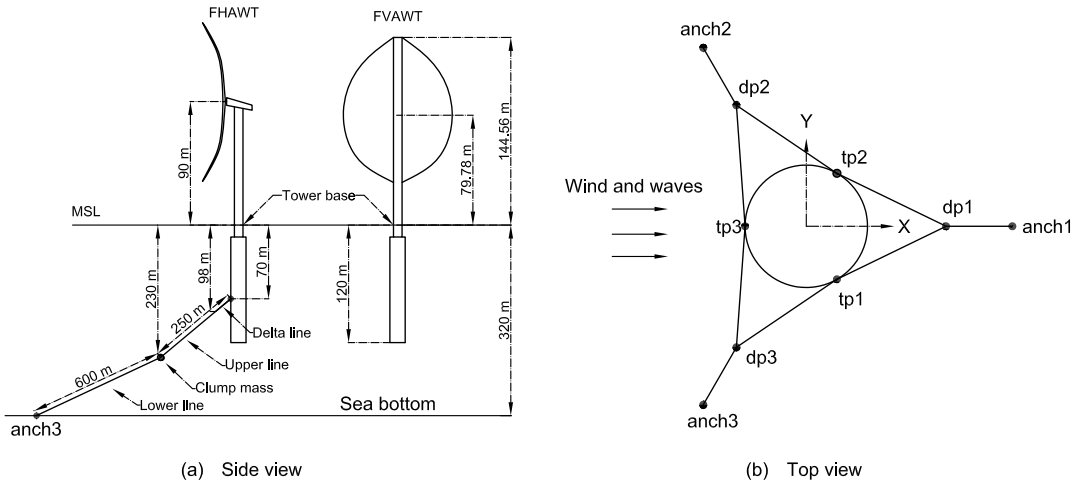

Figure 1: Schematic of the floating wind turbines and mooring system

In this study, the same spar hull and mooring system were maintained to support a 5 MW Darrieus rotor, which was originally developed in the DeepWind project (Vita, 2011). It comprises of two blades and one rotating tower that spans from the top to the bottom which is connected to the direct drive generator. The specifications of the 5 MW Darrieus rotor and the NREL 5 MW reference wind turbine are provided in Table 1. It should be noted that the generator of the FVAWT is assumed to be located at the tower base. The mass of the rotor in the FVAWT only refers to the mass of two blades, whereas the mass of the rotor in the FHAWT comprises the masses of three blades and the hub. Due to this difference in rotor mass, the ballast of the spar hull for the FVAWT was adjusted to remain the same draft and displacement as that of the FHAWT. Because the mass difference between the two rotors is very small compared with the displacement, it is assumed that such adjustment do not significantly alter the hydrostatic performance. The geometrical, structural and hydrostatic properties of the spar floaters for the FHAWT and the FVAWT are described in Cheng et al. (2015a). In addition, free decay tests were conducted in Cheng et al. (2015a) to estimate the natural periods of rigid body motions for the floating wind turbine systems, as listed in Table 2.

Different coordinate systems are introduced to describe the dynamic responses of the two floating wind turbines. The platform motions and the tower base bending moments are all defined in the global coordinate system which originates along the tower centerline at mean sea level (MSL), as shown in Figure 1. Regarding the aerodynamic loads acting on the rotor, the thrust forces are also defined in the global coordinate system; however, the aerodynamic torque is defined with respect to the local coordinate system of the shaft with the z-axis along the shaft. This definition should be kept in mind when discussing of the differences in the aerodynamic loads.

Table 1: Specifications of HAWT and VAWT

Turbines	FVAWT	FHAWT
Rated power [MW]	5	5
Rotor radius [m]	63.74	63
Rotor height/hub height [m]	129.56	90
Chord [m]	7.45	1.419-4.652
Cut-in, rated, cut-out wind speed [m/s]	5 , 14 , 25	5 , 11.4 , 25
Rated rotor rotational speed [rpm]	5.26	12.1
Nacelle mass [kg]	0	240,000
Rotor mass [kg]	305,044	110,000
Shaft mass/Tower mass [kg]	449,182	249,718
Location of overall CM [m]	(0 , 0 , 75.6)	(-0.2 , 0 , 70.06)

Table 2: Properties of the floating wind turbine systems

Floater	FVAWT	FHAWT
Water depth [m]	320	320
Draft [m]	120	120
Diameter at MWL [m]	6.5	6.5
Platform mass, including ballast [ton]	7308.29	7466.33
Center of mass for platform [m]	(0, 0, -89.76)	(0, 0, -89.92)
Buoyancy in undisplaced position [kN]	80710	80710
Center of buoyancy [m]	(0, 0, -62.07)	(0, 0, -62.07)
Surge/Sway natural period [s]	130.8	130.4
Heave natural period [s]	27.3	31.5
Pitch/Roll natural period [s]	34.5	29.6
Yaw natural period [s]	8.5	8.2

2.2 Fully Coupled Analysis Method

Dynamic response analyses of floating wind turbine systems require sophisticated numerical tools to represent the aero-hydro-servo-elastic behaviors in time domain. Simo-Riflex-AeroDyn (Ormberg and Bachynski, 2012) and Simo-Riflex-DMS (Wang et al., 2013) are state-of-the-art fully coupled nonlinear time-domain simulation codes that can account for turbulent wind inflow, aerodynamics, hydrodynamics, control dynamics, structural dynamics and mooring line dynamics.

The FHAWT was modeled using the Simo-Riflex-AeroDyn code, which couples three computer codes to model the behavior of floating wind turbine systems in the time domain: Simo computes the rigid body hydrodynamic forces and moments on the hull; Riflex models the blades, tower, shaft and mooring lines as nonlinear finite elements, calculates the hydrodynamic loads on the mooring lines and provides links to the external controller and AeroDyn; and AeroDyn calculates the forces and moments on the blades according to the Blade Element Momentum (BEM) theory or the Generalized Dynamic Wake (GDW) theory. The external control system, which includes the generator torque controller below the rated wind speed and the blade pitch controller above the rated wind speed, was written in Java. The Simo-Riflex-AeroDyn code has been verified by comparing it with FAST and other comprehensive codes (Ormberg and Bachynski, 2012; Ormberg et al., 2011).

The FVAWT was modeled using the Simo-Riflex-DMS code, which was developed by Wang et al. (2013, 2015b). Two significant differences exist between the Simo-Riflex-DMS and Simo-Riflex-AeroDyn codes. The first difference is that the Double Multiple-Streamtube (DMS) model is employed to calculate the aerodynamic loads on the rotor in the Simo-Riflex-DMS code, rather than BEM or GDW theory, which are used in the Simo-Riflex-AeroDyn code. The DMS model includes the effects of variations in the Reynolds number and incorporates the Beddoes-Leishman dynamic stall model. The second difference is that only a PI generator torque controller is employed to adjust the electric torque to minimize the error between the measured rotational speed and the reference rotational speed in the Simo-Riflex-DMS code. The reference rotational speed is determined according to different operational regions, which are described in detail in the next section. The DMS model has been validated by comparing it with experimental data (Wang et al., 2015b). The Simo-Riflex-DMS code has been verified by a series of numerical comparisons with computer codes HAWC2 and Simo-Riflex-AC (Cheng et al., 2016b). In the Simo-Riflex-AC, the AC code based on the actuator cylinder flow model has been validated using experimental data as well (Cheng et al., 2016a).

In both models, the spar floater was considered as a rigid body. The added mass, radiation damping and first order wave forces were obtained from a potential flow model in Wadam (Wadam, 2010). In addition, viscous forces were applied to represent the quadratic damping on the hull and mooring system, and the corresponding drag coefficients were chosen as 0.6 and 1.0 (Jonkman, 2010), respectively. The mean wave drift forces were considered and Newman's approximation was used to estimate the second-order difference-frequency wave excitation forces. The tower, blades and shaft were modeled using beam elements, and the mooring lines were represented using bar elements and connecting joints. The nonlinear finite element solver in Riflex was used for a full dynamic analysis.

2.3 Control Strategy for the FVAWT

In the previous study (Wang et al., 2014b; Cheng et al., 2015a), a baseline PI generator control, developed by Svendsen et al. (2012) and Merz and Svendsen (2013), was used to enable variable-speed and fixed-pitch operation. The architecture of the baseline controller is highlighted in the green box in Figure 2. The generator rotational speed and electric torque are measured and low-pass filtered. The controller aims to minimize the error between the measured and filtered rotational speed Ω_{mes} and the reference rotational speed Ω_{ref},

$$\Delta\Omega = \Omega_{mes} - \Omega_{ref} \tag{1}$$

in which the reference rotational speed Ω_{ref} is defined as a function of the measured and low-pass filtered electric torque $\widehat{T}$ as follows

$$\Omega_{ref} = \begin{cases} \Omega_{opt}(\widehat{T}), & \text{If } \widehat{T} < T_{\Omega_N} \left(\text{or } \widehat{V} < V_{\Omega_N}\right) \\ \Omega_N, & \text{If } \widehat{T} \geq T_{\Omega_N} \left(\text{or } \widehat{V} \geq V_{\Omega_N}\right) \end{cases} \tag{2}$$

where $\widehat{V}$ is the measured and filtered wind speed, V_{Ω_N} is the wind speed for the rated rotational speed, T_{Ω_N} is the electric torque at wind speed V_{Ω_N}, Ω_N is the rated rotational speed, and Ω_{opt} is the optimal rotational speed that can maximize the power capture. The relationship between the reference rotor rotational speed and the wind speed is illustrated in Figure 3. In the controller studied the reference rotational speed is obtained using a look-up table. The rotational speed error $\Delta\Omega$ is then fed through the proportional, integral and derivative paths to obtain an updated value of the required electric torque, as follows,

$$T(t) = K_G\left(K_P\Delta\Omega(t) + K_I\int_0^t \Delta\Omega(\tau)d\tau + K_D\frac{d}{dt}\Delta\Omega(t)\right) \tag{3}$$

in which K_G is the generator stiffness, and K_P, K_I and K_D are the proportional, integral and derivative gains, respectively. Therefore, this controller is capable of maximizing the power capture for wind speeds below V_{Ω_N} and maintaining the rotational speed for wind speeds above V_{Ω_N}.

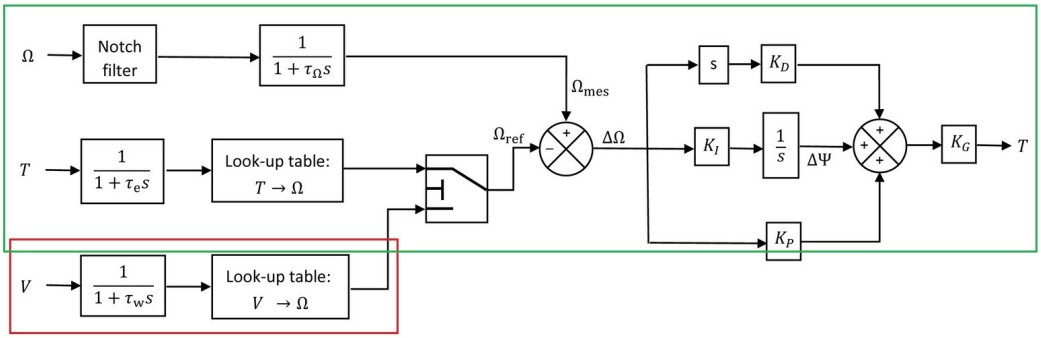

Figure 2: The generator torque control algorithm for FVAWT based on a PID architecture.

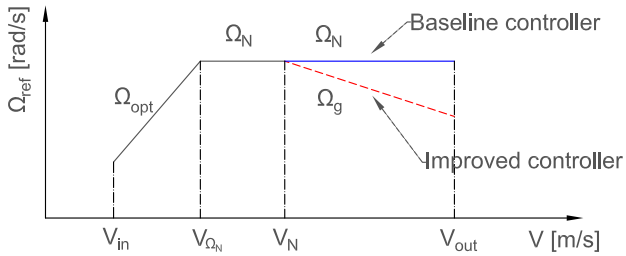

Figure 3: The relationship between the reference rotor rotational speed and the wind speed for the baseline and improved controllers

However, the above baseline control strategy does not limit the generator power and the generator power increases as the wind speed increases, even at above the rated wind speed V_N. At very high wind speed, very large aerodynamic thrust and torque are thus expected, which can cause large structural responses. Therefore it is of interest to figure out whether the generator power as well as aerodynamic loads on the rotor at above rated wind speed V_N should be limited.

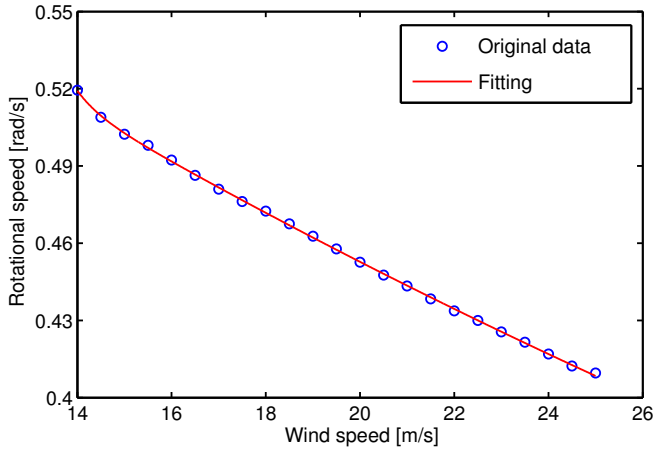

Figure 4: The relationship between the rotational speed and the wind speed for the considered Darrieus rotor with a constant mean aerodynamic power of 5.296 MW for the above rated wind speed

An improved control strategy that can hold the mean generator power constant above the rated wind speed was then proposed. The reference rotational speed above the rated wind speed is determined from the measured and filtered wind speed by using a look-up table, as shown in the red box in Figure 2. In reality, it is not easy to measure the hub height wind speed directly for the FVAWT. However, as similar to the FHAWT, the tower top wind speed of the FVAWT can be easily measured. Given the wind shear that relates the wind speed at hub height and tower top, the hub height wind speed can thus be determined approximately. The look-up table was based on the relationships between the rotational speed and wind speed, which can give the constant mean aerodynamic power. A series of simulations with various fixed

rotational speeds and wind speeds in the steady shear wind conditions were conducted to determine the mean aerodynamic power for the onshore rotor. Next, curve fitting based on the nonlinear least squares method was applied to obtain a curve of the rotational speed versus the wind speed for a constant mean aerodynamic power above the rated wind speed, as shown in Figure 4. The constant mean aerodynamic power was set as 5.296 MW, which was the same as that of the NREL 5MW wind turbine. Therefore, the reference rotational speed above the rated wind speed is a function of wind speed, which is the primary difference from the baseline controller. Because the look-up table is developed for an onshore rotor under steady wind conditions, the turbulent wind conditions and platform motions can both affect the aerodynamic power performance and result in small deviations in the mean aerodynamic power from the target, which will be addressed later. For turbulent wind conditions the wind speed is measured and low-pass filtered.

Similarly, the reference rotational speed for the improved controller can be written as

$$\Omega_{ref} = \begin{cases} \Omega_{opt}(\widehat{T}), & \text{If } \widehat{T} < T_{\Omega_N} \left(\text{or } \widehat{V} < V_{\Omega_N}\right) \\ \Omega_N, & \text{If } T_{\Omega_N} \le \widehat{T} < T_N \left(\text{or } V_{\Omega_N} \le \widehat{V} < V_N\right) \\ \Omega_g(\widehat{V}), & \text{if } T_N \le \widehat{T} \left(\text{or } V_N \le \widehat{V}\right) \end{cases} \tag{4}$$

where Ω_g is the rotational speed for the constant power above the rated wind speed. One example of the reference rotational speed for the onshore VAWT is the mean rotational speed as shown in Figure 6 (d).

In addition, all of the parameter values in the improved controller, except for the proportional gain K_P, were chosen to equal those used in Svendsen et al. (2012) and Merz and Svendsen (2013). Because different modeling methods are used for wind turbine systems, the proportional gain K_P was set to be 0.06 in this study to avoid low-frequency electric torque variations at very high wind speed.

2.4 Fatigue Damage Estimation

The periodic aerodynamic loads acting on the VAWT may cause considerable response oscillation for some structural components. The short-term fatigue damage of the wind turbine components is addressed in this study. A Matlab-based computer program MLife developed by NREL (Hayman, 2012) is used to estimate the short-term damage equivalent fatigue loads (DEFLs) for each component. The short-term DEFL is a constant-amplitude load that occurs at a fixed load-mean and frequency and can produce damage that is equivalent to that of the variable spectrum loads. In this study, a DEFL frequency of 1 Hz was assumed. The Wohler exponent was set to be 3 for the tower base and mooring lines. Because the studied floating wind turbines are generalized concepts, fatigue damage analysis is performed without applying the Goodman correction.

3 Load Cases

Several load cases (LCs) were defined to study the dynamic responses of the FHAWT and FVAWT, as given in Table 3-5. LC1 and LC2 were steady and turbulent wind conditions, respectively, and were used to investigate the stability and dynamic performance of the improved controller for the FVAWT.

LC3 with correlated and directionally aligned wind and waves was used to compare the FHAWT and FVAWT.

Table 3: Load Cases –steady wind only conditions

	U_w [m/s]	Wind Cond.	Sim. Length [s]
LC1.1	5	NWP	800
LC1.2	10	NWP	800
LC1.3	14	NWP	800
LC1.4	18	NWP	800
LC1.5	22	NWP	800
LC1.6	25	NWP	800

Table 4: Load Cases –turbulent wind only conditions

	U_w [m/s]	Wind Cond.	Sim. Length [s]
LC2.1	5	NWP+NTM	3600
LC2.2	10	NWP+NTM	3600
LC2.3	14	NWP+NTM	3600
LC2.4	18	NWP+NTM	3600
LC2.5	22	NWP+NTM	3600
LC2.6	25	NWP+NTM	3600

Table 5: Load Cases –combined wind and waves

	U_w (FVAWT) [m/s]	U_w (FHAWT) [m/s]	H_s [m]	T_p [s]	Wind Cond.	Sim. Length [s]
LC3.1	5	5.09	2.10	9.74	NWP+NTM	3600
LC3.2	8	8.14	2.55	9.86	NWP+NTM	3600
LC3.3	10	10.17	2.88	9.98	NWP+NTM	3600
LC3.4	12	12.20	3.24	10.12	NWP+NTM	3600
LC3.5	14	14.24	3.62	10.29	NWP+NTM	3600
LC3.6	18	18.31	4.44	10.66	NWP+NTM	3600
LC3.7	22	22.37	5.32	11.06	NWP+NTM	3600
LC3.8	25	25.43	6.02	11.38	NWP+NTM	3600

For steady wind conditions, the normal wind profile (NWP) was applied, in which the wind profile $U(z)$ is the average wind speed as a function of height z above MSL, and is given by the following power law

$$U(z) = U_{ref}\left(\frac{z}{z_{ref}}\right)^{\alpha} \tag{5}$$

where U_{ref} is the reference wind speed, z_{ref} the height of reference wind speed and α the power law exponent.the value of α was chosen to be 0.14 for the floating wind turbines according to IEC 61400-3

(IEC, 2005). The values of z_{ref} were set to 90 m (hub height) and 79.78 m (vertical center of the blades) above MSL for the FHAWT and FVAWT, respectively. For turbulent wind conditions, the NWP and normal turbulence model (NTM) were both applied. The three dimensional turbulent wind fields were generated using NREL's TurbSim program (Jonkman, 2009) according to the Kaimal turbulence model for IEC Class C. The JONSWAP wave model was used to generate the wave history. The significant wave height (Hs) and peak period (Tp) were set based on their correlation with wind speed for the Statfjord site in the northern North Sea (Johannessen et al., 2002).

To obtain a more reasonable comparison of the FHAWT and FVAWT, the same wind field and wave elevation were applied to both the FVAWT and FHAWT. The reference wind speeds at hub height for the FHAWT were computed based on the FVAWT according to Equation 5, as the U_w given in Table 5. For LC2 with turbulent wind and LC3 with turbulent wind and waves, each simulation lasted 4600 s, in which the first 1000 s was removed to eliminate the start-up transient effects and to form a one-hour dynamic analysis. Five identical and independent one-hour simulations with different seeds for turbulent winds and irregular waves were carried out for each LC to reduce the stochastic variations. The comparative study was based on the statistical values obtained from the simulations. The mean value and standard deviation of the dynamic responses were obtained by averaging the mean values and standard deviations of the five one-hour ensembles.

4 Results and Discussion

4.1 Performance of the Improved Controller for the FVAWT

Prior to the comparative study of the FHAWT and FVAWT, a series of steady and turbulent wind conditions were conducted to study the stability and dynamic performances of the improved controller. Figure 5 demonstrates the mean value of the generator power and thrust for the onshore HAWT and VAWT with baseline and improved control strategies in the steady wind condition. Compared with the baseline controller, the improved controller for the VAWT greatly reduces the generator power above the rated wind speed and can maintain an approximately constant mean generator power at 5 MW, which can be regarded as the rated power. Due to the variations of the aerodynamic torque, the generator power could be larger than 5 MW. Furthermore, the improved controller for the VAWT could decrease the aerodynamic thrust acting on the rotor, and help reduce the structural responses such as the tower base fore-aft bending moments. However, the mean thrust of the VAWT is much larger than that of the HAWT above the rated wind speed, implying that the VAWT may have a much larger structural response despite the relatively shorter torque arm.

In addition, the effect of wind turbulence on the wind turbine performance for the onshore and floating VAWT with the improved controller were investigated, as shown in Figure 6. Figure 6 presents the mean values and standard deviations of the generator power, thrust, aerodynamic torque and rotational speed for onshore and floating VAWTs with the improved controller under steady and turbulent wind conditions. The responses are plotted against the mean wind speed.

The steady state generator power and rotational speed of the onshore VAWT above the rated wind speed follow the curve implemented in the controller, but there is a small reduction in the generator power of the spar FVAWT above the rated wind speed under steady wind conditions, which is due to the

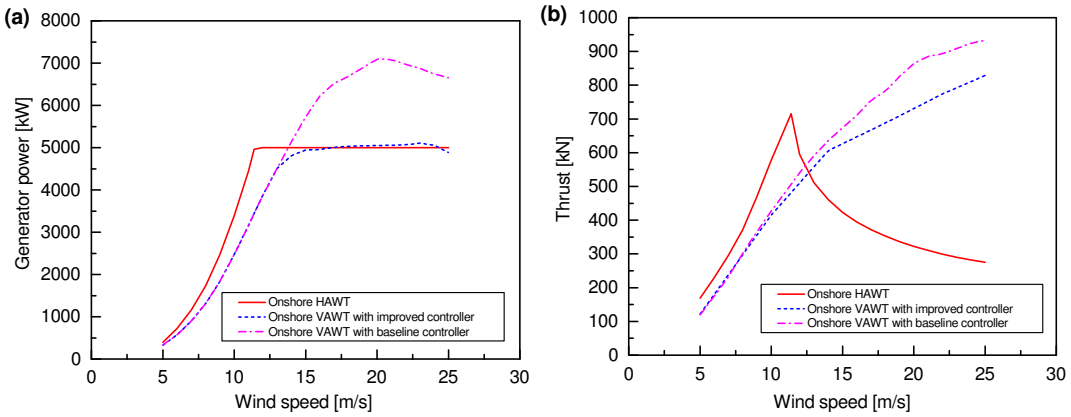

Figure 5: Steady-state mean generator power and thrust of the onshore HAWT and VAWT with different control strategies

tower tilt caused by the platform roll and pitch motions and the reduced standard deviation of rotational speed. Under turbulent wind conditions, the mean values of the rotational speed can follow the pre-calculated curve above the rated wind speed; however, the standard deviations increase significantly in turbulent wind conditions, and are approximately 50% larger than those during steady wind conditions. Consequently, the mean values of the generator power and aerodynamic torque increase slightly under turbulent wind conditions, and their standard deviations significantly increase. Despite these large fluctuations, the mean values of the generator power for the spar FVAWT reach 5 MW under turbulent wind conditions and vary slightly around 5 MW as the mean wind speed increases. Therefore, the improved controller used in this study shows good stability with respect to the mean generator power performance, and can be applied to conduct comparative studies on the dynamic responses of the FHAWT and FVAWT in turbulent wind and wave conditions.

4.2 Performance in Turbulent Wind and Wave Conditions

4.2.1 Wind Turbine Performance

Figure 7 shows the mean values and standard deviations of generator power, aerodynamic thrust and torque, and rotational speed for the FHAWT and FVAWT. The rated wind speed for the FHAWT and FVAWT are 11.4 m/s and 14 m/s, respectively. Above the rated wind speed, the mean generator powers of the FHAWT and FVAWT are very close to the rated power of 5 MW, which makes the comparison between the FHAWT and FVAWT more reasonable. For wind speeds below 14 m/s, the mean generator power of the FHAWT is always much greater than that of the FVAWT due to the higher power coefficient. Because the long-term wind speeds commonly follow the Weibull distribution with the majority below 14 m/s (Johannessen et al., 2002), the FHAWT can harvest more wind energy than the FVAWT during the same period; However, a yaw control device is also required for the FHAWT as the winds are generally not unidirectional, while VAWT is independent of wind direction.

Different control strategies were applied to the FHAWT and FVAWT, respectively. For the FHAWT,

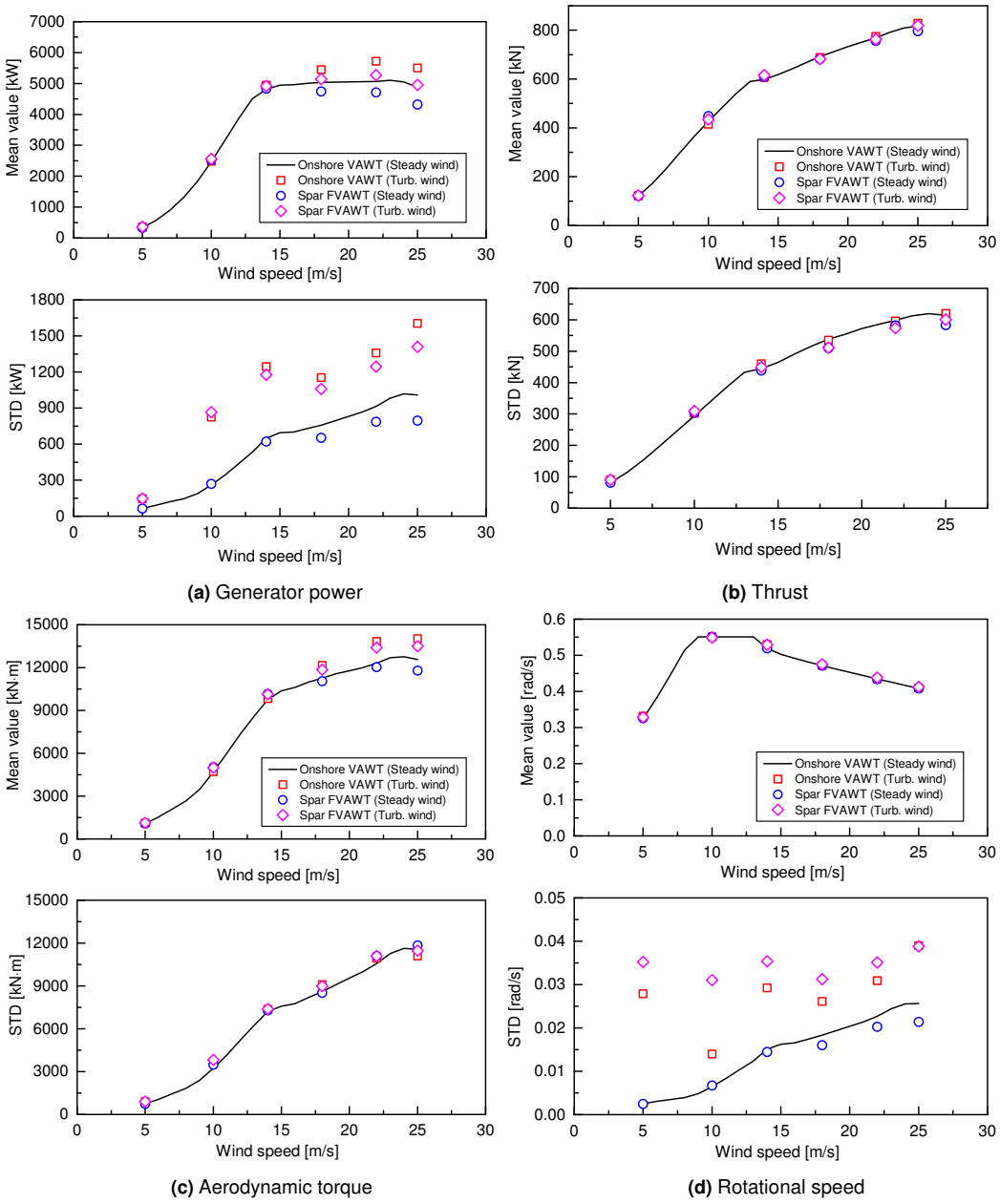

Figure 6: Mean values and standard deviations of the generator power, thrust, aerodynamic torque and rotational speed for landbased VAWT and spar-type FVAWT with the improved control strategy for steady and turbulent wind conditions.

the generator-torque controller and the blade-pitch controller with constant torque were employed below and above the rated wind speed of 11.4 m/s, respectively, which caused the maximum thrust to occur at the rated wind speed and a constant torque above the rated wind speed, as shown in Figure 7 (b) and (c). Regarding the FVAWT, only the generator-torque controller was used as described above and both the mean aerodynamic thrust and torque increased as the wind speed increased.

Figure 7 (d) presents the mean value and standard deviation of the rotor rotational speeds of the FHAWT and FVAWT. The mean rotational speed for the FVAWT above the rated wind speed follows a predetermined curve to achieve an approximately constant generator power, as illustrated in Figure 7 (a). It is very interesting to observe that the FHAWT has not only a much larger standard deviation of the rotational speed, but also a much smaller standard deviation of the generator power. This is due to more stable aerodynamic loads acting on the rotor (standard deviations are given in Figure 7 (b) and (c)). The characteristics of the aerodynamic loads acting on the rotor of the spar-type FHAWT and FVAWT have also been studied in Cheng et al. (2015a) and Wang et al. (2014b). Because the azimuthal angle of the shaft varies periodically in the FVAWT at the rotational speed, the angle of attack encountered by each blade changes correspondingly, leading to the periodic fluctuations in the aerodynamic load on each blade. The rotational frequency corresponding to the rotational speed can be denoted as the 1P frequency. Thus, the resulting aerodynamic loads for the considered 2-bladed FVAWT are considered to vary with the 2P frequency. Moreover, the thrust and aerodynamic torque range from approximate zero to double the mean value.

4.2.2 Platform Motions

Due to the difference in the aerodynamic load acting on the rotor and the dynamic characteristics of the two concepts, the FVAWT and FHAWT have different platform motions. Figure 8 shows the mean value and standard deviation of the surge, roll, pitch and yaw motions of the FVAWT and FHAWT. The trends in the mean values of the surge, heave and pitch are very similar to those of the mean thrust acting on the rotors of the FHAWT and FVAWT. This is because that the mean values of the platform motions are mainly related to wind thrust force. As the center of gravity of the spar buoy is more than 70 m below MSL and the fairleads are located well below the line of action of the aerodynamic forces, the pitch motion contributes a lot to the surge motion, resulting in much larger surge motions for the FHAWT and FVAWT. The mean values of the sway, roll and yaw motions of the FHAWT are very small, because the aerodynamic lateral force and yaw moment are small due to symmetry. However, the FVAWT has much larger mean values in sway, roll and yaw motions, especially at high wind speed. The sway and roll motions are caused by the aerodynamic lateral force that acts on the rotor, and the much larger yaw motion results from the aerodynamic torque acting on the rotor of the FVAWT, which leads to the considerable yaw moment on the spar hull.

Despite the significant fluctuations of the aerodynamic loads acting on the FVAWT, the standard deviation of the platform motions for the FVAWT are the same order of magnitude as those of the FHAWT. Although the standard deviation of thrust for the FHAWT is much smaller than that of the FVAWT, the standard deviations of surge and pitch motions for the FHAWT are larger than those of the FVAWT below the rated wind speed of 11.4 m/s, due to the larger surge and pitch responses that results from the low-frequency turbulent wind, the difference-frequency wave force and the first order wave force, as shown in Figure 9 for LC3.3. The FHAWT has a larger wave-induced pitch resonant

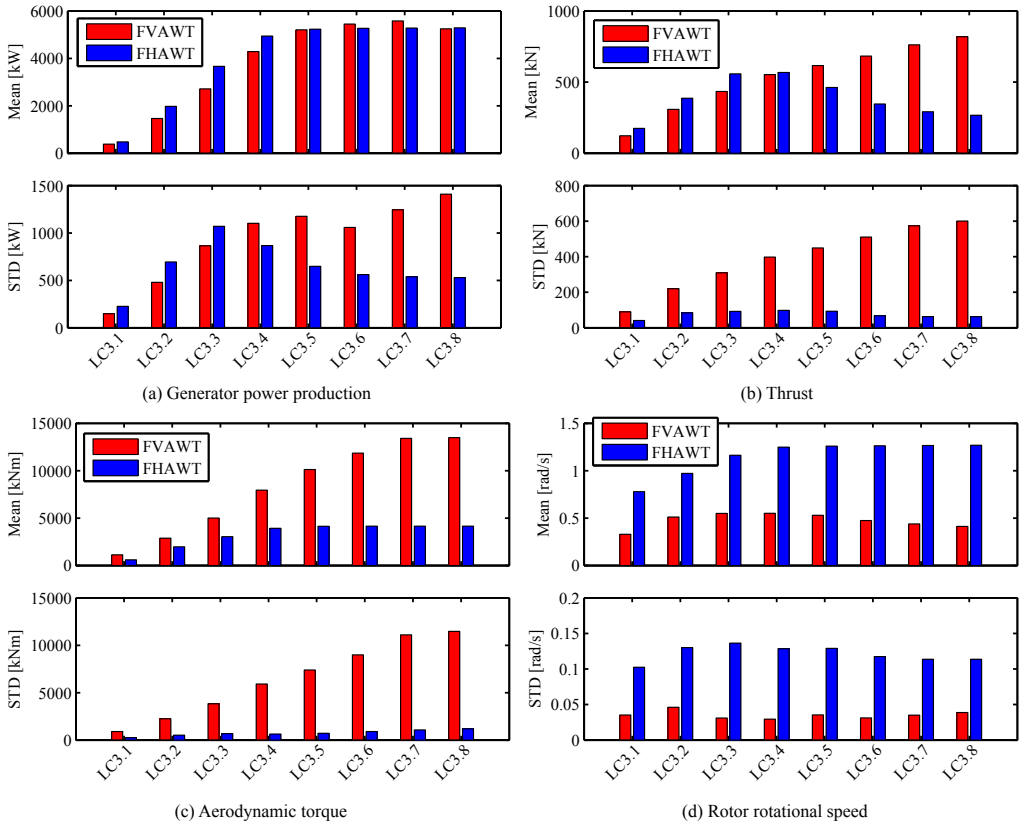

Figure 7: Mean values and standard deviations of (a) generator power, (b) thrust, (c) aerodynamic torque and (d) rotational speed for the FHAWT and FVAWT under turbulent wind conditions.

response and wave frequency response than the FVAWT. Moreover, the response corresponding to the 2P frequency of the surge and pitch motions can be clearly observed for the FVAWT, but their contributions to the standard deviation are very small. However, above the rated wind speed, the surge and pitch responses due to the low-frequency turbulent wind become increasing dominating for the FVAWT, as shown in Figure 10. Consequently, the standard deviations of the surge and pitch motions of the FVAWT are much larger than those of the FHAWT. In addition, the yaw response of the FHAWT is mainly induced by the low-frequency turbulent wind, while that of the FVAWT is primarily excited by the low-frequency turbulent wind and the 2P aerodynamic torque.

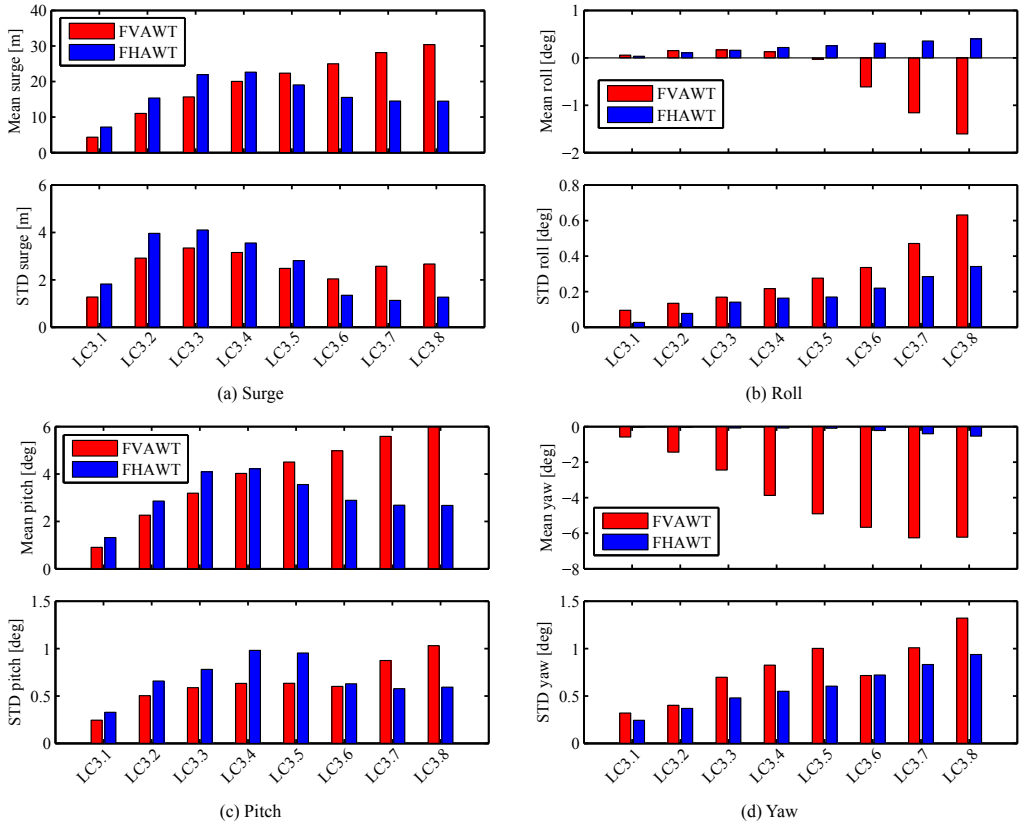

Figure 8: Mean values and standard deviations of the platform (a) surge, (b) roll, (c) pitch, (d) yaw motions for the FHAWT and FVAWT under turbulent wind conditions.

4.2.3 Tower Base Bending Moments

It was assumed that the tower bottom considered for the FVAWT was located below the bearings of the generator shaft. The detailed structural design of the connection is not considered here. For the FHAWT and the FVAWT, the tower base bending moments are both driven by the aerodynamic loads acting on

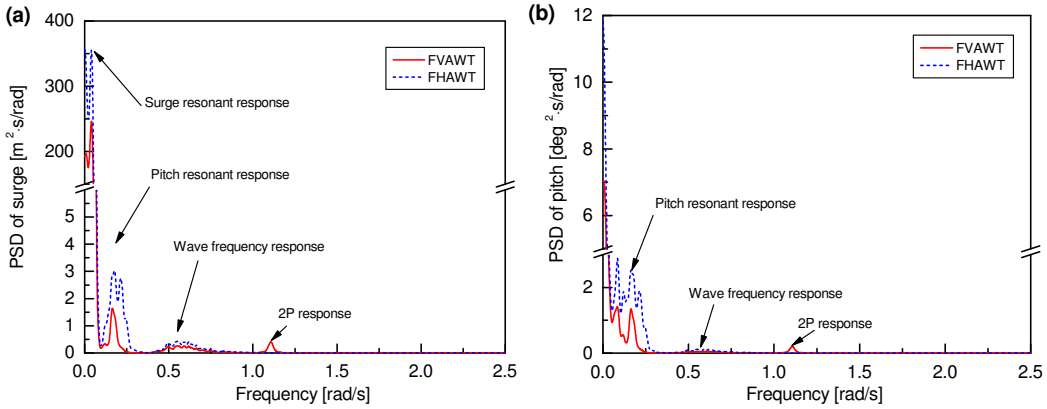

Figure 9: Power spectra of the platform (a) surge and (b) pitch motions for the FHAWT and FVAWT in LC3.3 with U_w=10 m/s.

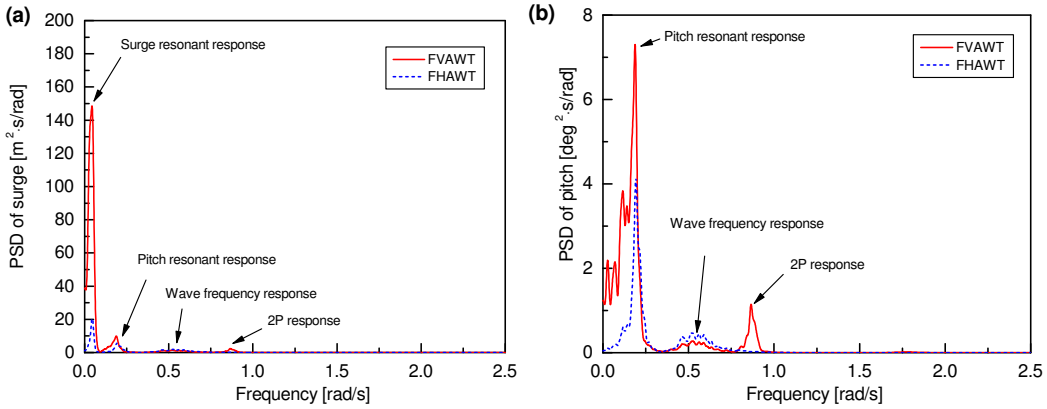

Figure 10: Power spectra of the platform (a) surge and (b) pitch motions for the FHAWT and FVAWT in LC3.7 with U_w=22 m/s.

the rotor and by the weight of the rotor, which can result in a large bending moment due to platform pitch or tower bending. Here both the tower base fore-aft bending moment and the side-to-side bending moment were studied.

Figure 11 shows the power spectra of the tower base fore-aft and side-to-side bending moment for the FHAWT and FVAWT in LC3.5. Obviously the response corresponding to the 2P frequency is considerably dominating in the tower base fore-aft and side-to-side bending moments for the FVAWT. As illustrated above, the aerodynamic loads acting on the FVAWT vary significantly and periodically with the azimuthal angle of the rotor, which can result in considerable variations in the tower base bending moment. Moreover, the tower base fore-aft bending moment for the FVAWT also includes prominent low-frequency turbulent wind induced response and wave frequency response. With respect to the FHAWT, the tower base fore-aft bending moment consists of significant low-frequency turbulent wind induced response, pitch resonant response and wave frequency response. The pitch resonant response mainly results from the relatively large platform pitch motion. In addition, the tower base of the FHAWT is mainly affected by the fore-aft bending moment, while the side-to-side bending moment can be neglected.

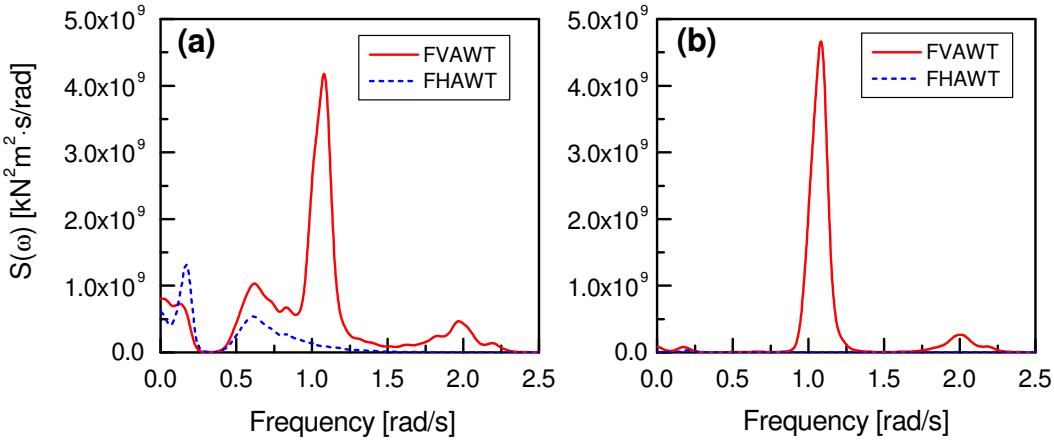

Figure 11: Power spectra of the tower base (a) fore-aft bending moment and (b) side-to-side bending moment for the FHAWT and FVAWT in LC3.5

Both the extreme structural response and fatigue damage, which are related to the maximum value and standard deviation of the structural responses, respectively, are of concern for floating wind turbines. Figure 12 compares the mean values, standard deviations and maximum values of the tower base fore-aft and side-to-side bending moments for the FHAWT and FVAWT under different loads. The mean values, standard deviations and maximum values of the tower base bending moments for the FVAWT, except for the mean values below the rated wind speed, are much larger than those of the FHAWT. Thus the tower base of the FVAWT will suffer relatively larger fatigue damage than that of the FHAWT, as shown by the 1 Hz DEFLs in Figure 13. The DEFL of the fore-aft bending moment for the FVAWT above the rated wind speed is approximately twice that of the FHAWT. Moreover, the DEFL of the side-to-side bending moment for the FVAWT is more than six times greater than that of the FHAWT.

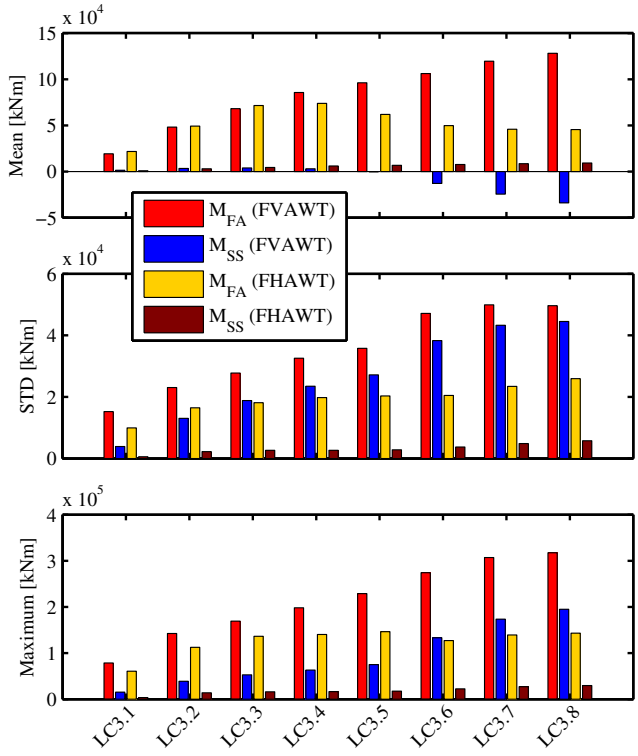

Figure 12: Mean values, standard deviation and maximum value of the tower base fore-aft bending moment (M_{FA}) and side-to-side bending moment (M_{SS}) for the FHAWT and FVAWT

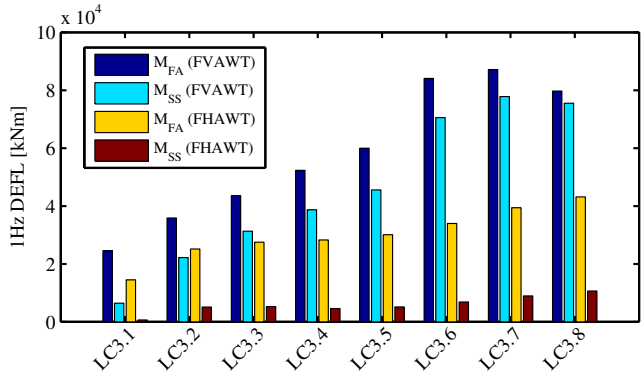

Figure 13: 1 Hz damage equivalent fatigue loads (DEFLs) of the tower base fore-aft bending moment (M_{FA}) and side-to-side bending moment (M_{SS}) for the FHAWT and FVAWT

4.2.4 Mooring Line Tensions

In this study, identical catenary chain mooring systems with delta lines and clump weights were applied to the FHAWT and FVAWT. Each mooring line is composed of two upper delta lines, a upper line, a clump mass and a lower line, as shown in Figure 1. The lower line tension and delta line tension at the three anchor points and the three fairlead points are studied here. Only the normal operational conditions are considered in the present study. Extreme conditions and fault conditions will be studied in the future.

The lower line tensions are compared for the FHAWT and FVAWT in Figure 14, including the mean value, standard deviation and maximum value. The mean value of the lower line tensions is primarily wind-induced. Because wind moves in the positive x direction, the tensions in the lower lines 2 and 3 are much larger than that in lower line 1. Moreover, due to the larger mean thrust below the rated wind speed, the tensions in lower lines 2 and 3 for the FHAWT are slightly larger than those for the FVAWT. Similarly, above the rated wind speed the lower line tensions in mooring lines 2 and 3 of the FVAWT are larger than those of the FHAWT as a result of the much larger mean thrust, as shown in Figure 7(b). However, the discrepancy in the lower line tensions between the FHAWT and the FVAWT is very small compared to the mean value.

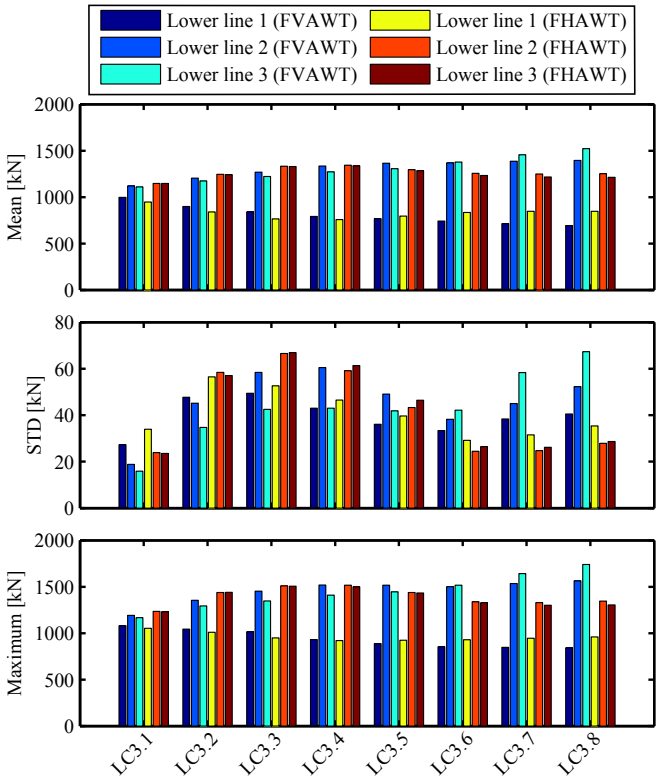

Figure 14: Mean values, standard deviation and maximum values of the tension in the lower lines for the FHAWT and FVAWT

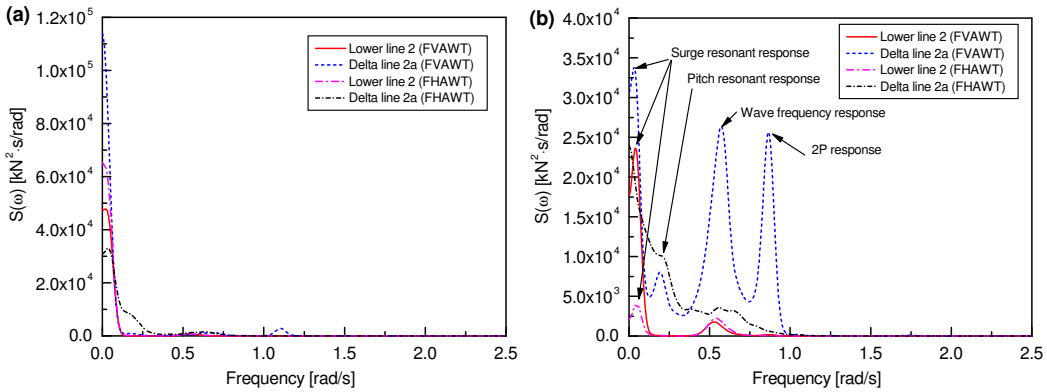

Figure 15: Power spectra of the tension in lower line 2 and delta line 2a for the FHAWT and FVAWT in (a) LC3.3 with $U_w = 10\ m/s$ and (b) LC3.7 with $U_w = 22\ m/s$.

The tensions in the delta lines for the FHAWT and FVAWT are also of concern, especially for the FVAWT at high wind speeds as shown in Figure 16. Due to the large yaw motion experienced by the FVAWT above the rated wind speed, the mean values of tension among the six delta lines vary significantly. In LCs 3.7 and 3.8, the mean tension in delta line 3a reaches approximately 1588 kN, which is very similar to the largest mean tension in the lower line 3.

Figure 15 shows the power spectra of the tension in lower line 2 and delta line 2a for the FHAWT and the FVAWT at LC3.3 and LC3.7, respectively. The low-frequency turbulent wind induced response of mooring line tension is always very dominating for the FHAWT and FVAWT. In LCs with higher significant wave height, the wave frequency responses in the delta line tensions and in the lower line tensions have become more obvious for both the FHAWT and FVAWT. Significant pitch resonant responses are also excited in the delta lines for the FHAWT and FVAWT.

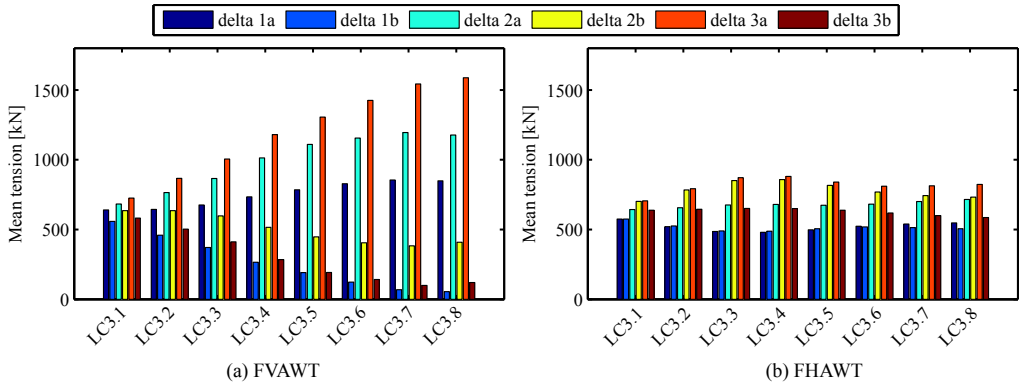

Figure 16: Mean values of the tension in the delta lines for the FHAWT and FVAWT

In addition, the 2P response is observed in the delta lines for the FVAWT and increases significantly

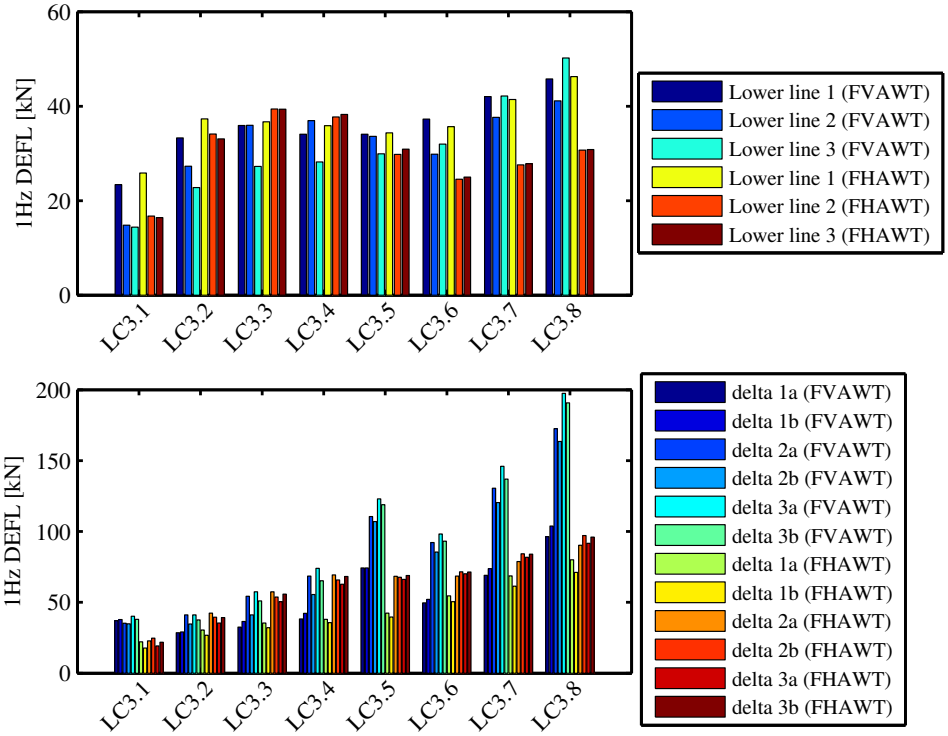

Figure 17: 1 Hz damage equivalent fatigue loads (DEFLs) of the tension in the lower lines and delta lines for the FHAWT and FVAWT

as the wind speed increases. However, despite the prominent 2P response in the delta line tensions, the corresponding 2P response in the lower line tensions is negligible, because the catenary mooring lines can absorb the 2P excitations and alleviate or even dampen out the 2P response in the lower line tensions.

Fatigue damages of the lower lines and delta lines are also studied using the MLife code, as the 1 Hz tension DEFLs show in Figure 17. The DEFLs of the tension in the lower lines are obviously close to each other for the FVAWT and FHAWT. However, in the delta lines, the DEFLs of the tension for the FVAWT are much larger than the FHAWT in delta lines 2a, 2b, 3a and 3b above the rated wind speed.

5 Conclusions

This paper deals with a comparative study on the dynamic responses of a FHAWT and FVAWT, with identical spar buoys and catenary mooring systems. The FHAWT uses the NREL 5 MW reference wind turbine, while the FVAWT employs a 5 MW Darrieus rotor. It should be noted that it is a preliminary comparison, since the DeepWind rotor used in this work is not as optimized as the HAWT and the FVAWT can be further improved. Due to the difference in rotor mass, the ballast of the spar for the FVAWT was adjusted to maintain the same draft and displacement as that of the FHAWT. Fully coupled time domain simulations were carried out to study the dynamic responses using the state-of-the-art codes Simo-Riflex-AeroDyn and Simo-Riflex-DMS for the FHAWT and FVAWT, respectively. The same environmental conditions with directionally aligned and correlated wind and wave were applied for the FHAWT and FVAWT.

An improved control strategy for the FVAWT is introduced first to maintain an approximately constant generator power above the rated wind speed. This control was achieved by determining the reference rotational speed as a function of the measured hub height wind speed based on a pre-calculated curve of the rotational speed versus the wind speed. The improved controller can help hold the mean generator power approximately constant for onshore and floating VAWTs above the rated wind speed, regardless of the presence of steady or turbulent wind conditions. However, during turbulent wind conditions, the standard deviations of the generator power and rotational speed are much larger. Due to the improved controller, the rated power for the FHAWT and FVAWT are very close to each other, which makes the comparative study more reasonable. Using the improved controller for the FVAWT, a series of simulations were conducted to investigate the response characteristics for the FHAWT and FVAWT, including the wind turbine performance, platform motions, tower base bending moments and mooring line tensions.

Due to the higher power coefficient, the FHAWT can harvest more wind energy below the rated wind speed than the FVAWT. However, the aerodynamic loads acting on the 2-bladed FVAWT show significant periodic variations compared with those of the FHAWT. Consequently, the variations of the generator power for the FVAWT are much larger. The variations of the aerodynamic loads are expected to be mitigated by increasing the blade number or introducing helical blades at the cost of higher manufacturing costs. More advanced control strategies, such as model predictive control, are also possible for the FVAWT. All of these strategies can help alleviate the variations in generator power for the FVAWT.

For the above rated wind speed, the increasing aerodynamic loads for the FVAWT result in much larger platform motions, especially in surge, pitch and yaw. However, despite the considerable fluctuations of the aerodynamic loads, the standard deviations of the platform motions for the FVAWT are only

slightly larger than those of the FHAWT. The motion responses are dominated by the low-frequency wind induced response, motion resonant response and wave frequency response.

Regarding the structural response, such as the tower base bending moment, the 2P responses of the fore-aft and side-to-side bending moments of the FVAWT are dominant. However, for the FHAWT the pitch resonant response of the fore-aft bending moment is dominant. All of the mean values, standard deviations and maximum values of the tower base bending moments for the FVAWT, except the mean values below the rated wind speed, are much larger than those for the FHAWT. Moreover, the FVAWT can suffer larger fatigue damage than the FHAWT.

The mean values of the mooring line tensions are mainly wind-induced. In the lower line, the mean value, standard deviation and maximum value of the tension of the FVAWT are close to those of the FHAWT at low and mediate wind speeds. However, at very high wind speeds the tensions in mooring line 2 and 3 for the FVAWT are larger than those for the FHAWT. In the delta line, the tensions for the FVAWT vary significantly among delta lines due to the large yaw motion experienced. Moreover, prominent 2P response and wave frequency response are observed in the delta line tension in the LCs with higher significant wave height and higher wind speed. The corresponding 2P and wave frequency responses in the lower line tension are very small due to the mitigation of the catenary mooring lines and clump weights.

Although the spar buoy and the mooring system are originally designed to support the NREL 5 MW wind turbine, it is still reasonable to use them to support the Darrieus rotor because the hydrostatic performance does not change very much with small differences in the rotor mass when compared with the displacement. By minimizing the differences between the FHAWT and FVAWT, this comparative study illustrates the dynamic response characteristics of each concept and can serve as a basis for their further development.

Acknowledgments

The authors would like to acknowledge the financial support from the EU FP7 project MARE WINT (project NO. 309395) through the Centre for Ships and Ocean Structures (CeSOS) and Centre for Autonomous Marine Operations and Systems (AMOS) at the Department of Marine Technology, Norwegian University of Science and Technology (NTNU), Trondheim, Norway. The first author would also like to thank Dr. Erin Bachynski from MARINTEK for kindly helping with using the simulation codes.

References

Akimoto, H., Tanaka, K., Uzawa, K., 2011. Floating axis wind turbines for offshore power generationâĂŤa conceptual study. Environmental Research Letters 6 (4), 044017.

Bachynski, E., Moan, T., 2012. Design considerations for tension leg platform wind turbines. Marine Structures 29 (1), 89–114.

Borg, M., Collu, M., 2015. A comparison between the dynamics of horizontal and vertical axis offshore

floating wind turbines. Philosophical Transactions of the Royal Society of London A: Mathematical, Physical and Engineering Sciences 373 (2035), 20140076.

Borg, M., Shires, A., Collu, M., 2014. Offshore floating vertical axis wind turbines, dynamics modelling state of the art. part i: Aerodynamics. Renewable and Sustainable Energy Reviews.

Cahay, M., Luquiau, E., Smadja, C., Silvert, F., 2011. Use of a vertical wind turbine in an offshore floating wind farm. In: Offshore Technology Conference. Houston, Texas, USA.

Cheng, Z., Madsen, H. A., Gao, Z., Moan, T., 2016a. Aerodynamic modeling of floating vertical axis wind turbines using the actuator cylinder method. Submitted to Energy Procedia.

Cheng, Z., Madsen, H. A., Gao, Z., Moan, T., 2016b. A fully coupled method for numerical modeling and dynamic analysis of floating vertical axis wind turbines. Submitted to Renewable Energy.

Cheng, Z., Wang, K., Gao, Z., Moan, T., 2015a. Comparative study of spar type floating horizontal and vertical axis wind turbines subjected to constant winds. In: Proceedings of EWEA Offshore 2015. Copenhagen, Denmark.

Cheng, Z., Wang, K., Gao, Z., Moan, T., 2015b. Dynamic response analysis of three floating wind turbine concepts with a two-bladed darrieus rotor. Journal of Ocean and Wind Energy 2, 213–222.

Collu, M., Brennan, F. P., Patel, M. H., 2014. Conceptual design of a floating support structure for an offshore vertical axis wind turbine: the lessons learnt. Ships and Offshore Structures 9 (1), 3–21.

Dabiri, J. O., 2011. Potential order-of-magnitude enhancement of wind farm power density via counter-rotating vertical-axis wind turbine arrays. Journal of Renewable and Sustainable Energy 3 (4), 043104.

Eriksson, S., Bernhoff, H., Leijon, M., 2008. Evaluation of different turbine concepts for wind power. Renewable and Sustainable Energy Reviews 12 (5), 1419–1434.

Hayman, G., 2012. Mlife theory manual for version 1.00.

IEC, 2005. International standard 61400-1, wind turbines, part 1: Design requirements.

Islam, M., S.Mekhilef, R.Saidur, 2013. Progress and recent trends of wind energy technology. Renewable and Sustainable Energy Reviews 21, 456–468.

Johannessen, K., Meling, T. S., Haver, S., 2002. Joint distribution for wind and waves in the northern north sea. International Journal of Offshore and Polar Engineering 12 (1).

Jonkman, B. J., 2009. Turbsim user's guide: Version 1.50.

Jonkman, J., 2010. Definition of the floating system for phase IV of OC3. Tech. Rep. NREL/TP-500-47535, NREL, Golden, CO, USA.

Jonkman, J. M., Butterfield, S., Musial, W., Scott, G., 2009. Definition of a 5-mw reference wind turbine for offshore system development. Tech. Rep. NREL/TP-500-38060, NREL, Golden, CO, USA.

Karimirad, M., Moan, T., 2011. Extreme dynamic structural response analysis of catenary moored spar wind turbine in harsh environmental conditions. Journal of Offshore Mechanics and Arctic Engineering 133 (4), 041103.

Karimirad, M., Moan, T., 2012. Wave and wind induced dynamic response of a spar-type offshore wind turbine. Journal of Waterway, Port, Coastal, and Ocean Engineering 138 (1), 9âĂŞ20.

Kinzel, M., Mulligan, Q., Dabiri, J. O., 2012. Energy exchange in an array of vertical-axis wind turbines. Journal of Turbulence 13 (38), 1–13.

Kvittem, M. I., Bachynski, E. E., Moan, T., 2012. Effects of hydrodynamic modelling in fully coupled simulations of a semi-submersible wind turbine. Energy Procedia 24, 351–362.

Merz, K. O., Svendsen, H. G., 2013. A control algorithm for the deepwind floating vertical-axis wind turbine. Journal of Renewable and Sustainable Energy 5 (6), 063136.

Ormberg, H., Bachynski, E. E., 2012. Global analysis of floating wind turbines: Code development, model sensitivity and benchmark study. In: Proceedings of the 22th International Offshore and Polar Engineering Conference. Rhodes, Greece.

Ormberg, H., Passano, E., Luxcey., N., 2011. Global analysis of a floating wind turbine using an aero-hydro-elastic model: Part 1 code development and case study. In: Proceedings of the 30th International Conference on Ocean, Offshore and Arctic Engineering. Rotterdam, The Netherlands.

Paquette, J., Barone, M., 2012. Innovative offshore vertical-axis wind turbine rotor project. In: EWEA 2012 Annual Event. Copenhagen, Denmark.

Paraschivoiu, I., 2002. Wind turbine design: with emphasis on Darrieus concept. Polytechnic International Press., Montreal, Canada.

Paulsen, U. S., Borg, M., Madsen, H. A., Pedersen, T. F., Hattel, J., Ritchie, E., Ferreira, C. S., Svendsen, H., Berthelsen, P. A., Smadja, C., 2015. Outcomes of the deepwind conceptual design. Energy Procedia 80, 329–341.

Robertson, A., Jonkman, J., Masciola, M., Song, H., Goupee, A., Coulling, A., Luan, C., 2012. Definition of the semisubmersible floating system for phase II of OC4.

Roddier, D., Cermelli, C., Aubault, A., Weinstein, A., 2010. Windfloat: A floating foundation for offshore wind turbines. Journal of Renewable and Sustainable Energy 2 (3), 033104.

Shires, A., 2013. Design optimisation of an offshore vertical axis wind turbine. Proceedings of the ICE-Energy 166 (EN1), 7–18.

Svendsen, H. G., Merz, K. O., Endegnanew, A. G., 2012. Control of floating vertical axis wind turbine. In: European Wind Energy Conference and Exhibition. Copenhagen, Denmark.

Global Wind Energy Council, 2015. Global wind statistics 2014.

Vita, L., 2011. Offshore floating vertical axis wind turbines with rotating platform. Phd thesis, Technical University of Denmark.

Wadam, 2010. Wave analysis by diffraction and morison theory. SESAM user manual. Det Norske Veritas, Høvik.

Wang, K., Cheng, Z., Moan, T., Hansen, M. O. L., 2015a. Effect of difference-frequency forces on the dynamics of a semi-submersible type FVAWT in misaligned wave-wind condition. In: Proceedings of the 25th International Ocean and Polar Engineering Conference. Kona, Big Island, Hawaii, USA.

Wang, K., Hansen, M., Moan, T., 2015b. Model improvements for evaluating the effect of tower tilting on the aerodynamics of a vertical axis wind turbine. Wind Energy 18, 91–110.

Wang, K., Hansen, M. O. L., Moan, T., 2014a. Dynamic analysis of a floating vertical axis wind turbine under emergency shutdown using hydrodynamic brake. Energy Procedia 53, 56–69.

Wang, K., Luan, C., Moan, T., Hansen, M. O. L., 2014b. Comparative study of a FVAWT and a FHAWT with a semi-submersible floater. In: Proceedings of the 24th International Ocean and Polar Engineering Conference. Busan, South Korea.

Wang, K., Moan, T., Hansen, M. O. L., 2013. A method for modeling of floating vertical axis wind turbine. In: Proceedings of the 32th International Conference on Ocean, Offshore and Arctic Engineering. Nantes, France.

Wang, K., Moan, T., Hansen, M. O. L., 2016. Stochastic dynamic response analysis of a floating vertical-axis wind turbine with a semi-submersible floater. Wind Energy.

Appendix B

List of previous PhD theses at Dept. of Marine Tech.

Previous PhD theses published at the Department of Marine Technology
(earlier: Faculty of Marine Technology)
NORWEGIAN UNIVERSITY OF SCIENCE AND TECHNOLOGY

Report No.	Author	Title
	Kavlie, Dag	Optimization of Plane Elastic Grillages, 1967
	Hansen, Hans R.	Man-Machine Communication and Data-Storage Methods in Ship Structural Design, 1971
	Gisvold, Kaare M.	A Method for non-linear mixed-integer programming and its Application to Design Problems, 1971
	Lund, Sverre	Tanker Frame Optimalization by means of SUMT-Transformation and Behaviour Models, 1971
	Vinje, Tor	On Vibration of Spherical Shells Interacting with Fluid, 1972
	Lorentz, Jan D.	Tank Arrangement for Crude Oil Carriers in Accordance with the new Anti-Pollution Regulations, 1975
	Carlsen, Carl A.	Computer-Aided Design of Tanker Structures, 1975
	Larsen, Carl M.	Static and Dynamic Analysis of Offshore Pipelines during Installation, 1976
UR-79-01	Brigt Hatlestad, MK	The finite element method used in a fatigue evaluation of fixed offshore platforms. (Dr.Ing. Thesis)
UR-79-02	Erik Pettersen, MK	Analysis and design of cellular structures. (Dr.Ing. Thesis)
UR-79-03	Sverre Valsgård, MK	Finite difference and finite element methods applied to nonlinear analysis of plated structures. (Dr.Ing. Thesis)
UR-79-04	Nils T. Nordsve, MK	Finite element collapse analysis of structural members considering imperfections and stresses due to fabrication. (Dr.Ing. Thesis)
UR-79-05	Ivar J. Fylling, MK	Analysis of towline forces in ocean towing systems. (Dr.Ing. Thesis)
UR-80-06	Nils Sandsmark, MM	Analysis of Stationary and Transient Heat Conduction by the Use of the Finite Element Method. (Dr.Ing. Thesis)
UR-80-09	Sverre Haver, MK	Analysis of uncertainties related to the stochastic modeling of ocean waves. (Dr.Ing. Thesis)

Report No.	Author	Title
UR-81-15	Odland, Jonas	On the Strength of welded Ring stiffened cylindrical Shells primarily subjected to axial Compression
UR-82-17	Engesvik, Knut	Analysis of Uncertainties in the fatigue Capacity of Welded Joints
UR-82-18	Rye, Henrik	Ocean wave groups
UR-83-30	Eide, Oddvar Inge	On Cumulative Fatigue Damage in Steel Welded Joints
UR-83-33	Mo, Olav	Stochastic Time Domain Analysis of Slender Offshore Structures
UR-83-34	Amdahl, Jørgen	Energy absorption in Ship-platform impacts
UR-84-37	Mørch, Morten	Motions and mooring forces of semi submersibles as determined by full-scale measurements and theoretical analysis
UR-84-38	Soares, C. Guedes	Probabilistic models for load effects in ship structures
UR-84-39	Aarsnes, Jan V.	Current forces on ships
UR-84-40	Czujko, Jerzy	Collapse Analysis of Plates subjected to Biaxial Compression and Lateral Load
UR-85-46	Alf G. Engseth, MK	Finite element collapse analysis of tubular steel offshore structures. (Dr.Ing. Thesis)
UR-86-47	Dengody Sheshappa, MP	A Computer Design Model for Optimizing Fishing Vessel Designs Based on Techno-Economic Analysis. (Dr.Ing. Thesis)
UR-86-48	Vidar Aanesland, MH	A Theoretical and Numerical Study of Ship Wave Resistance. (Dr.Ing. Thesis)
UR-86-49	Heinz-Joachim Wessel, MK	Fracture Mechanics Analysis of Crack Growth in Plate Girders. (Dr.Ing. Thesis)
UR-86-50	Jon Taby, MK	Ultimate and Post-ultimate Strength of Dented Tubular Members. (Dr.Ing. Thesis)
UR-86-51	Walter Lian, MH	A Numerical Study of Two-Dimensional Separated Flow Past Bluff Bodies at Moderate KC-Numbers. (Dr.Ing. Thesis)
UR-86-52	Bjørn Sortland, MH	Force Measurements in Oscillating Flow on Ship Sections and Circular Cylinders in a U-Tube Water Tank. (Dr.Ing. Thesis)
UR-86-53	Kurt Strand, MM	A System Dynamic Approach to One-dimensional Fluid Flow. (Dr.Ing. Thesis)
UR-86-54	Arne Edvin Løken, MH	Three Dimensional Second Order Hydrodynamic Effects on Ocean Structures in Waves. (Dr.Ing. Thesis)

Report No.	Author	Title
UR-86-55	Sigurd Falch, MH	A Numerical Study of Slamming of Two-Dimensional Bodies. (Dr.Ing. Thesis)
UR-87-56	Arne Braathen, MH	Application of a Vortex Tracking Method to the Prediction of Roll Damping of a Two-Dimension Floating Body. (Dr.Ing. Thesis)
UR-87-57	Bernt Leira, MK	Gaussian Vector Processes for Reliability Analysis involving Wave-Induced Load Effects. (Dr.Ing. Thesis)
UR-87-58	Magnus Småvik, MM	Thermal Load and Process Characteristics in a Two-Stroke Diesel Engine with Thermal Barriers (in Norwegian). (Dr.Ing. Thesis)
MTA-88-59	Bernt Arild Bremdal, MP	An Investigation of Marine Installation Processes – A Knowledge-Based Planning Approach. (Dr.Ing. Thesis)
MTA-88-60	Xu Jun, MK	Non-linear Dynamic Analysis of Space-framed Offshore Structures. (Dr.Ing. Thesis)
MTA-89-61	Gang Miao, MH	Hydrodynamic Forces and Dynamic Responses of Circular Cylinders in Wave Zones. (Dr.Ing. Thesis)
MTA-89-62	Martin Greenhow, MH	Linear and Non-Linear Studies of Waves and Floating Bodies. Part I and Part II. (Dr.Techn. Thesis)
MTA-89-63	Chang Li, MH	Force Coefficients of Spheres and Cubes in Oscillatory Flow with and without Current. (Dr.Ing. Thesis
MTA-89-64	Hu Ying, MP	A Study of Marketing and Design in Development of Marine Transport Systems. (Dr.Ing. Thesis)
MTA-89-65	Arild Jæger, MH	Seakeeping, Dynamic Stability and Performance of a Wedge Shaped Planing Hull. (Dr.Ing. Thesis)
MTA-89-66	Chan Siu Hung, MM	The dynamic characteristics of tilting-pad bearings
MTA-89-67	Kim Wikstrøm, MP	Analysis av projekteringen for ett offshore projekt. (Licenciat-avhandling)
MTA-89-68	Jiao Guoyang, MK	Reliability Analysis of Crack Growth under Random Loading, considering Model Updating. (Dr.Ing. Thesis)
MTA-89-69	Arnt Olufsen, MK	Uncertainty and Reliability Analysis of Fixed Offshore Structures. (Dr.Ing. Thesis)
MTA-89-70	Wu Yu-Lin, MR	System Reliability Analyses of Offshore Structures using improved Truss and Beam Models. (Dr.Ing. Thesis)

Report No.	Author	Title
MTA-90-71	Jan Roger Hoff, MH	Three-dimensional Green function of a vessel with forward speed in waves. (Dr.Ing. Thesis)
MTA-90-72	Rong Zhao, MH	Slow-Drift Motions of a Moored Two-Dimensional Body in Irregular Waves. (Dr.Ing. Thesis)
MTA-90-73	Atle Minsaas, MP	Economical Risk Analysis. (Dr.Ing. Thesis)
MTA-90-74	Knut-Ariel Farnes, MK	Long-term Statistics of Response in Non-linear Marine Structures. (Dr.Ing. Thesis)
MTA-90-75	Torbjørn Sotberg, MK	Application of Reliability Methods for Safety Assessment of Submarine Pipelines. (Dr.Ing. Thesis)
MTA-90-76	Zeuthen, Steffen, MP	SEAMAID. A computational model of the design process in a constraint-based logic programming environment. An example from the offshore domain. (Dr.Ing. Thesis)
MTA-91-77	Haagensen, Sven, MM	Fuel Dependant Cyclic Variability in a Spark Ignition Engine – An Optical Approach. (Dr.Ing. Thesis)
MTA-91-78	Løland, Geir, MH	Current forces on and flow through fish farms. (Dr.Ing. Thesis)
MTA-91-79	Hoen, Christopher, MK	System Identification of Structures Excited by Stochastic Load Processes. (Dr.Ing. Thesis)
MTA-91-80	Haugen, Stein, MK	Probabilistic Evaluation of Frequency of Collision between Ships and Offshore Platforms. (Dr.Ing. Thesis)
MTA-91-81	Sødahl, Nils, MK	Methods for Design and Analysis of Flexible Risers. (Dr.Ing. Thesis)
MTA-91-82	Ormberg, Harald, MK	Non-linear Response Analysis of Floating Fish Farm Systems. (Dr.Ing. Thesis)
MTA-91-83	Marley, Mark J., MK	Time Variant Reliability under Fatigue Degradation. (Dr.Ing. Thesis)
MTA-91-84	Krokstad, Jørgen R., MH	Second-order Loads in Multidirectional Seas. (Dr.Ing. Thesis)
MTA-91-85	Molteberg, Gunnar A., MM	The Application of System Identification Techniques to Performance Monitoring of Four Stroke Turbocharged Diesel Engines. (Dr.Ing. Thesis)
MTA-92-86	Mørch, Hans Jørgen Bjelke, MH	Aspects of Hydrofoil Design: with Emphasis on Hydrofoil Interaction in Calm Water. (Dr.Ing. Thesis)
MTA-92-87	Chan Siu Hung, MM	Nonlinear Analysis of Rotordynamic Instabilities in Highspeed Turbomachinery. (Dr.Ing. Thesis)

Report No.	Author	Title
MTA-92-88	Bessason, Bjarni, MK	Assessment of Earthquake Loading and Response of Seismically Isolated Bridges. (Dr.Ing. Thesis)
MTA-92-89	Langli, Geir, MP	Improving Operational Safety through exploitation of Design Knowledge – an investigation of offshore platform safety. (Dr.Ing. Thesis)
MTA-92-90	Sævik, Svein, MK	On Stresses and Fatigue in Flexible Pipes. (Dr.Ing. Thesis)
MTA-92-91	Ask, Tor Ø., MM	Ignition and Flame Growth in Lean Gas-Air Mixtures. An Experimental Study with a Schlieren System. (Dr.Ing. Thesis)
MTA-86-92	Hessen, Gunnar, MK	Fracture Mechanics Analysis of Stiffened Tubular Members. (Dr.Ing. Thesis)
MTA-93-93	Steinebach, Christian, MM	Knowledge Based Systems for Diagnosis of Rotating Machinery. (Dr.Ing. Thesis)
MTA-93-94	Dalane, Jan Inge, MK	System Reliability in Design and Maintenance of Fixed Offshore Structures. (Dr.Ing. Thesis)
MTA-93-95	Steen, Sverre, MH	Cobblestone Effect on SES. (Dr.Ing. Thesis)
MTA-93-96	Karunakaran, Daniel, MK	Nonlinear Dynamic Response and Reliability Analysis of Drag-dominated Offshore Platforms. (Dr.Ing. Thesis)
MTA-93-97	Hagen, Arnulf, MP	The Framework of a Design Process Language. (Dr.Ing. Thesis)
MTA-93-98	Nordrik, Rune, MM	Investigation of Spark Ignition and Autoignition in Methane and Air Using Computational Fluid Dynamics and Chemical Reaction Kinetics. A Numerical Study of Ignition Processes in Internal Combustion Engines. (Dr.Ing. Thesis)
MTA-94-99	Passano, Elizabeth, MK	Efficient Analysis of Nonlinear Slender Marine Structures. (Dr.Ing. Thesis)
MTA-94-100	Kvålsvold, Jan, MH	Hydroelastic Modelling of Wetdeck Slamming on Multihull Vessels. (Dr.Ing. Thesis)
MTA-94-102	Bech, Sidsel M., MK	Experimental and Numerical Determination of Stiffness and Strength of GRP/PVC Sandwich Structures. (Dr.Ing. Thesis)
MTA-95-103	Paulsen, Hallvard, MM	A Study of Transient Jet and Spray using a Schlieren Method and Digital Image Processing. (Dr.Ing. Thesis)
MTA-95-104	Hovde, Geir Olav, MK	Fatigue and Overload Reliability of Offshore Structural Systems, Considering the Effect of Inspection and Repair. (Dr.Ing. Thesis)

Report No.	Author	Title
MTA-95-105	Wang, Xiaozhi, MK	Reliability Analysis of Production Ships with Emphasis on Load Combination and Ultimate Strength. (Dr.Ing. Thesis)
MTA-95-106	Ulstein, Tore, MH	Nonlinear Effects of a Flexible Stern Seal Bag on Cobblestone Oscillations of an SES. (Dr.Ing. Thesis)
MTA-95-107	Solaas, Frøydis, MH	Analytical and Numerical Studies of Sloshing in Tanks. (Dr.Ing. Thesis)
MTA-95-108	Hellan, Øyvind, MK	Nonlinear Pushover and Cyclic Analyses in Ultimate Limit State Design and Reassessment of Tubular Steel Offshore Structures. (Dr.Ing. Thesis)
MTA-95-109	Hermundstad, Ole A., MK	Theoretical and Experimental Hydroelastic Analysis of High Speed Vessels. (Dr.Ing. Thesis)
MTA-96-110	Bratland, Anne K., MH	Wave-Current Interaction Effects on Large-Volume Bodies in Water of Finite Depth. (Dr.Ing. Thesis)
MTA-96-111	Herfjord, Kjell, MH	A Study of Two-dimensional Separated Flow by a Combination of the Finite Element Method and Navier-Stokes Equations. (Dr.Ing. Thesis)
MTA-96-112	AEsøy, Vilmar, MM	Hot Surface Assisted Compression Ignition in a Direct Injection Natural Gas Engine. (Dr.Ing. Thesis)
MTA-96-113	Eknes, Monika L., MK	Escalation Scenarios Initiated by Gas Explosions on Offshore Installations. (Dr.Ing. Thesis)
MTA-96-114	Erikstad, Stein O., MP	A Decision Support Model for Preliminary Ship Design. (Dr.Ing. Thesis)
MTA-96-115	Pedersen, Egil, MH	A Nautical Study of Towed Marine Seismic Streamer Cable Configurations. (Dr.Ing. Thesis)
MTA-97-116	Moksnes, Paul O., MM	Modelling Two-Phase Thermo-Fluid Systems Using Bond Graphs. (Dr.Ing. Thesis)
MTA-97-117	Halse, Karl H., MK	On Vortex Shedding and Prediction of Vortex-Induced Vibrations of Circular Cylinders. (Dr.Ing. Thesis)
MTA-97-118	Igland, Ragnar T., MK	Reliability Analysis of Pipelines during Laying, considering Ultimate Strength under Combined Loads. (Dr.Ing. Thesis)
MTA-97-119	Pedersen, Hans-P., MP	Levendefiskteknologi for fiskefartøy. (Dr.Ing. Thesis)

Report No.	Author	Title
MTA-98-120	Vikestad, Kyrre, MK	Multi-Frequency Response of a Cylinder Subjected to Vortex Shedding and Support Motions. (Dr.Ing. Thesis)
MTA-98-121	Azadi, Mohammad R. E., MK	Analysis of Static and Dynamic Pile-Soil-Jacket Behaviour. (Dr.Ing. Thesis)
MTA-98-122	Ulltang, Terje, MP	A Communication Model for Product Information. (Dr.Ing. Thesis)
MTA-98-123	Torbergsen, Erik, MM	Impeller/Diffuser Interaction Forces in Centrifugal Pumps. (Dr.Ing. Thesis)
MTA-98-124	Hansen, Edmond, MH	A Discrete Element Model to Study Marginal Ice Zone Dynamics and the Behaviour of Vessels Moored in Broken Ice. (Dr.Ing. Thesis)
MTA-98-125	Videiro, Paulo M., MK	Reliability Based Design of Marine Structures. (Dr.Ing. Thesis)
MTA-99-126	Mainçon, Philippe, MK	Fatigue Reliability of Long Welds Application to Titanium Risers. (Dr.Ing. Thesis)
MTA-99-127	Haugen, Elin M., MH	Hydroelastic Analysis of Slamming on Stiffened Plates with Application to Catamaran Wetdecks. (Dr.Ing. Thesis)
MTA-99-128	Langhelle, Nina K., MK	Experimental Validation and Calibration of Nonlinear Finite Element Models for Use in Design of Aluminium Structures Exposed to Fire. (Dr.Ing. Thesis)
MTA-99-129	Berstad, Are J., MK	Calculation of Fatigue Damage in Ship Structures. (Dr.Ing. Thesis)
MTA-99-130	Andersen, Trond M., MM	Short Term Maintenance Planning. (Dr.Ing. Thesis)
MTA-99-131	Tveiten, Bård Wathne, MK	Fatigue Assessment of Welded Aluminium Ship Details. (Dr.Ing. Thesis)
MTA-99-132	Søreide, Fredrik, MP	Applications of underwater technology in deep water archaeology. Principles and practice. (Dr.Ing. Thesis)
MTA-99-133	Tønnessen, Rune, MH	A Finite Element Method Applied to Unsteady Viscous Flow Around 2D Blunt Bodies With Sharp Corners. (Dr.Ing. Thesis)
MTA-99-134	Elvekrok, Dag R., MP	Engineering Integration in Field Development Projects in the Norwegian Oil and Gas Industry. The Supplier Management of Norne. (Dr.Ing. Thesis)
MTA-99-135	Fagerholt, Kjetil, MP	Optimeringsbaserte Metoder for Ruteplanlegging innen skipsfart. (Dr.Ing. Thesis)

Report No.	Author	Title
MTA-99-136	Bysveen, Marie, MM	Visualization in Two Directions on a Dynamic Combustion Rig for Studies of Fuel Quality. (Dr.Ing. Thesis)
MTA-2000-137	Storteig, Eskild, MM	Dynamic characteristics and leakage performance of liquid annular seals in centrifugal pumps. (Dr.Ing. Thesis)
MTA-2000-138	Sagli, Gro, MK	Model uncertainty and simplified estimates of long term extremes of hull girder loads in ships. (Dr.Ing. Thesis)
MTA-2000-139	Tronstad, Harald, MK	Nonlinear analysis and design of cable net structures like fishing gear based on the finite element method. (Dr.Ing. Thesis)
MTA-2000-140	Kroneberg, André, MP	Innovation in shipping by using scenarios. (Dr.Ing. Thesis)
MTA-2000-141	Haslum, Herbjørn Alf, MH	Simplified methods applied to nonlinear motion of spar platforms. (Dr.Ing. Thesis)
MTA-2001-142	Samdal, Ole Johan, MM	Modelling of Degradation Mechanisms and Stressor Interaction on Static Mechanical Equipment Residual Lifetime. (Dr.Ing. Thesis)
MTA-2001-143	Baarholm, Rolf Jarle, MH	Theoretical and experimental studies of wave impact underneath decks of offshore platforms. (Dr.Ing. Thesis)
MTA-2001-144	Wang, Lihua, MK	Probabilistic Analysis of Nonlinear Wave-induced Loads on Ships. (Dr.Ing. Thesis)
MTA-2001-145	Kristensen, Odd H. Holt, MK	Ultimate Capacity of Aluminium Plates under Multiple Loads, Considering HAZ Properties. (Dr.Ing. Thesis)
MTA-2001-146	Greco, Marilena, MH	A Two-Dimensional Study of Green-Water Loading. (Dr.Ing. Thesis)
MTA-2001-147	Heggelund, Svein E., MK	Calculation of Global Design Loads and Load Effects in Large High Speed Catamarans. (Dr.Ing. Thesis)
MTA-2001-148	Babalola, Olusegun T., MK	Fatigue Strength of Titanium Risers – Defect Sensitivity. (Dr.Ing. Thesis)
MTA-2001-149	Mohammed, Abuu K., MK	Nonlinear Shell Finite Elements for Ultimate Strength and Collapse Analysis of Ship Structures. (Dr.Ing. Thesis)
MTA-2002-150	Holmedal, Lars E., MH	Wave-current interactions in the vicinity of the sea bed. (Dr.Ing. Thesis)
MTA-2002-151	Rognebakke, Olav F., MH	Sloshing in rectangular tanks and interaction with ship motions. (Dr.Ing. Thesis)
MTA-2002-152	Lader, Pål Furset, MH	Geometry and Kinematics of Breaking Waves. (Dr.Ing. Thesis)

Report No.	Author	Title
MTA-2002-153	Yang, Qinzheng, MH	Wash and wave resistance of ships in finite water depth. (Dr.Ing. Thesis)
MTA-2002-154	Melhus, Øyvin, MM	Utilization of VOC in Diesel Engines. Ignition and combustion of VOC released by crude oil tankers. (Dr.Ing. Thesis)
MTA-2002-155	Ronæss, Marit, MH	Wave Induced Motions of Two Ships Advancing on Parallel Course. (Dr.Ing. Thesis)
MTA-2002-156	Økland, Ole D., MK	Numerical and experimental investigation of whipping in twin hull vessels exposed to severe wet deck slamming. (Dr.Ing. Thesis)
MTA-2002-157	Ge, Chunhua, MK	Global Hydroelastic Response of Catamarans due to Wet Deck Slamming. (Dr.Ing. Thesis)
MTA-2002-158	Byklum, Eirik, MK	Nonlinear Shell Finite Elements for Ultimate Strength and Collapse Analysis of Ship Structures. (Dr.Ing. Thesis)
IMT-2003-1	Chen, Haibo, MK	Probabilistic Evaluation of FPSO-Tanker Collision in Tandem Offloading Operation. (Dr.Ing. Thesis)
IMT-2003-2	Skaugset, Kjetil Bjørn, MK	On the Suppression of Vortex Induced Vibrations of Circular Cylinders by Radial Water Jets. (Dr.Ing. Thesis)
IMT-2003-3	Chezhian, Muthu	Three-Dimensional Analysis of Slamming. (Dr.Ing. Thesis)
IMT-2003-4	Buhaug, Øyvind	Deposit Formation on Cylinder Liner Surfaces in Medium Speed Engines. (Dr.Ing. Thesis)
IMT-2003-5	Tregde, Vidar	Aspects of Ship Design: Optimization of Aft Hull with Inverse Geometry Design. (Dr.Ing. Thesis)
IMT-2003-6	Wist, Hanne Therese	Statistical Properties of Successive Ocean Wave Parameters. (Dr.Ing. Thesis)
IMT-2004-7	Ransau, Samuel	Numerical Methods for Flows with Evolving Interfaces. (Dr.Ing. Thesis)
IMT-2004-8	Soma, Torkel	Blue-Chip or Sub-Standard. A data interrogation approach of identity safety characteristics of shipping organization. (Dr.Ing. Thesis)
IMT-2004-9	Ersdal, Svein	An experimental study of hydrodynamic forces on cylinders and cables in near axial flow. (Dr.Ing. Thesis)
IMT-2005-10	Brodtkorb, Per Andreas	The Probability of Occurrence of Dangerous Wave Situations at Sea. (Dr.Ing. Thesis)
IMT-2005-11	Yttervik, Rune	Ocean current variability in relation to offshore engineering. (Dr.Ing. Thesis)

Report No.	Author	Title
IMT-2005-12	Fredheim, Arne	Current Forces on Net-Structures. (Dr.Ing. Thesis)
IMT-2005-13	Heggernes, Kjetil	Flow around marine structures. (Dr.Ing. Thesis
IMT-2005-14	Fouques, Sebastien	Lagrangian Modelling of Ocean Surface Waves and Synthetic Aperture Radar Wave Measurements. (Dr.Ing. Thesis)
IMT-2006-15	Holm, Håvard	Numerical calculation of viscous free surface flow around marine structures. (Dr.Ing. Thesis)
IMT-2006-16	Bjørheim, Lars G.	Failure Assessment of Long Through Thickness Fatigue Cracks in Ship Hulls. (Dr.Ing. Thesis)
IMT-2006-17	Hansson, Lisbeth	Safety Management for Prevention of Occupational Accidents. (Dr.Ing. Thesis)
IMT-2006-18	Zhu, Xinying	Application of the CIP Method to Strongly Nonlinear Wave-Body Interaction Problems. (Dr.Ing. Thesis)
IMT-2006-19	Reite, Karl Johan	Modelling and Control of Trawl Systems. (Dr.Ing. Thesis)
IMT-2006-20	Smogeli, Øyvind Notland	Control of Marine Propellers. From Normal to Extreme Conditions. (Dr.Ing. Thesis)
IMT-2007-21	Storhaug, Gaute	Experimental Investigation of Wave Induced Vibrations and Their Effect on the Fatigue Loading of Ships. (Dr.Ing. Thesis)
IMT-2007-22	Sun, Hui	A Boundary Element Method Applied to Strongly Nonlinear Wave-Body Interaction Problems. (PhD Thesis, CeSOS)
IMT-2007-23	Rustad, Anne Marthine	Modelling and Control of Top Tensioned Risers. (PhD Thesis, CeSOS)
IMT-2007-24	Johansen, Vegar	Modelling flexible slender system for real-time simulations and control applications
IMT-2007-25	Wroldsen, Anders Sunde	Modelling and control of tensegrity structures. (PhD Thesis, CeSOS)
IMT-2007-26	Aronsen, Kristoffer Høye	An experimental investigation of in-line and combined inline and cross flow vortex induced vibrations. (Dr. avhandling, IMT)
IMT-2007-27	Gao, Zhen	Stochastic Response Analysis of Mooring Systems with Emphasis on Frequency-domain Analysis of Fatigue due to Wide-band Response Processes (PhD Thesis, CeSOS)
IMT-2007-28	Thorstensen, Tom Anders	Lifetime Profit Modelling of Ageing Systems Utilizing Information about Technical Condition. (Dr.ing. thesis, IMT)

Report No.	Author	Title
IMT-2008-29	Berntsen, Per Ivar B.	Structural Reliability Based Position Mooring. (PhD-Thesis, IMT)
IMT-2008-30	Ye, Naiquan	Fatigue Assessment of Aluminium Welded Box-stiffener Joints in Ships (Dr.ing. thesis, IMT)
IMT-2008-31	Radan, Damir	Integrated Control of Marine Electrical Power Systems. (PhD-Thesis, IMT)
IMT-2008-32	Thomassen, Paul	Methods for Dynamic Response Analysis and Fatigue Life Estimation of Floating Fish Cages. (Dr.ing. thesis, IMT)
IMT-2008-33	Pákozdi, Csaba	A Smoothed Particle Hydrodynamics Study of Two-dimensional Nonlinear Sloshing in Rectangular Tanks. (Dr.ing.thesis, IMT/ CeSOS)
IMT-2008-34	Grytøyr, Guttorm	A Higher-Order Boundary Element Method and Applications to Marine Hydrodynamics. (Dr.ing.thesis, IMT)
IMT-2008-35	Drummen, Ingo	Experimental and Numerical Investigation of Nonlinear Wave-Induced Load Effects in Containerships considering Hydroelasticity. (PhD thesis, CeSOS)
IMT-2008-36	Skejic, Renato	Maneuvering and Seakeeping of a Singel Ship and of Two Ships in Interaction. (PhD-Thesis, CeSOS)
IMT-2008-37	Harlem, Alf	An Age-Based Replacement Model for Repairable Systems with Attention to High-Speed Marine Diesel Engines. (PhD-Thesis, IMT)
IMT-2008-38	Alsos, Hagbart S.	Ship Grounding. Analysis of Ductile Fracture, Bottom Damage and Hull Girder Response. (PhD-thesis, IMT)
IMT-2008-39	Graczyk, Mateusz	Experimental Investigation of Sloshing Loading and Load Effects in Membrane LNG Tanks Subjected to Random Excitation. (PhD-thesis, CeSOS)
IMT-2008-40	Taghipour, Reza	Efficient Prediction of Dynamic Response for Flexible amd Multi-body Marine Structures. (PhD-thesis, CeSOS)
IMT-2008-41	Ruth, Eivind	Propulsion control and thrust allocation on marine vessels. (PhD thesis, CeSOS)
IMT-2008-42	Nystad, Bent Helge	Technical Condition Indexes and Remaining Useful Life of Aggregated Systems. PhD thesis, IMT
IMT-2008-43	Soni, Prashant Kumar	Hydrodynamic Coefficients for Vortex Induced Vibrations of Flexible Beams. PhD thesis, CeSOS

Report No.	Author	Title
IMT-2009-43	Amlashi, Hadi K.K.	Ultimate Strength and Reliability-based Design of Ship Hulls with Emphasis on Combined Global and Local Loads. PhD Thesis, IMT
IMT-2009-44	Pedersen, Tom Arne	Bond Graph Modelling of Marine Power Systems. PhD Thesis, IMT
IMT-2009-45	Kristiansen, Trygve	Two-Dimensional Numerical and Experimental Studies of Piston-Mode Resonance. PhD thesis, CeSOS
IMT-2009-46	Ong, Muk Chen	Applications of a Standard High Reynolds Number Model and a Stochastic Scour Prediction Model for Marine Structures. PhD-thesis, IMT
IMT-2009-47	Hong, Lin	Simplified Analysis and Design of Ships subjected to Collision and Grounding. PhD-thesis, IMT
IMT-2009-48	Koushan, Kamran	Vortex Induced Vibrations of Free Span Pipelines, PhD thesis, IMT
IMT-2009-49	Korsvik, Jarl Eirik	Heuristic Methods for Ship Routing and Scheduling. PhD-thesis, IMT
IMT-2009-50	Lee, Jihoon	Experimental Investigation and Numerical in Analyzing the Ocean Current Displacement of Longlines. Ph.d.-Thesis, IMT.
IMT-2009-51	Vestbøstad, Tone Gran	A Numerical Study of Wave-in-Deck Impact usin a Two-Dimensional Constrained Interpolation Profile Method, Ph.d.thesis, CeSOS.
IMT-2009-52	Bruun, Kristine	Bond Graph Modelling of Fuel Cells for Marine Power Plants. Ph.d.-thesis, IMT
IMT-2009-53	Holstad, Anders	Numerical Investigation of Turbulence in a Sekwed Three-Dimensional Channel Flow, Ph.d.-thesis, IMT.
IMT-2009-54	Ayala-Uraga, Efren	Reliability-Based Assessment of Deteriorating Ship-shaped Offshore Structures, Ph.d.-thesis, IMT
IMT-2009-55	Kong, Xiangjun	A Numerical Study of a Damaged Ship in Beam Sea Waves. Ph.d.-thesis, IMT/CeSOS.
IMT-2010-56	Kristiansen, David	Wave Induced Effects on Floaters of Aquaculture Plants, Ph.d.-thesis, CeSOS.
IMT-2010-57	Ludvigsen, Martin	An ROV-Toolbox for Optical and Acoustic Scientific Seabed Investigation. Ph.d.-thesis IMT.
IMT-2010-58	Hals, Jørgen	Modelling and Phase Control of Wave-Energy Converters. Ph.d.thesis, CeSOS.

Report No.	Author	Title
IMT-2010-59	Shu, Zhi	Uncertainty Assessment of Wave Loads and Ultimate Strength of Tankers and Bulk Carriers in a Reliability Framework. Ph.d. Thesis, IMT/ CeSOS
IMT-2010-60	Shao, Yanlin	Numerical Potential-Flow Studies on Weakly-Nonlinear Wave-Body Interactions with/without Small Forward Speed, Ph.d.thesis, CeSOS.
IMT-2010-61	Califano, Andrea	Dynamic Loads on Marine Propellers due to Intermittent Ventilation. Ph.d.thesis, IMT.
IMT-2010-62	El Khoury, George	Numerical Simulations of Massively Separated Turbulent Flows, Ph.d.-thesis, IMT
IMT-2010-63	Seim, Knut Sponheim	Mixing Process in Dense Overflows with Emphasis on the Faroe Bank Channel Overflow. Ph.d.thesis, IMT
IMT-2010-64	Jia, Huirong	Structural Analysis of Intect and Damaged Ships in a Collission Risk Analysis Perspective. Ph.d.thesis CeSoS.
IMT-2010-65	Jiao, Linlin	Wave-Induced Effects on a Pontoon-type Very Large Floating Structures (VLFS). Ph.D.-thesis, CeSOS.
IMT-2010-66	Abrahamsen, Bjørn Christian	Sloshing Induced Tank Roof with Entrapped Air Pocket. Ph.d.thesis, CeSOS.
IMT-2011-67	Karimirad, Madjid	Stochastic Dynamic Response Analysis of Spar-Type Wind Turbines with Catenary or Taut Mooring Systems. Ph.d.-thesis, CeSOS.
IMT-2011-68	Erlend Meland	Condition Monitoring of Safety Critical Valves. Ph.d.-thesis, IMT.
IMT-2011-69	Yang, Limin	Stochastic Dynamic System Analysis of Wave Energy Converter with Hydraulic Power Take-Off, with Particular Reference to Wear Damage Analysis, Ph.d. Thesis, CeSOS.
IMT-2011-70	Visscher, Jan	Application of Particla Image Velocimetry on Turbulent Marine Flows, Ph.d.Thesis, IMT.
IMT-2011-71	Su, Biao	Numerical Predictions of Global and Local Ice Loads on Ships. Ph.d.Thesis, CeSOS.
IMT-2011-72	Liu, Zhenhui	Analytical and Numerical Analysis of Iceberg Collision with Ship Structures. Ph.d.Thesis, IMT.
IMT-2011-73	Aarsæther, Karl Gunnar	Modeling and Analysis of Ship Traffic by Observation and Numerical Simulation. Ph.d.Thesis, IMT.

Report No.	Author	Title
IMT-2011-74	Wu, Jie	Hydrodynamic Force Identification from Stochastic Vortex Induced Vibration Experiments with Slender Beams. Ph.d.Thesis, IMT.
IMT-2011-75	Amini, Hamid	Azimuth Propulsors in Off-design Conditions. Ph.d.Thesis, IMT.
IMT-2011-76	Nguyen, Tan-Hoi	Toward a System of Real-Time Prediction and Monitoring of Bottom Damage Conditions During Ship Grounding. Ph.d.thesis, IMT.
IMT-2011-77	Tavakoli, Mohammad T.	Assessment of Oil Spill in Ship Collision and Grounding, Ph.d.thesis, IMT.
IMT-2011-78	Guo, Bingjie	Numerical and Experimental Investigation of Added Resistance in Waves. Ph.d.Thesis, IMT.
IMT-2011-79	Chen, Qiaofeng	Ultimate Strength of Aluminium Panels, considering HAZ Effects, IMT
IMT-2012-80	Kota, Ravikiran S.	Wave Loads on Decks of Offshore Structures in Random Seas, CeSOS.
IMT-2012-81	Sten, Ronny	Dynamic Simulation of Deep Water Drilling Risers with Heave Compensating System, IMT.
IMT-2012-82	Berle, Øyvind	Risk and resilience in global maritime supply chains, IMT.
IMT-2012-83	Fang, Shaoji	Fault Tolerant Position Mooring Control Based on Structural Reliability, CeSOS.
IMT-2012-84	You, Jikun	Numerical studies on wave forces and moored ship motions in intermediate and shallow water, CeSOS.
IMT-2012-85	Xiang, Xu	Maneuvering of two interacting ships in waves, CeSOS
IMT-2012-86	Dong, Wenbin	Time-domain fatigue response and reliability analysis of offshore wind turbines with emphasis on welded tubular joints and gear components, CeSOS
IMT-2012-87	Zhu, Suji	Investigation of Wave-Induced Nonlinear Load Effects in Open Ships considering Hull Girder Vibrations in Bending and Torsion, CeSOS
IMT-2012-88	Zhou, Li	Numerical and Experimental Investigation of Station-keeping in Level Ice, CeSOS
IMT-2012-90	Ushakov, Sergey	Particulate matter emission characteristics from diesel enignes operating on conventional and alternative marine fuels, IMT
IMT-2013-1	Yin, Decao	Experimental and Numerical Analysis of Combined In-line and Cross-flow Vortex Induced Vibrations, CeSOS

Report No.	Author	Title
IMT-2013-2	Kurniawan, Adi	Modelling and geometry optimisation of wave energy converters, CeSOS
IMT-2013-3	Al Ryati, Nabil	Technical condition indexes doe auxiliary marine diesel engines, IMT
IMT-2013-4	Firoozkoohi, Reza	Experimental, numerical and analytical investigation of the effect of screens on sloshing, CeSOS
IMT-2013-5	Ommani, Babak	Potential-Flow Predictions of a Semi-Displacement Vessel Including Applications to Calm Water Broaching, CeSOS
IMT-2013-6	Xing, Yihan	Modelling and analysis of the gearbox in a floating spar-type wind turbine, CeSOS
IMT-7-2013	Balland, Océane	Optimization models for reducing air emissions from ships, IMT
IMT-8-2013	Yang, Dan	Transitional wake flow behind an inclined flat plate – Computation and analysis, IMT
IMT-9-2013	Abdillah, Suyuthi	Prediction of Extreme Loads and Fatigue Damage for a Ship Hull due to Ice Action, IMT
IMT-10-2013	Ramìrez, Pedro Agustìn Pèrez	Ageing management and life extension of technical systems. Concepts and methods applied to oil and gas facilities, IMT
IMT-11-2013	Chuang, Zhenju	Experimental and Numerical Investigation of Speed Loss due to Seakeeping and Maneuvering. IMT
IMT-12-2013	Etemaddar, Mahmoud	Load and Response Analysis of Wind Turbines under Atmospheric Icing and Controller System Faults with Emphasis on Spar Type Floating Wind Turbines, IMT
IMT-13-2013	Lindstad, Haakon	Strategies and measures for reducing maritime CO2 emissons, IMT
IMT-14-2013	Haris, Sabril	Damage interaction analysis of ship collisions, IMT
IMT-15-2013	Shainee, Mohamed	Conceptual Design, Numerical and Experimental Investigation of a SPM Cage Concept for Offshore Mariculture, IMT
IMT-16-2013	Gansel, Lars	Flow past porous cylinders and effects of biofouling and fish behavior on the flow in and around Atlantic salmon net cages, IMT
IMT-17-2013	Gaspar, Henrique	Handling Aspects of Complexity in Conceptual Ship Design, IMT
IMT-18-2013	Thys, Maxime	Theoretical and Experimental Investigation of a Free Running Fishing Vessel at Small Frequency of Encounter, CeSOS

Report No.	Author	Title
IMT-19-2013	Aglen, Ida	VIV in Free Spanning Pipelines, CeSOS
IMT-1-2014	Song, An	Theoretical and experimental studies of wave diffraction and radiation loads on a horizontally submerged perforated plate, CeSOS
IMT-2-2014	Rogne, Øyvind Ygre	Numerical and Experimental Investigation of a Hinged 5-body Wave Energy Converter, CeSOS
IMT-3-2014	Dai, Lijuan	Safe and efficient operation and maintenance of offshore wind farms, IMT
IMT-4-2014	Bachynski, Erin Elizabeth	Design and Dynamic Analysis of Tension Leg Platform Wind Turbines, CeSOS
IMT-5-2014	Wang, Jingbo	Water Entry of Freefall Wedged – Wedge motions and Cavity Dynamics, CeSOS
IMT-6-2014	Kim, Ekaterina	Experimental and numerical studies related to the coupled behavior of ice mass and steel structures during accidental collisions, IMT
IMT-7-2014	Tan, Xiang	Numerical investigation of ship's continuous-mode icebreaking in leverl ice, CeSOS
IMT-8-2014	Muliawan, Made Jaya	Design and Analysis of Combined Floating Wave and Wind Power Facilities, with Emphasis on Extreme Load Effects of the Mooring System, CeSOS
IMT-9-2014	Jiang, Zhiyu	Long-term response analysis of wind turbines with an emphasis on fault and shutdown conditions, IMT
IMT-10-2014	Dukan, Fredrik	ROV Motion Control Systems, IMT
IMT-11-2014	Grimsmo, Nils I.	Dynamic simulations of hydraulic cylinder for heave compensation of deep water drilling risers, IMT
IMT-12-2014	Kvittem, Marit I.	Modelling and response analysis for fatigue design of a semisubmersible wind turbine, CeSOS
IMT-13-2014	Akhtar, Juned	The Effects of Human Fatigue on Risk at Sea, IMT
IMT-14-2014	Syahroni, Nur	Fatigue Assessment of Welded Joints Taking into Account Effects of Residual Stress, IMT
IMT-1-2015	Bøckmann, Eirik	Wave Propulsion of ships, IMT
IMT-2-2015	Wang, Kai	Modelling and dynamic analysis of a semi-submersible floating vertical axis wind turbine, CeSOS
IMT-3-2015	Fredriksen, Arnt Gunvald	A numerical and experimental study of a two-dimensional body with moonpool in waves and current, CeSOS

Report No.	Author	Title
IMT-4-2015	Jose Patricio Gallardo Canabes	Numerical studies of viscous flow around bluff bodies, IMT
IMT-5-2015	Vegard Longva	Formulation and application of finite element techniques for slender marine structures subjected to contact interactions, IMT
IMT-6-2015	Jacobus De Vaal	Aerodynamic modelling of floating wind turbines, CeSOS
IMT-7-2015	Fachri Nasution	Fatigue Performance of Copper Power Conductors, IMT
IMT-8-2015	Oleh Karpa	Development of bivariate extreme value distributions for applications in marine technology, CeSOS
IMT-9-2015	Daniel de Almeida Fernandes	An output feedback motion control system for ROVs, CeSOS/AMOS
IMT-10-2015	Bo Zhao	Particle Filter for Fault Diagnosis: Application to Dynamic Positioning Vessel and Underwater Robotics, CeSOS
IMT-11-2015	Wenting Zhu	Impact of emission allocation in maritime transportation, IMT
IMT-12-2015	Amir Rasekhi Nejad	Dynamic Analysis and Design of Gearboxes in Offshore Wind Turbines in a Structural Reliability Perspective, CeSOS
IMT-13-2015	Arturo Jesùs Ortega Malca	Dynamic Response of Flexibles Risers due to Unsteady Slug Flow, CeSOS
IMT-14-2015	Dagfinn Husjord	Guidance and decision-support system for safe navigation of ships operating in close proximity, IMT
IMT-15-2015	Anirban Bhattacharyya	Ducted Propellers: Behaviour in Waves and Scale Effects, IMT
IMT-16-2015	Qin Zhang	Image Processing for Ice Parameter Identification in Ice Management, IMT
IMT-1-2016	Vincentius Rumawas	Human Factors in Ship Design and Operation: An Experiential Learning, IMT
IMT-2-2016	Martin Storheim	Structural response in ship-platform and ship-ice collisions, IMT
IMT-3-2016	Mia Abrahamsen Prsic	Numerical Simulations of the Flow around single and Tandem Circular Cylinders Close to a Plane Wall, IMT
IMT-4-2016	Tufan Arslan	Large-eddy simulations of cross-flow around ship sections, IMT
IMT-5-2016	Pierre Yves-Henry	Parametrisation of aquatic vegetation in hydraulic and coastal research, IMT

Report No.	Author	Title
IMT-6-2016	Lin Li	Dynamic Analysis of the Instalation of Monopiles for Offshore Wind Turbines, CeSOS
IMT-7-2016	Øivind Kåre Kjerstad	Dynamic Positioning of Marine Vessels in Ice, IMT
IMT-8-2016	Xiaopeng Wu	Numerical Analysis of Anchor Handling and Fish Trawling Operations in a Safety Perspective, CeSOS
IMT-9-2016	Zhengshun Cheng	Integrated Dynamic Analysis of Floating Vertical Axis Wind Turbines, CeSOS